

UNIVERSITY
OF COLOGNE

MACRO TO MICRO: MULTI-SCALE ANALYTICAL APPROACHES FOR RESEARCHING PAST HUMAN-LANDSCAPE INTERACTIONS

INAUGURALDISSERTATION
ZUR ERLANGUNG DES DOKTORGRADES
DER MATHEMATISCH-NATURWISSENSCHAFTLICHEN FAKULTÄT
DER UNIVERSITÄT ZU KÖLN

vorgelegt von

MIRIJAM CHRISTINA REBECCA ZICKEL

KÖLN, 2026

ABSTRACT

Geoarchaeology and landscape reconstruction aim to decipher past environments from fragmented evidence, residues, and excerpts. This undertaking necessitates substantial interdisciplinary collaboration and result reproducibility, which sometimes requires methodological innovation. Information gathered at various scales, ranging from extensive land cover data to micromorphological observations in soils and (archaeo-) sediments, can illuminate distinct facets of landscape evolution or traces of prehistoric human activity. Both are crucial for constructing a comprehensive understanding of past landscapes as well as past human-landscape interactions. Our comprehension is shaped not only by direct field observations but also by the interpretation of individual analysis results. Consequently, multi scale approaches are indispensable in palaeoenvironmental science and geoarchaeology, as integrating disciplinary insights (perspectives) and evidence helps to complete the picture of past landscapes and human interaction with them. Continuous methodological development is essential to facilitate the comparison and integration of results from diverse analytical techniques, thereby enhancing compatibility. Integrative approaches, such as site location analysis, are valuable for comprehending prehistoric human behaviour and enabling the detection of important archaeological sites. At a large scale, using an example from the Southern Levant, this research demonstrates how archaeological field survey data can be effectively combined with (palaeo-) environmental geodata, including hydrogeological and land cover information, to assess the potential for undiscovered Upper Palaeolithic sites within the study area using Multi Criteria Decision Analysis (MCDA). In this way promising areas for future archaeological surveys were identified. This demonstrates that comprehending site selection of prehistoric humans and identifying areas likely to preserve archaeological sites are fundamental not only for more focused fieldwork but also for the protection of cultural heritage. Furthermore, at the meso scale, comprehensive landscape reconstruction is crucial for elucidating landscape evolution in conjunction with prehistoric land use. However, site catchment analysis, particularly in data-scarce regions, remains challenging. The Bronze Age site of Toboliu in western Romania, situated at the edge of the Carpathian Basin, exemplifies a remote area with significant research potential but limited palaeoenvironmental knowledge. Taking the differentiation between landscape features resulting from human (Bronze Age) landscape interaction ∼3600 years ago before present (BP) and those shaped by natural processes as a key challenge of this case study, multi scale methods for landscape

reconstruction are applied. This includes chronostratigraphic (luminescence and radiocarbon dating), soil, and palynological analyses, which are combined with the interpretation of geospatial data such as digital elevation, multispectral, and geomagnetic imagery. The results reveal a complex pattern of landscape evolution and Bronze Age land use, indicating that relief and soil primarily developed through earlier natural processes, dominated by Pleistocene-Holocene loess-derivate deposition and fluvial activity. Furthermore, it has been demonstrated that closed depressions (CDs), which were initially suspected to result from Bronze Age land use, are in fact attributable to earlier landscape-forming, periglacial processes during the Pleistocene. Focusing on the microscale of the local Bronze Age tell settlement, a primary objective is to identify materials used for construction, such as floorings and coverings, and to determine their raw material sources. In this context and based on a proof of concept from a well-studied Loess-palaeosol sequence (LPS) in Rheindahlen, Germany, a method for digital analysis of micromorphological samples derived from the tell profiles was developed. It can be shown that machine learning (ML)-based image and spatial analysis on thin section scans can augment traditional micromorphological analysis. Additionally, Micro-XRF analysis proves to be valuable for micromorphological studies and is therefore explored more extensively in the context of house floors from the tell sequence. Using Micro-XRF it can be demonstrated that diverse combinations of local minerogenic materials—primarily loess-derivate-based from the surroundings of the settlement were used to create a high variability of different house floors. Additionally, sophisticated coverings, such as wooden planks and plasters can be characterised by their chemical composition. Essentially, this research underscores the significant potential of the multi-scalar approach, which integrates different analytical approaches in geoarchaeology and landscape reconstruction, to enhance our understanding of a complex palaeogeographic picture.

ZUSAMMENFASSUNG

Geoarchäologie und Landschaftsrekonstruktion zielen darauf ab, vergangene Umwelten anhand fragmentierter Hinweise, Rückstände und Auszüge zu entschlüsseln. Dieses Unterfangen erfordert erhebliche interdisziplinäre Zusammenarbeit, die Reproduzierbarkeit der Ergebnisse und in diesem Zusammenhang technische Innovationen, welche es ermöglichen unterschiedlichste Methoden zusammenzubringen. Informationen, die in verschiedenen Maßstäben gesammelt werden, von weiträumigen Landbedeckungsdaten bis hin zu kleinräumigen mikromorphologischen Beobachtungen in Böden und (Archäo-) Sedimenten, können unterschiedliche Facetten der Landschaftsentwicklung oder Spuren prähistorischer menschlicher Aktivität beleuchten. Beides ist entscheidend für den Aufbau eines umfassenden Verständnisses vergangener Landschaften und prähistorischer Mensch-Landschaft Interaktion. Unser Verständnis wird aber nicht nur durch direkte Feldbeobachtungen, sondern auch durch die Interpretation individueller Analyseergebnisse geprägt. Folglich sind multiskalige Ansätze in der Paläo-Umweltwissenschaft und Geoarchäologie unerlässlich, da die Integration Disziplin-bezogener (perspektivischer) Erkenntnisse und Nachweise dazu beiträgt, das Bild vergangener Landschaften und der menschlichen Interaktion mit ihnen zu vervollständigen. Eine kontinuierliche methodische Entwicklung ist unerlässlich, um den Vergleich und die Integration von Ergebnissen verschiedener analytischer Techniken zu erleichtern und so die Kompatibilität zu verbessern. Integrative Ansätze, wie die archäologische Fundstellen-Standortanalyse, sind entscheidend für das Verständnis von prähistorisch-menschlichen Aktionsräumen und das Detektieren von wichtigen archäologischen Fundstätten. In großem Maßstab, am Beispiel der südlichen Levante, zeigt der gewählte Forschungsansatz *Multi Criteria Decision Analysis* (MCDA), wie archäologische Fundstelleninformationen effektiv mit (paläo-) umweltbezogenen Geodaten, einschließlich hydrogeologischer und Landbedeckungsinformationen, kombiniert werden können, um das Potenzial für unentdeckte jungpaläolithische Stätten im Untersuchungsgebiet zu bewerten. So konnten vielversprechende Flächen für zukünftige archäologische Feldforschung erkannt werden. Es wird gezeigt, dass gewonnen Erkenntnisse über die Standortwahl von prähistorischen Menschen sowie die Identifizierung von Gebieten mit guten Erhaltungsbedingungen für archäologische Fundstellen, grundlegend für eine fokussierte Feldforschung und für den Schutz von kulturellem Erbe sind. Des Weiteren ist auf der Mesoebene eine umfassende Landschaftsrekonstruktion entscheidend für die Aufklärung der Landschaftsentwicklung in Verbindung mit prähis-

torischer Landnutzung. Die Einzugsgebietsanalyse, insbesondere in datenarmen Regionen, stellt allerdings eine Herausforderung dar. Die bronzezeitliche Fundstätte Toboliu in Westrumänien (Karpatenbeckenrand) ist ein Beispiel für ein abgelegenes Gebiet mit erheblichem Forschungspotenzial, aber begrenzten paläoumweltbezogenen Daten. Um der zentralen Herausforderung, zwischen Landschaftselementen zu unterscheiden, die aus bronzezeitlicher Landschaftsinteraktion vor ∼3600 Jahren **before present** (BP) resultieren, und solchen, die durch natürliche Prozesse entstanden sind, zu begegnen wurde eine multiskalige Methode für die Landschaftsrekonstruktion für die Fallstudie gewählt. Dies beinhaltet chronostratigraphische (Lumineszenz- und Radiokarbondatierung), Boden-, und palynologische Analysen in Kombination mit der Interpretation von Geodaten wie digitalen Höhenmodellen, multispektralen und geomagnetischen Aufnahmen, sowie historischer Karten. Die Ergebnisse der Fallstudie zeigen ein komplexes Muster der Landschaftsentwicklung und der bronzezeitlichen Landnutzung, was darauf hindeutet, dass Relief und Boden hauptsächlich durch natürliche Prozesse, dominiert von pleistozän-holozäner Löss-Derivat-Ablagerungen und fluvialer Aktivität, entstanden sind. Zudem konnte gezeigt werden, dass geschlossene Hohlformen, bei denen zunächst vermutet wurde sie resultieren aus bronzezeitlicher Landnutzung, auf frühere landschaftsformende, periglaziale Prozesse während des Pleistozäns zurückgehen. Mit Fokus auf die Mikroebene der bronzezeitlichen Tellsiedlung in der Fallstudie ist ein primäres Ziel die Identifizierung der verwendeten Baumaterialien, wie mineralische Fußbodenbestandteile und -beläge, und die Bestimmung der Rohmaterialquelle. In diesem Zusammenhang und basierend auf einem Machbarkeitsnachweis zu einer gut untersuchten Löss-Paläoboden-Sequenz (LPS) in Rheindahlen, Deutschland, wurde eine Methode zur digitalen Analyse mikromorphologischer Proben aus den Tellprofilen entwickelt. Es kann gezeigt werden das maschinelle Lernen (ML)-basierte Bildanalyse und räumliche Analyse anhand von Dünnschliffscans die klassische mikromorphologische Analyse sinnvoll ergänzen können. Zusätzlich erweist sich die Mikro-XRF-Analyse ebenfalls als wertvoll für mikromorphologische Studien und wurde im Kontext der Analyse der Hausfußböden aus der Tellsequenz erprobt. Damit ist ersichtlich, dass verschiedene Kombinationen lokaler minerogener Rohmaterialien, hauptsächlich Löss-Derivate aus der Siedlungsumgebung verwendet wurden, um vielfältige Hausbodentypen zu schaffen. Zusätzlich können aufwändigere Bodenbeläge, wie Holzplanken und Estrich, über ihre chemische Zusammensetzung charakterisiert werden. Im Wesentlichen unterstreicht diese Forschung das erhebliche Potenzial des multiskalaren Ansatzes, der verschiedene analytische Ansätze in Geoarchäologie und Landschaftsrekonstruktion integriert, um unser Verständnis eines komplexen paläogeographischen Bildes zu verbessern.

CONTENTS

I Introduction

1 Introduction 33
- 1.1 Addressing challenges in Landscape Reconstruction and Geoarchaeology 33
- 1.2 Research Objectives 36
- 1.3 Case Study: The Bronze Age site Toboliu, Romania 38
- 1.4 Research Methodology: From Macro to Micro Scale 41
- 1.5 Dissertation structure 44

II Research results

2 Upper Palaeolithic site distribution in the Levant 47
- 2.1 Introduction 50
- 2.2 Regional setting 53
- 2.3 Material and methods 57
  - 2.3.1 Geodata 58
  - 2.3.2 Location and accession of archaeological data 60
- 2.4 Results 62
  - 2.4.1 Spatial pattern 64
  - 2.4.2 Wadi Sabra case study: A comparison to field observation and high- resolution modelling 67
- 2.5 Discussion 72
- 2.6 Conclusion 78

3 Pleistocene-Holocene Landscape Evolution in Toboliu 81
- 3.1 Introduction 84
- 3.2 Study Area 85
- 3.3 Material and Methods 87
  - 3.3.1 GIS and Remote Sensing 87
  - 3.3.2 Field work and sampling 88
  - 3.3.3 Laboratory analysis and statistics 89
  - 3.3.4 Palynology 89
  - 3.3.5 Chronology 90
- 3.4 Results 91
  - 3.4.1 Geospatial context and Closed Depression morphometry 91
  - 3.4.2 Lithostratigraphy 92
  - 3.4.3 Geochronology 100
- 3.5 Discussion 101
  - 3.5.1 Soil-landscape evolutionary context 101
  - 3.5.2 Closed depression formation and palaeogeography 108

3.5.3 Thoughts on Bronze Age human-landscape interaction 110
3.6 Conclusion 113
4 MiGIS: micromorphological analysis using image classification 115
4.1 Introduction 118
4.2 Materials and methods 121
4.2.1 Micromorphological samples, analysis, and class definitions 122
4.2.2 Thin section imagery acquisition and pre-processing 123
4.2.3 Semi-supervised classification of thin section imagery 124
4.2.4 MiGIS toolbox 126
4.3 Results 130
4.3.1 MiGIS classification performance 131
4.3.2 Digital micromorphological results 132
4.4 Discussion 133
4.4.1 Methodological implications of MiGIS 133
4.4.2 Interpretation of the digital micromorphological results 138
4.4.3 Implications for micromorphology 139
4.5 Conclusion 141
5 Micromorphology and Micro-XRF analysis of house floors in Toboliu 149
5.1 Introduction 152
5.2 Setting 153
5.2.1 Sample context 153
5.3 Methods 156
5.3.1 Micromorphological analysis 156
5.3.2 Micro-XRF analysis 156
5.4 Results 158
5.4.1 Micromorphology 158
5.4.2 Micro-XRF measurements of selected microfacies 163
5.5 Discussion 171
5.5.1 Synthesis and characterisation of the flooring units 171
5.5.2 Origin and alteration of the construction materials 173
5.5.3 Bronze Age flooring techniques 174
5.5.4 Potential and limits of combined Micro XRF and micromorphological analyses 177
5.6 Conclusion 179

III Discussion
6 Discussion 183

6.1 Landscape reconstruction methods 183
6.1.1 Macro scale - landscape analysis (objective 1.1) 183
6.1.2 Meso scale - landscape analysis (objective 1.2) 184
6.2 Micromorphological advances 186
6.2.1 Micromorphology and image classification (objective 2.1) 186
6.2.2 Micromorphology and Micro-XRF (objective 2.2) 187

IV Conclusion
7 Conclusion 191

V Appendix
A Upper Palaeolithic sites and where to find them 195
A.1 Methods 195
A.1.1 Pre-processing 195
A.1.2 Processing 196
A.1.3 Analysis 196
A.2 Results 201
A.2.1 Area statistics 201
A.3 Data 213
B Pleistocene-Holocene Landscape Evolution and Closed Depressions in Toboliu 219
B.1 TDZ22 corings 219
B.2 Field work and surveying 219
B.3 Geospatial imagery 220
B.3.1 LiDAR imagery acquisition, ANCPI 2009-2014) 220
B.3.2 WorldView-3 satellite imagery 220
B.3.3 Geomagnetic imagery 220
B.4 Laboratory analysis, element ratios, and statistics 221
B.4.1 D.1 Sample preprocessing 221
B.4.2 Grain size analysis 221
B.4.3 Carbon analysis 221
B.4.4 Element concentrations 221
B.4.5 Geochemical ratios, statistics, and data visualisation 222
B.5 Chronology - Optical stimulated luminescence dating 222
B.6 Dust source indicators 227
B.7 Core 12 data and main chronostratigraphic units 228
B.8 Grain size frequency plots of Cores 5, 12, and 13 229
B.9 Core 15 data and main chronostratigraphic units 230
C MiGIS: micromorphological soil and sediment thin section analysis 231
C.1 Implemented geoalgorithms in QGIS 3 231
C.2 Classification results and accuracy for the Rheindahlen thin sections 232
C.3 Exemplary individual feature class visualisation 235

D Micromorphology and Micro-XRF analysis of house floors in Toboliu 237
D.1 TS 1, micromorphological sample description 237
D.2 TS 12, micromorphological sample description 239
D.3 TS 21-1, micromorphological sample description 241
D.4 TS 16, micromorphological sample description 243
D.5 TS 5, micromorphological sample description 245
D.6 TS 19-2, micromorphological sample description 247
D.7 Single values of the micro-XRF measurements in selected flooring microfacies 249
D.8 Micro-XRF measurement results per thin section 250
References 255

LIST OF FIGURES

Figure 1.1 Overview map for the case study in Toboliu 39

Figure 2.1 Left: Elevation model of the study area with regions mentioned in the text, right: precipitational map of the Southern Levant (Schiebel, 2013) and locational map of the study area. Lake Tiberias in the north, to the south the present Jordan river valley, an endorheic basin (Frumkin et al., 2017) containing the present Dead Sea and the southern Wadi Araba. To the east, the Transjordan Rift Escarpment marks the transition to the wide-open Jordanian plains which are not part of this study. 54

Figure 2.2 Workflow diagram of the performed site expectancy (grade of preservation) analysis. It shows the datasets used and their processing within the main work steps: pre-processing, processing and analysis. Pre-processing is mainly concerned with data acquisition and general adjustments in Geographic Information System (GIS). In processing, the data is adapted to the extent of the study area and the geodata is linked to the archaeological site database. In the analysis stage, the data prepared in the previous steps are processed in the Multi Criteria Decision Analysis (MCDA), the maps are produced and subjected to a revision, and the results thus obtained are checked in the accuracy assessment. The displayed procedure serves to establish criteria for determining areas with the maximum likelihood of archaeological sites in the study area. 59

Figure 2.3 Histograms of site preservation on different factors. Classes for each parameter see Table 2.4,Fig. 2.1 and Appendix Figs. A.2-A.9 63

Figure 2.4 Class name lists for Fig.2.3 64

Figure 2.5 Multi Criteria Decision Analysis (MCDA) derived archaeological site preservation. Site ID# see Appendix, Table A.8 68

Figure 2.6 Detailed predicted site expectancy: a) North, b) Dead Sea, c) Central Negev, d) Wadi Sabra. Site ID# see Appendix, Table A.8. 69

Figure 2.7 Computed archaeological site expectancy (Multi Criteria Decision Analysis MCDA) for the Reference Dataset (a) and Detection Change in comparison with the original dataset (b). Note: Only areas present in the original dataset are computed. 70

Figure 2.8 Upper Wadi Sabra landform classification a) Landform classification overview, b) detail Sabra 4, c) outcrop of sediment remnant with clean profiles in the upper part and detritic cones in the lower part, d) Multi Criteria Decision Analysis MCDA results original dataset, e) MCDA results, reference dataset. 71

Figure 3.1 a) Study area at the eastern Carpathian Basin (CB) fringe in Romania, close to the river Crişul Repede in the north and the Apuseni mountains to the east (Overview: hillshade by ESRI (2019), Digital Elevation Model (DEM) basemap: USGS - United States Geological Survey (2009), National borders by Natural-Earth (2021). Generalised permafrost boundaries of the Last Glacial Maximum (LGM) (Lehmkuhl et al. 2020). Loess and loess derivates as compiled by Lindner et al. (2017a). b) Study area (Light Detection and Ranging (LiDAR) elevation data by National Agency for Cadastre and (ANCPI) (2014) showing the tell, Closed Depression (CD)s, and coring locations related to this study. Violet, filled diamonds, black numbers: main cores presented in detail; violet, open diamonds, grey numbers: additional cores mentioned in the text. Figures for Core 12 (Appendix,Fig. B.5) and Core 15 (Appendix, Fig. B.7), as well as a cross-section scheme are in Appendix, Fig. B.1. 87

Figure 3.2 a) colour-infrared (CIR) image based on multispectral WorldView-3 data, March 2021 (DigitalGlobe, 2021). b) LiDAR digital elevation model (National Agency for Cadastre and (ANCPI), 2014), with yellow to orange colour for elevated parts and light yellow to greenish colour for low level areas in the study area. Linear (channel-like) surface features are indicated by grey arrows in a) whitish soil marks and b) light yellow to white linear features of relatively low elevation. c) Geomagnetic imagery (Kienlin, 2021), showing subsurface features by magnetic orientation discontinuities in the sediments, such as fine linear features which are marked by red arrows. Closed depressions (CD) (this study) locations are indicated by numbers in a) and b). d) Detail of a georeferenced historical map of the region (László ffy et al., 1938), showing water bodies and flood risk areas before river regulations (Section 3.2). 92

Figure 3.3 a) Geomagnetic imagery combined with DEM information, showing the spatial distribution of the listed closed depressions (CDs) in relation to noticeable elevation and subsurface features (Fig3.2), b) table with 'rim-to-rim' measurements (diameter based on geomagnetic data) and depth based on the DEM for the listed CDs, c) geomagnetic imagery detail of CD2, d) photograph showing the full dimensions (DEM based) of CD2 in the study area, e) DEM sourced elevation profile of CD2, the transect position is displayed in a), note that rims are not visible on the surface. 93

Figure 3.4 Core 5 data and main stratigraphical units. Depth is given in m above mean sea level (a.m.s.l.), sample depth and numbers are highlighted by yellow dots. The core plot displays the mean grain size ($\bar{x}$), carbonate and organic carbon (Org. C) contents, as well as rubidium (Rb)/strontium (Sr) ratio and the Chemical Proxy of Alteration (CPA) considered as weathering/pedogenesis proxies. Proxy details can be found in Section 3.3.3 and Appendix B.4. 94

Figure 3.5 Grain Size Distribution (GSD) for the lower a) Silt phase 1 and the upper b) Silt phase 2 described in Core 5. A similar GSD for Silt phase 1 and 2 can be found in the analysed reference cores 2 ,3 ,8 ,12 and 14. Samples (S.+№) are displayed using separate colour palettes per core. Sampling depth is indicated using m a.m.s.l. values. Intra-profile grain size frequencies for Cores 5, 12, and 13 can be found in Appendix B.8, Figure B.6c) Results of a Principal Component Analysis (PCA) using geochemical/-physical data X-ray fluorescence (XRF), grain size fractions, organic carbon and carbonate concentrations) of all sampled cores, Principal Component (PC)1 and PC2 explain 50% variance in the data set. The PCA results underline the different character of Silt phase 1 and 2 which becomes apparent in the GSD plots. The violet dots (loam) represent very sandy silt samples from the lowest section of Silt phase 1. 95

Figure 3.6 Geochemical and granulometric data for the top of Core 5 (Units 4, Silt phase 2) and 5 (Topsoil) for soil type definition after IUSS (WRB) WG (2015). Yellow dots: sample positions show pH sampling positions. ICv: Silt phase 2, fAh: mollic Ah-horizon covered by D(h)j: colluvium (Hartmann et al., 2024), and Ap: ploughing zone. 96

Figure 3.7 Core 13 data and main stratigraphical units. Depth is given in metres above mean sea level (a.m.s.l.), and sample depth and numbers are indicated by yellow dots. Mean grain size ($\bar{x}$) is displayed by the core plot. Carbonate and organic carbon contents, as well as Rb/Sr ratios (weathering proxy) and the Chemical Proxy of Alteration (CPA) as weathering/pedogenesis proxy. aluminium (Al)/calcium (Ca), and iron (Fe)/manganese (Mn), and Fe/sulphur (S) ratio are considered as proxies for different hydromorphic settings. phosphorus (P)/silicon (Si) ratio is used as indicator for terrestrial input, such as biological/agricultural activity. Proxy details can be found in Section 3.3.3 and Appendix B.4. 98

Figure 3.8 Proportions of selected pollen types, spores and non-palynomorphs (NPPs) from the bottom and central dark layer in Units 3 (lower/upper limnic phase) and 4 (Siltation) of Core 13. 99

Figure 3.9 Synthesised spatial analysis results (Section 3.4.1). Colour-infrared CIR WorldView-3 image of March 2021 (DigitalGlobe, 2021). Red colours show vegetation. Bare soil is represented by dark colours with increased soil moisture or turbid water (dark green, petrol), light colours (white, cyan) indicate dry (e.g. sandy/permeable substrata) areas. Former wetland extent/flooded area (white dashed lines) based on historical data (Timár et al., 2006; Lászlóffy et al., 1938), interconnected river network (yellow dashed lines), and closed depressions CDs (black dashed lines) are based on DEM and historical data (Fig. 3.2b, d). Key coring locations are indicated by orange dots. 104

Figure 3.10 Stacked image scans of the presented Cores 5 (local stratigraphy) and 13 (Closed Depression 2) as well as reference cores from the year 2022 drilling campaign (Fig. 3.1) in relation to the identified chronostratigraphical units (this study). Main stratigraphical units are 1: Fluvial phase, 2: Loess derivate phase 1, 3: Palaesol, 4: Loess derivate 2, 5: Holocene soil. Below colluvium (Section 3.4.2: Soil unit) a siltation phase can be identified on top of a pond bottom unit in Core 13. A comparable stratigraphy can be observed in Core 15. 106

Figure 3.11 a) Formation and degradation of a closed system type pingo after Mackay (1998). process illustration for the closed depressions (CDs) along the grey arrow, b) closed system pingo growing in an oxbow of a braided river system, the oxbow course is indicated by the white dotted line c) fully degraded closed system pingo showing a typical circular rim around a water-filled depression (initial pingo ruin) in Tombstone National Park, Canada. Discharge direction is indicated by the white dashed arrow (Photos by Julius Kunz, University of Würzburg, Germany, 2018-2023). 111

Figure 4.1 Workflow diagram showing digital thin section (TS) analysis principles and main processing steps. transmitted light (TL): Transmitted light; cross-polarised light (XPL): Cross-polarised light; reflected light (RL): Reflected light; Coordinate Reference System (CRS): Cooordinate reference system; region of interest (ROI): Region of interest. 120

Figure 4.2 Random single-pixel values for different abundant materials in sediment thin sections (TSs) captured from TS A4. The "signatures" of the features are illustrated by artificial lines between the measured pixel values to highlight differences. 125

Figure 4.3 Micromorphological Geographic Information System (MiGIS) integrated region of interest (ROI) assessment illustrates training data set validity: class value ranges and standard deviation for each of the reflected light RL, transmitted light TL, and cross-polarised light XPL red–green–blue (RGB) bands 1–9. Data of TS B7 imagery. 129

Figure 4.4 Details of selected classification results (Class. map) compared to captures of the transmitted (TL), cross-polarised (XPL), and reflected light (RL) scans of B2: linear basic distribution pattern; A7 (top): clay coating in a vugh; A4: coarse sand grain; A7 (bottom): orthic manganese oxide and iron hydroxide nodule. 144

Figure 4.5 Confusion matrices for the classification examples of TS A4 with an overall accuracy of 100 %, B7 with an overall accuracy of 97 %, and C5 with an overall accuracy of 87 %. 145

Figure 4.6 Comparison of classified area (CA) proportions and class accuracy parameter (overall, producer's accuracy (PA), and user's accuracy (UA)) for thin section (TS) C5, scanned with 1200 and 2400 dpi resolution (data: C.2). 145

Figure 4.7 Comparison of class area proportions derived from results based on a classification model trained on the same thin section (TS) versus opposite TS. Note the various y-axis scale ranges to ensure the illustration of relative differences within the classes. 146

Figure 4.8 Input and output of the image classification of thin section (TS) A4, B7, and C5, which originate from Bt horizons of the Rheindahlen sequence. The classification maps on the right combine the multi-RGB information of the trns-mitted light (TL), cross-polarised light [XPL), and reflected light (RL) input images and visualise the spatial distribution patterns of the micromorphological features. 147

Figure 4.9 Results of the class-based area assessment for thin section A4, B7, and C5. Po: pore space; Gm1: Groundmass 1 (bleached); Gm2: Groundmass 2 (iron hydroxide abundance); Sg: medium and coarse sand and fine gravel; Cc: clay coatings; Ccd: dark clay coatings; Fe: iron hydroxide concretions; Mn: manganese oxide concretions; PA: producer's accuracy; UA: user's accuracy (data: Appendix C.2). 148

Figure 5.1 a) Shuttle Radar Topography Mission (SRTM) digital elevation model (DEM) (USGS - United States Geological Survey, 2009), Loess distribution (Lindner et al., 2017a), Rivers + lake centerlines (Natural-Earth, 2021), edited version of Zickel et al. (sub.) b) Worldview-3 scene from 2021-03-25, (DigitalGlobe, 2021) on magnetographic imagery (Kienlin, 2021) showing the position of excavation Unit 1. 154

Figure 5.2 Sampled excavation profiles of Unit 1, excavated in the year 2017, and location of the settlement phases: a) western, b) northern, and c) eastern section. The purple dots indicate micromorphological sample positions. 156

Figure 5.3 Selected thin sections (TS) from the Tell Toboliu stratigraphy. Determined microfacies are labelled with capital letters. Grey lines show microfacies borders and violet lines mark wood fragments. 158

Figure 5.4 Micrographs of TS 1: a) overview of silty sediment of MF 1D, with calcitic silt-sized quartz fragments (arrow) and mica in plane polarised light (PPL), b) the same in XPL; c) overview of organic silty material MF 1E with an open porphyric c/f related distribution pattern, coarse fraction sand-sized quartz; d) the same in XPL; g) articulated phytoliths (ELONGATES ENTIRE) in pseudomorphic in MF 1E in PPL h) fine domestic waste within the silty material of MF 1D, isolated ELONGATE DENTATE (white arrow) in PPL. 160

Figure 5.5 Micrographs of TS 12: a) overview of the clayey silt floor (MF 12D) composed of a double spaced porphyric c/f related distribution with a dominant silt-sized coarse fraction and a mostly parallel striated b-fabric in PPL, b) the same in XPL; c) multilaminated limpid clay coatings (cc) in PPL, d) the same in XPL; e) mineralised wood fragments (wf, within dotted white lines) located in a fine use layer in PPL, h) same in XPL; e) detail of the mineralised wood fragment with cell structure, the same in XPL. 161

Figure 5.6 Micrographs of TS 21-1: a) overview of MF 21-1E clayey silt floor with horizontally orientated plant temper (cereal chaff) and calcitic fragments (white arrows) in PPL, b) same in XPL; c) overview of MF 21-1D strongly clayey silt floor with horizontally orientated plant temper (cereal chaff) and calcitic fragments (cf) in PPL, d) same in XPL; e) strongly clayey silt of MF 21-1D in PPL f) causing a parallel and granostriated b-fabric in XPL, g) calcitic fragments in MF 21-1D in PPL; h) plant temper of MF 21-1D articulated ELONGATES DENTATE in PPL. 162

Figure 5.7 Micrographs of TS 16 and TS 5: TS 16 a) overview of MF 16G humic silty patches (H) mixed with clayey silt sediment (S) in PPL, b) same in XPL; c) overview impure calcareous silty sediment (MF 16E), partly layered with horizontally aligned pseudomorphic voids in PPL, d) the same in XPL; e) pseudomorphic voids derived from decayed plant material. TS5 f) mineralised wood fragment with former cell structure (MF 5A) in PPL; g) overview of a calcareous clayey silt floor (MF 5B) in PPL, h) the same in XPL. 164

Figure 5.8 Micrographs of TS 19-2: a) overview of MF 19-2E an impure clayey silt cover with micro charcoal (ch) and a calcitic fragments (cf) in PPL, b) the same in XPL; c) overview of a pure calcareous silt cover (MF 19-2C) with d) a calcitic-crystallitic b-fabric in XPL; e) mineralised wood fragments of different colour (white arrows) in A in PPL, f) the same in XPL. 165
Figure 5.9 Elemental mappings sourced from Micro X-ray fluorescence (Micro-XRF) of all thin sections (TS)s, post processed as described in Section. 5.3.2 Capital letters label the determined microfacies (Table 5.3), white squares indicate the centre points of measured area of interest (AOI)s for each microfacies. 168
Figure 5.10 Mean (dots) and scatter (polygon area) of Micro-XRF element point measurements per sediment flooring microfacies. 169
Figure 5.11 Results of a principal component analysis (PCA), based on Micro-XRF element point measurements. 170
Figure 5.12 Micro-XRF element point measurement results of wood residue samples, normalised and scaled values. 171
Figure 5.13 Scheme of (sub-) floorings and coverings found in the Tell Toboliu stratigraphy. Different (sub-) flooring types could have been determined in the following microfacies (microfacies (MF)). Silty: 1E; Clayey silt: 12E; Tempered (and silty/-clayey): 21-1D, 21-1E; Mottled: 16G. Wood coverings can be found in 12D, 5A and 19-2A. 19-2C represents a plastered covering. 175
Figure A.1 Weighted overlay function for suitability map calculation. x is the weight assigned to the specific raster dataset (criteria grid) 197
Figure A.2 Aspect. 204
Figure A.3 Elevation. 205
Figure A.4 Geomorphology. 206
Figure A.5 Hydrogeology. 207
Figure A.6 Potential river network. 208
Figure A.7 Slope. 209
Figure A.8 Terrain Ruggedness Index (Terrain Ruggedness Index (TRI)). 210
Figure A.9 Vegetation. 211
Figure A.10 Reference site ranking. 212

Figure B.1 Exemplary coring transect scheme for the NE to SE section. Core 4 was drilled in a low terrain position (channel-like elevation feature/-soil mark) and documented during field work only. The position of Core 12 lies beyond the transect, but was adjusted for illustrative reasons in this figure. 219

Figure B.2 Results of the dose recovery tests on samples C-L5377 (100-200 µm potassium-rich feldspars (FSP), 2mm aliquots, n=3), C-L5379 (100-200 µm FSP, 2mm aliquots, n=3), C-L5371 (4-11 µm Q, n=5) and C-L5374 (4-11 µm Q, n=5). Quartz measurements are shown as blue circles, while feldspar Post-Infrared Infrared Stimulated Luminescence (pIRIR) measurements are shown in red diamonds. The results of the single aliquots are indicated in lighter colours, while the means incl. standard errors are shown in stronger colours. Errors of Q are so small that they vanish behind the symbols. The acceptable recovered/given dose ratio of 1.0±0.1 is indicated with the dashed lines. 224

Figure B.3 Exemplary Optically Stimulated Luminescence (OSL) signals (A, D), dose response curves (B, E) and Tx/Tn plots (C, F) of a FSP sample (left) and a quartz sample (right). 225

Figure B.4 Bi-plots of common element oxides used for dust source determination in Loess Palaeosol Sequence (LPS). The displayed data set contains loess unit measurement values of eight analysed cores (this study). 227

Figure B.5 Core 12 data and main stratigraphic units. Depth is given in metres above mean sea level (a.m.s.l.), sample depth and numbers are highlighted by yellow points. Mean grain size ($\bar{x}$) is displayed by the core plot. Carbonate and Organic carbon (Org. C) contents (percentage of sample weight), as well as the Rb/Sr ratio to illustrate weathering intensity and the Chemical Proxy of Alteration (CPA) as weathering/pedogenesis proxies are displayed. Proxy details can be found in Appendix B.4. 228

Figure B.6 Intra-profile grain size frequencies and derivates for Cores 5, 12, and 13 after Schulte et al. (2018). 229

Figure B.7 Core 15 data and main chronostratigraphic units. Depth is given in metres above mean sea level (a.m.s.l.), sample depth and numbers are highlighted by yellow points. Mean grain size ($\bar{x}$) is displayed by the core plot. Black boxes show areas of core loss. Dating results are listed in calibrated years (cal a) before present (Before Present (BP)), reference year 1950). Carbonate and organic carbon contents (percentage of sample weight), as well as theRb/ Sr ratio to illustrate weathering intensity and the Chemical Proxy of Alteration (CPA) as weathering/pedogenesis proxies are displayed.Al/Ca, and Fe/Mn, andFe/S ratio highlight hydromorphic modes. P/Si ratio is used as indicator for biological/agricultural activity. 230

Figure C.1 Individual visualisation of classified feature classes, derived from the classification map of thin section A4. 236

Figure D.1 Thin section Tob 1: a) Transmitted (TL), equivalent to plane polarised light (PPL), scanned thin section image and mapped microfacies labels. b) Sample composition classification based on TL, cross-polarised light (XPL), and reflected light (RL) scanned imagery and Random Forest Algorithm (Zickel et al., 2024). 237

Figure D.2 Thin section Tob 12: a) Transmitted light (TL), equivalent to plane polarised light (PPL), scanned thin section image and mapped microfacies labels. b) Sample composition classification based on TL, cross-polarised light (XPL), and reflected light (RL) scanned imagery and Random Forest Algorithm (Zickel et al., 2024). 239

Figure D.3 Thin section Tob 21-1: a) Transmitted light (TL), equivalent to plane polarised light (PPL), scanned thin section image and mapped microfacies labels. b) Sample composition classification based on TL, cross-polarised light (XPL), and reflected light (RL) scanned imagery and Random Forest Algorithm (Zickel et al., 2024). 241

Figure D.4 Thin section Tob 16: a) Transmitted light (TL), equivalent to plane polarised light (PPL), scanned thin section image and mapped microfacies labels. b) Sample composition classification based on TL, cross-polarised light (XPL), and reflected light (RL) scanned imagery and Random Forest Algorithm (Zickel et al., 2024). 243
Figure D.5 Thin section Tob 5: a) Transmitted light (TL), equivalent to plane polarised light (PPL), scanned thin section image and mapped microfacies labels. b) Sample composition classification based on TL, cross-polarised light (XPL), and reflected light (RL) scanned imagery and Random Forest Algorithm (Zickel et al., 2024). 245
Figure D.6 Thin section Tob 19-2: a) Transmitted light (TL), equivalent to plane polarised light (PPL), scanned thin section image and mapped microfacies labels. b) Sample composition classification based on TL, cross-polarised light (XPL), and reflected light (RL) scanned imagery and Random Forest Algorithm (Zickel et al., 2024). 247
Figure D.7 Micro-XRF point measurements (single value scatter) on thin sections for the sediment flooring and calcareous covering classes, normalised and scaled values. 249
Figure D.8 Micro-XRF measurements of microfacies E in thin section 1. 250
Figure D.9 Micro-XRF measurements of microfacies G in thin section 16. 251
Figure D.10 Micro-XRF measurements of microfacies D and E in thin section 21-1. 251
Figure D.11 Micro-XRF measurements of the wooden residues in microfacies D and E in thin section 12. 252
Figure D.12 Micro-XRF measurements of the wooden residues in microfacies A in thin section 5. 252
Figure D.13 Micro-XRF measurements of the wooden residues in microfacies A and the calcareous flooring in C in thin section 19-2. 253

LIST OF TABLES

Table 2.1 Statistical testing of single parameters. Basic data for the calculation see in the Appendix (Tables A.2-A.6). *if two datasets are normally distributed a t-test was conducted instead of Mann-Whitney U. 66

Table 3.1 Core sampling context: Core locations are shown in Figure 3.1, CD refers to 'Closed depression'. Two different sampling tubes were used: open probes (diameter: 8 cm) and additional closed liners with 10 cm in diameter. Sampling depth is given in metres above mean sea level (a.m.s.l.). Sample size (n) per core implies the number of samples used for sediment (grain size - laser diffraction, elemental composition - XPL, and organic carbon/carbonate - DIMATOC) analysis, radiocarbon (accelerator mass spectrometry - AMS) and luminescence (Quartz and Feldspar OSL) dating. 88

Table 3.2 OSL dating results for samples from Cores 5 and 13. Sampling depth is given in metres above mean sea level (a.m.s.l.). Dates are listed in kilo years (ka) before today (reference year 2022 as the year of sampling and sample preparation) with 1σ error. Equivalent doses (D_e) and total dose rates are given with standard error. 100

Table 3.3 Results of accelerator mass spectrometry (AMS) for ^{14}C dating of bulk samples from Cores 5 and 13. Dates are listed in kilo years (ka) before present (BP), referring to the common reference year 1950. The calibrated kilo years (calibrated kilo years (cal ka)) age range has a confidence of 95.4% (2-sigma). Italicised letters imply unreliable dating results. 102

Table 4.1 Micromorphological features observed in thin sections (TSs) from the Rheindahlen loess–palaeosol sequence and class codes for semi-supervised TS image classification. 123

Table 4.2 MiGIS processing steps and related time expenditure per sample (Intel i7 processor, 32 GB RAM). 127

Table 5.1 Micromorphological sampling and archaeological context information for the sampled profiles (Fig. 5.2) of Unit 1 (excavation 2017). Dating is provided by uncalibrated radiocarbon ages. 155
Table 5.2 Overview for the micromorphological results of the selected samples. 166
Table 5.3 Micro-XRF classes based on the selected microfacies. 166
Table A.1 GIS processing and analysis tools of the QGIS environment (QGIS Development Team, 2022c) that were applied in the workflow. 200
Table A.2 **Geomorphology**; Count: No. of polygons, m^2: Total area of class, Frequency: No of sites in class 201
Table A.3 **Drainages**; Count: No. of polygons, m^2: Total area of class, Frequency: No of sites in class 202
Table A.4 **Hydrogeology**; Count: No. of polygons, m^2: Total area of class, Frequency: No of sites in class 202
Table A.5 **Vegetation**; Count: No. of polygons, m^2: Total area of class, Frequency: No of sites in class 202
Table A.6 **Elevation**; Count: No. of polygons, m^2: Total area of class, Frequency: No of sites in class 203
Table A.7 Confusion matrix for the reference dataset 203
Table A.8 Original sites; only the original dataset is referred to by number on the maps. This is a copy of the supplementary data, which can be found on the Quaternary International journal webpage. (*Continued on next page*) 214
Table A.9 Reference sites, only the original dataset is referred to by number on the maps. This is a copy of the supplementary data, which can be found on the Quaternary International journal webpage.(*Continued on next page*) 216
Table B.1 Different luminescence measurement protocols used in this study, following Murray and Wintle (2003) and Murray and Wintle (2000), Thomsen et al. (2008), and Kars et al. (2012). 224
Table B.2 Detailed OSL measurement data, giving the depth in metre above mean sea level (Depth m a.m.s.l.), grain size range, water content (W), accepted/measured aliquots (n/N), recycling ratios, concentrations of U, Th, and K, average D_e, dose rate and age. 226

Table C.1 Implemented geoalgorithms in MiGIS toolbox with references. 231
Table C.2 Total thin section (TS) classification results for the Rheindahlen stratigraphy. TS image classifications presented in Sect. 4.3 are highlighted. overall accuracy (OA); producer's accuracy (PA); user's accuracy (UA); n/a: respective constituent (feature class) not present in the TS. Quality criteria: 100 %–90 % class accuracy – very good; * 90 %–80 % class accuracy – good; ** < 80 % class accuracy – poor. 233
Table C.3 Total thin section (TS) classification results for the Rheindahlen stratigraphy. TS image classifications presented in Sect. 4.3 are highlighted. OA; producer's accuracy (PA); user's accuracy (UA); n/a: respective constituent (feature class) not present in the TS. Quality criteria: 100 %–90 % class accuracy – very good; * 90 %–80 % class accuracy – good; ** < 80 % class accuracy – poor. 234
Table D.1 Detailed micromorphological characterisation of sample TS 1: Microstructure, pores, groundmass properties, archaeological materials, and pedofeatures. 238
Table D.2 Detailed micromorphological characterisation of sample TS 12: Microstructure, pores, groundmass properties, archaeological materials, and pedofeatures. 240
Table D.3 Detailed micromorphological characterisation of sample TS 21-1: Microstructure, pores, groundmass properties, archaeological materials, and pedofeatures. 242
Table D.4 Detailed micromorphological characterisation of sample TS 16: Microstructure, pores, groundmass properties, archaeological materials, and pedofeatures. 244
Table D.5 Detailed micromorphological characterisation of sample TS 5: Microstructure, pores, groundmass properties, archaeological materials, and pedofeatures. 246
Table D.6 Detailed micromorphological characterisation of sample TS 19-2: Microstructure, pores, groundmass properties, archaeological materials, and pedofeatures. 248

LIST OF ABBREVIATIONS

AL aluminium

AOI area of interest

A.M.S.L. above mean sea level

AS arsenic

BA barium

BP Before Present

BCE Before Common Era

B.S.L. below surface level

CA calcium

CAL A calibrated years

CAL KA calibrated kilo years

CB Carpathian Basin

CD Closed Depression

CIR colour-infrared

CL chloride

CPA Chemical Proxy of Alteration

CRS Coordinate Reference System

DEM Digital Elevation Model

DSTFS Dead Sea Transform Fault System

FE iron

FSP potassium-rich feldspars

GIS Geographic Information System

GSD Grain Size Distribution

K potassium

KA kilo years

LGM Last Glacial Maximum

LIDAR Light Detection and Ranging

LPS Loess Palaeosol Sequence

MCDA Multi Criteria Decision Analysis

MF microfacies

MG manganese

MICRO-XRF Micro X-ray fluorescence

MIGIS Micromorphological Geographic Information System

MIS Marine Isotope Stage

ML Machine Learning

MN manganese

NA sodium

NPP Non-Palynomorph

OA overall accuracy

OBIA Object-Based Image Analysis

OIL oblique incident light

OSL Optically Stimulated Luminescence

P phosphorus

PA producer's accuracy

PB lead

PC Principal Component

PCA Principal Component Analysis

PPL plane polarised light

QZ Quartz

RB rubidium

RGB red–green–blue

RL reflected light

ROI region of interest

S sulphur

SI silicon

SR strontium

SRTM Shuttle Radar Topography Mission

TI titanium

TL transmitted light

TPI Topographic Position Index

TRI Terrain Ruggedness Index

TS thin section

UA user's accuracy

UTM Universal Transverse Mercator

WGS84 World Geodetic System 1984

XPL cross-polarised light

XRF X-ray fluorescence

ZR zirconium

Part I

INTRODUCTION

1 INTRODUCTION

1.1 ADDRESSING CHALLENGES IN LANDSCAPE RECONSTRUCTION AND GEOARCHAEOLOGY

The study of ancient landscapes and the interactions between human societies and their environments represents a complex and multifaceted endeavor. Geoarchaeology, as an interdisciplinary field within archaeology, plays a crucial role in reconstructing these landscapes and understanding the site formation processes that have shaped archaeological records over time (Siart et al., 2018c). This interdisciplinary domain integrates methodologies from earth sciences, archaeology, and environmental studies to provide insights into past human-environment interactions. However, the field faces significant methodological challenges that must be continuously addressed to enhance the accuracy and comprehensiveness of landscape reconstructions.

Soil-landscape systems and the archaeological context

One of the primary challenges in landscape reconstruction is the interpretation of geomorphological data, particularly in environments where organic proxies are scarce (i.e., poorly preserved). The integration of spatially extensive geoproxy records with other palaeoenvironmental data is essential yet challenging, as it necessitates careful consideration of context and local conditions (Thomas, 2013). The scarcity of continuous proxy records for palaeoenvironmental reconstructions, especially in remote regions with complex soil-landscape evolution, can lead to gaps in understanding and hinder comprehensive landscape reconstructions (Fitchett et al., 2016). However, the relationship between natural geomorphological features and archaeological sites is crucial in landscape reconstruction. Investigating soil-landscape systems across both past and present provides a means of reconstructing and understanding the regional environmental and geomorphic context of archaeological site settings. This approach enables researchers to explore site formation processes and the resources available to past societies (Renfrew, 1976; Siart et al., 2018c). Historically, the application of geoscience techniques to archaeological questions has evolved significantly since the 1970s. The integration of geoarchaeology with environmental archaeology and Quaternary geology has produced innovative approaches in physical geography, fostering interdisciplinary exchange (Hill, 2017). One ongoing challenge is the need for effective collaboration between different disciplines, such as physical geography and archaeology. Geoarchaeologists often encounter difficulties

in conveying geoscientific methods or results to archaeologists, complicating interdisciplinary dialogue and collaboration (Berna, 2019). A significant example is the use of micromorphology in the analysis of archaeosediments and a certain lack of result reproducibility. Effectively communicating microscopic observations and the spatial relationships among micromorphological phenomena presents challenges due to technical limitations (e.g. certain findings are difficult to illustrate through microphotography alone), which typically necessitates pedological and lithological knowledge for the accurate interpretation of micromorphological results (Shahack-Gross, 2016; Nicosia and Stoops, 2017). In conclusion, reconstructing past environments frequently entails working with incomplete or ambiguous data from diverse scales, which complicates the process of drawing definitive conclusions regarding human-environment interactions (Siart et al., 2018c). Consequently, Gladfelter (1977) underscored the importance of comprehensively integrating geoarchaeologists into archaeological excavations to effectively capture the micro, meso, and macro aspects of the soil, landscape, and archaeological context and promote interdisciplinary communication.

Integrating the different scales of geoarchaeology

The interpretation of geoarchaeological data frequently requires consideration of multiple scales, from particle to landscape level. This necessitates the development of methods that can effectively integrate data across these scales (Ghilardi, 2021). Particularly, computational techniques, such as data dimensionality reduction, can play a significant role in integrating data across different scales, enhancing analysis result reproducibility, and interdisciplinary communication. In recent years, the emergence of Digital Geoarchaeology has provided a new framework for integrating computational techniques with traditional landscape reconstruction methods, including for example chronostratigraphy and methods frequently applied in geoarchaeology, such as micromorphology. This promotes the classical holistic geographical research perspective, wherein various components and levels of soil-landscape systems are integrated to examine their relationships in space and time. Digital Geoarchaeology aims to facilitate the analysis of spatial relationships in geoarchaeology and landscape reconstruction. This approach can be employed, for example, to predict the locations of archaeological sites in extensive, inaccessible areas (Chapter 2), to analyse landforms related to human activity in regions with sparse data (Chapter 3), to utilise image classification for examining micromorphological patterns in thin sections (Chapter 4), or to explore environmental resource utilisation in settlement constructions (Chapter 5). The potential of this integrative approach to enhance our understanding of ancient landscapes and their formation processes is evident; however, comprehensive collaboration between archaeology, geosciences, and informatics remains rare (Siart et al., 2018c).

Research aim

This thesis examines specific methods in landscape reconstruction and geoarchaeology, tackling the aforementioned methodological challenges and evaluating their innovative potential. By examining the integration of diverse data types from different scales, interdisciplinary collaboration, and technological advancements, it seeks to contribute to a more nuanced understanding of landscape evolution and the complex interactions between prehistoric humans and their environments. Through this holistic, multi-perspective approach, the aim is to highlight the significance of innovative methodologies by utilising examples from three distinct contexts, spanning from macro to micro scales, with a specific focus on a case study at the remote Bronze Age site of Toboliu in Romania (Section 1.3). In this regard, this contribution seeks to address the challenges encountered in the field of geoarchaeology and to offer insights into future research directions within this dynamic and evolving discipline.

1.2 RESEARCH OBJECTIVES

As previously outlined, the effective integration of geoscientific and archaeological information across various scales is essential for advancing our understanding of prehistoric human-landscape interactions (Chapter 1.1). Establishing a robust methodological framework (Section 1.4) is a prerequisite for harmonising diverse data types and disciplinary formats, which will facilitate the synthesis of heterogeneous (palaeo-) geographical data, enabling a comprehensive investigation of landscape evolution and archaeological sites. The findings derived from this research will serve for methodological advancement in general, with a strong focus on a case study conducted at the Bronze Age site Toboliu in Romania (Section 1.3). This essentially involves effectively connecting information across various scales. Certainly, site location analysis serves as a classical example of such an integrative geoarchaeological approach (Verhagen, 2018), wherein archaeological field survey data is combined with (palaeo-) environmental information, including hydrogeological and land cover data, to assess the potential for prehistoric sites within a specific terrain. To effectively conduct comprehensive fieldwork, it is crucial to comprehend the locations chosen by prehistoric humans and to identify areas where archaeological site preservation is likely to occur. To evaluate how site selection analysis can be effectively applied on the macro scale, the southern Levant, known for an extensive archaeological record, in the Eastern Mediterranean was chosen. Furthermore, for a successful analysis of human-landscape interaction at a regional scale, it is crucial to discern which landforms result from natural landscape evolution and which are attributable to human activities. As an example for site catchment analysis (Volkmann, 2018) on the meso scale, the archaeological site Toboliu (Romania) was selected, as the evolution of its soil-landscape system is largely undefined. Therefore, a thorough reconstruction of the landscape is crucial to clarify landscape genetics and prehistoric land use.

Accordingly, two research objectives can be formulated concerning landscape reconstruction:

1. Research objective: Landscape analysis approaches
    - 1.1 Using GIS to integrate geoscientific information, and archaeoloigcal field data: Is it feasible to effectively integrate heterogeneous (palaeo-) geographical datasets with archaeological site information for predictive archaeological site location analysis? (Southern Levant)
    - 1.2 Based on chronostratigraphical and spatial data: Can we differentiate between anthropogenic and natural landscape features using stratigraphical information from sediment cores and geospatial information? (Toboliu case study)

The second focus of this work is to enhance the integration of qualitative micromorphological information with landscape analysis. A well-studied site with a distinct stratigraphy, such as the Loess-Palaeosol sequence of Rheindahlen in Germany (Kehl et al., 2024), serves as an excellent test ground for investigating spatial patterns at the microscale and determining whether the accessibility of micromorphological results can be improved by applying image classification and quantification techniques to thin section scans. The investigation should further explore whether this innovative approach can be applied to more complex archaeosediments and potentially enhanced through the use of Micro-XRF analysis of thin sections, which would facilitate a geochemical characterisation of the sampled materials. This would allow for a direct comparison between micromorphological on-site observations and lithostratigraphical information (derived from corings) from the surroundings. To test this hypothesis, we utilise micromorphological thin sections from the tell stratigraphy in our case study of Toboliu.

Consequently, two further research objectives can be formulated to develop novel analytical approaches for micromorphology:

2. Research objective: Integrating micromorphology with landscape analysis
    - 2.1 Utilising image classification on thin section scans: Can machine learning be effectively employed to classify and quantify micromorphological features? (Rheindahlen)
    - 2.2 Micro-XRF Measurements on Thin Sections: Can geochemical information enhance micromorphological analysis and link it to off-site analyses on the landscape level? (Toboliu case study)

The upcoming chapter will present the research methodology, accompanied by a concise overview of the integrated publications and manuscripts.

1.3 CASE STUDY: THE BRONZE AGE SITE TOBOLIU, ROMANIA

Geographical Context

Toboliu is situated approximately 15 km west of Oradea, in Bihor County, Romania in the vicinity of the border to Hungary. The site is located within the intermediate lowlands at the easternmost margin of the CB, with an elevation ranging from 100 to 104 meters above mean sea level. To the east, the foothills of the Apuseni Mountains extend, while the River Criųl Repede delineates the area to the north-west, merging with the Alceu River to the south (Fig. 1.1a). The area lies at the interface of the Criųl Repede floodplain and the High Plain of Miersig. A channel south of the study area, which, alongside the Alceu River, contributes to a marshy region to the west of the tell (Fig. 1.1b). Historical alterations, including dam constructions, have likely reduced the extent of this wetland, which was once more expansive (Dóka, 1997; Lie et al., 2019), however local palynological studies from 2021 could not find pollen bearing sediments which would enable vegetation derived landscape reconstruction. Nevertheless, a formerly wetland dominated landscape was documented in historical military surveys since the Habsburg Empire era (Timár et al., 2006). In Toboliu, the small, marshy area in the southwest may represent a remnant of these wetlands (Lászlóffy et al., 1938). The study area, classified as part of the Pannonian zone, experiences a Dfb-climate according to the Köppen-Geiger classification (Kottek et al., 2006), characterised by warm, humid summers and cold, relatively dry winters, with an average annual precipitation of approximately 550 mm. Most rainfall occurs between May and July (Ruszkiczay-Rüdiger and Kern, 2016; Crocetti et al., 2020). Currently, the vegetation is primarily degraded wooded-steppe, with agricultural practices dominating the landscape. Climate and vegetation reconstructions suggest that during the Holocene, the area was predominantly forested or wooded steppe before the advent of agriculture (Magyari et al., 2010). Typical soil types after IUSS (WRB) WG (2022) for this landscape are those from the Phaeozem group. According to Lindner et al. (2017b) soils formed in loess and loess derivates deposits (Fig. 1.1a). However, the soil in Toboliu has been significantly altered by intensive land use and drainage measures since the 18th century (Dóka, 1997), impacting original vegetation, soil, and archaeological contexts. As typical for the CB the area features a homogenous relief, interrupted by some slight lifts and smooth CDs. Most CDs are located around the tell and on the elongated lift to the east. All are situated at a relatively low local elevation of approximately 102 m a.m.s.l.. An elongated basin in the south can be identified by a relatively abrupt drop in elevation (Fig. 1.1b).

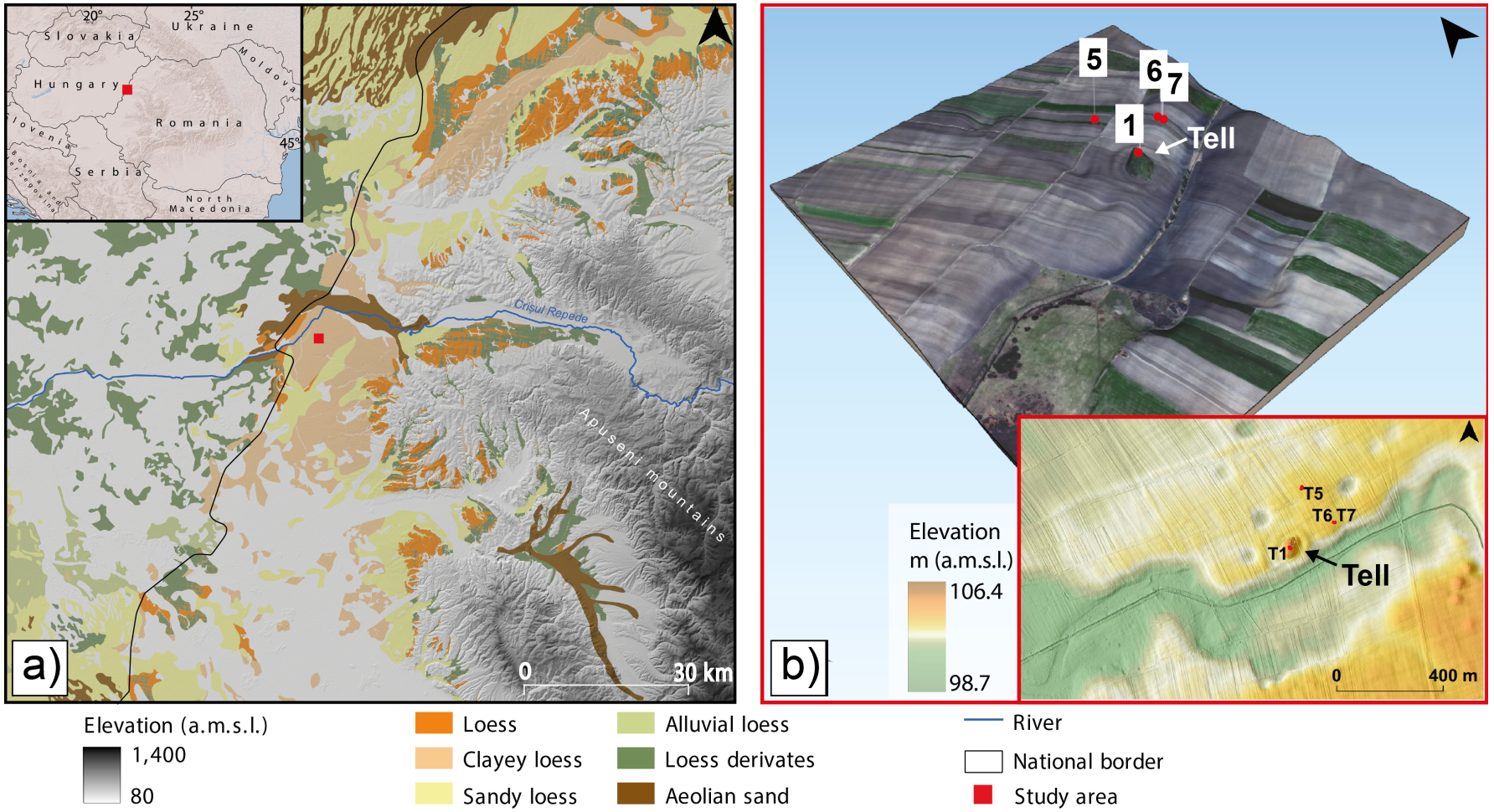

Figure 1.1: a) illustration of the spatial properties using a SRTM digital elevation model (DEM) (USGS - United States Geological Survey, 2009), Loess distribution (Lindner et al., 2017a) and rivers and lake centerlines (Natural-Earth, 2021); edited version of (Zickel et al., sub.) b) 3D visualisation of a Worldview-3 scene from 2021-03-25 (DigitalGlobe, 2021) and Light Detection and Ranging (LiDAR)-sourced DEM (National Agency for Cadastre and (ANCPI), 2014) with the the position of the excavation units (T) 1, 5, 6, and 7.

Archaeological Significance

A tell settlement is defined as an artificial mound formed by the accumulation of debris from large clay structures (i.e. houses), often fortified with ditches or earthen ramparts. Chronologically, Bronze Age tell settlements in the CB emerged between approximately 4500 and 3500 BP. Despite extensive archaeological investigations, many aspects of their development and function still remain unclear. The Toboliu site has been recognised in archaeological literature since the early 20th century, with initial excavations conducted in 1960. However, many findings from these early excavations remain unpublished (Gogâltan, 2018; Lie et al., 2019). In Toboliu a typical Bronze Age tell enclosed by two concentric ditches and a rampart can be found (Fig. 1.1b). Modern excavations resumed in 2014, supported by the Institute of Archaeology and History of Art in Cluj-Napoca, in collaboration with the CriÇounty Museum (Lie et al., 2019). The project has since expanded to include the Archaeological Institute of the University of Cologne, resulting in an interdisciplinary initiative funded by the German Research Foundation (DFG), which commenced in 2020. Investigative methods employed include archaeological excavations, topographic surveys, systematic field-walks, geomagnetic measurements, core drilling (lithostratigraphical, macrobotanical, and palynological analysis), specific sampling for micromorphology and luminescence dating, and aerial photography. Excavations have focused on the multiphased tell (Trench 1) settlement and on an outer settlement (Trench 5, 6, 7) in the suroundings (Fig. 1.1b), revealing important indicators of housing activity, such as flooring layers, wall daub fragments, postholes, and hearths. According to radiocarbon dating the area was settled approximately from 3880 to 3600 BP by Bronze Age groups (Lie et al., 2019; Gavan et al., 2024).

1.4 RESEARCH METHODOLOGY: FROM MACRO TO MICRO SCALE

This chapter outlines the research methodology employed in the exploration of innovative methods in landscape reconstruction and geoarchaeology across various scales. The integration of archaeological findings with geoscientific evidence is crucial for understanding human-environment interactions over time. This methodology draws upon the contribution of scholars such as Gladfelter (1977) and Cordova (2017), who emphasise the importance of different geomorphological scales in reconstructing palaeoenvironments and the comprehensive integration of such results. A key aspect of this research is the emphasis on interdisciplinary collaboration. The integration of methodologies from the humanities, natural sciences, and informatics and the multi scale approach allows for a comprehensive understanding of ancient landscapes and their forming processes. This approach aligns with the findings of Siart et al. (2018a) in the framework of Digital Geoarchaeology, who argue that multidisciplinary approaches significantly contribute to the understanding of cultural heritage and environmental dynamics.

Data Collection and Analysis Data collection involves a combination of field surveys, sediment core sampling, and the analysis of existing archaeological and geospatial datasets. The research employs both qualitative (e.g. micromorphology) and quantitative (e.g. geochemical and grain size analysis) methods to analyse the data.

Visualisation and Communication To bridge the scales and overcome communication barriers between disciplines, the research emphasises the development of appropriate visualisation methods. These methods aim to classify and visualise geoscientific findings, making them accessible to experts from various fields. This is crucial for fostering dialogue and collaboration among researchers and practitioners in geoarchaeology and related disciplines (Berna, 2019; Coeli et al., 2024).

Research Design The research adopts a multiscale framework, focusing on three primary scales: macroscale, mesoscale, and microscale. Each scale addresses different aspects of human-environment interactions and challenges in studying them and employs specific methods tailored to the research questions at hand.

1. **Macroscale Analysis** At the macroscale, the research investigates site location analysis using archaeological site location data and various geospatial datasets, such as DEM, land cover, landform, and hydrological mappings of the southern Levant (Eastern Mediterranean). This GIS based approach aligns with Verhagen (2018)'s assertion that site location analysis is a versatile tool

for exploring prehistoric settlement patterns and preferences over large areas. To investigate whether this approach can be applied to a large area, such as the Southern Levant, the study employs MCDA as outlined by Malczewski (2006). This analysis utilises the mentioned spatial data to identify regions with a high potential for Upper Palaeolithic archaeological sites (approximately 45,000-20,000 years ago in the Levant), emphasizing the impact of geomorphological and hydrogeological factors on the distribution of sites from this period (Chapter 2). This predictive modelling approach is informed by previous studies that demonstrate how early humans selected locations based on terrain characteristics and resource availability (Kretschmer, 2014; Schmidt and Zimmermann, 2019; Goldberg and Macphail, 2006, e.g.), as well taking site preservation factors into account (Uthmeier, 2004; Goldberg and Macphail, 2006, e.g.).

2. **Mesoscale Analysis** An example of the significant contribution of mesoscale analysis is its focus on landscape evolution at archaeological sites to understand regional human-environment interactions. This analysis is often motivated by inquiries into prehistoric land use strategies and resource exploitation. It effectively links landscape reconstruction with geoarchaeological analysis, a process that can also be referred to as geoarchaeological site catchment analysis (Vita-Finzi et al., 1970; Volkmann, 2018). Typically, this approach involves spatial analysis utilizing GIS and remote sensing data, as the operational radius for most prehistoric sites is generally expected to range from one to ten kilometers (Volkmann, 2018). At the case study site of Toboliu (Section 1.3) in the Romanian part of the eastern CB, a specific focus is placed on the formation processes that led to the creation of several CDs surrounding the Bronze Age tell. To determine whether these features were part of anthropogenic geomorphology, sediment corings provided high-resolution chronostratigraphical data, which were integrated with multispectral satellite imagery and historical map information. This integration aims to clarify the relationship between these landforms, the lithostratigraphic environment, and prehistoric settlement pattern (Chapter 3). Moreover, this approach necessitates the incorporation of macroscale information, such as palaeoenvironmental data for the CB, underlining the importance of scale-crossing analysis in the field of landscape reconstruction.

3. **Microscale Analysis** At the microscale, this research employs micromorphological soil and sediment analysis after the framework of Stoops (2020) to investigate how past societies, specifically the Bronze Age settlers at Tell Toboliu, utilised environmental resources, exemplified by the house flooring layers within the

tell stratigraphy. However, as previously outlined (Section 1.1), micromorphology presents certain methodological challenges related to result reproducibility, quantification, and the spatial relationships of phenomena observed under the microscope. In recent years, a variety of new techniques potentially applicable to micromorphology have been undergoing thorough examination. In the scholarly work of Nicosia and Stoops (2017), several of these techniques were compiled and discussed by experts in the field. As a contribution to such methodological innovation, this endeavour aims to display and quantify micromorphological observations. Utilising the robust test environment of the well-documented loess palaeosol sequence in Rheindahlen, Germany (Kehl et al., 2024), the objective is to determine whether the development of a thin section image analysis based micromorphological GIS facilitates the analysis of soil and sediment features and enhances the transfer of micromorphological knowledge (Chapter 4). Furthermore, regarding the case study in Toboliu, it should be assessed whether this approach can be applied to the recently investigated and more complex stratigraphy of the Bronze Age tell. An additional challenge, linked to the initial investigations of (Mentzer, 2017) and the collection of Nicosia and Stoops (2017), involves the use and integration of Micro-XRF measurements in micromorphological analysis. This integration could provide geochemical data at the microfacies level, and it should be tested whether Micro-XRF element mappings and high-resolution point measurements can be utilised to characterise house flooring construction materials and techniques (Chapter 5). Moreover, integrating micromorphology with semi-quantitative geochemical data has the potential to connect microscale insights to mesoscale results concerning regional sediment deposits from the previously outlined site catchment analysis, thereby tracing back and comparing the sources of minerogenic construction materials.

1.5 DISSERTATION STRUCTURE

The thesis is based on two publications and two manuscripts. The publication in Chapter 2 introduces the multi scale method by focussing on overarching macro scale aspects of landscape reconstruction and geoarchaeology within the framework of site location analysis. This is exemplified by the analysis of Upper Palaeolithic site distribution in the southern Levant. This research topic is deepened in an additional manuscript in Chapter 3, which details the case study of this thesis. It demonstrates the potential of integrating macro and meso scale data for landscape reconstruction and site catchment analysis, specifically enhancing our understanding of human-landscape interaction during the Bronze Age at the archaeological site of Toboliu in Romania. Additionally, the publication in Chapter 4 lays the groundwork for a comprehensive micro scale analysis, emphasising the processing of micromorphological information to to facilitate its integration with meso and macro scale data through image classification techniques. To complete the multi scale approach, the manuscript in Chapter 5 applies the innovative system presented in the previous chapter (Chapter 4) on-site for the case study and augmented by Micro-XRF derived geochemical information. This detailed investigation of the house flooring layers could thus provide enhanced stratigraphical information for the Bronze Age tell stratigraphy and settlement history in Toboliu. All results obtained and research questions raised in Section 1.2 are synthesised in Chapter 6 and critically discussed in each subchapter. Finally, Chapter 7 will provide a conclusion along with an outlook on the findings of this PhD thesis.

Part II

RESEARCH RESULTS

2

UPPER PALAEOLITHIC SITES AND WHERE TO FIND THEM: A PREDICTIVE MODELLING APPROACH TO ASSESS SITE EXPECTANCY IN THE SOUTHERN LEVANT

The author contributions are structured by categories, namely: Conceptualization and Methodology, Software and Data Curation, Formal analysis, Investigation, Visualization, Supervision, Project administration, Funding acquisition, Writing –Original Draft, and Writing – Review and Editing. The individual authors' contributions to each category are subsequently listed by their initials.

Conceptualization and Methodology: HR and MZ; Software and Data Curation: MZ; Formal analysis: MZ and HM; Investigation: HR and MZ; Visualization: MZ; Supervision: HR; Project administration and Funding acquisition: HR; Writing – Original Draft: HR and MZ ; Writing – Review and Editing: HR and MZ.

Hannah Rohringer (née Parow-Souchon)[1], Mirijam Zickel[2], Heiko Manner[3]

Manuscript submitted to the Journal *Quaternary International, Elsevier* and published on 2022-09-18 https://doi.org/10.1016/j.quaint.2021.05.020

1 , Austrian Archaeological Institute, Austrian Academy of Sciences, Dominikanerbastei 16 1010 Vienna, Austria
2 Research Group for Geomorphology & Geochronology, Institute of Geography, Faculty of Mathematics and Natural Sciences, University of Cologne, Zülpicher Straße 45, 50674 Cologne, Germany
3 Independent researcher

Abstract

Site preservation and associated terrain characteristics are among the major agents controlling the spatial distribution and discoverability of late Quaternary archaeological sites. However, site expectancy in extensive areas can be determined using a combination of geoarchaeological investigation and digital spatial analysis. In that sense a prediction model, respectively the result of a Multi Criteria Decision Analysis (MCDA), is presented to highlight areas with a high potential to contain Upper Palaeolithic sites in the Eastern Mediterranean and bordering arid margins. Based on detailed on-site analysis in the Wadi Sabra region, with its many sites and the location of other well-known sites in the southern Levant, eight individual parameters, aspect (cardinal point), elevation, geomorphology, hydrogeology, drainage network, slope inclination, vegetation, and a Terrain Ruggedness Index (TRI) are evaluated and tested for significance. The statistical results confirm a significant divergence of the spatial distribution of Upper Palaeolithic sites from the distribution of natural terrain position factors. This allows for a definition of parameter classes with a high site expectancy and their use in a predictive model. For the results map, the site expectancy factors determined in this way were intersected with each other, thus enabling a distinction between areas with a high and low site occurrence probability. The accuracy of the presented result is assessed by the implementation of another MCDA pass based on an independent dataset of archaeological survey sites and compared to the original. Both datasets complement each other and can show the potential for further investigations with more numerous site datasets as well as more detailed spatial information. A local classification based on high-resolution elevation information and field data is evaluated for the Wadi Sabra, Southern Jordan, which can confirm yet further specify the result from the MCDA.

2.1 INTRODUCTION

Many of Prehistoric archaeology's most important questions – past land use, demography, settlement patterns, and others – are evaluated via the distribution of archaeological sites in the landscape (Kretschmer, 2014; French, 2015; Tallavaara et al., 2015; Lundstrom and Riede, 2019; Schmidt and Zimmermann, 2019). A crucial precondition for any such analysis is an estimation of factors shaping or influencing this distribution and thus potentially biasing cultural historic interpretations of spatial data. These processes are well-known to influence the spatial distribution of sites and their specific preservation and discovery conditions (Uthmeier, 2004; Goldberg and Macphail, 2006; Diez-Martín, 2010; Domínguez-Solera, 2010; Eren et al., 2011; Jiménez-Sanchez et al., 2011; Dischamps et al., 2019; Holcomb et al., 2020).

Especially in geomorphologically heterogeneous environments such as the southern Levant, local sedimentary deposits can vary greatly. Accordingly, the discovery of archaeological sites, especially such found in open-air localities, can be expected to be largely determined by specific local preservation. A climatic gradient from hyper-arid to Mediterranean conditions, according to the steep local relief, further influences the site distribution. Such strong environmental contrasts are challenging to geoarchaeological prospection yet predominantly shape our perception of the southern Levantine Late Pleistocene record. Thus, an assessment of the spatial distribution of site-carrying sediments is a prime factor in the estimation of discovery conditions and represents a precondition for spatial analyses of the preserved inventories.

Sedimentation and erosion processes in the Late Quaternary shape preservation and discovery probability. Large-scale erosion events can remove site-carrying sediments, while alluvial deposits, especially in relief depressions, can bury sites under many meters of sediment and render them inaccessible. Additionally, campsite selection of Upper Palaeolithic humans as well as the modern research history of surveys and excavations influence the spatial distribution of known Late Quaternary sites. Prehistoric humans can be expected to have a list of attributes which determine a favourable spot for making camp, and these might vary according to functionally different types of campsite. The distance to water can be expected as a factor, the evenness and dryness of the ground, possibly the available viewshed and other factors we cannot reconstruct from today's viewpoint. Modern survey or excavation patterns are dependent on the research history of the region. For example, many of the known Upper Palaeolithic sites in the Negev are the result of two very large-scale survey projects, one of which was conducted in the framework of construction and heritage management activities (Marks, 1976; Marks, 1977; Marks, 1983a; Marks and Freidel, 1977; Goring-Morris, 1987).

Mapping these factors influencing our picture of the Upper Palaeolithic site distribution for the Southern Levant facilitates the conception of future survey projects as well as risk assessment considerations for heritage management (Gerlach, 2001; Gerlach, 2003; Gerlach and Eckmeier, 2012). This study aims to contribute to this question and conducts a preliminary GIS-based assessment of preservation and discovery of Upper Palaeolithic sites in the Southern Levant (Fig. 2.1).

This should give a novel perspective and an impetus for the spatial expansion of archaeological research in the study area. Accordingly, the maps created can provide a tool for targeted field surveys. In return, additional and more accurate site data can refine a future spatial analysis and hence reduce research bias.

The presented digital survey combines archaeological and geographical data in a spatial analysis in order to gain and discuss a first thematic overview over the study area and give a first estimation which regions warrant a more detailed investigation. Looking forward to subsequent work in various regions of the study area, ecological, geomorphological, and digital elevation information of higher spatial resolution is required for locally more precise prediction models. One such high resolution regional model, related to our own on-site study area in the Wadi Sabra in Southern Jordan will be presented here.

The timeframe for the study was set to encompass the Upper Palaeolithic, thus the timeframe from roughly 40–45 000 years ago to about 20 000 years ago (Belfer-Cohen and Goring-Morris, 2003; Belfer-Cohen and Goring-Morris, 2014). The Upper Palaeolithic of the study region fully begins with the onset of the Ahmarian culture (Gilead, 1981; Marks, 1981) which locally develops out of the Initial Upper Palaeolithic, a transitional industry to the Middle Palaeolithic (Volkmann, 1983; Volkmann, 1989; Skrdla, 2003). The Ahmarian is characterised by a highly sophisticated blade technology out of narrow-fronted lithic cores. The lithic tool inventory includes El-Wad points, burins, endscrapers and truncations (Gilead, 1981; Marks, 1981; Davidzon and Goring-Morris, 2003; Monigal, 2003; Goring-Morris and Davidzon, 2006; Hussain, 2015; Goring-Morris and Belfer-Cohen, 2018; Parow-Souchon, 2020). The Ahmarian is a pan-Levantine phenomenon with the earliest occurrences in the north of the study area, in the sites of Manot (Marder et al., 2013; Barzilai et al., 2016; Alex et al., 2017; Abulafia, 2018; Abulafia et al., 2019), Qafzeh (Ronen and Vandermeersch, 1972; Bar-Yosef and Belfer-Cohen, 2004; Vandermeersch and Bar-Yosef, 2017) and Kebara (Belfer-Cohen and Bar-Yosef, 2015; Bar-Yosef and Belfer-Cohen, 2019) Caves, as well as the sites of Ksar Akil Rockshelter (Azoury, 1986; Bergman, 1987; Williams and Bergman, 2010; Douka et al., 2013; Bergman et al., 2017) and Üçağızlı Cave (Kuhn, 2004; Kuhn et al., 2009) in Lebanon and Turkey outside the selected study area. The earliest 14C dates currently come from the site of Manot, where the Ahmarian begins around 45/46 000 years ago (Alex et al., 2017).

The Ahmarian occurrences in the north of the study area can be technologically differentiated from the ones in the south of the study area (Kadowaki et al., 2015), which appear to be generally younger.

Assumed to be intrusive to the local Upper Palaeolithic record, possibly representing a back-migration into the Levant (Bar-Yosef and Belfer-Cohen, 1996; Bar-Yosef and Belfer-Cohen, 2010; Belfer-Cohen and Goring-Morris, 2003; Barzilai et al., 2016; Alex et al., 2017; Marder et al., 2019), is the Levantine Aurignacian, prominently represented in the sites of Hayonim (Belfer-Cohen and Bar-Yosef, 1981; Chazan, 2001), Manot (Barzilai et al., 2012; Barzilai et al., 2014; Barzilai et al., 2016; Hershkovitz and Arensburg, 2017; Marder et al., 2019; Sarig et al., 2019), Sefunim (Ronen, 1968; Ronen and Ben-Tor, 1984; Shimelmitz et al., 2018), El Wad (Garrod, 1937) and Raqefet (Lengyel, 2007) caves within the study area as well as in Ksar Akil (Azoury, 1986; Williams and Bergman, 2010; Bergman et al., 2017) and Yabrud II Rockshelter (Rust, 1950; Solecki and Solecki, 1986; Demidenko and Hauck, 2017; Frahm and Hauck, 2017) in Syria outside the study area. The Aurignacian is characterised by the appearance of carinated technology, Dufour bladelets and the advent of a sophisticated bone and antler industry (Newcomer, 1974; Tejero et al., 2016; Tejero et al., 2020; Yeshurun et al., 2018), only sparsely known from the Ahmarian to date. Levantine Aurignacian sites are currently only known from the northern Mediterranean parts of the study area. Traditionally dated to a short chronological timeframe around 30 000 years ago, most recent dates, again from Manot, push the timeframe of the Aurignacian back towards 38–34 000 years ago (Alex et al., 2017). Past about 30 000 years ago the previous two cultures are being replaced by a number of smaller subunits, the typological differentiation of which are a constant subject to debate. These cultures include the Atlitian, mainly in the north, the Arqov-Divshon, mainly in the south, as well as the Late Ahmarian and Masraqan, all differentiated on account of different toolsets and discussed to be related to either the Ahmarian or the Aurignacian tradition (Belfer-Cohen and Bar-Yosef, 1973; Goring-Morris, 1980b; Gilead, 1991; Gilead, 1993; Henry, 1995; Coinman, 1998; Belfer-Cohen and Goring-Morris, 2003; Goring-Morris and Belfer-Cohen, 2003; Williams, 2003a; Williams, 2003b; Belfer-Cohen et al., 2004; Kuhn, 2004; Schyle, 2015c). All these cultures are connected to modern humans (Bailey et al., 2009; Higham et al., 2011; Hershkovitz and Arensburg, 2017; Timmermann, 2020) and include a hunter-gatherer socio-economic setup in interpleniglacial conditions (Marks, 1977; Goring-Morris, 1987; Henry, 1995). The timeframe of study was set to the Upper Palaeolithic due to the expectation of differences in settlement patterns, site location choices and also sedimentological constraints in comparison to the Middle Palaeolithic which ranges much further back in time. The exclusion of the Epipalaeolithic was made on account of, again, different settlement patterns

and palaeo-environmental conditions, which should also be reflected in the sediments and thus the modelling output. The sites chosen, as outlined in the here grossly abbreviated summary, already include serious cultural and techno-typological differences yet retain a form of integrity especially in comparison with the preceding and following large-scaled temporal units. Further comparable analyses should include and compare different time slices to the current to investigate spatial differences in site occurrence.

2.2 REGIONAL SETTING

The region under study mainly comprises Israel, the Westbank and directly adjoining regions of Lebanon, Syria, Jordan and Egypt. The study area is characterised by a high abundance of small-scaled landscape units with their own characteristic geological and geomorphological setting. A full description of these numerous subunits is beyond the scope of this contribution and only a short overview can be given.

The study area can be divided into four large environmental units, each composed of numerous sub-units. From west to east these comprise the coastal plain, narrower in the north, and wider in the south and the mountainous backbone of central Israel, which reaches from the Galilee region in the North to the Negev mountains in the South. Adjoining this central massif, the Dead Sea Transform Fault System (DSTFS) includes Lake Tiberias in the north, to the south the present Jordan river valley, an endorheic basin (Frumkin et al., 2017) containing the present Dead Sea and the southern Wadi Araba. To the east, the Transjordan Rift Escarpment marks the transition to the wide-open Jordanian plains which are not part of this study.

During the Pleistocene, the area between Lake Tiberias to about 100 km south of the current Dead Sea was filled by the vast Palaeo-Lake Lisan (Klinger et al., 2003; Rohling, 2013; Torfstein et al., 2013; Stein and Goldstein, 2017; Torfstein and Enzel, 2017). The approximate extent of the lake in the Upper Palaeolithic period was computed based on the work of Torfstein et al. (2015). In combination with corresponding palaeo-coastlines, which were produced using the same method and published in Zickel et al. (2016), the landmass to water ratio of two Upper Palaeolithic time slices, 23 and 38 ka BP, can be studied on the maps in this contribution.

The study area is characterised by a stark relief originating from major tectonic processes. The main determinant for the tectonic and thus also geomorphological development is the movement of the DSTFS, the northern section of the Great African Rift System. The Sinai microplate, containing Israel, is moving southwards, while the Arabian plate is moving northwards causing ruptures and breakages at its margin (Garfunkel, 1981; Avni, 2017; Matmon and Zilberman, 2017). Thus, changes in altitude and slope inclination can be very abrupt.

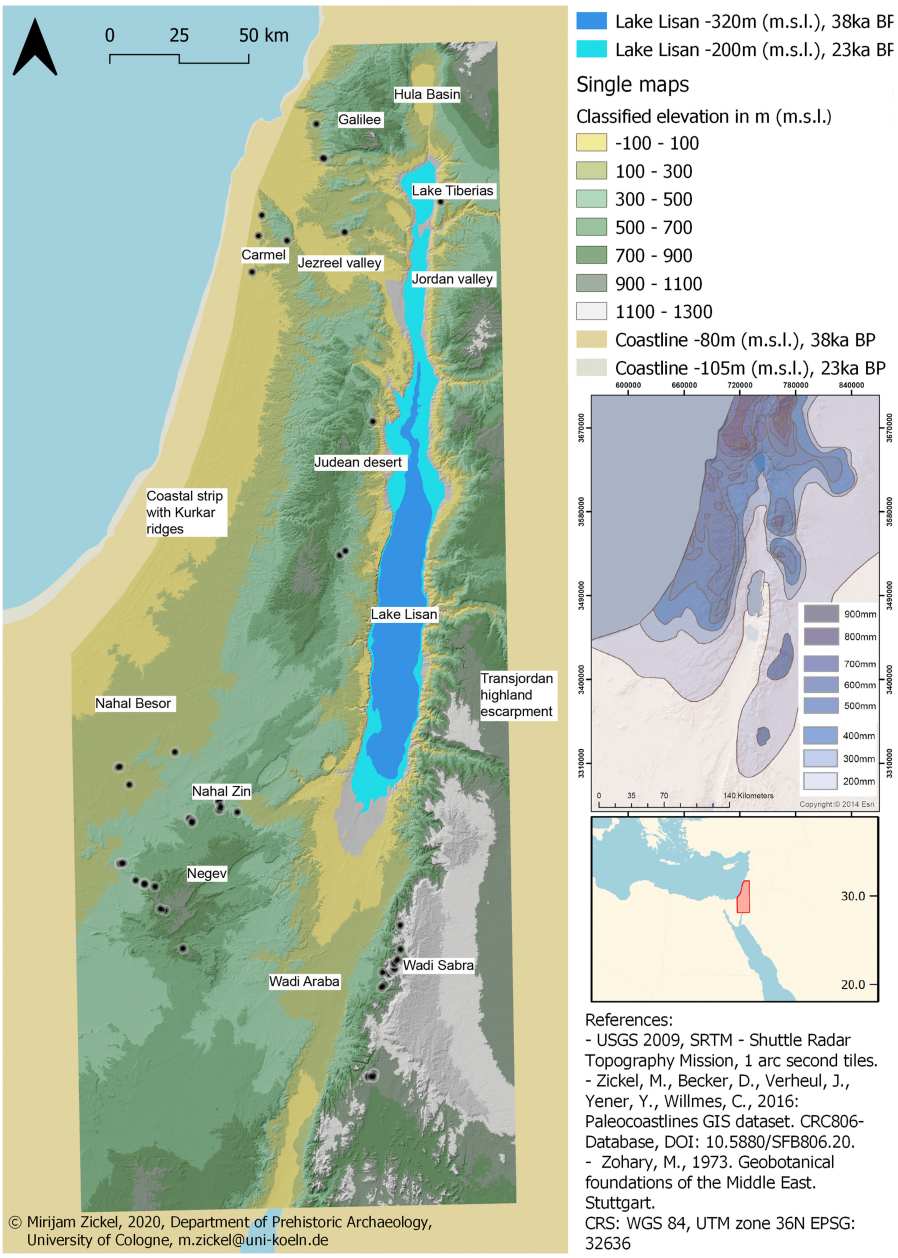

Figure 2.1: Left: Elevation model of the study area with regions mentioned in the text, right: precipitational map of the Southern Levant (Schiebel, 2013) and locational map of the study area. Lake Tiberias in the north, to the south the present Jordan river valley, an endorheic basin (Frumkin et al., 2017) containing the present Dead Sea and the southern Wadi Araba. To the east, the Transjordan Rift Escarpment marks the transition to the wide-open Jordanian plains which are not part of this study.

Consequentially, and in relation to differing climatic conditions as well as the precipitation regime, a regionally diverse geo- and biosphere developed across the millennia, which shall now be shortly outlined.

The geological backbone of the study area is formed by Cretaceous and Eocene limestone, chalk and marl formations dominating both, the central massif and the Transjordan highland escarpment (Sneh et al., 1997; Sneh et al., 2014; Avni, 2017). Tectonic processes initiated the DSTFS and formed a watershed at the central mountain ridge which guides the drainage of the central massif either westwards to the sea, or eastwards into the tectonic depression. Likewise, the beginning of the rift-formation includes the subsidence of the Wadi Araba and the uplift of the Transjordan Rift Escarpment during the terminal Oligocene and initiated a dissection of the rift escarpment into deeply incised wadis (Avni, 2017). Sediment deposition in the mountainous areas of the central massif is mainly governed by aeolian dust influx from the Sinai and the Saharan desert limestones. In the northern parts of the study area the dust underwent pedogenic processes including the dissolution of the carbonate fraction. The resulting terra rossa soils only form a thin sediment cover on the limestone hills of the central ridge (Erel et al., 2017). Other soil formation products are brown or pale rendzinas and vertisols in alluvial depressions (Dan et al., 1975). Archaeological site occurrence in the Mediterranean North is mainly tied to karstic cave sites.

The Judean desert has formed on the leeward flanks of the Judean mountains as a rainshadow desert (Steinberger et al., 1990; Frumkin et al., 2017). It is currently one of the driest regions of the Southern Levant, yet speleothems and the high Lisan Lake levels indicate considerably wetter conditions in the terminal Pleistocene (Frumkin et al., 2017) and references within). Bedrock discharge under Holocene conditions is one of the highest in the world during single discharge events such as flash floods. The annual sediment load is limited due to the rarity of discharge events as could be shown for the Nahal Rahaf drainage system, a typical ephemeral fluvial system in the Judean desert (Cohen and Laronne, 2005). Soils are predominantly terra rossa, brown and pale rendzinas in the upper altitudes, while the descent to the Dead Sea is marked by a progression through brown and pale rendzinas, brown lithosols, loessial arid brown soils, loessian serozems down to bare rocks and desert lithosols at the shoreline (Dan et al., 1975). Few Upper Palaeolithic sites, both caves and open-air sites, are known from the Judean desert, yet the region is not well studied to date.

In the Negev, however, prominent dune field incursions began in the terminal Pleistocene from about 100 to 40 ka onwards with major phases during the LGM and the Younger Dryas (Roskin and Tsoar, 2017). The majority of Upper Palaeolithic sites in the Negev are tied to aeolian deposits (Goring-Morris, 2017). Alluvial terraces

formed in the main drainage channels reworking and redepositing the aeolian sediments (Avni, 2017; Greenbaum and Zilberman, 2017). Soil formation is dominated by brown lithosols and loessian serozems, sandy regosols and arid brown soils, sand dunes, reg desert pavements and coarse or fine desert alluviums (Dan et al., 1975; Crouvi et al., 2008; Crouvi et al., 2017; Goring-Morris, 2017). Dune field incursions and resulting temporal damming of the fluvial systems resulted in several ephemeral and sometimes, as in e.g. Nahal Zihor, even stable waterbodies (Greenbaum and Zilberman, 2017; Mischke et al., 2017). The Negev and especially the Central Negev are known for a high occurrence of open-air sites dated into the Upper Palaeolithic.

The current coastal plain represents a complex system of glacial and interglacial relict landscapes with ongoing geomorphological and pedogenic processes (Harel et al., 2017). On a basis of Pliocene Nilotic sediments, up to 200 m of fluvio-aeolian Pleistocene sediments were deposited. Prominent north-south oriented calcareous sandstone ridges, termed Kurkar, with reddish Hamra soils (Greenbaum and Zilberman, 2017; Sivan and Greenbaum, 2017) structure the landscape. During the Pleistocene the low global sea level leads to an extension of the coastal plain especially in the southern part (Sivan and Greenbaum, 2017). From the Mid-Pleistocene to the Early Holocene short-lived wetlands formed on the palaeo-coast, which includes the current coastal plain as well as regions further to the west which are currently submerged (Sivan and Greenbaum, 2017). Fluvial and aeolian sediments during the late Quaternary partially covered these sediments and altered the drainage pattern of the area (Greenbaum and Zilberman, 2017). The coastal plain seems to be largely devoid of Upper Palaeolithic sites to date.

The Wadi Sabra study area, providing a detailed regional case study, lies in southern Jordan, roughly 8 km away from the well-known Nabatean site of Petra. In direct proximity to the main Dead Sea fault in the Wadi Araba, its morphology is strongly influenced by tectonic processes. The Upper part discussed herein is a wide-open U-shaped valley located in Cambrian Umm Ishrin Sandstones (Barjous, 2003; Bertrams, 2013). On both wadi flanks large Pleistocene sediment remnants are preserved, more extensive on the northern bank and cut by the modern wadi course at the southern side of the wadi. They are covered by an approximately 0.5 m thick calcareous duricrust of roughly LGM age, protecting the underlying sandy deposits from erosion (Bertrams, 2013). The Wadi Sabra shows a high occurrence of Upper Palaeolithic open air sites.

Thus, the study area can be differentiated into many subunits with an individual characteristic environmental setting which influences the preservation and discovery probability for archaeological sites. This requires a detailed spatial estimation of these different parameters and

their local expressions thus promises to yield a comparable overview for the whole region.

2.3 MATERIAL AND METHODS

Synchronous to the significant improvement of remotely sensed data quality in general and the massive increase in spatial and spectral resolution of open data products in particular, predictive modelling and digital geoarchaeology has increased in importance over the years (Nsanziyera et al., 2018; Whitley et al., 2010, e.g.) and were even systemically included in modern heritage management systems in some regions (Verhagen and Whitley, 2012). Accordingly, computational progress, especially in the GIS-sector, facilitates a spatial combination of geoscientific and remotely sensed environmental information and archaeological field data and enables the combination of information from multiple perspectives and of different scales. In general, this progress provides a good basis for identifying archaeological sites or generally determining the potential of an area in this regard. In a narrower sense, there are a few possibilities in predictive modelling for dealing with archaeological data in order to counteract the definitional uncertainty typical to archaeology in the formation of criteria.

The central method used in this study is the well-established MCDA (Malczewski, 2006; Malczewski and Rinner, 2015; Lloyd, 2010). The method summarises multiple spatial datasets (Lloyd (2010), p. 71) which can be weighted according to their perceived importance (Malczewski (2006), p. 703). Here, the MCDA targets the identification of areas with a high site expectancy or in other words: areas with the maximum archaeological site likelihood.

Consequentially, a systematic multi criteria decision framework for archaeological purposes, which is described in detail in Verhagen (2006), offers the highest possible transparency and control of the variables during the individual decision steps (Verhagen (2006), 176ff). The MCDA was chosen for this study to account for the variability of spatial as well as archaeological data. The different parameters used include various datatypes which are difficult to combine with traditional spatial statistics (Verhagen, 2008; Verhagen and Whitley, 2012).

As a value judgement a spatial query with the archaeological site database (see Section 2.3.2) was used to determine weightable environmental criteria from the geodatasets (described in Section 2.3.1) which are obligatory for site discoverability and reflect Upper Palaeolithic site selection and in conclusion can be defined as archaeological suitability or site expectancy. The result is a new spatial dataset which is a combination of the reclassified and rescaled criteria whose spatial fit likelihood is represented by index values. This value is therefore

not based on a physical unit but represents the fulfilment of the set of criteria.

The analytical setup comprises the manual selection of eight different environmental parameters (geomorphology, drainage system, hydrogeology, vegetation, elevation, aspect, slope, and a topographic roughness index, see below) as a criteria foundation which are first tested for normal distribution. Then the significance of the difference between the distribution of the chosen archaeological site dataset (n = 92) on classes of these parameters is evaluated in comparison to the natural distribution of the classes in the landscape. The criteria were formed according to the frequency of occurrence of certain values or categories, dependent on the data type. Then these parameters are entered into the MCDA process. Since an experimental study on the applicability of the described procedure was conducted here, all datasets were weighted equally. Experiments on a meaningful weighting are currently still being conducted.

In order to test the result a second independent dataset was extracted from the IAA survey database and another MCDA pass run with the same parameters as the previous one, a method e.g. suggested by Verhagen (2008). These two model output results are compared with a change detection grid as well as a high-resolution spatial sample in the Wadi Sabra, Southern Jordan.

Such a multi-perspective, multidisciplinary approach can contribute to minimise research bias which is of importance, facing complex ongoing surface processes in an uncertain past (Siart et al., 2018a). GIS can play an integrative role by identifying territories that unite specific required features of multiple datasets (Lloyd, 2010). Moreover, it gives the opportunity to extrapolate this insight to areas lacking data which is especially important for archaeological prospections.

2.3.1 *Geodata*

Evaluated terrain morphology parameters integrated in the study are aspect, elevation, slope inclination and TRI as derived from a 30 m resolution SRTM (USGS - United States Geological Survey, 2009), DEM. Site location in relation to potential watercourses is evaluated by the analysis of the SRTM derived HydroRIVERS drainage network (Lehner et al., 2008). Hydrogeological (Schöler et al., 1990), geomorphological (Nir, 1978) and vegetational (plant communities) (Zohary, 1973) information is derived from analogue maps and implemented in the analysis in digitised form. The workflow in Fig. 2.2 summarises the major methodical steps that were implemented in the study.

The study was performed with the GIS software QGIS 3.14, the algorithms used in this computational environment are also listed in the Appendix (Table A.1). In addition, there is also a detailed

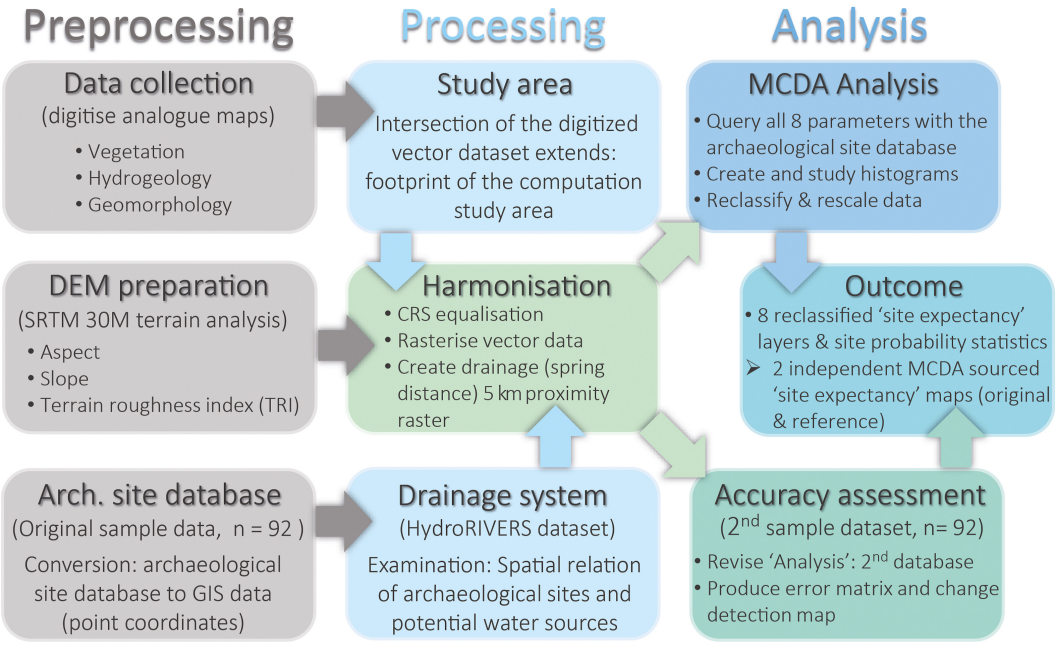

Figure 2.2: Workflow diagram of the performed site expectancy (grade of preservation) analysis. It shows the datasets used and their processing within the main work steps: pre-processing, processing and analysis. Pre-processing is mainly concerned with data acquisition and general adjustments in GIS. In processing, the data is adapted to the extent of the study area and the geodata is linked to the archaeological site database. In the analysis stage, the data prepared in the previous steps are processed in the MCDA, the maps are produced and subjected to a revision, and the results thus obtained are checked in the accuracy assessment. The displayed procedure serves to establish criteria for determining areas with the maximum likelihood of archaeological sites in the study area.

description of the work steps which can only be touched upon here (Appendix A.1).

First, a spatial query of the eight datasets mentioned above is generated using the archaeological site database (92 Upper Palaeolithic sites) as sample dataset. Subsequently, classes are formed based on site frequency in the spatially assigned types or intervals of the different criteria datasets. For example, distinct types are certain plant communities like 'Saharo Arabian' (Appendix, Fig. A.8) which are present in the vegetation dataset, while intervals are formed in the DEM-derived datasets (e. g. 0–10°slope inclination) (Appendix, Fig. A.7). Each individual parameter is statistically tested, classified by relevance according to the archaeological site occurrence within its margin which forms the criterion. The classified datasets are then combined in the site expectancy analysis using the MCDA method. Subsequently, the results are mapped by ranked estimation of site preservation (or in other words archaeological suitability) for the study area. In order

to obtain a statement about accuracy deviation and probability, for example class omission and commission errors, an accuracy assessment including a classical error matrix (Congalton and Green, 2009) is carried out (Appendix, Table A.7). To produce it a second MCDA is performed by the implementation (see processing steps) of a second independent archaeological site dataset (IAA site database, described in 3.2). This result is not discussed in detail as it is part of the accuracy assessment, but statistics and the overall accuracy are given along-side the results of the original dataset throughout.

In order to get an impression of the spatial distribution of the differences between the original MCDA and the control results, a change detection grid was calculated in addition (see Appendix, Table A.1).

The accuracy assessment of the MCDA analysis is supplemented by high-resolution information (combined field and remote sensing data) of the Wadi Sabra, Southern Jordan. The information for the Wadi Sabra is based on Pleiades satellite imagery (Airbus Defence and Space) as well ' as a comprehensive survey and excavation programme by the CRC 806 – Our Way to Europe providing a first detailed investigation in one of the regions with a very high site expectancy. From the satellite data an elevation model was calculated by Andreas Bolten, Project Z2, CRC 806. The resulting DEM has a resolution of 0.5 m. On this basis it was possible to compute a landform classification using the Topographic Position Index (TPI) first presented by Weiss (2001).

2.3.2 *Location and accession of archaeological data*

The conducted research uses a database of 92 Upper Palaeolithic sites compiled for a settlement pattern analysis published elsewhere (Parow-Souchon, 2020). This dataset is integrated to assess the influence of individual parameters on the location of archaeological sites. The spatial information for the archaeological sites is collected from the published original site reports and the coordinates or maps given therein. This dataset contains the majority of well-known and well-published Upper Palaeolithic sites in the study area (Ronen, 1968; Belfer-Cohen and Bar-Yosef, 1973; Marks, 1976; Marks, 1977; Marks, 1977; Goring-Morris, 1980a; Goring-Morris, 1980b; Goring-Morris, 1980b; Goring-Morris, 1987; Goring-Morris, 1980b; Gilead, 1981; Gilead, 1993; Belfer-Cohen and Goring-Morris, 1986; Henry, 1995; Kuhn, 2004; Lengyel, 2007; Barzilai et al., 2012; Richter and Schyle, 2015; Schyle, 2015c). The method of data collection and unification has also been described in detail (Parow-Souchon, 2020). This study is part of a larger investigation into the settlement patterns of Upper Palaeolithic hunter-gatherers in the Levant and describes the necessary first step to evaluate the presence of site-carrying sediments before any attempts on a spatial analysis of the preserved sites can

be undertaken. These 92 sites are published in sufficient detail to be included in a systematic statistical techno-typological analysis which will follow-up on this investigation.

The overarching goal of these analyses includes the use of a standard site database used throughout. This procedure omits several site clusters which are not sufficiently published to date or are located outside the current map boundaries (see below for a detailed discussion).

The information for the reference dataset is derived from the online survey database of the Israel Antiquities Authority (Authority, 2020) and is the result of a query of "Upper Palaeolithic" sites. The number of sites was chosen to equal that of the original dataset. The given information was carefully evaluated and the provided information about preservation, cultural attribution, surveyor, and survey-year recorded. In comparison to the original dataset, this reference dataset includes inherent limitations. It contains mostly unpublished findspots only partially reported by schooled prehistorians. Two of the included regions, covered by the Ze'elim geological map sheet/Nahal Besor (Zilberman, 2010), as well as the Jezreel Valley, yield a high number of findspots recorded by non-prehistorians during the 1970s and 1980s, thus including the potential for a reduced accuracy of cultural designations. Another group of sites, however, was surveyed by several well-known and experienced Prehistorians, including Moshe Stekelis, Bernard Vandermeersch, Ofer Marder, Rene Neuville and Steven A. Rosen, and are thus reliably placed in the Upper Palaeolithic. Some of these survey sites include post-depositional issues, several contain multiple periods e.g. are surface scatters with material from the Upper Palaeolithic to the Byzantine period and many are surface scatters of unknown condition. This dataset thus has to be interpreted with more caution. To give credit to this complexity, a reliability rating has been added to these sites ranging from 1 to 5. This rating, together with the reported taphonomic situation (if reported), divided into cave, subsurface preservation, and surface scatter is mapped in the Appendix (Fig. A.10).

Even with the issues discussed above, the publication of these sites in a comprehensive online resource allows for the compilation of an independent dataset to test the site expectancy model. Therefore, it is a great asset for research as this one.

Both datasets combined do not yet contain all Upper Palaeolithic sites known in the area, and not all large survey projects. However, the Carmel survey by Olami ((Olami and Ronen, 1977; Olami, 1984; Olami, 1988) reportedly yielded the five caves contained in our calculations (Olami, 1988), with the addition of only one more cave (included in the reference dataset) and a questionable surface site (Olami and Ronen, 1977). Also the large site cluster in the Wadi Hasa (Coinman, 1993; Coinman, 1998; Coinman, 2003; Coinman, 2005) is missing from the

calculation as it is just east of the extent of the used geomorphological map. The same holds true for all sites in the Sinai also excluding the material from Gebel Maghara (Gilead, 1981). The most recent survey results as e.g. in the Nahal Besor (Goder-Goldberger et al., 2019) could not be incorporated in the calculations, but are highly revealing for a comparison.

The majority of sites included are associated with a single cultural unit, even though they might include several occupations (e.g. Ain Aqev, Boker BE, the Ras en-Naqb sites), some are clear single occupations (e.g. Nahal Nizzana XIII, Sabra 4 Palmview 3). The cave sites include multiple periods containing also material from earlier or later periods than the Upper Palaeolithic. Most open-air sites in the original dataset, however, are exclusively tied to the Upper Palaeolithic (Appendix, Tables A.8 and A.9). Sparse evidence so far seems to indicate a differing spatial preservation in comparison to Upper and Middle Palaeolithic surface sites (e. g. in the Besor the majority of sites found were Middle Palaeolithic, even though Upper Palaeolithic strata should have been accessible too, (Goder-Goldberger et al., 2019), similarly Lower Palaeolithic sites can occur quite close (4–5 m) under the current surface, as e.g. Revadim (Marder et al., 2008; Rabinovich et al., 2012) or Jaljulia (Zupancich et al., 2021), showing that a specific mapping of sediments of the same age either on the surface or in drillings might be used to predict additional sites of that timeframe. The sedimentation and climate history in the study region is very complex and includes major changes in between the Lower, Middle, Upper and Epipalaeolithic in addition to the general change in depositional regime with the onset of the Holocene. Each of these timeframes should thus be assessed individually to understand the spatial presence of related sediments and the potential of site preservation within these sediments. A general change can be expected from a predominance of preservational bias in the oldest periods in time, to a predominance of anthropogenic site selection criteria in the youngest periods as in the Neolithic.

2.4 RESULTS

The analysis of the selected eight individual parameters (detailed results and maps are given in the Appendix A.2) shows Upper Palaeolithic sites to be differently distributed than the distribution of natural terrain position factors. Both, the analysis of the histogram data (Fig. 2.3; Fig. 2.4) and statistical significance tests (Table 2.1) confirm sites to be predominantly present in one of the single classes of each individual parameter dataset.

Thus, the results suggest that sites are predominantly exposed in geomorphological situations containing bare rocks with small sedimentary pockets or on fossil desert surfaces (desert pavements like

reg or hamada). The coastal plain, the Wadi Araba and the local sinks, as the Jezreel valley, are devoid of Late Pleistocene sites. Additionally, sites are predominantly predicted in the upper reaches of the local drainage systems.

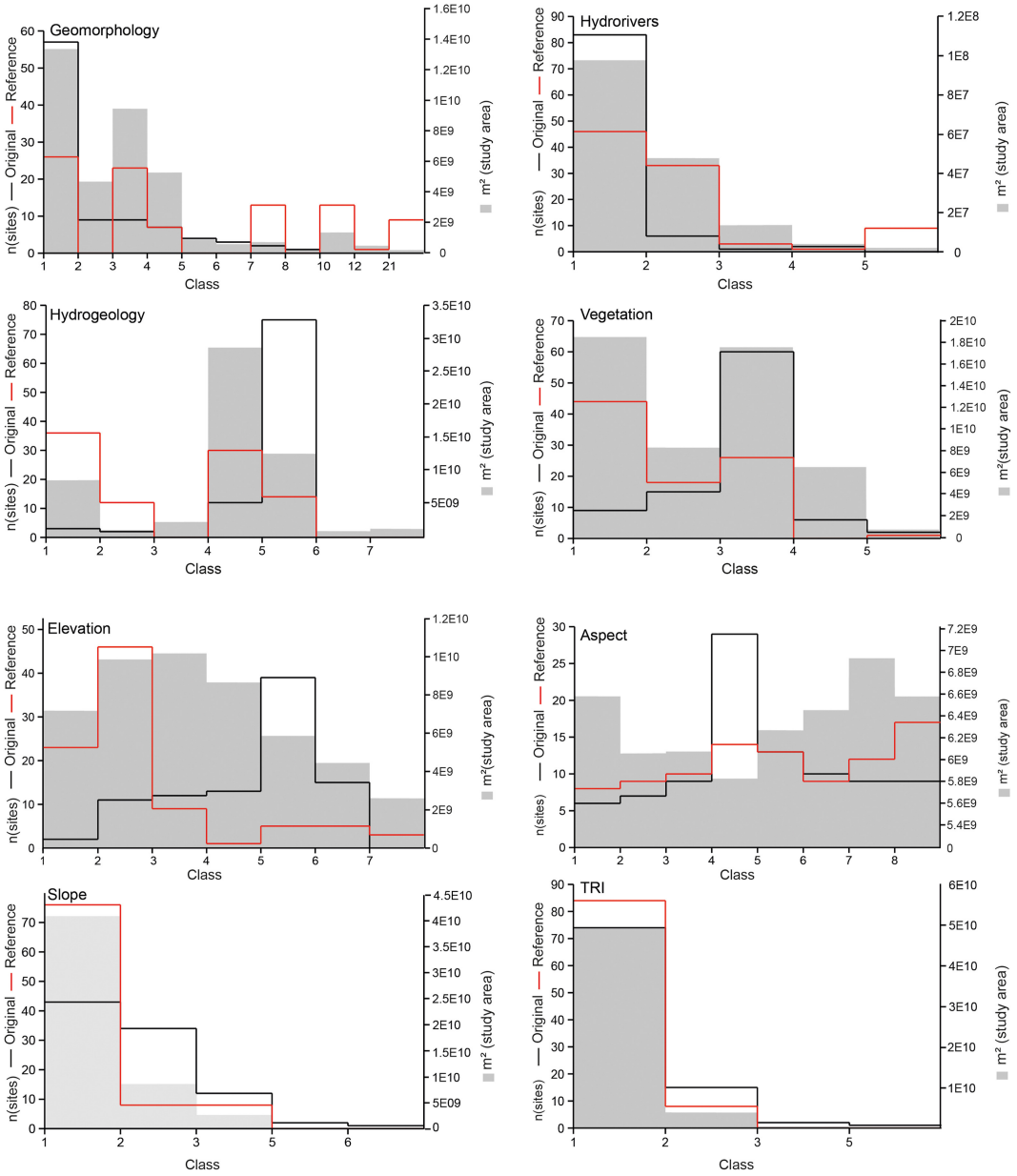

Figure 2.3: Histograms of site preservation on different factors. Classes for each parameter see Table 2.4,Fig. 2.1 and Appendix Figs. A.2-A.9

Most of the sites can be found close (5 km perimeter) to the first 22 river-kilometres from the spring. Hydrogeologically, a clear correlation to strata lacking productive aquifer systems is indicated. The sites, however, are predominantly located close to the outcrops of productive aquifer systems (Appendix, Fig. A.5) and thus border the discharge areas of the aquifers. Mainly desertic vegetation types, as

Geomorphology

Class	Class Name
1	Rocky basement
2	Reg / rocky basement
3	Limestone sediments
4	Hamada / limestone sediments
5	Reg / limestone sediments
6	Hamada / rocky basement
7	Crescentic dunes / Pleistocene alluvial sediments
8	Calcerous crust
10	Calcerous crust / limestone sediments
12	Crescentic dunes
21	Pleistocene Tertiary Conglomerates

Hydrology

1	Intergranular aquifers: extensive and highly productive
2	Intergranular aquifers: local or discontinous productive
3	Fissured/ karstic aquifers: extensive and highly productive
4	Fissured/ karstic aquifers: local or discontinous productive aquifers
5	Strata with local and limited groundwater resources

Vegetation

1	Mediterranean woodland
3	Irano-Turanian
4	Saharo-Arabian
5	Sudanian and Sub-Sudanian
6	Halo- and Hydrophytic

Drainages

Class	Interval from	to (km)
1	0	22
2	22.1	42
3	42.1	62
4	62.1	82
5	82.1	102

Elevation

Class	Interval from	to (m a.s.l.)
1	-100	100
2	100.1	300
3	300.1	500
4	500.1	700
5	700.1	900
6	900.1	1100
7	1100.1	1300

Aspect

Class	Interval from	to (degrees)
1	337.6	22.5
2	22.6	67.5
3	67.6	112.5
4	112.6	157.5
5	157.6	202.5
6	202.6	247.5
7	247.6	292.5
8	292.6	337.5

Slope

Class	Interval from	to (degrees)
1	0	10
2	10.1	20
3	20.1	30
4	30.1	40
5	40.1	50
6	50.1	60

TRI

Class	Interval from	to (index val.)
1	0	5
2	5.1	10
3	10.1	15
4	15.1	20
5	20.1	25

Figure 2.4: Class name lists for Fig.2.3

well as the higher altitudes of 700–900 m show a high site expectancy. Southwards or south-eastwards oriented site locations are most common. Northern aspects are uncommon, as are steep slopes above 20°inclination. Generally, gentle terrain with a slope inclination of 0–20°and a low topographic roughness index could yield the majority of Upper Palaeolithic sites.

2.4.1 *Spatial pattern*

Based on the statistical results the determined and classified parameters were combined using the MCDA method (see section 2.3). The resulting site preservation map makes it possible to narrow down areas predicted to contain Upper Palaeolithic sites (Fig. 2.5). The prediction clearly differentiates the study area into territories where sites can be present (coloured) and areas where sites are not expected at all (grey). Areas that possibly contain sites are further differentiated in seven grades, between an excellent and poor expectancy.

The map (Fig. 2.5) implies that no sites occur along the complete coastal strip, the low-lying sink areas as well as the Wadi Araba and

the Hula basin. These regions specify areas with recent, respectively Holocene, alluviums as designated in the geomorphological map (Appendix, Fig. A.4). The green colour range, indicating all areas with a good to excellent site expectancy, is mainly located in the higher elevations of the mountain ranges in the study area. Poorer site expectancy occurs at the north-eastern fringes of these mountain ranges, reflecting the rare representation of these aspects in the dataset, as well as in the dune fields in the north-western Negev. In general, the map specifies numerous regions with good or excellent site expectancy, which have not yet yielded major site clusters or have not yet been surveyed and might prove promising for future research activities.

If evaluated in more detail (Fig. 2.6) an abundance of favourable areas to the west of Lake Lisan is noticeable. The steep slopes of the Galilee region (Fig. 2.6a) result in extensive areas where poor site expectancy is given, especially in the wadis and on the northern slopes. In contrast, good expectancy characterises the southern slopes, which is confirmed by the presence of well-known archaeological sites like Manot Cave (80), Hayonim Cave (76) and Meged Rockshelter (14). Sefunim on the other hand, is the rare case example for a northern aspect, as well as El- Wad (74) and Kebara (78) for a western aspect, generally leading to a more diverse picture in the less linearly organised drainage pattern of the Carmel range. East of Lake Tiberias the mountain ranges offer a generally good site expectancy except for unsuitable areas at the northern slopes of the main tributary wadis.

In the Negev (Fig. 2.6c) large areas especially in the central part yield positive predictions including areas where large well-known site clusters (as e.g. in the Nahal Zin) are located. The area is generally characterised by positive prediction results which are now more closely defined by the map (Fig. 2.5). Generally, the currently higher sea level in comparison to the late Pleistocene (see map Fig. 2.5) leads to a loss of possibly inhabitable areas to the sea. In reverse, the area covered by Lake Lisan in the late and especially terminal Pleistocene cannot yield sites of this timeframe and site occurrences will be restricted to the past lake shore (see Ohalo II, Nadel (2017)).

Two additional maps were created to assess the accuracy of the MCDA results. The first (Fig. 2.7a) shows the results of the MCDA for the reference dataset, while the second (Fig. 2.7b) shows the difference between both datasets and the newly designated areas. The calculated confusion matrix (Appendix, Table A.7) informs in detail about the accurate class internal correspondence of the two datasets. Overall, regarding the pure pixel-based class correspondence respectively commission and omission the two datasets correspond to an extent of 32.96%. Generally, both datasets complement each other and densely surveyed areas in the one fill voids in the other.

Table 2.1: Statistical testing of single parameters. Basic data for the calculation see in the Appendix (Tables A.2-A.6). *if two datasets are normally distributed a t-test was conducted instead of Mann-Whitney U.

			Shapiro-Wilk test for normal distribution			**Mann-Whitney U test for significance***		
		sample size	W	p	result	z	p	result
geomorphology	area	32	0.55415	0.00000	negative			
	site frequency (original)	32	0.30478	0.00000	negative	-7.0564	1.709E-12	**significant**
	site frequency (reference)	32	0.49782	0.00000	negative	-7.0821	1.42E-12	**significant**
drainages	area	16	0.47370	0.0000	negative			
	site frequency (original)	16	0.31127	0.00000	negative	-4.9365	7.955E-07	**significant**
	site frequency (reference)	16	0.49793	0.00000	negative	-4.9053	9.331E-07	**significant**
hydrogeology	area	7	0.76262	0.01716	negative			
	site frequency (original)	7	0.56417	0.00010	negative	-3.0802	0.0002	**significant**
	site frequency (reference)	7	0.84571	0.11223	**positive**	-3.0802	0.0007	**significant**
vegetation	area	5	0.91133	0.47565	**positive**			
	site frequency (original)	5	0.73594	0.02194	negative	-2.5067	0.0121	**significant**
	site frequency (reference)	5	0.91998	0.52980	**positive**	t: 3.0296	0.0163*	**significant**
elevation	area	12	0.90502	0.18413	**positive**			
	site frequency (original)	12	0.70868	0.00102	negative	-4.1598	3.184E-05	**significant**
	site frequency (reference)	12	0.631880	0.00020	negative	-4.147	3.368E-05	**significant**
aspect	area	8	0.97035	0.90075	**positive**			
	site frequency (original)	8	0.67279	0.00110	negative	-3.3179	0.0009	**significant**
	site frequency (reference)	8	0.93141	0.52898	**positive**	t: 51.74	2.165E-17*	**significant**
slope	area	8	0.55889	0.0005	negative			
	site frequency (original)	8	0.72305	0.00409	negative	-3.3179	0.0009	**significant**
	site frequency (reference)	8	0.51416	0.00002	negative	-3.3605	0.0002	**significant**
TRI	area	9	0.43460	0.00000	negative			
	site frequency (original)	9	0.50212	0.00001	negative	-3.5691	0.0003	**significant**
	site frequency (reference)	9	0.43828	0.00000	negative	-3.6388	0.0003	**significant**

***retrieved from: StatistikGuru by Hemmerich (2018)** PAST 4:(Hammer et al., 2001)

2.4.2 *Wadi Sabra case study: A comparison to field observation and high-resolution modelling*

Lastly, the Wadi Sabra in Southern Jordan (Figs. 2.6 and 2.8) is evaluated in further detail. It can serve as a first high-resolution window into one of the regions with a high site density and complement the larger-scaled picture gained so far. It can further serve to compare and test the presented predictive map with field data and narrow down the specific conditions in which the sites are preserved and accessible in the micro- topography of the case study.

Here the dominating lithology is rocky basement indicating only a shallow or spatially limited distribution of sediments. Large remnants of Pleistocene sediment layers are preserved containing the sites. The calculated MCDA prediction map (Fig. 2.6d; 2.8) indicates excellent preservation throughout the majority of the wadi range. The reference MCDA (Fig. 2.8e) shows a slight decrease in site expectancy, the previous excellent expectancy changes to a good expectancy, in general though, the Wadi Sabra retains its good general prediction. In addition to extensive survey activities in the field under the direction of Daniel Schyle (Richter and Schyle, 2015), the additional landform classification was executed (Fig. 2.8a and b). The results of the high resolution landform classification for the Wadi Sabra show the erosional margin of the sediment remnant to be flatter at the top, and steeper at the bottom. This flat upper part of the stratigraphy consists of intermittent steep profiles and small terraces formed by denser or more compacted sediment layers above the top of the detritic cones (Fig. 2.8c). The map resulting from the landform classification (Fig. 7a and b) explains the site distribution in more detail. Nearly all sites are preserved on mountain tops, high ridges, upland drainages, headwaters or upper slopes, mesas. Sites on top of the sediment remnant weathered out where the overlying calcareous crust was cut by erosion. Four in-situ sites (Sabra 4 Palmview 3 (S4PV3), 2010/6, Sabra 3 South and Sabra 3 North (Schyle and Uerpmann, 1988; Richter and Schyle, 2015; Schyle, 2015a; Schyle, 2015b; Schyle, 2015c; Schyle, 2015d; Schyle, 2015e; Parow-Souchon, 2020) were found at the margin of the sediment remnant. The Qalkhan surface site of Sabra 3 Centre (Richter and Schyle, 2015; Schyle, 2015a) lies atop the calcareous crust, while the aurignacoid/Arqov-Divshon assemblage of Sabra 4 Palmview 1 (S4PV1) is located on the surface on a step in the sediment remnant. The wide-open U-shape of the Upper Wadi Sabra thus serves to shelter the sediments from blanket erosion, while the wadi course opens a profile into the stratigraphy. The sites recovered within lie generally at the very top of the stratigraphy, as the dendritic cones from the erosional processes hinder access to the lower part of the stratigraphy and the sites potentially contained therein. A few isolated surface finds of Levallois points and El Wad points hint at the presence of

potentially older sites in the lower part of the sediment outcrop. Sites on the surface of the calcareous crust are mainly of Epipalaeolithic and younger age, confirming the dating of the crust into the Last Glacial Maximum (Bertrams, 2013). A few Middle Palaeolithic surface occurrences high up the wadi flanks suggest the remnants of older terrace remains indicating a higher sediment fill, than the preserved Pleistocene one.

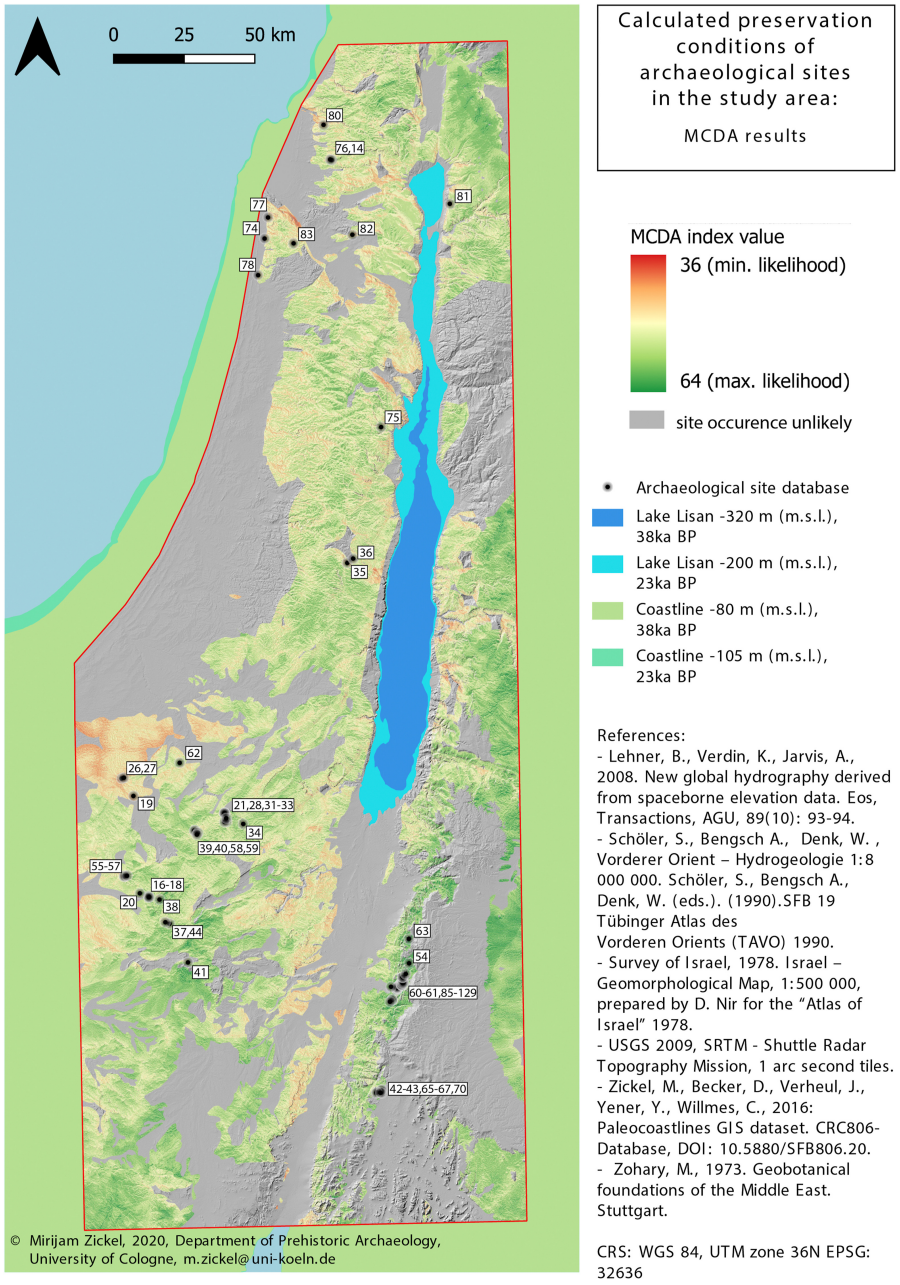

Figure 2.5: Multi Criteria Decision Analysis (MCDA) derived archaeological site preservation. Site ID# see Appendix, Table A.8

The generally wide and flat morphology of the Upper Wadi Sabra leads to an increased site preservation chance, mirrored in the high

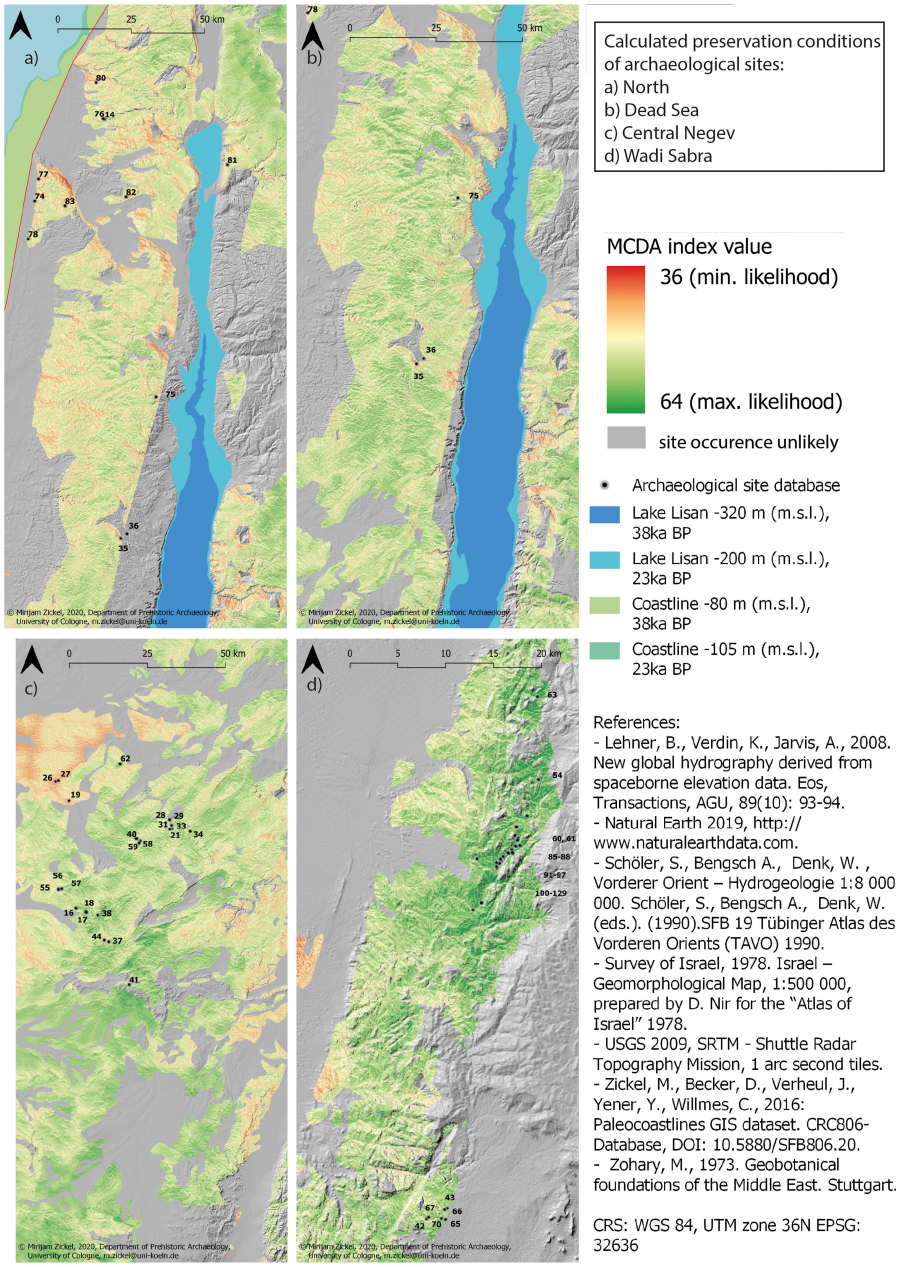

Figure 2.6: Detailed predicted site expectancy: a) North, b) Dead Sea, c) Central Negev, d) Wadi Sabra. Site ID# see Appendix, Table A.8.

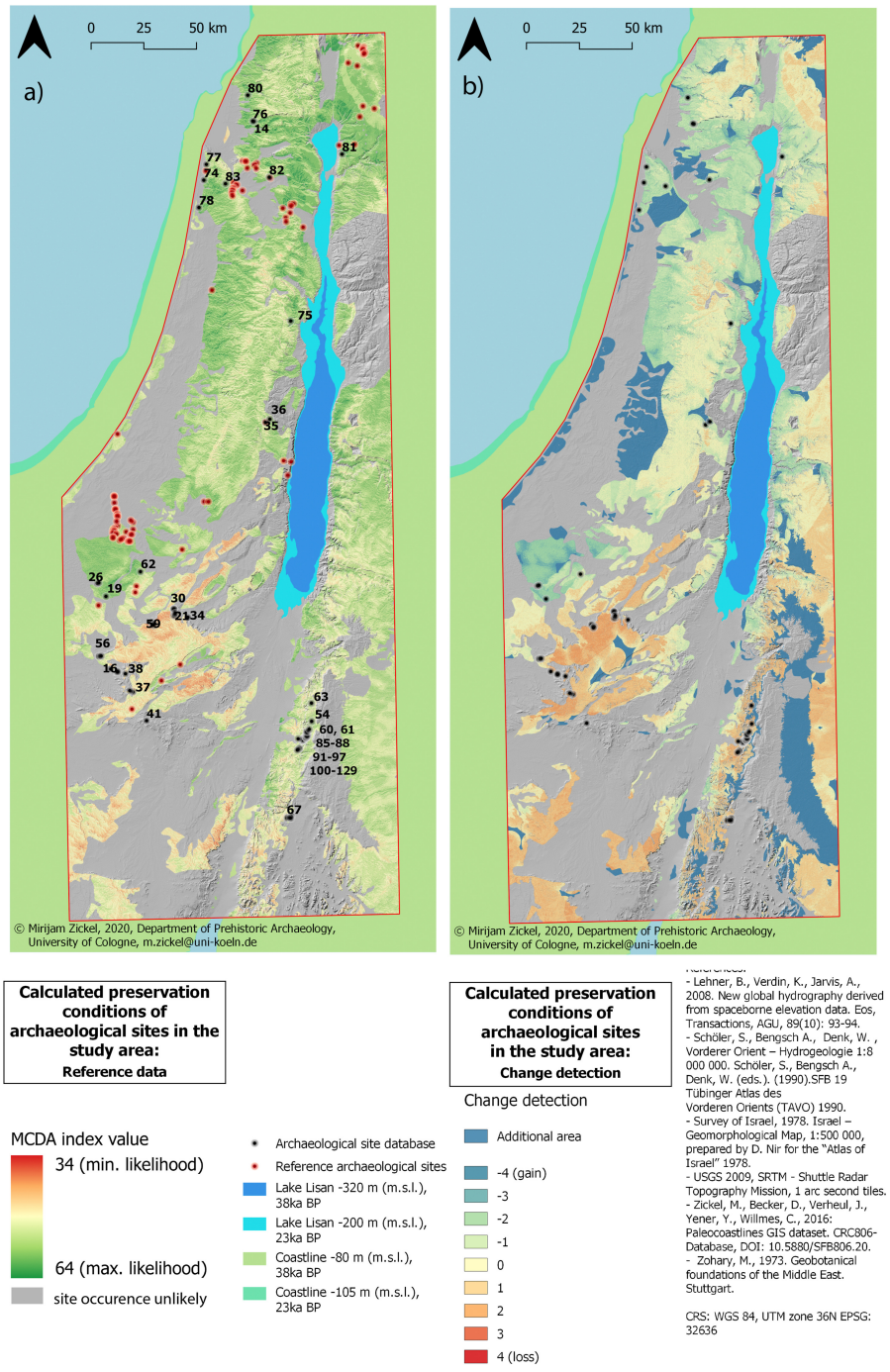

Figure 2.7: Computed archaeological site expectancy (Multi Criteria Decision Analysis MCDA) for the Reference Dataset (a) and Detection Change in comparison with the original dataset (b). Note: Only areas present in the original dataset are computed.

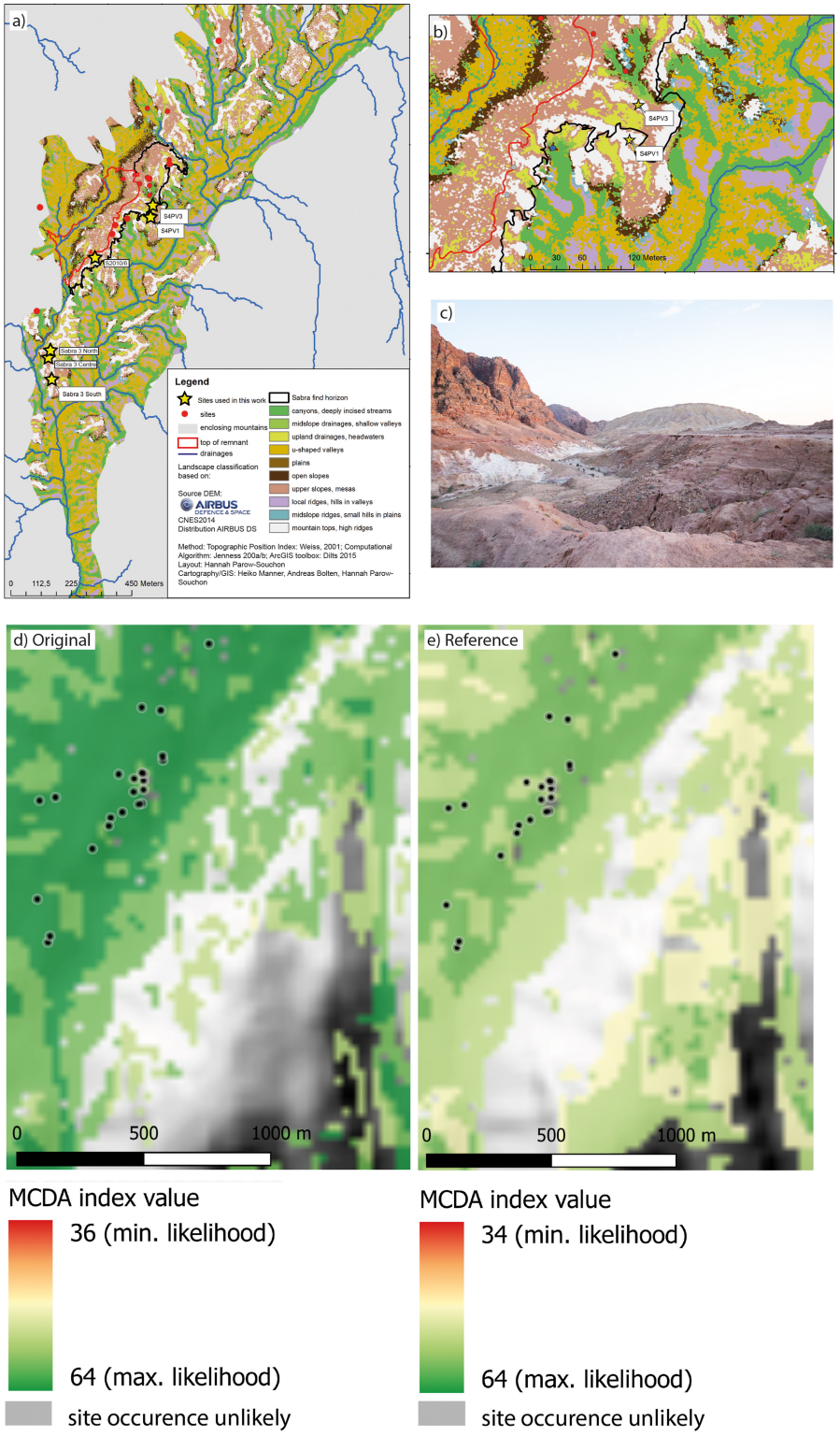

Figure 2.8: Upper Wadi Sabra landform classification a) Landform classification overview, b) detail Sabra 4, c) outcrop of sediment remnant with clean profiles in the upper part and detritic cones in the lower part, d) Multi Criteria Decision Analysis MCDA results original dataset, e) MCDA results, reference dataset.

number of recovered inventories, the presented predictive maps, the landform classification as well as a previous multispectral remote sensing approach which enables the mapping of site-carrying goethite-rich sediments and their spatial distribution in the wider surroundings of the Wadi Sabra (Lohrer et al., 2013).

In comparison, the coarser-scaled positive result of the MCDA (Fig. 2.8d and e) can be refined by the data from the Pleiades satellites. While the complete wadi floor yields a positive prediction during the MCDA, the high-resolution DEM is able to differentiate the loss of the current wadi course, the slope of the outcrop escarpment including the presence of detritic cones as well as the flat top of the calcerous crust hindering access to the lower layers.

A combination of coarse but wide range and high resolution but detailed mapping, pedestrian survey and landform classifications can closely narrow down the site recovery conditions in the highly geomorphologically active region of the Jordan highland escarpment, and might possibly be translated to similar situations in the adjacent regions.

2.5 DISCUSSION

The results contain numerous points for discussion and a number of possible avenues for future research. One of the main discussion points is the scale of a study like this and the pertaining explanatory value. Predictive modelling in an area as large and as diverse as the one studied herein is obviously challenging and includes some inherent extrapolation and generalisation of very different conditions in the local meso- and micro-situations. Geoarchaeological studies on the scale chosen here are relatively rare, but are occasionally conducted with helpful results (Kondo et al., 2012; Luo et al., 2014; Beyin et al., 2019). The large scale was intentionally selected to include a first overview over the general conditions. From the gained results especially the north-eastern Galilee, the south-eastern slopes of Mitzpe Ramon, and parts of the Jordan Highland Escarpment, especially east of the current Dead Sea and around Jafr would be prominent case studies for future more detailed investigations. One of such is already given for the case example of the Upper Wadi Sabra in Southern Jordan. If the results of both analyses are compared, the MCDA slightly overestimates the spatial area where sites can be expected. This is likely an artefact of the relatively coarse scaled geomorphological information for the area which does not differentiate bedrock and sedimentary pockets (Nir, 1978).

In general, predictive modelling studies for the Levant are exceptionally rare and the method applied here has not yet been tested. Other methods, as for example logistic regression and maximal entropy

(Wachtel et al., 2018), have been successfully tested on case studies in the Levant.

Comparing the results of the MCDA, the predictive map calculated on the basis of the original dataset of published sites positively predicts nearly half of the reference sites. Mainly the sites in the large site clusters in Nahal Besor/Ze'elim area, the Jezreel Valley and in the Golan Heights were not correctly predicted together with two sites on the shores of the Dead Sea. 43 of 92 reference sites already lie within the positive prediction of the original MCDA (46.7%), while 36 of the incorrectly predicted sites (n =49) are located in the three major site clusters where the data was missing (see discussion below). In reverse, the reference MCDA correctly predicts 71 of 92 sites from the original dataset (77.2%), while omitting the sites in Nahal Zin, Ain Aqev, Qadesh Barnea, Ein Qadis and a few other isolated findspots in the Central Negev. The observed concordance of both datasets of 32.96% is a relatively low value, if discrete (natural) land cover classes are assumed. However, the artificial classification applied herein represents a gradual transition from poor to excellent site expectancy. Therefore, such a result of compliance is to be expected when artificially classified datasets are compared.

The data quality has a fundamental influence on the content output which therefore has to be discussed in relation. With regard to the used data sources a number of limiting factors have to be taken into account. On the one hand, site coordinate precision varies. Even while being recorded with utmost care, conversion and transmission errors must be expected over time. This can easily lead to incorrect DEM query values, especially if the sites mis-location exceeds the spatial resolution of the DEM raster cells (30 m). Especially for sites recorded before the widespread availability of handheld GPS devices, these limiting factors need to be considered. However, no such case has been observed in the results so far.

On the other hand, the historical research focus has to be taken into account as it entails a certain bias. For both datasets a broadly incomplete survey of the large study area with regard to Prehistoric sites is a limiting factor. Thus, dense site clusters dominate the picture in both, the original and reference datasets on a large and small scale. The original dataset contains many site clusters in the Central Negev, both by the Emergency Archaeological Survey (Goring-Morris, 1987) as well as by the works of Marks (Marks, 1976; Marks, 1977; Marks, 1983a; Marks, 1983a), in the Wadi Sabra (Schyle, 2015b; Parow-Souchon, 2020), the Ras-en-Naqb (Henry, 1995) and others. The reference dataset is dominated by site clusters in Ze'elim/Nahal Besor, the Jezreel Valley and the Golan heights. These localised site clusters heavily influence the calculational output to both, beneficial and problematic, results. They closely describe small densely surveyed areas and give a high-resolution output for the presence and potentially observed

absence of sites. However, with regard to the complex and small-scaled geomorphological situation, it is unclear if the local conditions of these site hotspot regions can be extrapolated to other regions. For example, the sites in the Nahal Zin are tied to very small, localised sediment remnants preserved just after the widening of the narrow, deeply cut Upper Zin canyon (Goldberg and Brimer, 1983; Marks, 1983b; Goldberg and Macphail, 2006), leading to a securely overestimated positive prediction for the Upper Zin. In contrast, the lower Zin is negatively predicted, even though the geomorphology of the area is by far more likely to allow for site preservation than the deeply incised canyon upstream.

The strong influence which both, the Ze'eelim and the Jezreel valley clusters, both of problematic origin, have on the calculational output of the reference dataset recommends a cautious interpretation. This result illustrates very well the strengths and weaknesses of the chosen method. Thus, a reliable dataset, verified by the scientific community, is crucial for the reproducibility of the results, especially when standardised field data is unavailable. In order to avoid a too one-sided weighting or cluster formation, the sites could be sampled to represent a more even spatial distribution. Regions with a large number of verified sites could also be treated separately with the method presented here. This would also be an interesting step with regard to the high spatial variation of Pleistocene sediments in the study area. The prediction accuracy of an MCDA of a smaller spatial unit as, for example, the Negev desert, would probably be significantly higher. The case example of the Upper Wadi Sabra has shown that even within a small area micro-regional site preservation varies greatly and distinct chronological phases can be tied to different stratigraphic and topographic positions. Studies of such high detail, however, can only be conducted for areas where both, the local topography is well-understood and high-resolution spatial data is available.

Further limitations of both datasets can be expected on account of the age and scale of several of the included maps. Especially the vegetational map (Zohary, 1973), the geomorphological map (Nir, 1978) and the hydrogeological map (Schöler et al., 1990) are not up-to-date and relatively coarse scaled and should be replaced by more updated versions. Concerning the SRTM (USGS - United States Geological Survey, 2009) digital elevation model, as well as DEM derivates like the applied HydroRIVERS dataset (Lehner et al., 2008), RADAR recording and processing errors can influence the modelling output (Lillesand et al., 2015, e.g.). However, the relatively coarse spatial resolution (30 m) of the DEM can be advantageous here as it minimises irrelevant unevenness in the analysis. In addition, modern artefacts, which can negatively influence the analysis, such as roads, are not included (Becker et al., 2017). As suggested by Lehner et al. (2008), the regional drainage system represented by the HydroRIVERS dataset should be

understood as "potential" river network, since it is unclear if all of the indicated drainage systems carried water at the time of the Upper Palaeolithic (known river systems e.g. Nahal Yarkon, Nahal Taninim, Nahal Lachish, Nahal Soreq, Nahal Besor and others cf. (Greenbaum and Zilberman, 2017).

The evaluation of the individual parameters yields clear results for a selection of specific parameter classes, yet their nature and origin as well as their influence on the result have to be evaluated.

The location of the sites on the outcrops of productive aquifer systems can most likely be considered as a result of Pleistocene human agency and choice for areas with increased water availability. Confined and covered aquifer systems can only discharge water vertically through fissures in the rock (Holting and Coldewey, 2009), thus the availability of surface water and springs can be expected to be markedly reduced above aquiferous geology in some parts of the study area. In situations, where aquifer layers are outcropping, tectonic or gravitational pressure from overlying strata can lead to an increased discharge and spring formation.

An easily visible regional "gap" in the prediction west of the current Jordan river valley requires an explanation. Here, the porous karst systems (compare layer class: 'fissured/karstic aquifers: extensive and highly productive') cover highly productive aquifers but impede access to water which only discharges into adjoining areas. A site location at the edge to but not on top of these aquifer layers can thus be expected to yield the highest freshwater availability, the hydrogeology is thus the reason for the lack of site expectancy.

The absence of sites in the lower parts of the drainage system is most likely of post-depositional origin. The regions close to the big collection streams seem to lack archaeological sites (Appendix, Fig. A.6). In the flood plains and on the riverbanks of large collective streams, potential surface sites may have been eroded, relocated or covered by thick Holocene alluvial sediments. Upper Palaeolithic agent's decision against the lower drainages could only be explained by the dangers of flooding, which, however, could be easily avoided by choosing one of various localities outside of flood plains. It is thus most likely that the reduced accessibility of sites is responsible for the lack of assemblages in the lower drainages.

The picture provided by the current vegetation can be expected to be largely correlated to the much-increased visibility of archaeological remains on sparsely vegetated or unaltered (fossil) desert surfaces, accordingly to the much-increased facility of conducting survey in these terrains. A densely forested Mediterranean woodland with a high amount of underbrush and increased soil formation hinders systematic survey activities and limits the chance encounter of Upper Palaeolithic sites. It also negatively affects continuous erosion which could provide access to covered sites. Thus, site discovery in

the Mediterranean zone is mostly connected to easily visible cave sites which can be accessed by targeted effort and subsequently sampled. Upper Palaeolithic surface sites are entirely absent or invisible in the Mediterranean zone. This factor might be one of the major determinants for a difference in spatial distribution of Late Pleistocene sites in Mediterranean areas and arid margins.

In terms of the palaeo-vegetation, the current vegetation can at best be understood as a proxy for the summarisation of large-scaled landscape units potentially existing also in the Late Pleistocene with some deviations. During the Late Pleistocene, the currently strongly expressed vegetational gradient is expected to be markedly reduced (Miebach, 2016) though opinions differ on the exact climatic mechanisms responsible for this development (Hayes et al., 1999; Rohling, 2013; Torfstein et al., 2013; Stockhecke et al., 2016; Torfstein and Enzel, 2017). The interplay between changes in precipitation and evaporation in the Late Pleistocene Levantine climate is a topic of constant discussion as is the reason – however not the effect – on large water bodies as Lake Lisan showing marked highstands in the final Pleistocene and sharp drops during Heinrich-events (Torfstein et al., 2013; Torfstein and Enzel, 2017). Thus, habitable conditions can be expected to have prevailed throughout much of the study area with exceptional conditions surrounding the large water bodies as Lake Lisan.

Compared to the previously discussed results, elevation, aspect and slope are less susceptible to change from Late Pleistocene conditions. The most strongly represented aspects are South and Southeast indicating a human choice for sun-exposed localities. Northern aspects are largely avoided even though present in sufficient abundance in the local topography. Flat slopes of 0–20°are most strongly represented in both, site locality and general prevalence in the study area. The preservation of open-air sites is obviously depended on relatively gentle slopes evading complete erosive removal but enabling access. The slope inclination thus could have preservation-related, as well as anthropogenic implications: A smooth terrain could be regarded to include both: better preservation and Upper Palaeolithic agent's preference for a relatively even settlement area.

The Northern cave sites, however, are usually found in steep escarpments with sometimes almost vertical expression. Sheer steep escarpments are difficult to capture in digital elevation models because of technical limitations in RADAR remote sensing (Lillesand et al., 2015). An elevation model with a relatively coarse resolution, as the here used 30 m DEM, can be expected to disregard parts of steep escarpments. In theory the resulting prediction model thus only has a limited ability to predict cave sites. In contrast, it can be expected that open air sites are detected without such constraints.

In summary thus, the evaluation of the individual parameters indicates that the influence of the geomorphological setting, the location of

the site in relation to the potential drainage system, the slope and the TRI can be considered to be of post-depositional origin. The visibility of sites and their accessibility in the field leads to a high representation of desertic vegetation types in the result. The clear trend towards localities with certain hydrogeological, elevation and aspect characteristics can be considered to be most likely a result of Upper Palaeolithic campsite selection.

The two predictive maps, based on the original and reference datasets, show in parts quite startling differences (Figs. 2.5 and 2.7). Especially consulting the change detection raster (Fig. 2.7b) it is easily apparent, which parameters are responsible for this result. The Kurkar-ridges on the coastline are now included in the positive prediction, as a result of the single site of Nahal Shiqma (South), but also confirmed by site A306a (Gilead, 1984) located at the beach of northern Sinai outside the study area. The reference dataset contains fewer sites from the Central Negev thus leading to a reduced representation of this area in the result. In contrast, the high number of sites in the Ze'elim area and Nahal Besor, not present in the original dataset, leads to a positive prediction for the sand dunes and the late Pleistocene sediments found in this area (Zilberman, 2010). Similarly, a high density of recorded findspots in the Jezreel valley (see Figs. 2.1 and 2.7), both inside the valley and on the surrounding slopes, as well as an additional cave in the Carmel (Oren Cave by Stekelis), expands the area of positive prediction in the whole region. A large number of findspots in the north-eastern corner of the study area does likewise.

Nahal Besor represents an interesting case example, as a most recent survey (Goder-Goldberger et al., 2019) revisited the locality and brought back high-resolution spatial information. The sites included in this study, originate from the IAA Survey database and have been recorded by Dan Gazit. While he extensively surveyed the Holocene (Zilberman, 2010) sand dunes in the south-west of the Bezor stream, today inaccessible military restricted area, he also recorded a number of sites in the streambed of the recent fluvial channel of the Besor river. The presence of Pleistocene sites within dunes mapped to be of Holocene origin (Zilberman, 2010) requires clarification. These sites might either be connected to small outcrops of Pleistocene sediments not mapped sufficiently, be relocated by post-depositional processes, or are potentially not securely dated into the Upper Palaeolithic period. As the area is currently inaccessible, the situation cannot be resolved by a reassessment. The new survey results by Goder-Goldberger et al. (2019), however, clearly indicate a high concentration of Middle Palaeolithic and a few Upper Palaeolithic sites within the erosional margin of the recent streambed. The predominance of Middle Palaeolithic over Upper Palaeolithic sites, however, requires an explanation. While Middle Palaeolithic site preservation is not the topic of the current analysis, these results might cautiously point to a difference

in campsite preference between the Middle and Upper Palaeolithic. Thus, it might indeed provide a small hint towards an intentional avoidance of the lower drainages or altitudes by Upper Palaeolithic hunter-gatherers. Alternatively, or additionally, potential erosive processes might have removed Upper Palaeolithic strata, but did not reach the Middle Palaeolithic. An observed strong fluvial impact on late Middle Palaeolithic to early Upper Palaeolithic strata in the northern cave sites (Bar-Yosef et al., 1972) might have also acted on the surface site distribution in the Mediterranean zone. The case of the Besor stream thus illustrates the importance of obligatory detailed local evaluation of the presented results in the diverse environment of the study area. The implementation of these on-site studies would redefine the extrapolation and continuously improve the output of the digital survey.

2.6 CONCLUSION

An MCDA predictive model based on the evaluation of eight individual parameters is presented and tested, both by a reference dataset covering the complete study area and an additional model in the small region of the Wadi Sabra. The results yield a clearly different preservation of Upper Palaeolithic sites connected to both, the post-depositional situation as well as results of Upper Palaeolithic human agency. The study was successful in delineating areas with high site expectancy in addition to such where no sites can be expected. It thus yields a first, coarse-scaled estimate in the form of a digital survey, which can, and should be, further investigated.

The local geomorphology as well as the slope inclination and the terrain ruggedness TRI were found to influence erosional processes or the lack thereof. The current vegetation is largerly responsible for the visibility of sites during survey activities. The site location in the upper areas of the drainage network and the presence of aquiferous geology are interpreted as a result of past human agency. The absence or invisibility of sites in the lower drainages is most likely a product of large scale fluvial sedimentation processes. Both elevation and aspect of the chosen campsites are also parameters we consider to be a result of Upper Palaeolithic agency, selecting sun exposed places with a wide view of the immediate surroundings.

In total, there is no adequate method to deal with the bundle of possibly uneven representation when dealing with the past (Verhagen, 2018), especially regarding the dimensions of the study area. However, a basically heuristic approach, proven in several GIS applications, a trial and error method based on set theory (Usery, 1993) and aiming to ensure a 'step-by-step and as-individual-as-possible treatment' of the spatial datasets seems to be currently the best possible option (Malczewski and Rinner, 2015). Moreover, it is a good way to deal

with a potpourri of continuous, discontinuous, as well as more or less dependent or independent datasets in one analysis.

Even though coarse-scaled, the presented analysis yields clearly positive results and shows a high potential for future more detailed investigations. Subsequent research should both, aim to refine the presented results and test them in the field, as well as add additonal timeframes to assess Middle or Lower Palaeolithic site preservation. Especially research into the older periods might greatly profit from such endeavours as matters of both, preservation and accessibility of site- carrying sediments gains increasing importance further back in time.

Future assessments can base on this considerable potential and refine the found results. In this sense, a reasonable step for future assessments could be the restructuring of the archaeological site dataset according to geo-location and cultural attribution. A screening and sorting of the large site clusters in the study area and the addition of reviewed sites of the reference dataset from areas in which no sites are recorded in the original dataset could counteract a polarization of the results. As not all map quadrants were surveyed with respect to Prehistoric sites, the record of survey topics should be extracted from the IAA database and added to the calculation. The processing of the here presented information, however, would be a project in itself and will be included in a future study.

A number of future additions to the methodology can yield more detailed results. The use of new remote sensing data such as a higher-resoluted DEM (12 m TanDEM-X by DLR – German Aerospace Centre), but also subsequent surveying, mapping and modelling (e.g. palaeoclimate modelling as in Miebach et al. (2019) as well as the addition of reviewed sites will be major steps in order to gain a wide-ranging, informative Upper Palaeolithic survey map. Modern impact on the landscape, due to farming, soil (mass) movements, erosion or coverage of whole areas through sedimentation processes or build-up areas, has not yet been included in the calculation and should be added in the future. Likewise, – if possible – the effectively surveyed area in the vicinity of the site clusters should be taken into account. An assessment of the equidirectionality of parameters added into the calculation should also be included in a re-assessment of the presented calculations. It would certainly also be a good course to support the prediction model with the help of multispectral satellite data (Zickel, 2020; van der Meer et al., 2014).

Predictive modelling in an area as diverse as the one analysed here includes both, challenges and rewards, yet offers great potential for understanding the spatial distribution of archaeological sites, the conceptualisation of survey projects as well as for risk assessment considerations in heritage management and infrastructure projects.

ACKNOWLEDGEMENTS

We would like to thank Jürgen Richter and Daniel Schyle for the great opportunity to work in the Wadi Sabra. We would also like to thank Thomas Wolter and Andreas Bolten for their continued support over the years and the material and advice they have provided us with. Additionally, we would like to thank Maayan Shemer and Michal Birkenfeld for helpful remarks on an earlier version of the manuscript.

FUNDING This research has partially been funded by the Deutsche Forschungsgemeinschaft (DFG) in the frame of the Collaborative Research Centre 806 – Our Way to Europe (www.sfb806.de) at the University of Cologne.

DATA AVAILABILITY Supplementary data to this article can be found online at https://doi.org/10.1016 j.quaint.2021.05.020.

DECLARATION OF COMPETING INTEREST The co-authors state no conflict of interest.

3

PLEISTOCENE-HOLOCENE LANDSCAPE EVOLUTION AND CLOSED DEPRESSIONS AT THE EASTERN CARPATHIAN BASIN (TOBOLIU, ROMANIA)

The author contributions are structured by categories, namely: Conceptualization and Methodology, Software and Data Curation, Formal analysis, Investigation, Visualization, Supervision, Project administration, Funding acquisition, Writing –Original Draft, and Writing – Review and Editing. The individual authors' contributions to each category are subsequently listed by their initials.

Conceptualization and Methodology: MZ, JN, TR, SO; Software and Data Curation: MZ, DH; Formal analysis: MZ, JN, AR, SO, TR; Investigation: MZ, JN, DH, FS, NM, SR, TR; Visualization: MZ, DH; Supervision: TR; Project administration and Funding acquisition: AR and TR; Writing – Original Draft: MZ; Writing – Review and Editing: MZ, JN, AR, DH, FS, NM, SO, TR.

Mirijam Zickel[2], Janina J. Nett[2], Astrid Röpke[1], Stephan Opitz[2], Dennis Handy[2], Susen Rische[2], FLorian Steininger[2], Nicole Mantke[3], Tony Reimann[2]

Manuscript submitted on 2025-07-15 to the Journal *Journal of Quaternary Science, Wiley*

1 Laboratory of Archaeobotany, Institute of Prehistoric Archaeology, University of Cologne, 50923 Cologne, Germany
2 Department Soil Ecology, University Bayreuth, Bayreuth, Germany
3 Institute of Geology and Mineralogy, University of Cologne, Cologne, Germany

Abstract

In Toboliu, at the eastern fringe of the Carpathian Basin (CB), a principally flat, steppe-like landscape features Closed depressions (CDs) close to a Bronze Age tell and an elongated basin feature. Determining landscape formation is challenging due to superimposed effects of modern and prehistoric farming. As part of our project, 'Living Together or Apart?', which investigates a local Bronze Age settlement and associated land use, we tested previous hypothesis that the CDs represent anthropogenic loam-extraction pits. We combined spatial analysis, including a high-resolution elevation model, magnetographic, multispectral imagery, and historical geodata with sediment core analyses using lithostratigraphic, pedological, and palynological methods. The chronostratigraphic framework was established through Optically Stimulated Luminescence (OSL) and radiocarbon dating. Our findings show a landscape of a channel network and periglacial features suggesting that the CDs represent periglacial relict landforms. This is supported by the complex pedo-sedimentary record of Core 5, featuring fluvial, alluvial, aeolian, limnic, and pedogenic phases ranging from Marine Isotope Stage (MIS)-6 to Early Holocene. Moreover, we identified a well-preserved Early Holocene pollen sequence in the backfill of one core (Core 13), representing a rare instance of pollen preservation in the eastern CB.

3.1 INTRODUCTION

Prehistoric human-environment interactions are examined across diverse spatial and temporal scales to deepen our understanding of their influence on soil-landscape evolution. Since Neolithic times, settlements increasingly emerge along streams in the eastern CB (Bánffy and Books, 2019). Prehistoric site selection at its fringe, situated between the Carpathian and Apuseni mountains to the east and the Great Hungarian Plain, may have been influenced not only by farming opportunities but also by intense upland-lowland interactions, which enhanced resource availability and mobility (Duffy et al., 2019; Glatz and Casana, 2016). Near the river Crişul Repede and the Apuseni Mountains, our study area around Toboliu's Bronze Age tell (anthropogenic mound) seems to correspond to such a transitional landscape.

Archaeological work at Toboliu began in 2014, including excavations and non-invasive investigations (Lie et al. 2024). In this framework, a geomagnetic survey was performed to assess the spatial extent of an outer settlement (Găvan et al., 2021). Our research project, 'Living together or apart? Unravelling the development, internal organization and social structure of a complex Bronze Age tell settlement at Toboliu, western Romania', focuses on the Bronze Age occupation (i.e, ∼3800 to 3300 BP surrounding the tell (Găvan et al., 2022; Lie et al., 2024). Between 2021 and 2023, excavations yielded settlement contexts on an elongated lift east of the tell.

Understanding Bronze Age land-use requires knowledge about the natural environment before human interference. However, intensive land use, both modern and prehistoric, has led to erosion of landforms and archaeological contexts. Beyond the relatively well-preserved elevated tell, differentiating between natural and anthropogenic landscape features in the flat terrain poses a challenge. This is particularly evident concerning several CDs in the vicinity of the tell (Fig. 3.1a)(Fig. 3.1b). This raises key questions about the formation processes of these depressions and the state of the soil-landscape system before Bronze Age settlements. The literature on natural drivers of landscape evolution in the region is limited, with only few uncertain pedological and lithological data available. However, studies from the broader CB and neighboring areas offer valuable insights into regional landscape evolution. Research by Kiss et al. (2015), Gábris and Nádor (2007), and Nádor et al. (2007) examined fluvial network development during the Quaternary. Additionally, Kiss (2019) explored the surface water network prior to large-scale river regulation efforts.

Spatial loess and loess derivate distributions were recently compiled for the eastern CB by Lindner et al. (2017a). Concerning loess derivates, it is important to note that Loess-Palaeosol Sequences (LPS) in the eastern CB often consist of complex pedo-sedimentary records, characterised by additional alluvial or fluvial contributions, which con-

trasts with plain LPS, such as the Krems-Wachtberg record in Austria (Sprafke et al., 2020). Several complex pedo-sedimentary records or LPS were recorded, for example, in northeastern Hungary by Bösken et al. (2019)(Bodrogkeresztúr) and (Schatz et al., 2012)(Tokaj), in western Romania by (Pötter et al., 2021)(Semlac) and in northern Serbia by Antoine et al. (2009), Marković et al. (2007), and Stevens et al. (2011) (Vojvodina region). Interstadial soil formation in LPS and the Pleistocene-Holocene climatic transition along the CB (among others) were discussed in detail by Constantin et al. (2021). Concerning further palaeoclimatic proxies, Gábris and Nádor (2007), Lehmkuhl et al. (2021), Ruszkiczay-Rüdiger and Kern (2016), van Vliet-Lanoë et al. (2004) discuss permafrost boundaries for the marginal areas of the CB. Compared to mountain sites, past vegetation reconstructions for the CB are still scarce, and only one site encompassing the Holocene in the larger region is reported from Sarló-hát, Hungary (Magyari et al., 2010).

To shed light on the formation of typical landscape features in the study area, we test two hypotheses on CD formation: CDs formed as loam extraction pits through human activity during the Bronze Age (compare Gerlach et al. (2006)), bomb craters, or by natural soil-geomorphological processes (compare Kołodyńska-Gawrysiak and Poesen (2017)). One possible natural process in Toboliu's flat, loess landscape covered by 'clayey loess' deposits, is the formation of loess dolines (Lindner et al., 2017b). Such landforms were studied by Lukić et al. (2009) and Zeeden et al. (2007) in the Vojvodina region (Serbia), as well in Dobdrudja (Romania) by Romanescu et al. (2018). Additionally, the likely presence of regional permafrost during extremely cold phases of the last glacial period is considered for the formation of periglacial landforms, such as ice wedges and pingo remnants (Gábris and Nádor, 2007; Lehmkuhl et al., 2021; Ruszkiczay-Rüdiger and Kern, 2016; van Vliet-Lanoë et al., 2004). To scrutinise these hypotheses, we combine spatial landscape analysis using GIS, remote sensing, and historical geodata with the analyses of sediment cores. Therefore, we established a chronostratigraphical framework for the study area based on sedimentological, geochemical and palynological data in combination with OSL and radiocarbon dating.

3.2 STUDY AREA

Toboliu lies ∼15 km west of Oradea, a city in Bihor County, Romania. The landscape is part of intermediate lowlands at the easternmost CB margin, at an elevation of ∼100 to 104 meters above mean sea level (a.m.s.l.). Close-by, in the east, the Apuseni mountain foothills stretch out. Coming from this direction, the River Crişul Repede frames the area in the north-west by its confluence with Alceu River to the south.

The study area (Pannonian zone after Metzger et al. (2005), features a Dfb (warm humid continental) climate according to the Köppen-Geiger classification (Kottek et al., 2006). It experiences a warm, humid continental climate characterised by warm summers and cold, relatively dry winters (annual precipitation average:∼550 mm). Most rainfall occurs from May to July, (Crocetti et al., 2020; Ruszkiczay-Rüdiger and Kern, 2016). The current vegetation is primarily degraded wooded-steppe, which is occasionally used for grazing, although agricultural cultivation is more prevalent.

Climate and vegetation reconstructions of Magyari et al. (2010) suggest that wide parts resembled a forest or wooded steppe environment during the Holocene, before adopting agricultural practices. The typical soil group under a wooded steppe in a loess landscape would be a Phaeozem (IUSS (WRB) WG, 2015) which is also very likely in Toboliu (Lie et al., 2024). Intense land-use has heavily modified, both soils and vegetation (Magyari et al., 2010; Magyari et al., 2024). In Toboliu, ploughing activity profoundly impacts Bronze Age archaeological sediment, which is abundant in the first meter (Găvan et al., 2022).

According to Lindner et al. (2017a) loess and loess derivate mappings, the topsoil developed in 'clayey loess' deposits. Notably, 'clayey loess' corresponds to 'loess derivates' after Lehmkuhl et al. (2021) and Lindner et al. (2017b), which is abundant in Hungary (Fig. 3.1a). This relates to various national loess classification systems. Sümegi et al. (2015) emphasise that the deposition process is crucial for classification, suggesting that 'clayey loess' could be categorised as lacustrine or alluvial sediment if aeolian deposition is excluded. Thus, we will initially adopt the more neutral term 'loess derivate'. Moreover, during the LGM, the region might have been affected by permafrost (Fig. 3.1a), as indicated by proximate generalised boundaries drawn by Gábris and Nádor (2007) and Lehmkuhl et al. (2021). The displayed, generalised boundaries align with elevated levels in the region, but discontinuous permafrost likely exists at lower levels, depending on local topography and sediments. Also, Gábris and Nádor (2007) identify the eastern CB as a potential part of the periglacial zone.

The study area (∼4 km^2) shows gentle relief interrupted by several shallow CDs. These are mostly circular to oval with depths down to 2 m according to the DEM. Three CDs can be found near the tell and on the elongated lift to the east. All are situated in a comparatively low local elevation level of ∼102 m a.m.s.l. (Fig. 3.1b). A broad, elongated basin south of the tell is characterised by significant elevation differences along its northern slope (Fig. 3.1b). An artificial channel, a tributary of the Alceu River that merges with the Crişul Repede to the west, was excavated along the basin's longitudinal axis (Fig. 3.1b). This modification likely occurred during extensive river regulations in the 18th century, which drained wetlands and left only small remnants (Dóka, 1997; Lie et al., 2024). However, the formerly wetland

dominated landscape was documented in historical military surveys since the Habsburg Empire era (Timár et al., 2006). In Toboliu, a small, relatively humid area in the southwest may represent a remnant of these wetlands (Lászlóffy et al., 1938).

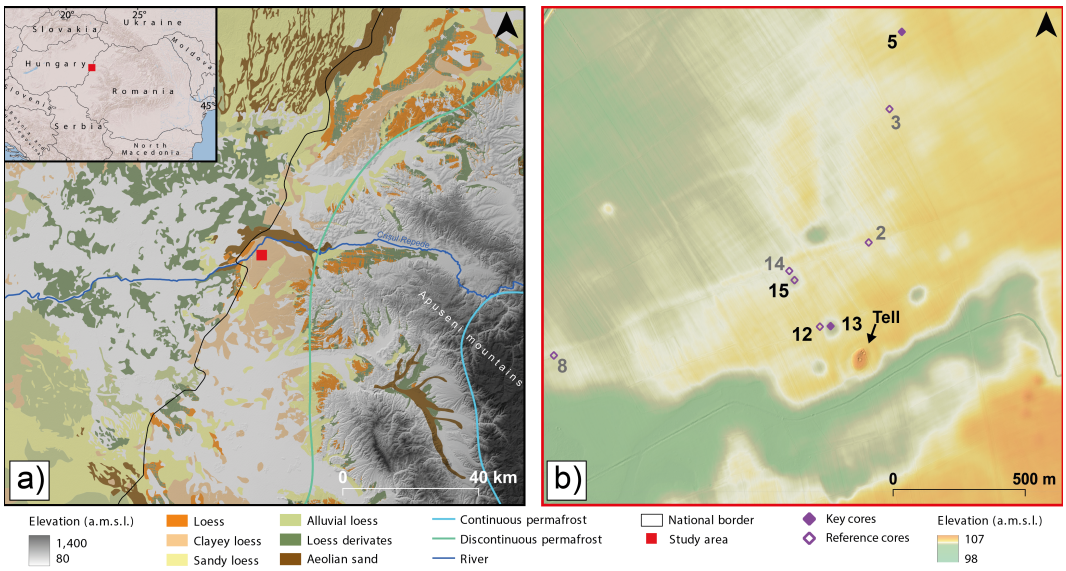

Figure 3.1: a) Study area at the eastern CB fringe in Romania, close to the river Crişul Repede in the north and the Apuseni mountains to the east (Overview: hillshade by ESRI (2019), DEM basemap: USGS - United States Geological Survey (2009), National borders by Natural-Earth (2021). Generalised permafrost boundaries of the LGM (Lehmkuhl et al. 2020). Loess and loess derivates as compiled by Lindner et al. (2017a). b) Study area (LiDAR elevation data by National Agency for Cadastre and (ANCPI) (2014) showing the tell, CDs, and coring locations related to this study. Violet, filled diamonds, black numbers: main cores presented in detail; violet, open diamonds, grey numbers: additional cores mentioned in the text. Figures for Core 12 (Appendix,Fig. B.5) and Core 15 (Appendix, Fig. B.7), as well as a cross-section scheme are in Appendix, Fig. B.1.

3.3 MATERIAL AND METHODS

3.3.1 *GIS and Remote Sensing*

We utilised various remote sensing products and geodata to analyse spatial relationships and integrate them with downcore sediment core trends. As mentioned in Section 3.1, we accessed geomagnetic imagery from an archaeological survey conducted between 2016 and 2019 (Kienlin, 2021). We also employed a high-resolution DEM from 2017, sourced from LiDAR with a pixel size of 1x1 m, provided by National Agency for Cadastre and (ANCPI) (2014). Additionally, multispectral imagery from WorldView-3, covering shortwave blue to near-infrared

wavelengths, was obtained from DigitalGlobe (2021). Pansharpening this imagery resulted in a high resolution of 31x31 cm, which was used to create a color-infrared (CIR) image. Further details are available in Appendix, B.3.2.

3.3.2 *Field work and sampling*

Eight sediment cores (percussion coring, 8-10 cm diameter) were obtained (Fig. 3.1b, Table 3.1). below surface level (b.s.l.) sample depths were synchronised by converting coring depths to a.m.s.l. values (World Geodetic System 1984 (WGS84) reference) based on measured borehole elevations, facilitating stratigraphical classification across different elevation levels.

Table 3.1: Core sampling context: Core locations are shown in Figure 3.1, CD refers to 'Closed depression'. Two different sampling tubes were used: open probes (diameter: 8 cm) and additional closed liners with 10 cm in diameter. Sampling depth is given in metres above mean sea level (a.m.s.l.). Sample size (n) per core implies the number of samples used for sediment (grain size - laser diffraction, elemental composition - XPL, and organic carbon/carbonate - DIMATOC) analysis, radiocarbon (accelerator mass spectrometry - AMS) and luminescence (Quartz and Feldspar OSL) dating.

Core	Site type	Sampling tube	Borehole elevation (m a.m.s.l.)	Core length (m)	Sediment analysis (n)	Additional laboratory analyses (n)	Radiocarbon dating (n)	Luminescence dating (n)
2	Flat terrain	Open	102.67	6	16	-	-	-
3	Flat terrain	Open + liner	102.7	5	27	-	-	-
5	Flat terrain	Open + liner	103.07	6	20	pH value (6)	8	8
8	Flat terrain	Open	101.98	5	15	-	-	-
12	Close to CD2	Open + liner	102.98	5	19	-	-	-
13	Within CD2	Open + liner	101.24	3	15	Pollen (8)	3	1
14	Close to CD5	Open	102.27	5	20	-	-	-
15	Within CD5	Open	101.59	4	13	Pollen (1)	2	-

We selected four cores (5, 12, 13, 15) for detailed analysis (Table 3.1,(Fig. 3.1b. Core 5 is considered representative for the study area. Core 13 was taken in the centre of one circular CD and Core 12 near the western fringe of the CD as link to Core 5. Core 15 was drilled in a shallow, irregular CD for comparison with Core 13 from a deep depression. The other cores (2, 3, 14, and 8) provide additional lithostratigraphic information not further discussed. Additionally, a transect scheme illustrating the terrain conditions and stratigraphic relationships between cores of the northern section (Table 3.1) is provided in Appendix B.1. More details on field description methods and surveying can be found in Appendix B.2.

3.3.3 *Laboratory analysis and statistics*

All sediment samples (Table 3.1) were analysed in the laboratories at the University of Cologne. The samples were pre-processed: GSD were determined by laser diffraction using a Beckman Coulter LS 13 320 Particle Size Analyser (Beckman Coulter, Inc., 2011), following the preparation protocol of Schulte et al. (2016) and the analysis methods of Folk and Ward (1957) and Blott and Pye (2001). Notably, the clay fraction is generally underestimated due to methodological constraints (Konert and Vandenberghe, 1997; Schulte et al., 2018). Additionally, for the characterisation of the Holocene soil in Core 5, pH analysis was conducted in water as well as calcium chloride suspension (ISO 10390:2005). The geochemical analyses included carbonate and organic carbon measurements using a Dimatec DIMATOC. Elemental composition (Al, arsenic (As), Ca, chloride (Cl), Fe, potassium (K), Mn, manganese (Mg), sodium (Na), P, lead (Pb), Rb, S, Si, Sr, titanium (Ti), zirconium (Zr)) was measured by energy dispersive x-ray fluorescence analysis (EDXRF) using an Spectro Xepos P spectrometer (SPECTRO Analytical Instruments Ltd.). We conducted PCA (Davies et al., 2015). For the entire dataset (eight cores, Fig. B.1) and calculated standardised element oxide bi-plots for comparative analysis (Fig. B.4). Further details on ratios and data processing are provided in Appendix B.4. We utilised classifications from (IUSS (WRB) WG, 2022), (IUSS (WRB) WG, 2015), and the KA 6M by (Hartmann et al., 2024) to appropriately describe soil types/groups like human modified Phaeozems, which include horizons not fully explained by the IUSS (WRB) WG (2022). This follows an approach which was successfully applied in the study of Scherer et al. (2023).

To analyse stratigraphical layer formation, we employed various element ratios from XPL measurements, including Al/Ca: authigenic carbonate deposition (Davies et al., 2015), Fe/Mn and Fe/S: proxies for redox and reducing (limnic) conditions (Boyle, 2001; Davies et al., 2015; Sheldon and Tabor, 2009), and P/Si: phosphorus enrichment (Boyle, 2001; Lubos et al., 2013; Ottaway and Matthews, 1988; Ruttenberg and Goñi, 1997; Smeck, 1985). Rb/Sr and the CPA were used to assess weathering and soil formation in LPS (Buggle et al., 2011).

3.3.4 *Palynology*

Eight subsamples from 98.58-98.66 m a.m.s.l. were taken in the layered sediments from Cores 13 and one from Core 15 at a depth of 98.97 m a.m.s.l. (Table 3.1). They were processed to isolate pollen using standard physical and chemical methods (Moore et al., 1991). Lycopodium tablets were added to calculate pollen concentrations (pollen grains/cm 3) (Stockmaar, 1971). The pollen sum is very low. Between ∼100 pollen grains per sample were counted and at least 500 Lycopdia.

Pollen grains and Non-Palynomorphs (NPPs) were identified under a light microscope using the Archaeobotany Laboratory reference collection (Department of Prehistoric Archaeology) at University of Cologne (Germany) and standard keys (Faegri and Iversen, 1989; Moore et al., 1991; Punt et al., 1995; Reille, 1998). The results are presented as percentage diagrams designed with the Tilia program (Grimm, 2020). Pollen sums were based on the pollen of trees, shrubs, and herbs; spores, aquatic and local pollen were excluded.

3.3.5 *Chronology*

Bulk samples from Core 5 and 13 were ^{14}C Accelerator Mass Spectrometry (AMS) dated at the Poznań Radiocarbon Laboratory in Poland. Two additional samples from Core 15 (Table 3.1) were radiocarbon-dated by BETA Analytic in Miami, USA. All samples were extracted from discrete stratigraphic units. Resulting dates were calibrated using the IntCal20 curve (Reimer et al., 2020), applying OxCal 4.4 software (Bronk Ramsey, 2009).

The samples from Cores 5 and 13 for luminescence dating were retrieved in the dark (Table 3.1). Standard preparation procedures were followed to gain fine grain (4-11 µm) and the 100-200 µm coarse FSP and Quartz (Qz) extracts for equivalent dose (D_e) determination (details: Table B.1). All measurements were performed with an automated Risø TL/OSL reader equipped with a ^{90}Sr/^{90}Y source, blue LEDs emitting at ∼470 nm in combination with Hoya U-340 filter for Q measurements (Murray and Wintle, 2003), preheat = 240°C, cut-heat = 220°C); and IR LEDs emitting at ∼870 nm, with a 410 nm interference filter for Post-IR 50 IRSL225 measurements on FSP (following Thomsen et al. (2008) and Kars et al. (2012), see TableB.5). Preheat plateau and dose recovery tests were performed on some of the samples to determine the reliability of the measurement protocols. Radionuclide concentrations (uranium, thorium, potassium) were determined by gamma ray spectrometry to calculate the dose rates. Conversion factors by Liritzis et al. (2013), attenuation factors by Bell (1980), Guérin et al. (2012), and Brennan (2003) as well as values of 0.11±0.011 (Kreutzer et al., 2014) for FSP and 0.04±0.002 (Rees-Jones, 1995) for fine-grain Q measurements were used. Water contents, as determined in the laboratory (± 5%), were used for age calculation. Total dose rates and final ages were calculated in DRAC, v. 1.2 (Durcan et al., 2015).

3.4 RESULTS

3.4.1 *Geospatial context and Closed Depression morphometry*

Large areas show light whitish to cyan colours in CIR imagery. This reflectance feature (i.e., soil mark) appears in linear, curved forms (Fig. 3.2a). Likewise, these features can be followed in the DEM, highlighted by light yellow to white traces at ∼102 m a.m.s.l. elevation (Fig. 3.2b). During fieldwork, we noted thick sand deposits and upwelling groundwater at one of these locations (Fig. B.1).

They are visible in the geodata but are strongly overprinted onsite by intense modern cultivation, as highlighted by densely packed field plots (Fig. 3.2a, 3.2c). The elongated basin located south of the tell is connected to the wetland relict that remains present in the southwestern part of the study area. The extent is visible through dark cyan or green shades (Fig. 3.2a). In the DEM, this area is highlighted by a distinct drop in elevation and represented by a light green colour at an elevation of ∼100 m (a.m.s.l.). The artificial (i.e., drainage) channel becomes apparent at the eastern end of this delineated landform. The outline agrees with a flooded area depicted in a historical map by Lászlóffy et al. (1938) (data collection years: 1766-1898) indicating the flood risk within the CB before the realisation of major river regulation works (Kiss, 2019). The map shows an elongated 'flooded' area in the study area, which is east-west oriented but shares a north-south oriented overall course with several other elongated water bodies to its south (Fig. 3.2d). According to the historical map, the flood risk was higher along the west banks of the Crişul Repede than at the eastern bank. Besides furrows and smaller archaeological contexts, the geomagnetic imagery highlights more extensive linear subsurface features (anomalies). Six of several CDs in the study area are also visible (Fig. 3.2c). In contrast to their indistinct appearance in the field (Fig. 3.3d), they are clearly visible in the geomagnetic data and the DEM, where their diameter is slightly larger (Fig. 3.2b, c and (Fig. 3.3a).

All CDs (except CD3) are situated within linear soil and elevation features (Fig. 3.2a and b). Based on their shape in the geomagnetic imagery (Fig3.2c and Fig. 3.3b), they range from ∼40 to 70 m in diameter with a depth of ∼30 to 200 cm (Fig. 3.3b). Most show a regular round to oval form, whereas some have irregular diamond-like shapes (Fig. 3.2c). The latter type (CD5, 6) is shallower and comparatively small, whereas CD1 to 4 are more extensive and deeper (Fig. 3.3a, b). These CDs show a distinct rim-like feature in the geomagnetic imagery only (Fig. 3.3c, e). Notably, this feature does not appear in the elevation data.

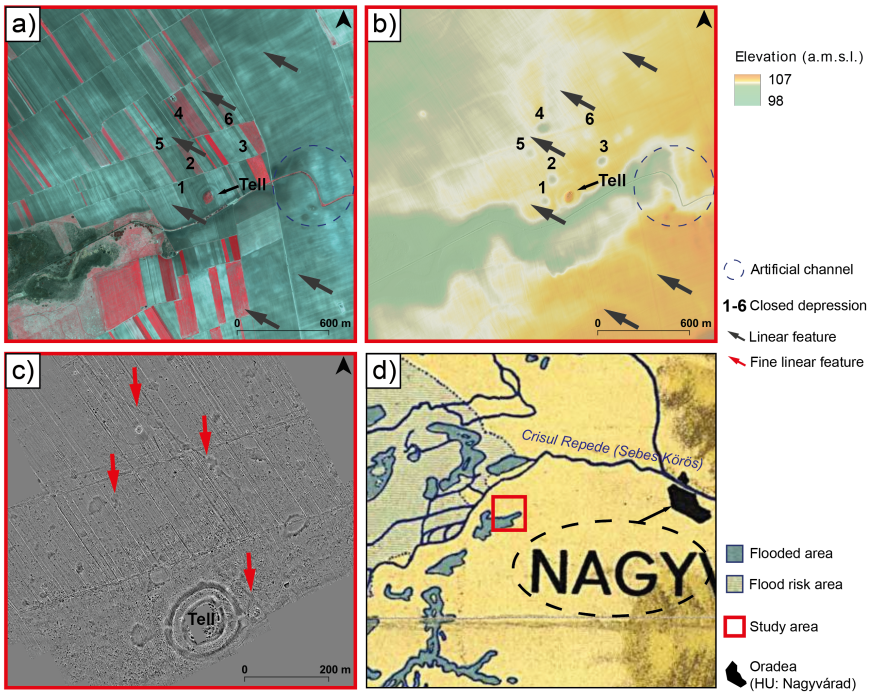

Figure 3.2: a) CIR image based on multispectral WorldView-3 data, March 2021 (DigitalGlobe, 2021). b) LiDAR digital elevation model (National Agency for Cadastre and (ANCPI), 2014), with yellow to orange colour for elevated parts and light yellow to greenish colour for low level areas in the study area. Linear (channel-like) surface features are indicated by grey arrows in a) whitish soil marks and b) light yellow to white linear features of relatively low elevation. c) Geomagnetic imagery (Kienlin, 2021), showing subsurface features by magnetic orientation discontinuities in the sediments, such as fine linear features which are marked by red arrows. Closed depressions (CD) (this study) locations are indicated by numbers in a) and b). d) Detail of a georeferenced historical map of the region (Lászlóffy et al., 1938), showing water bodies and flood risk areas before river regulations (Section 3.2).

3.4.2 *Lithostratigraphy*

The lithostratigraphy of Core 5 reflects the overall pattern of the study area, while Core 13 (CD2) is representative for sedimentation in a CD. In the following, we describe the key stratigraphic units of Cores 5 and 13. Additional information from cores 2, 3, 8, 12, and 14 are in the supplement. Core 12 (Fig.B.5 and Fig. B.6) is located just outside CD2 at an intermediate position between deposition in a CD and Core 5 in the northern part of the study area. Grain size frequency comparisons among Cores 5, 12, and 13 are presented in heatmaps (after Schulte et al. 2018) in the Appendix B.8 (Fig. B.6). Lithostratigraphic information from less well-preserved Core 15 that exhibit similarities to Core 13, are provided in the Appendix B.9 (Fig. B.7).

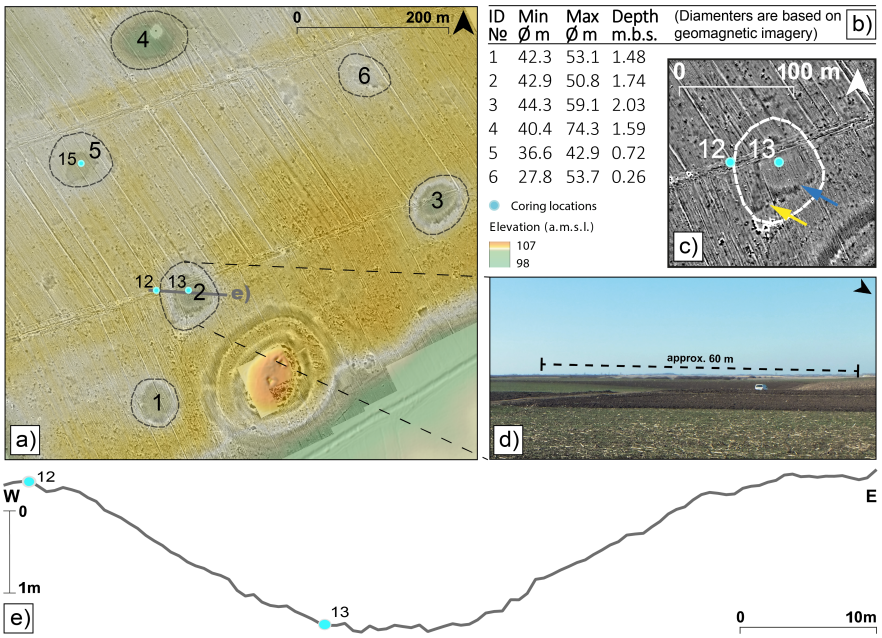

Figure 3.3: a) Geomagnetic imagery combined with DEM information, showing the spatial distribution of the listed closed depressions (CDs) in relation to noticeable elevation and subsurface features (Fig3.2), b) table with 'rim-to-rim' measurements (diameter based on geomagnetic data) and depth based on the DEM for the listed CDs, c) geomagnetic imagery detail of CD2, d) photograph showing the full dimensions (DEM based) of CD2 in the study area, e) DEM sourced elevation profile of CD2, the transect position is displayed in a), note that rims are not visible on the surface.

Results from Core 5

UNIT 1 - SAND PHASE (96.80–97.95 M A.M.S.L.) At the bottom of Core 5, we encounter fine and medium-sized rounded gravel (Fig.B.1). This layer is followed by banded, poorly-sorted fine and medium-sized sands, highlighted by varying intensities of iron oxide staining. The whole unit is dominated by these banded sand deposits interrupted by a thin layer of very coarse silt at a depth of ~97.5 m a.m.s.l. which shows increased Rb/Sr and Chemical Proxy of Alteration (CPA) values.

UNIT 2 - SILT PHASE 1 (97.95–99.80 M A.M.S.L.) On top of the sand unit, the silt fraction ranges from 64 to 75%, with the coarse silt fraction being dominant (~34%) and a fine sand fraction range from 16 to 27% (Fig. 3.5) shows a general fining upward transitional phase with uni- to bimodal GSD curves of the lowermost samples 15 and 16 of Core 5, and a trimodal distribution of sample 14. The clay fraction rises from approximately 3% to 8% between samples 14 and 15. Accordingly, the Rb/Sr ratio and CPA values are increased. At a depth of approximately 98.8-99.3 m a.m.s.l., dark humic aggregates can be observed. This thin layer with a clay fraction <20% might

indicate eroded topsoil. The top of this part (~99.3-99.8 m a.m.s.l.) consists of fine sand (up to ~27%) and coarse silt (~33%), displaying a weakly laminated structure with coarser layers of fine to medium sand and finer layers enriched in organic content (Fig. 3.4). Whereas organic carbon is only slightly increased, the carbonate content is high and shows a negative correlation to Rb/Sr values. PCA results (Fig. 3.5c) based on grain size and geochemical measurements of silt samples, including reference cores (Fig. 3.1), reveal two distinct clusters: Silt phase 1 and Silt phase 2 (subsequently) in the PC 1 and 2 biplot. Silt phase 1 and loamy samples from below the CD bottom (Section 3.4.2, subsequently) exhibit similar characteristics. The GSD of Silt phase 1 shows a heterogeneous pattern, indicating variable deposition (Fig. 3.5a). However, PCA reveals that Silt phase 1 is also influenced by weathering indicated by proxies such as Rb, Pb, barium (Ba), and Al. In contrast, Silt phase 2 (subsequently) is more dependent on grain size properties(Fig. 3.5b, c). PC 1 and 2 explain only 50% of the total variance, restricting further interpretations.

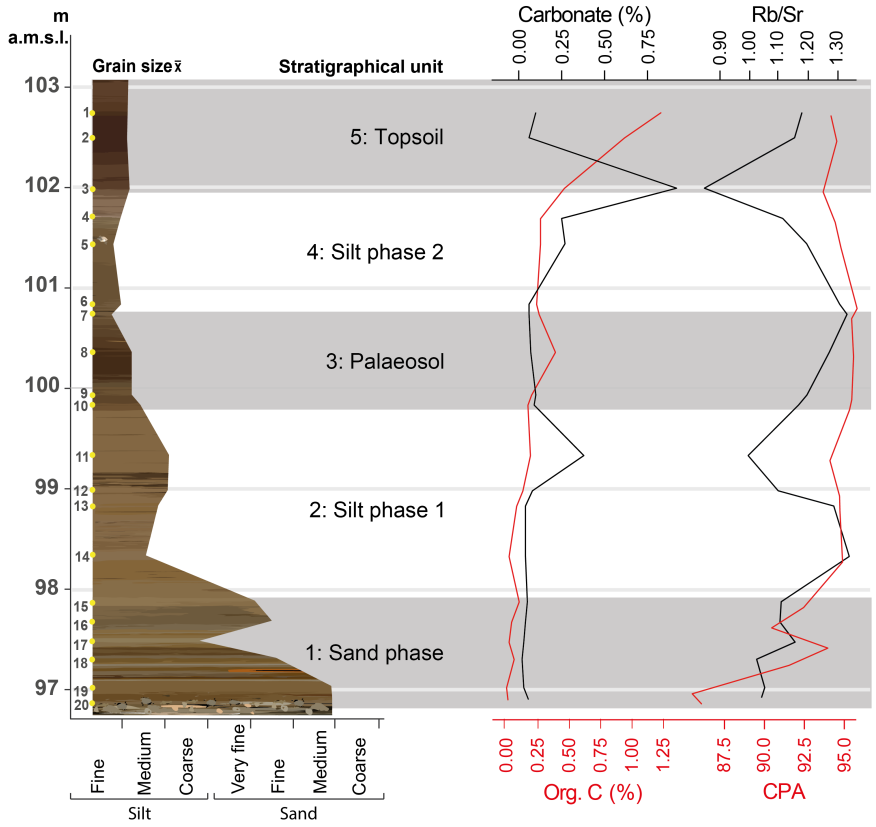

Figure 3.4: Core 5 data and main stratigraphical units. Depth is given in m a.m.s.l., sample depth and numbers are highlighted by yellow dots. The core plot displays the mean grain size ($\bar{x}$), carbonate and organic carbon (Org. C) contents, as well as Rb/Sr ratio and the CPA considered as weathering/pedogenesis proxies. Proxy details can be found in Section 3.3.3 and Appendix B.4.

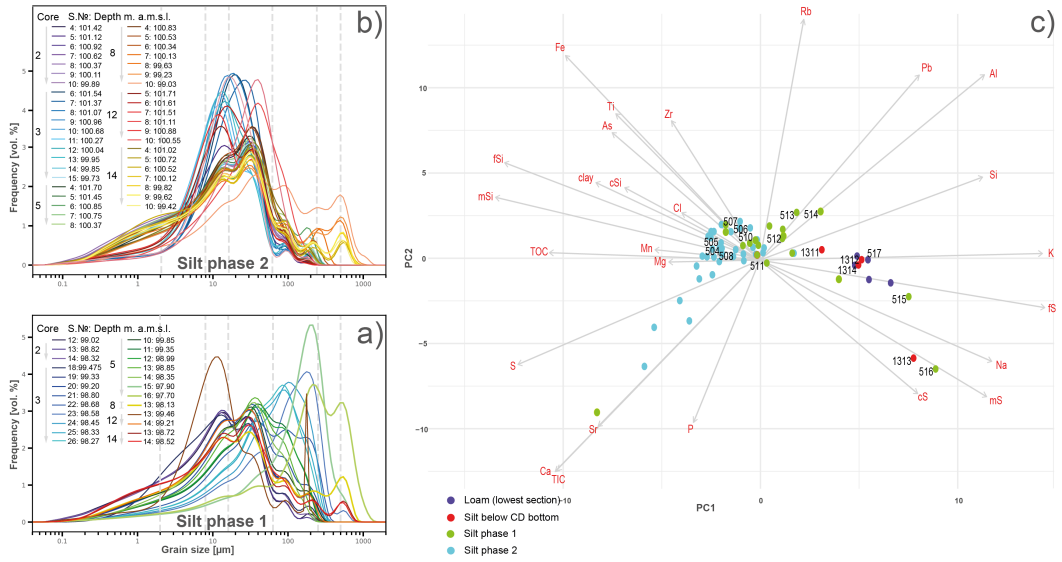

Figure 3.5: GSD for the lower a) Silt phase 1 and the upper b) Silt phase 2 described in Core 5. A similar GSD for Silt phase 1 and 2 can be found in the analysed reference cores 2 ,3 ,8 ,12 and 14. Samples (S.+№) are displayed using separate colour palettes per core. Sampling depth is indicated using m a.m.s.l. values. Intra-profile grain size frequencies for Cores 5, 12, and 13 can be found in Appendix B.8, Figure B.6c) Results of a PCA using geochemical/-physical data XRF, grain size fractions, organic carbon and carbonate concentrations) of all sampled cores, PC1 and PC2 explain 50% variance in the data set. The PCA results underline the different character of Silt phase 1 and 2 which becomes apparent in the GSD plots. The violet dots (loam) represent very sandy silt samples from the lowest section of Silt phase 1.

UNIT 3 -PALAEOSOL (99.80-100.76 M A.M.S.L.) Based on Unit 2 an approximately 70 cm thick palaeosol developed. The soil exhibits a dark brown colour, increased clay fraction (∼12%), organic carbon content (∼0.4%) and less fine sand (15-12%) than in silt phase 1. Along with high CPA, and Rb/Sr ratio values this might indicate a fossil Ah horizon in the upper part of the unit.

UNIT 4 - SILT PHASE 2 (100.76-101.96 M A.M.S.L.) This unit features thick silt deposits, with some samples displaying higher clay content and a generally reduced fine sand compared to Silt Phase 1 (Fig. 3.5b). The grain sizes are less sorted, and some samples exhibit unimodal trends in the medium to coarse silt fraction, suggesting loess derivate, a mixed aeolian and alluvial origin (Schulte et al., 2018). The PCA implies that Silt phase 2's composition is rather grain size driven (Fig. 3.5b, c). However, this unit shows upwards increasing carbonate contents, probably reflecting macroscopically visible small to medium-sized carbonate concretions (Fig. 3.4 and Fig. B.1). Rb/Sr rations show

a negative correlation to carbonate implying arid conditions (Marković et al., 2007).

UNIT 5 - SOIL (101.96-103.07 M A.M.S.L.) A dark mollic Ah-Horizon has been developed in the lCv-horizon of the clayey Silt phase 2 (Fig. 3.6). It has been modified by human influence forming a colluvium (D(h)j and a ploughing horizon (Ap) (Hartmann et al., 2024). The GSD is homogenous with clayey silt as the main GSD class, the boundary between the mollic Ah-horizon and the lCv is marked by a slight increase of clay values (from ~11.7 to 13.6%). Pedogenesis lead to decalcification of the soil, reflected by a pH increase from weakly acidic to weakly alkaline in the lCv-horizon. The lowest pH values are reached in the Ap (5,82) and the upper D(h)j (5,88) increasing in the fAh (5,99) up to over 7 in the lCv. The organic carbon contents rise from transition lCv/fAh horizon (0,27%) up to 1,2% in the upper part of the soil. This combination of characteristics, including its dark-brownish colour caused by the accumulation of organic matter, indicates the formation of a Phaeozem (IUSS (WRB) WG, 2015). However, the P/Si values, which typically indicate human activity, do not show a clear signal.

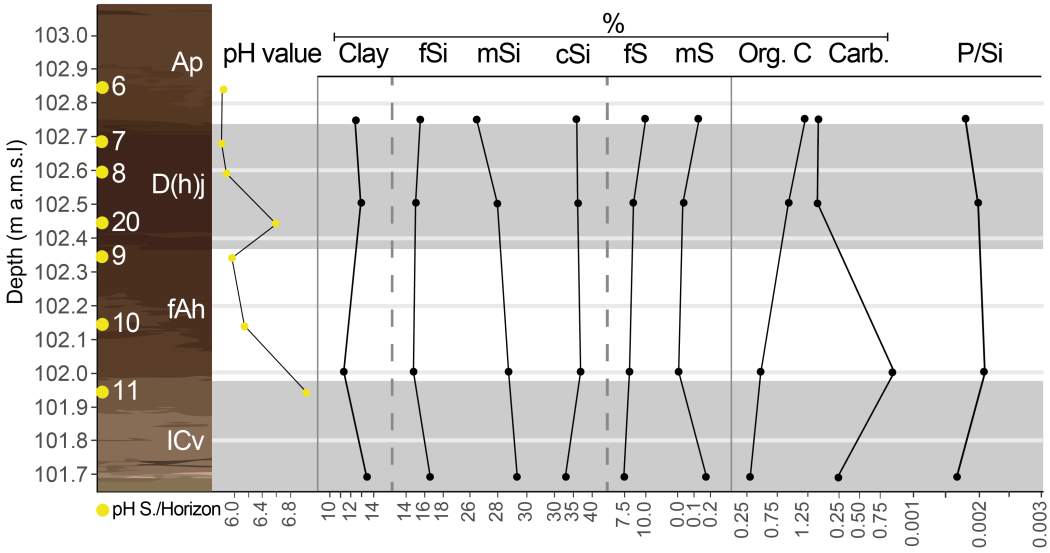

Figure 3.6: Geochemical and granulometric data for the top of Core 5 (Units 4, Silt phase 2) and 5 (Topsoil) for soil type definition after IUSS (WRB) WG (2015). Yellow dots: sample positions show pH sampling positions. lCv: Silt phase 2, fAh: mollic Ah-horizon covered by D(h)j: colluvium (Hartmann et al., 2024), and Ap: ploughing zone.

Results from Core 13 (CD2)

Core 13 from the centre of CD2 (Fig. 3.3 represents deposition in a typical depression.

UNIT 1 -SAND PHASE (97.6-98.0 M A.M.S.L.) We encounter medium to fine sand at the bottom of the sequence, briefly interrupted by a thin layer of coarse silt to fine sand. Organic carbon and carbonate content are very low; in contrast, the CPA values are slightly elevated. This unit likely corresponds to the sand phase at the base of Core 5 (Fig. 3.6).

UNIT 2 - SILT PHASE (97.6-98.45 M A.M.S.L.) Unit 2 consists of greyish coarse to medium, sandy silt. This unit is much thinner than Silt phase 1 in Core 5 (Unit 2) but does not continue with a sand-rich top layer. However, the greyish colour and increased Al/Ca, and Fe/Mn ratio values (Fig. 3.7) appear similar to the upper part of Unit 2 in Core 5. Also, the PCA results (Fig. 3.5) reveal similarities (high Pb/Al/K/Na and sand dominated) to Silt phase 1and loamy deposits at the base of Core 5 (Fig. 3.5c). A vertical root channel with humic infilling in the upper part of the unit extends into Unit 3. This unit shows increased permeability (~5% medium sand), underlined by the partially strongly increased sand content (e.g. S.13: 46%). This is contrary to Silt phase 1 in Core 5, which basically exhibited a fining upward trend (Fig. B.8). Despite the prevalence of observed overprinting hydromorphic features, and thickness this unit exhibits geochemical and sedimentological similarities in a comparable depth (97.6-98.45 m a.m.s.l.] with Silt Phase 1 of Core 5.

UNIT 3 - CLOSED DEPRESSION BOTTOM (98.45 M-98.65 M A.M.S.L.) The depression bottom unit comprises alternating layers of medium silt and dark brown, clayey sediments. Moreover, the Fe/Mn and Fe/S ratios indicate alternating redoximorphic and anoxic wet conditions for this unit (Rothwell and Croudace, 2015). In comparison to a very thin intermediate dark layer at approximately 98.63 m a.m.s.l. with a clay fraction of ~9%, the thicker bottom layer exhibits a slightly elevated level of~12%. However, these values remain underestimated (Section 3.3.3, systematic laser-diffraction issue). Organic carbon contents increase in this unit to ~0.5%. Rb/Sr, and CPA values are high, with slightly reduced values in the central dark layer. Carbonate contents in the lower part is ~0.04% and increases in the upper part to ~0.06%. The lower layer displays elevated Al/Ca ratios and reduced Fe/S values, whereas the thin central dark layer exhibits the reverse characteristics. The bottom (S.10) and the central dark layer (S.7/8) exhibit higher phosphorus content (Fig. 3.7), while the upper central layer (S.9) appears to be influenced by anaerobic reducing conditions (Fe/S ratio). In contrast to geochemical differences of the

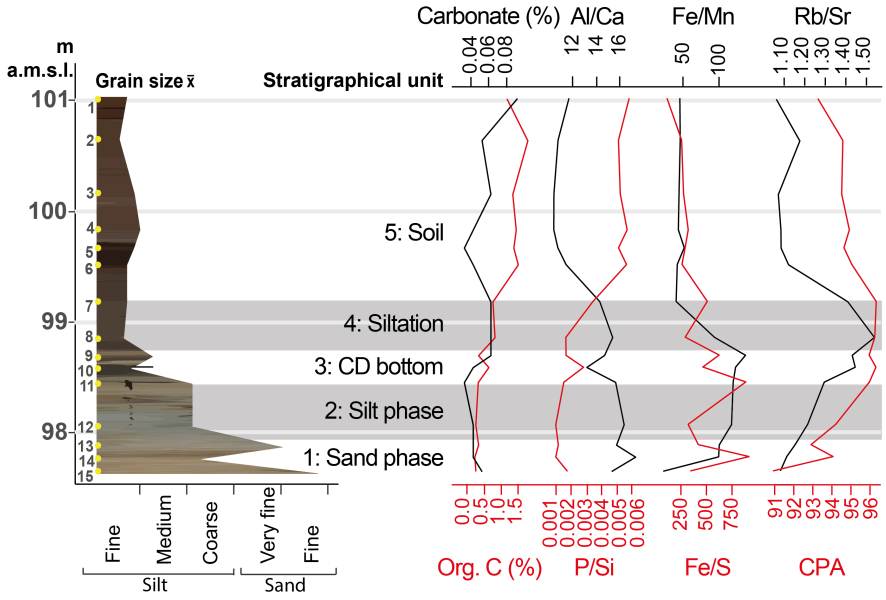

Figure 3.7: Core 13 data and main stratigraphical units. Depth is given in metres above mean sea level (a.m.s.l.), and sample depth and numbers are indicated by yellow dots. Mean grain size ($\bar{x}$) is displayed by the core plot. Carbonate and organic carbon contents, as well as Rb/Sr ratios (weathering proxy) and the Chemical Proxy of Alteration (CPA) as weathering/pedogenesis proxy. Al/Ca, and Fe/Mn, and Fe/S ratio are considered as proxies for different hydromorphic settings. P/Si ratio is used as indicator for terrestrial input, such as biological/agricultural activity. Proxy details can be found in Section 3.3.3 and Appendix B.4.

central and lower layer, pollen data of this unit indicate stable vegetation without major changes (Fig. 3.8). Arboreal pollen (AP) values vary between 31 and 43%, most frequently *Pinus* (6-16%), *Picea* (2 and 13%), *Salix* (2-8%) and *Ulmus* (~4%). Poaceae, the dominant pollen taxa, reach values of 11%, accompanied by Chenopodiaceae, Asteroideae, Artemisia and Cichorioideae. Moreover, typical wetland plants are abundant, such as sedges, lilies, water mint and water plantain (Cyperaceae, Liliaceae, *Mentha T.*, *Alisma*). Continuous occurrence of different non-palynomorphs (NPPs), mainly algae (Zynetmataceae, Spirogyra, Desmidiaceae) and diatoms imply limnic conditions during the formation of this unit (Fig. 3.8).

UNIT 4 - SILTATION (98.66-99.20 M A.M.S.L.) This unit is characterised by a drop in mean grain size to fine silt. Organic carbon and Rb/Sr values are increased compared to Unit 3. Also, high algae proportions indicate the presence of water. The uppermost pollen sample (Fig. 3.8) shows very high Cichorioideae values (~40%), indicating selective corrosion (non-preserved other pollen). Decreasing wetness is evidenced by lower Al /Ca and Fe/Mn ratios, which is further supported by an increase in Glomus indicating enhanced terrestrial input.

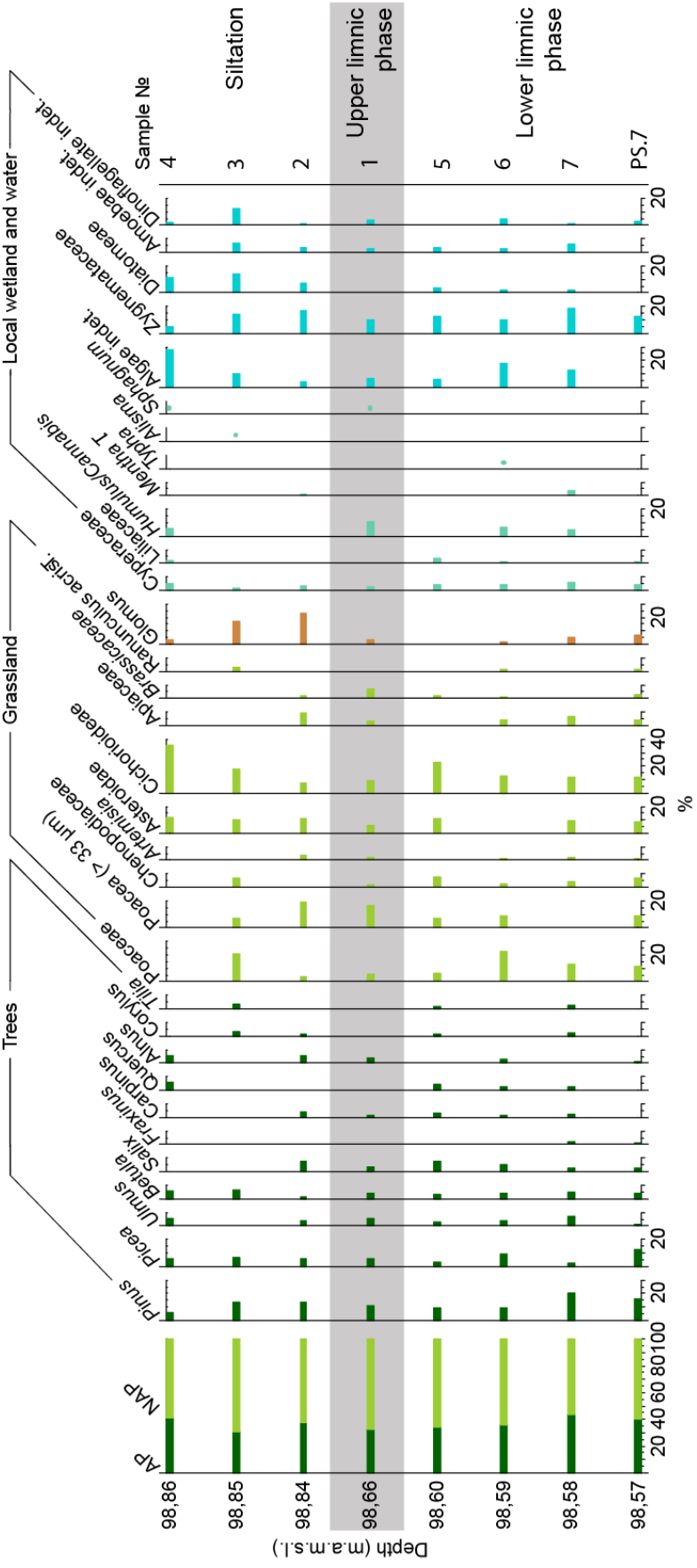

Figure 3.8: Proportions of selected pollen types, spores and non-palynomorphs (NPPs) from the bottom and central dark layer in Units 3 (lower/upper limnic phase) and 4 (Siltation) of Core 13.

UNIT 5 - SOIL (99.20-101.02 M A.M.S.L.) Macroscopically, the delimitation between siltation and overlying homogenous layer is very vague. No soil horizons can be observed. Nevertheless, organic carbon is increased, but carbonate contents are decreasing. Likewise, humidity decreases, which is shown by low Al /Ca, Fe/Mn, and Fe/S values. In contrast, increased terrestrial input is suggested by higher P/Si values (Fig. 3.7). From a depth of ~98.92 upwards, the P/Si ratio indicates an increasing accumulation of phosphorous with proceeding colluviation (Fig. 3.7). Vice versa Rb/Sr and CPA values both decrease, which might indicate a decreasing weathering degree.

3.4.3 *Geochronology*

Luminescence and radiocarbon dating results for Cores 5, 13, and 15 are listed in Table 3.2 and Table 3.3. Luminescence ages are based on fine-grain quartz OSL and coarse grain feldspar OSL measurements (Section 3.3.5). Details of the results of the performance tests are reported in Appendix B.5.

Table 3.2: OSL dating results for samples from Cores 5 and 13. Sampling depth is given in metres above mean sea level (a.m.s.l.). Dates are listed in ka before today (reference year 2022 as the year of sampling and sample preparation) with 1σ error. Equivalent doses (D_e) and total dose rates are given with standard error.

Sample code	Depth (m a.m.s.l)	Core	Mineral	Grain size (µm)	Palaeo D_e (Gy)	Dose rate (Gy/ka)	Age (ka)
C-L5374	100.6	5	FSP	100-200	127.0 ± 8.3	3.9 ± 0.2	32.7 ± 2.9
			Qz	4-11	138.2 ± 4.7	3.7 ± 0.1	37.0 ± 1.9
C-L5375	100	5	FSP	100-200	178.0 ± 2.9	3.8 ± 0.2	46.3 ± 2.9
			Qz	4-11	177.5 ± 1.1	3.7 ± 0.1	48.2 ± 1.8
C-L5376	99.6	5	FSP	100-200	331.6 ± 20.5	3.8 ± 0.2	87.3 ± 7.6
C-L5377	99	5	FSP	100-200	516.7 ± 34.5	4.1 ± 0.2	126 ± 11
C-L5378	98.1	5	FSP	100-200	624.1 ± 72.6	4.5 ± 0.3	138 ± 18
C-L5379	97.9	5	FSP	100-200	549.3 ± 33.0	3.9 ± 0.2	142 ± 12
C-L5380	97	5	FSP	100-200	452.6 ± 61.7	3.0 ± 0.2	150 ± 23
C-L5371	99.19	13	Qz	4-11	18.3 ± 0.3	3.6 ± 0.1	5.1 ± 0.2

The lowermost samples in Core 5 (Section 3.4.2) show penultimate glacial to last interglacial ages, ranging from the sand unit with 150±23 ka (C-L5380) to the upper Silt phase 1 which dates to 126±11 (C-L5377) ka ago (Table 3.2). Samples C-L5374, C-L5375, and C-L5376 consistently decrease from 87.3 ± 7.6 (Silt phase 1) to 32.7 ± 2.9 ka (Palaeosol). These ages are internally consistent also in terms of different minerals and grain-size fractions used for samples C-L5374 and C-L5375 (Table 3.2), confirming the validity of the OSL dating protocols used for Core 5.

Most of the radiocarbon dated samples of Core 5 exhibit very low carbon concentrations (<0.2 mgC) and display multiple age inversions (Table 3.3). The observed phenomenon may result from the age

mixing effect caused by a higher concentration of younger carbon compared to deposited organic matter (Scheidt et al., 2021). Comparing the radiocarbon dating results of sample 5/RC/7 (100.9 m a.m.s.l.) with an age of 23,400-24,500 cal a BP and the deeper sample 5/RC/9 (100.4 m a.m.s.l.) with an age of 21,900-22,600 cal a BP to the OSL results (C-L5374), which indicate a minimum age of 32.7±2.9 ka for the intermediate depth (100.6 m a.m.s.l.), raises concerns about the reliability of the radiocarbon dating results for the Palaeosol and Silt phase 2 unit. Consequently, we generally regard dates obtained from low carbon samples as unreliable (Table 3.3, in italic), at best representing minimum age estimates (Scheidt et al., 2021). Accordingly, samples collected from a depth of 100.77-101.96 m a.m.s.l. (Silt phase 2), dating from 17,400 to 24,500 cal BP, correspond loosely to the last glacial period, particularly in terms of their stratigraphical position. The same applies to the uppermost sample (5/RC/3) from the soil unit with a date range of 9,480 to 9,710 cal a BP vaguely pointing to the Early Holocene. In contrast, ^{14}C ages from Core 13 have higher carbon contents (up to 0.6 mg/C) and thus are considered reliable. Radiocarbon date 13/RC/6 from the CD bottom in Core 13 reveals an early Holocene age (9,910-10,200 cal ka BP). For the soil unit above a ^{14}C age of 4,970-5,300 cal a BP was obtained in agreement with the luminescence date (5.1 ± 0.2 ka, C-L5371) from about the same depth. The young age of the Silt phase in Core 13 (13/RC/7) likely indicates the presence of young organic matter, as the sample was collected from a root channel.

Our findings indicate that Toboliu's contemporary landscape is mainly shaped by processes from the penultimate glacial to the Holocene, preceding Bronze Age activities. Additionally, the chronostratigraphy and pollen analysis from CD2 (Core 13, (Section 3.4.2) shed light on the processes involved in CD formation.

3.5 DISCUSSION

3.5.1 *Soil-landscape evolutionary context*

The spatial analysis (Section 3.4.1) suggests the elongated basin south of the tell to be a palaeochannel segment. This feature is marked by low-elevation soil marks cutting the surface with the linear whitish CIR signatures (Figure 3.9), thus indicating a later erosion phase. The CDs along the older channels, visible in the DEM and geomagnetic imagery (Figure 3.2b, c), show no distinct surface signature (Figure 3.9), likely due to extensive field cultivation homogenizing the topsoil or the channels' impact on soil drainage.

Table 3.3: Results of accelerator mass spectrometry (AMS) for ^{14}C dating of bulk samples from Cores 5 and 13. Dates are listed in kilo years (ka) before present (BP), referring to the common reference year 1950. The calibrated kilo years (cal ka) age range has a confidence of 95.4% (2-sigma). Italicised letters imply unreliable dating results.

Sample code	Depth (m a.m.s.l.)	Core	Total C concentration (mgC)	^{14}C ka BP	Min cal ka BP	Max cal ka BP
5/RC/3	*102.4*	*5*	*0.19*	*8.60 ± 0.06*	*9.48*	*9.71*
5/RC/4	*101.8*	*5*	*0.16*	*17.0 ± 0.1*	*20.3*	*20.9*
5/RC/6	*101.1*	*5*	*0.13*	*15.1 ± 0.1*	*18.2*	*18.7*
5/RC/7	*100.9*	*5*	*0.10*	*19.9 ± 0.2*	*23.4*	*24.5*
5/RC/8	*100.7*	*5*	*0.07*	*14.5 ± 0.1*	*17.4*	*18.2*
5/RC/9	*100.4*	*5*	*0.13*	*18.3 ± 0.2*	*21.9*	*22.6*
5/RC/10	*100.2*	*5*	*0.20*	*17.2 ± 0.1*	*20.5*	*21.1*
5/RC/11	*100.1*	*5*	*0.09*	*19.2 ± 0.2*	*22.6*	*23.7*
13/RC/4	99.56	13	0.30	4.47 ± 0.04	4.97	5.30
13/RC/6	98.63	13	0.50	8.97 ± 0.06	9.91	10.2
13/RC/7	98.46	13	0.60	3.31 ± 0.04	3.45	3.63
BETA-630129	99.04	15	not available	6.88 ± 0.03	7.62	7.79
BETA-630130	98.82	15	not available	4.87 ± 0.03	5.48	5.66

Fluvial phase (MIS-6) and fluvial surface features (MIS-2)

We interpret the observed banded sands at the bottom of Core 5 as fluvial deposits. Feldspar OSL ages (Section 3.4.3) suggest that this fluvial unit was deposited between ~150±23 and 142±12 ka ago corresponding to MIS-6. Since we did not reach greater depths, this is regarded a minimum age and the onset of fluvial activity remains unclear (Fig. 3.10). The intermediate coarse silt layer suggests a less dynamic phase in sedimentation, likely indicating reworking, overbank deposits, or temporary channel cut-off induced oxbow formation (Brooks, 2003; Gretener and Strömquist, 1987; Harrison and Yair, 1998). Comparing our chronostratigraphic results (Sections 3.4.2, 3.4.3) to Gábris and Nádor (2007), Kiss et al. (2015), Nádor et al. (2007), Thamó-Bozsó and Kovács (2007) we have reached the last phase of regional fluvial activity during the penultimate glaciation at the bottom of the core (Fig. 3.10). The linear, whitish features observed in the CIR imagery at low elevations (Fig. 3.2a, b) suggest low soil moisture or increased subsurface permeability (Lillesand et al., 2015). These features can be interpreted as silted fluvial channels or oxbow lakes, which might correspond to the abundance of CDs (Fig. 3.9). The curved forms, indicate traces of an interconnected river network (Fig. 3.2a). Thamó-Bozsó and Kovács (2007) traced the evolution of the Palaeo-Körös (Crişul) river channels within the Körös basin (CB), spanning from the early Pleistocene to the late Pleniglacial. Likely, the late MIS-6

fluvial phase in Core 5 and its associated channels (Fig. 3.9 and Appendix B.1) correspond to this period of fluvial activity (Section 3.4.2). The elongated basin, cutting the MIS-6 fluvial features, south of the tell likely represents a former wetland (Section 3.4.1) that developed within a palaeo-channel segment. The extent of this basin is indicated by dark cyan or green soil marks indicating increased subsurface humidity (Fig. 3.9). The spatial orientation of the segment may suggest a branch of a major palaeo-channel, as illustrated by several isolated water bodies in (Fig. 3.2d). This might be linked to a riverbed shift, associated with various phases of CB subsidence and the uplift of the Apuseni Mountains, leading to temporally and spatially diverse river networks (Gábris and Nádor, 2007). For example, Palaeo-Körös (Crişul) and Palaeo-Tisza rivers underwent large east-west shifts, especially during the Late Pleistocene, which is discussed to have caused the contemporary course of Crişul Repede (Kiss et al. 2015, Nádor et al. 2007). The location and the approximately north-east-to-southwest orientation of this palaeochannel-segment in the study area can be aligned to a row of elongated, oxbow-like waters to the south, indicating a relationship with the Palaeo-Körös (Crişul; Section 3.4.1, Fig. 3.2). Nádor et al. (2007) and Kiss et al. (2015) suggest a phase of increased fluvial dynamics during MIS-2 which might be the period when this palaeochannel-section was still active. Considering the orientation of the palaeochannel-segments (Fig. 3.2d) and the distribution of loess (along the course of Crişul Repede) and derivates (north-east-to-southwest, linear: sandy loess and east to west, fan-like: clayey loess) in the region (Fig. 3.1a), the study area was likely part of the MIS-2 Palaeo-Körös floodplain. This is further supported by the Romanian soil map (Ovejanu et al., 1968), which traces former river courses through the distribution of fluvisols, stagnosols, and gleysols (Lindner et al., 2017b). However, currently coring data from this location is unavailable and this assumption relies on spatial analysis. Likely, the wetland developed in the still water, as suggested in the historical maps of Timár et al. (2006) and Lászlóffy et al. (1938), of an oxbow lake (palaeochannel-section) throughout the Holocene.

Loess derivate 1 (MIS-6 to 5) and Loess derivate 2 (MIS-2)

Both silt phases in Core 5 are interpreted as loess derivates with different characteristics. The lower silt unit on top of the fluvial deposits (Fig. 3.10) has sandy, reworked character and started to deposit from ~140 ka ago (Fig. 3.4). It may be associated with the 'Sandy loess' class after Lindner et al. (2017a) in Figure 3.1a. When considering underestimation of the clay fraction (Section 3.3.3), the trimodal, poorly sorted GSD, increased clay fraction, Rb/Sr, and CPA values (Appendix B.4) generally point to weathering and reworking of these increasingly silty deposits (Fig. 3.10). Strong weathering is also indicated by high scores for Rb/Sr and CPA (Section 3.4.2, Fig. 3.5). The slightly laminated

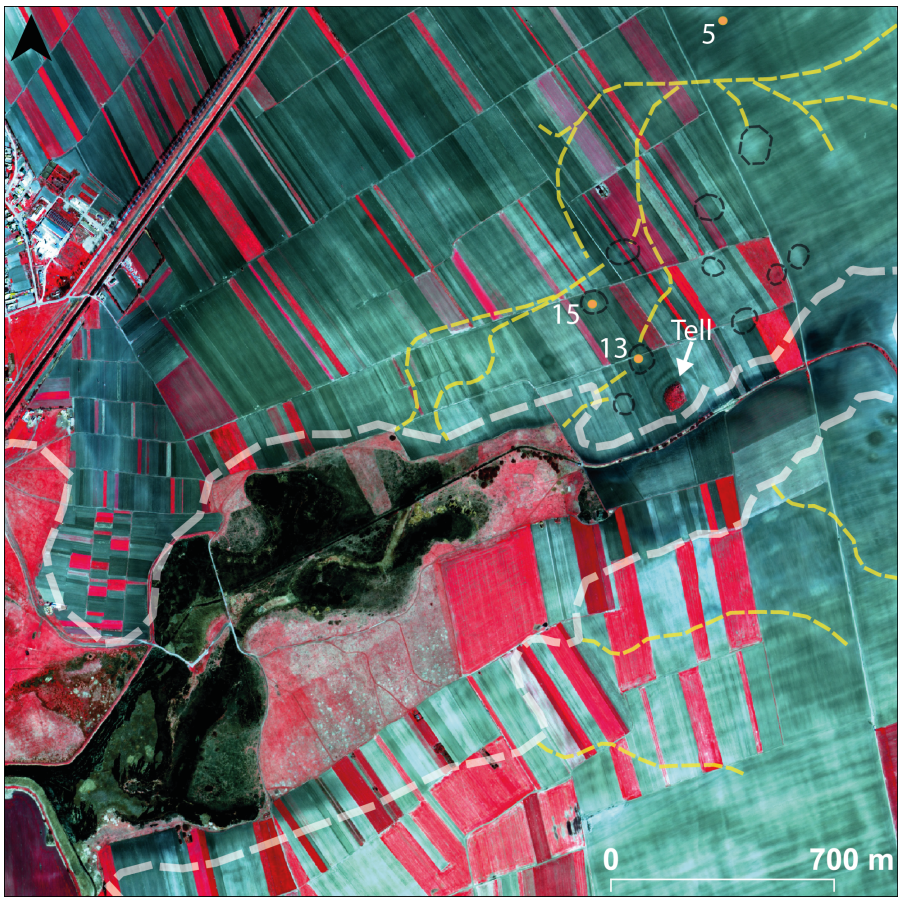

Figure 3.9: Synthesised spatial analysis results (Section 3.4.1). Colour-infrared CIR WorldView-3 image of March 2021 (DigitalGlobe, 2021). Red colours show vegetation. Bare soil is represented by dark colours with increased soil moisture or turbid water (dark green, petrol), light colours (white, cyan) indicate dry (e.g. sandy/permeable substrata) areas. Former wetland extent/flooded area (white dashed lines) based on historical data (Timár et al., 2006; Lászlóffy et al., 1938), interconnected river network (yellow dashed lines), and closed depressions CDs (black dashed lines) are based on DEM and historical data (Fig. 3.2b, d). Key coring locations are indicated by orange dots.

silt in the upper part of the unit (Fig. 3.10) suggests alluvial deposition influenced by fluctuating water levels, typical for floodplain environments (Brooks, 2003). The mean depositional age of ~87±8 ka suggests late MIS-5. Increased organic carbon and carbonate content in combination with low Rb/Sr values might be interpreted as a more arid period (Marković et al., 2007), which might be associated with periglacial conditions during this time.

Regarding central and eastern CB loess deposits, river alluvium, e.g. deposited along the Danube and Tisza, are suggested to be the main deflation areas of loess Lehmkuhl et al. (2021). In Toboliu, the north-south oriented Tisza floodplain and loess deposits along Crişul Repede (Fig. 3.1a) likely serve as primary dust sources for aeolian deposits in Loess derivate 2. Additionally, alluvial 'Clayey loess' deposited under periglacial conditions in the former Crişul Repede floodplain may explain the mixture of aeolian and alluvial deposits. Loess derivate 1 from MIS-6 to 5 and Loess derivate 2 from MIS-2 (Fig. 3.10) exhibit significant differences in grain size distributions (GSDs) and geochemical compositions in agreement with dust source proxies from Buggle et al. (2008). (Appendix, Fig. B.4). This might be related to the shifting tendency of Tisza and Crişul Repede during the Pleistocene (Kiss et al., 2015; Gábris and Nádor, 2007), affecting dust source distance and floodplain composition. However, the heterogeneous loess derivate deposits ('Sandy loess') of Phase 1 (Fig. 3.4) suggest dynamic, alluvial, possibly periglacial surface processes and accordingly variable climatic conditions during MIS-6 to 4 (Bösken et al., 2019; Schulte et al., 2018).

For Loess derivate 2, we assume mostly aeolian deposition (loess), which can be linked to cold and dry conditions (Schulte et al., 2018). The GSD and geochemical characteristics agree with 'Clayey loess', as suggested by (Lindner et al., 2017b) (Fig. 3.1a).

Concerning the availability of (unreliable) minimum ages for this unit (Section 3.4.3), we can only infer deposition during MIS-2. However, age mixing (Scheidt et al., 2021) and carbon relocation due to post-depositional processes in loess-like sediments, such as freeze/thaw cycles and humic acid infiltration (Jary et al., 2023; Zech et al., 2008), must be acknowledged. Nonetheless, given the reliable MIS-3 age of the underlying palaeosol (Fig. 3.10) and consistent findings from previous studies (e.g. Antoine et al. (2009), Bösken et al. (2019), Pötter et al. (2021), and Schatz et al. (2012), we assume deposition during relatively cold and dry conditions, most likely during MIS-2.

Palaeosols (MIS-5e and MIS-3)

The intermediate dark humic aggregates and the GSD in Loess derivate 1 in Core 5 (Section 3.4.2) may indicate the influx of detritus (i.e., eroded soil) around 126±11 ka ago, corresponding to early MIS-5 indicating an alluvial character of this unit. However, OSL dating of soils typically provide mixed ages ranging between the time of deposition

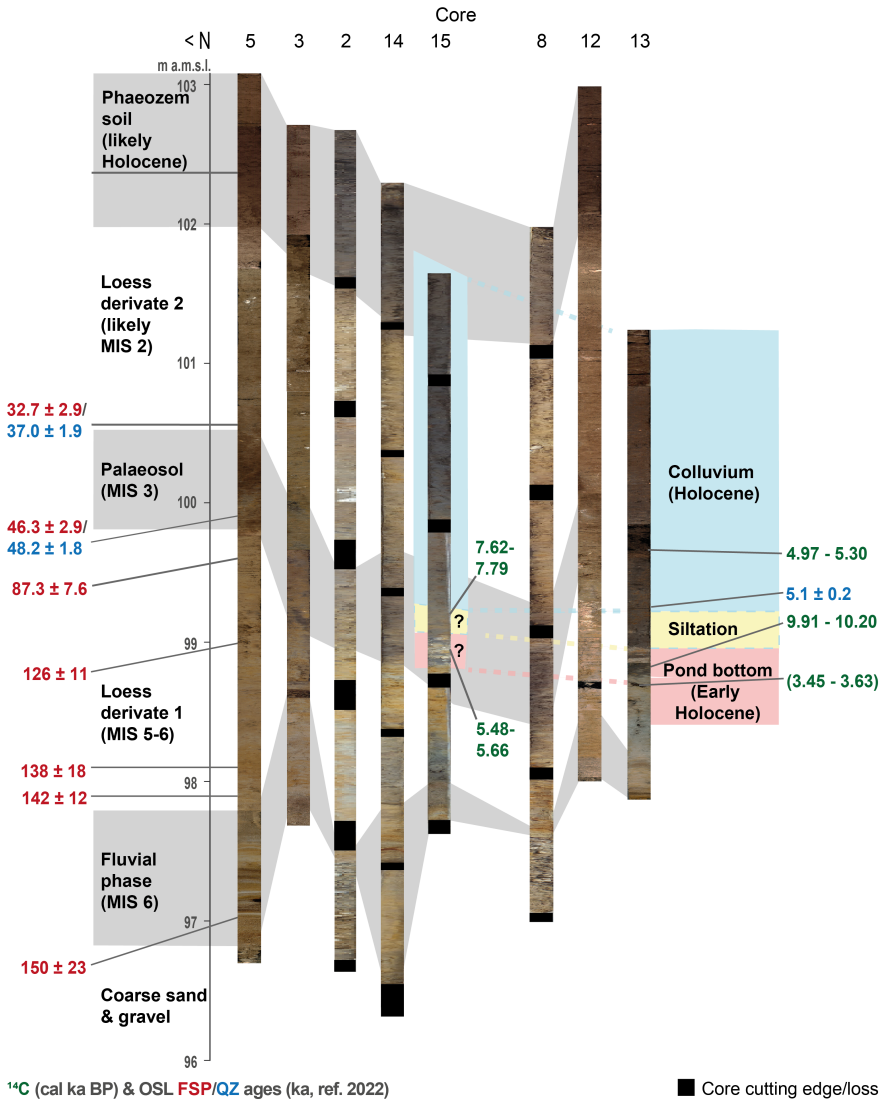

Figure 3.10: Stacked image scans of the presented Cores 5 (local stratigraphy) and 13 (Closed Depression 2) as well as reference cores from the year 2022 drilling campaign (Fig. 3.1) in relation to the identified chronostratigraphical units (this study). Main stratigraphical units are 1: Fluvial phase, 2: Loess derivate phase 1, 3: Palaesol, 4: Loess derivate 2, 5: Holocene soil. Below colluvium (Section 3.4.2: Soil unit) a siltation phase can be identified on top of a pond bottom unit in Core 13. A comparable stratigraphy can be observed in Core 15.

and the last phase of active soil mixing, e.g. by bioturbation (Reimann et al., 2017). For steppe soils bioturbation rates are typically high resulting in luminescence ages that predominately reflect the timing of active soil mixing and thus soil formation (von Suchodoletz et al., 2023).

However, concerning the age, the remnants might indicate an eroded Eemian soil, which is usually well established in comparable LPS (e.g. Marković et al., 2015; Perić et al., 2022).

The thick palaeosol unit on top of Loess derivate 1 is well developed and dated between 33±3 and 37±2 ka ago. The lowest sample with an age of ~48±2 ka (C-L5375) was taken from the former B horizon (Fig. 3.4) and is either linked to the age of silt accumulation in which the B horizon developed, the onset of soil formation or a mix of both processes (Fig. 3.10). However, this age range aligns with findings from previous LPS studies within the broader context of the CB. Comparable MIS-3 palaesoils were described in the region by Schatz et al. (2012): Tokaj (Hungary),~27±2 to 39±3 ka; Bösken et al. (2019): Bodrogkeresztúr (Hungary), ~29.5±2.2 ka; Pötter et al. (2021): Semlac (Romania), min. 23.6±1.6 ka; Antoine et al. (2009): Surduk (Serbia), ~32±3 to ~36±4 ka; and Stevens et al. (2011): Crvenka (Serbia), ~33±3 and ~38±4 ka. Accordingly, we suggest relatively warm-humid, but strongly oscillating temperatures and moisture, during the MIS-3 interstadial period for the eastern CB, which align well with supra-regional vegetation reconstructions (Feurdean et al., 2014; Nádor et al., 2011).

Holocene soil and vegetation

Pollen analyses from the CD bottom in Core 13 (9,910-10,200 cal a BP) indicate the formation of a wooded steppe dominated by pine, interspersed with temperate summer-green deciduous trees and various grassland species. This composition corresponds to the Early Holocene pollen zone of Sarló-hát (Magyari et al., 2010). However, the following characteristic expansion of Corylus (Magyari et al., 2024; Feurdean et al., 2013) is not reflected in our core. Here, Picea pollen is consistently present, a phenomenon noted in many lowland pollen sites in the CB (Magyari et al., 2024; Röpke, 2021; Gumnior and Stobbe, 2021). Spruce thrives in cool, humid (mountainous) conditions and likely originated from the Apuseni mountains (Magyari et al., 2024; Pató et al., 2020; Hegi, 1987).

Phaeozems are the typical soils for these wooded steppes in continental loess landscapes (IUSS (WRB) WG, 2015; IUSS (WRB) WG, 2022). In Toboliu, Phaeozem formation in Loess derivate 2 deposits (Core 5, Section 3.4.2) is characterised by a mollic horizon enriched in organic matter, decalcified, and homogenised by bioturbation (IUSS (WRB) WG, 2015; IUSS (WRB) WG, 2022). Radiocarbon dating (9,710-9,480 cal a BP) suggests a natural development of the Phaeozem during the Early Holocene (Fig. 3.10). This aligns with the classification of our

study site as a Phaeozem area by FAO & IIASA (2023) and supports Stănilă and Dumitru (2016), which position Toboliu's Phaeozems at the boundary of Luvisols. Comparing soils in Hungary with those in other regions is complicated by differing classification systems and environmental conditions. While 'Meadow soils' (Gley-Phaeozems) and 'steppe soils' (Chernozems/Castanozems) are recognised, there is no equivalent for wooded steppes (Michéli et al., 2019). So far, no samples from the bottom of the fAh-horizon were dated, making the onset of soil formation unclear. Additionally, because of the intensive bioturbation, radiocarbon dating results from the top of the fAh-horizon should be interpreted carefully. However, OSL-based chronologies to the east of the study area in more continental parts of Romania and Ukraine (Ramnicu Sarat: 10.3±0.7 ka, Kurortne: 9.1±0.6 ka, and Roxolany: 8.6±0.7 ka) show Early Holocene organic matter accumulation (Constantin et al., 2021).

The pollen data from the bottom of Core 13 prove deposition in the CD before evidenced human influence. Radiocarbon dates (from the CD bottom of Core 13 and from the mollic Ah-horizon in Core 5) suggest that the genesis is not human-induced, as suggested by Kempf (2021) for Chernozems in Hungary. However, cores and excavations in Toboliu indicate widespread prehistoric find contexts down to a depth of 60-70 cm, suggesting significant human modification (Lie et al., 2024).

3.5.2 *Closed depression formation and palaeogeography*

In the study area, human-modified Phaeozems are prevalent (Lie et al., 2024). In contrast, the closed depression (CD2) exhibits colluviation and limnic deposition (Fig. 3.10). Subsequently, we discuss different explanatory models based on findings from Core 13 and previous discussions on regional landscape evolution.

In a loess-dominated region, CDs may arise from piping processes, leading to the formation of loess (piping) dolines. The size of Toboliu's CDs resembles those described by Lukić et al. (2009), Zeeden et al. (2007), and Romanescu et al. (2018) in other regions. However, loess dolines typically exhibit a rimless, elongated shape, in contrast to the observed CDs. Additionally, piping requires a cliff or plateau margin for the removal of fine fractions, which is not present in our case. Loess dolines form above palaeosols, trapping a permeable sandy loess layer which is not found in Core 13 (Section 3.4.2).

In contrast, sandy deposits at the base of the CD (Core 13) are overlain by loess derivates (Section 3.4.2) rather than palaeosol (Lukić et al., 2009; Zeeden et al., 2007; Romanescu et al., 2018). The sandy unit in Core 13 shares characteristics and depth with the MIS-6 fluvial phase in Core 5 (Section 3.5.1). The Eemian soil remnants in the Loess derivate 1 alluvium of Core 5 suggests significant post-Eemian

soil erosion as proposed by (Hošek et al., 2017). Upsilting of the channel network might have favoured closed system pingo formation of CD2 (Fig. 3.11a). Accordingly, our findings suggest that CDs are associated with the formation of oxbow lakes in fluvial channels from the penultimate glacial period (Fig. 3.9).

The greyish hydromorphic silt (Core 13), covering the fluvial/alluvial sediments indicates stagnant water and shows upward increasing sand fraction, contrasting with the fining upward trend in Core 5. We propose that particle sorting due to reworking or freeze-thaw processes related to permafrost conditions (Zech et al., 2008) is the most likely explanation for our observations. Studies by Gábris and Nádor (2007), Lehmkuhl et al. (2021), and van Vliet-Lanoë et al. (2004), indicate periglacial conditions during the last glacial period (Fig. 3.1b), potentially resulting in relict landforms like thermokarst depressions and frost mount (e.g. pingo, palsa) ruins (van Vliet-Lanoë et al., 2004). Under permafrost conditions a sealed, semipermeable, water-saturated layer facilitates the formation of ice lenses in oxbow lakes (Fig. 3.11a, b). Hydrostatic pressure from freezing water above the saturated layer and surrounding impermeable permafrost pushes the water upwards, allowing the ice lens to grow (Mackay, 1998). It might be that later cold phases like the Oldest and Younger Dryas further favoured the growth of pingos (Fig. 3.11a, b) but dating is still lacking.

Nonetheless, pingo ruin size (50-200 m diameter, 1-8 m deep) and shape (circular to oval) resemble our CDs (Kluiving et al., 2010; van Vliet-Lanoë et al., 2004). Often, pingo ruins (Fig. 3.11c) show distinct rims (van Vliet-Lanoë et al., 2004), visible as subsurface remnants in our geomagnetic imagery around four of the six CDs (Fig. 3.3b). The smooth rims (Fig. 3.11c) are not discernible on the surface, likely because of tillage erosion. This observation also applies to the triangular feature near the rim (Fig. 3.3c), which resembles characteristics associated with meltwater discharge. (Fig. 3.11c). Warmer conditions cause the lens to melt, leading to mound (slope) collapse and, subsequently, depression formation (Fig. 3.11a). Core 12 (Appendix B.7), situated close by CD2 (Core 13), displays a coarser grain size and poorer sorting in Loess Derivate 2 compared to the general trend observed in Core 5 (Section B.6). This variation might be linked to downslope sediment translocation during the collapse phase, possibly in late MIS-2.

The CD bottom unit of Core 13 (Section 3.4.2) likely represent a former pond, the final phase of pingo decay after melting (Fig. 3.11a, c). It displays wet, partially anaerobic, limnic characteristics with typical Non-Palynomorph (NPP)s (Section 3.4.2). Radiocarbon dating of the limnic layer indicates a minimum age of 9,910-10,200 cal a BP. This timing aligns with the specific pollen assemblage, suggesting that it formed during the Early Holocene, prior to significant human land use in the region. According to Kluiving et al. (2010) and van Vliet-Lanoë et al. (2004), similar organic sediments (i.e., humid envi-

ronments: gyttja/peat) form in water-filled pingo ruins (Fig. 3.11c). In summary, the CD's rimmed circular outline, triangle-shaped features fitting meltwater discharge marks (Fig. 3.3), and the limnic bottom unit point to pingo (ruin) formation.

Another criterion for pingo ruins is their association with other periglacial landform relicts such as thermokarst lakes (Kluiving et al., 2010). Accordingly, several small depressions and meltwater discharge-like channels are visible in the geomagnetic imagery (Section 3.4.1, Fig. 3.2c). Moreover, CD5 (Core 15, B.9, Fig. B.7) exhibits lithostratigraphic similarities to CD2 (Core 13, Fig. 3.10), but is smaller and shallower, and has an irregular diamond-like shape (Fig. 3.3b). Also, even if poorly preserved, NPPs (e.g. algae) indicate limnic conditions during 5,480-5,660 cal a BP (BETA-630130 (C 15) and Section 3.4.2). Accordingly, CD5 might represent a thermokarst depression (another periglacial relict form) that contained a pond, latest until the Mid-Holocene (van Vliet-Lanoë et al., 2004).

The siltation of the pond commenced ~9,910 cal a BP and concluded before 5.1 ± 0.2 ka years ago (Fig. 3.10). This age marks the onset of colluviation, which is indicated by a lack of horizon development within the soil unit in Core 13. Backfilling began approximately 5.1 ± 0.2 ka (C-L5371, 99.19 m a.m.s.l.), with a radiocarbon date from a nearby elevation (99.56 m a.m.s.l.) indicating a similar timeframe (13/RC/4, 4,970-5,300 cal a BP).

The Early Holocene pollen assemblage (Section 3.4.2) in the CD bottom unit proves that natural processes formed the CD and that an origin through exploitation (e.g.loam pits) or disturbances (e.g. bomb craters) can be excluded. Furthermore, prehistoric extraction pits from the Neolithic and Iron Age are smaller (3 m) and exhibit variations in depth, diameter, and shape, contrasting with the uniform circular forms of about 50 m found in our study area (Gerlach et al., 2006; Kołodyńska-Gawrysiak and Poesen, 2017). The colluviation of the landform, marked by unstratified Soil unit (Section 3.4.2) commenced before the local Bronze Age occupation (3900 years ago) during the Neolithic period (i.e., 13/RC/4: 4,970-5,300 cal a BP). The rising phosphorus levels in colluvium suggest an increase in agricultural activity (Salisbury, 2016; Holliday and Gartner, 2007) since the Neolithic period, which is associated with intensified surface erosion and the subsequent filling of depressions.

3.5.3 *Thoughts on Bronze Age human-landscape interaction*

The colluvium in CD2 suggests that the residual pond experienced siltation prior to the Bronze Age. During this time, some other CDs may have been filled with still water, while others contained meadows. The depth of the CDs and its damming bottom unit (Section 3.4.2) likely helped retain moisture during dry periods, creating niches for land

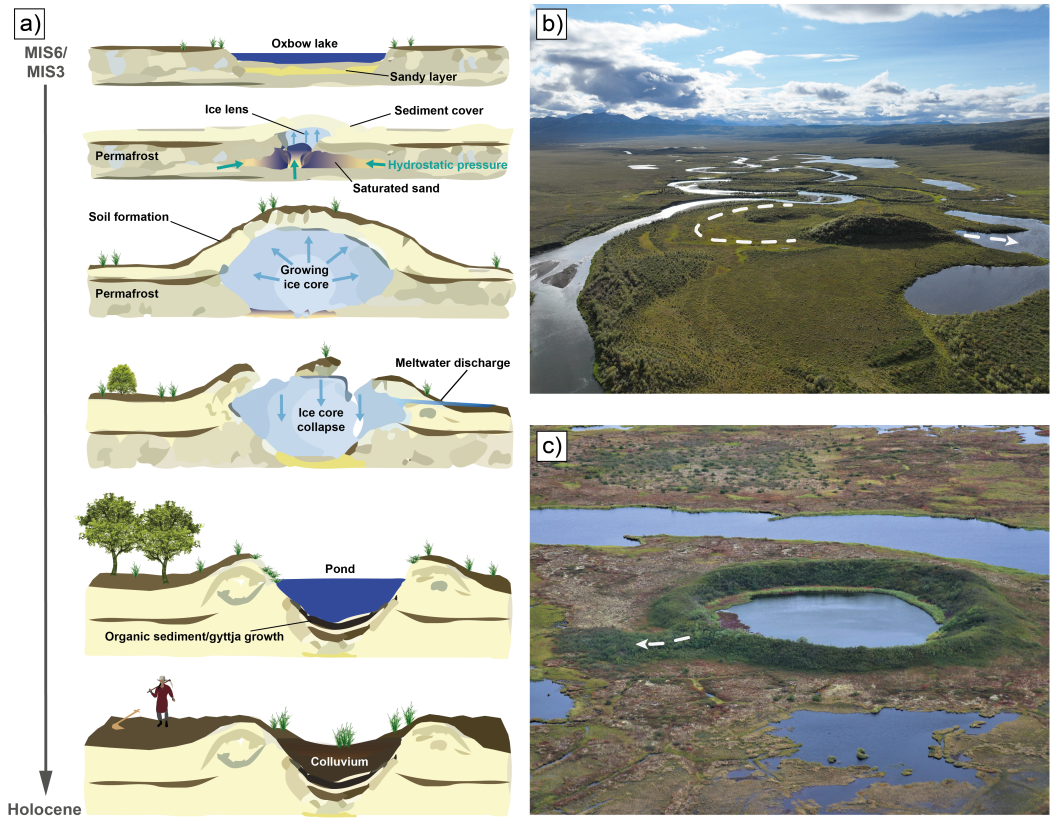

Figure 3.11: a) Formation and degradation of a closed system type pingo after Mackay (1998). process illustration for the closed depressions (CDs) along the grey arrow, b) closed system pingo growing in an oxbow of a braided river system, the oxbow course is indicated by the white dotted line c) fully degraded closed system pingo showing a typical circular rim around a water-filled depression (initial pingo ruin) in Tombstone National Park, Canada. Discharge direction is indicated by the white dashed arrow (Photos by Julius Kunz, University of Würzburg, Germany, 2018-2023).

use, such as dry-season gardening, in the predominantly flat terrain. However, factors like topography, highland-lowland interactions (e.g. trade between the Apuseni Mountains and the Crişul Repede), and soil properties were likely more influential in site selection during the Bronze Age. Phaeozem soils, known for their agricultural suitability (IUSS (WRB) WG, 2022), along with cultural factors and water access, likely influenced settlement decisions (Section 3.1).

Lászlóffy et al. (1938) noted a high flood risk along the west bank of Crişul Repede, while the eastern bank (Toboliu) had a lower risk, possibly due to westward subsidence trends (Gábris and Nádor, 2007). The map (Fig. 3.2d) also indicated that the proposed palaeochannel segment experienced permanent flooding, suggesting a persistent lake until the 18th century (Timár et al., 2006), although Kiss (2019) generally cautioned against potential overestimations of flooded areas in such historical maps. However, the presence of a water network among the Körös tributaries before regulatory measures has been documented. Proximity to a lake would have provided a reliable water supply without flooding risks. Similar small lakes likely served as fishponds throughout the Middle Ages (Kiss, 2019), which may also apply to the Bronze Age. Preliminary archaeozoological studies of lower tell layers indicate stagnant water nearby during the Middle Bronze Age, as evidenced by the abundance of still-water species (i.e. *Silurus glanis*, *Cyprinus carpio*, and *Rutilus rutilus*). The palaeochannel basin appears to be drainless, promoting subsequent wetland development over open water.

During drier Holocene phases, particularly in the Bronze Age, which is characterised by significant regional climate variability (Magyari et al., 2010), lake levels likely dropped, leading to wetland formation. The absence of pollen in Toboliu's relict-wetland (ascertained during palynological investigations in 2021, unpublished) may be linked to desiccation during alternating dry and wet phases, a trend also observed in other CB sites (Magyari et al., 2024).

The elongated lift along the northern banks may represent a buried sandbar or terrace of the palaeochannel, similar to contexts described by Nádor et al. (2007). Archaeological evidence (Găvan et al., 2022; Lie et al., 2024) suggests increased settlement activity (between ∼3800 and 3300 BP) in this area, indicating a preference for this location. In this elevated position, flooding risks were minimised, and the topography prior to regulatory measures supported this. This site likely offered a favourable vantage point within a flat landscape characterised by fertile soil and wetlands, advantageous for agriculture and pastoralism during the Bronze Age.

3.6 CONCLUSION

Based on thorough field observation, sedimentological, geochemical and palynological analyses as well as a first geochronological framework mainly based on OSL dating we conclude:

- The lithostratigraphy in the study area is primarily characterised by loess derivates: 'Sandy loess' from MIS-5-6 and 'Clayey loess' (most likely from MIS-2) that overlay fluvial deposits from MIS-6. In the probable last glacial deposits, we observed mixing of radiocarbon ages in the bulk samples, raising concerns about the reliability of radiocarbon dating for those sediments.
- Eroded soil material from the Eemian period, along with palaeosol formation during MIS-3 suggests a complex soil-landscape evolution that ultimately led to the formation of Holocene Phaeozem soil (MIS-1) that indicates the presence of an Early Holocene wooded steppe (Section 3.4.2).
- The formation of CDs in Toboliu is not associated with anthropogenic land use, such as prehistoric extraction pits, nor with loess dolines. Instead, they are most likely backfilled pingo ruins. Relicts of closed system pingos formed in several small oxbow lakes in association with other periglacial relicts, such as thermokarst depressions and meltwater discharge channels. The limnic ruin deposits (backfilling) are of Early Holocene age suggesting a formation of the pingos during very cold phases of the late pleniglacial.
- Furthermore, unlike many lakes or palaeochannels in the CB, we identified preserved Early Holocene pollen in the limnic phase of CD2. This discovery raises the question of whether we can find additional biostratigraphical markers in similar landforms. Our study highlights the advantages of a multi-method approach in reconstructing the complex soil-landscape evolution of the Toboliu site. It also advocates for further research to determine whether such CDs represent a supra-regional phenomenon and to elucidate their role within Bronze Age land-use systems.

ACKNOWLEDGEMENTS

The authors would like to thank the founders and team members of the project: Marian A. Lie (Institute of Archaeology Iaşi, Romania), Prof. Dr. Tobias L. Kienlin, Dr. Tanja Zerl, and especially Dr. Nadine Nolde, who provided preliminary archaeozoological results, and Dr. Alexandra Găvan (all from Institute of Prehistoric Archaeology, University of Cologne, Germany) for her constructive feedback

on the manuscript. Furthermore, we are grateful for the support provided by Marinel Gorgan and Nick Mikosch during fieldwork. We appreciate Dr. Philipp Schulte (LVR-Amt für Bodendenkmalpflege im Rheinland, Bonn) for his insights on interpreting the geochemical measurement results. Moreover, we thank Jun.-Prof. Dr. Julia Meister and Julius Kunz (both Julius-Maximilians-Universität of Würzburg, Germany) for their insightful discussions on the results and for providing photographs of comparable observations. Further, we extend our gratitude to the reviewers whose extensive and constructive feedback has greatly enhanced the quality of the manuscript.The project 'Living Together or Apart? Unravelling the Development, Internal Organization, and Social Structure of a Complex Bronze Age Tell Settlement at Toboliu, Western Romania' was funded by the Deutsche Forschungsgemeinschaft (DFG, German Research Foundation) – project number 436834905. This open-access publication is supported by the University of Cologne, Germany (DEAL agreement).

CONFLICT OF INTEREST The authors declare no potential conflict of interest. PERMISSION TO REPRODUCE MATERIAL FROM OTHER SOURCES Please find the publication permit for the Historical Hungarian Flood Risk Map of Lászlóffy et al. (1938) with the original title *Magyarország vízborította és árvízjárta területei az ármentesítő és lecsapoló munkálatok megkezdése előtt* (reference code B IX b 255) attached as a PDF file (Laszloffy1983-Publication permit). It was kindly provided by the Institute and Museum of Military History in Budapest, Hungary.

SUPPORTING INFORMATION/DATA AVAIABILITY The data supporting this study's findings will be made openly available on the Zenodo platform and provided with a DOI. Additional supporting information may be found in the online version of the article on the publisher's website.

4

MIGIS: MICROMORPHOLOGICAL SOIL AND SEDIMENT THIN SECTION ANALYSIS USING AN OPEN-SOURCE GIS AND MACHINE LEARNING APPROACH

The author contributions are structured by categories, namely: Conceptualization and Methodology, Software and Data Curation, Formal analysis, Investigation, Visualization, Supervision, Project administration, Funding acquisition, Writing –Original Draft, and Writing – Review and Editing. The individual authors' contributions to each category are subsequently listed by their initials.

Conceptualization and Methodology: MZ; Software and Data Curation: MZ and MG; Formal analysis: MZ; Investigation: MZ, MG and MK; Visualization: MZ and MG; Supervision: MK; Project administration and Funding acquisition: MK; Writing – Original Draft: MZ; Writing – Review and Editing: MZ, MG, AR, and MK.

Mirijam Zickel[2], Marie Gröbner[2], Astrid Röpke[1], Martin Kehl[1]

Manuscript submitted to the Journal *E&G Quaternary Science Journal, Copernicus* and published on 2024-01-26 https://egqsj.copernicus.org/articles/73/69/2024/

1 Department of Geography, Institute for Integrated Natural Sciences, Faculty 3 Mathematics and Natural Sciences, University of Koblenz, 56070 Koblenz, Germany

Abstract

Micromorphological analysis using a petrographic microscope is one of the conventional methods to characterise microfacies in rocks (sediments) and soils. This analysis of the composition and structure observed in thin sections (TSs) yields seminal, but primarily qualitative, insights into their formation. In this context, the following question arises: how can micromorphological features be measured, classified, and particularly quantified to enable comparisons beyond the micro scale? With the Micromorphological Geographical Information System (MiGIS), we have developed a Python-based toolbox for the open-source software QGIS 3, which offers a straightforward solution to digitally analyse micromorphological features in TSs. By using a flatbed scanner and (polarisation) film, high-resolution RGB images can be captured in transmitted light (TL), cross-polarised light (XPL), and reflected light (RL) mode. Merging these images in a multi-RGB raster, feature-specific image information (e.g. light refraction properties of minerals) can be combined in one data set. This provides the basis for image classification with MiGIS. The MiGIS classification module uses the random forest algorithm and facilitates a semi-supervised (based on training areas) classification of the feature-specific colour values (multi-RGB signatures). The resulting classification map shows the spatial distribution of thin section features and enables the quantification of groundmass, pore space, minerals, or pedofeatures, such nodules being dominated by iron oxide and clay coatings. We demonstrate the advantages and limitations of the method using TSs from a loess–palaeosol sequence in Rheindahlen (Germany), which was previously studied using conventional micromorphological techniques. Given the high colour variance within the feature classes, MiGIS appears well-suited for these samples, enabling the generation of accurate TS feature maps. Nevertheless, the classification accuracy can vary due to the TS quality and the academic training level, in micromorphology and in terms of the classification process, when creating the training data. However, MiGIS offers the advantage of quantifying micromorphological features and analysing their spatial distribution for entire TSs. This facilitates reproducibility, visualisation of spatial relationships, and statistical comparisons of composition among distinct samples (e.g. related sediment layers).

4.1 INTRODUCTION

A common task in petrography, sedimentology, and soil science is the microscopic characterisation of rocks (sediments) or soils aiming to describe the overall composition, facies type, or pedogenic features of the materials. This can provide valuable clues on their nature and formation. The analysis is usually done under the optical microscope using polarisation techniques (i.e. a petrographic microscope) and thin sections (TSs) prepared from the sample. While the principal optical techniques originate in petrography, the analytical method has been further elaborated and widely used in soil science and palaeopedology, where it is known as soil micromorphology (Bullock and Soil Science, 1985; FitzPatrick, 2012; Stoops et al., 2018), and more recently in sedimentology (Meer and Menzies, 2011) and archaeology (Canti and Huisman, 2015; Courty et al., 1989; Nicosia and Stoops, 2017).

Principally, conventional micromorphological analysis yields qualitative data on the size, shape, arrangement, and count of pores, minerals, and organic matter in the sediment or soil groundmass. This also applies to the analysis of pedofeatures, secondary accumulations that are diagnostic for soil formation (Stoops, 2020). Various light path modes, e.g. PPL, XPL, and oblique incident light (OIL), applied with a petrographic microscope are indispensable to identify and distinguish particles in TSs by their specific light refraction properties (e.g. FitzPatrick, 2012; Ligouis, 2017; Nesse, 2013). This procedure implies that fragmented, microscopic field-of-view observations must be recombined after completion of the TS analysis. In this concern, it is essential to follow accurate documentation and classification guidelines, such as the standards established by Georges Stoops (2020) for micromorphology. As a result, constituent (feature) quantities and spatial relationships, which are important to detect patterns (microstructure, groundmass composition, inclusions, pedofeature abundance, etc.), can be determined. This conventional procedure allows very precise statements on sediment or soil composition with regard to depositional and post-sedimentary formation processes (e.g. Bullock and Soil Science, 1985; FitzPatrick, 2012; Stoops et al., 2018). However, the conventional approach is laborious and requires intensive academic training. The same applies to the point counting technique, which is a common option to quantify micro-observations or to study spatial relationships (Drees and Ransom, 1994; Pires de Lima et al., 2020; Tang et al., 2020).

Recently, semi-quantitative approaches using standardised forms (e.g. estimation tables) have been employed to quantify micromorphological constituents, thereby enabling the comparison of microfacies (Brönnimann et al., 2020; Lo Russo et al., 2022). Nevertheless, expert analysis can be subjective, and the standardisation of micromorphological descriptions is still low (Stoops, 2020). Quantification and

spatial analysis are time-consuming, and interpretations are difficult to reproduce, display, and discuss. Usually, transparency requires a shared microscope session or workshops to study the respective TSs (Shahack-Gross, 2015).

To deal with these challenges, various approaches have already been developed involving the digitisation of TSs, for example by using TL, XPL, and RL flatbed scanning (Arpin et al., 2002; Haaland et al., 2018) or microphotography mosaicking techniques (Sauzet et al., 2017). Also, attempts have already been made to establish a microscopic information system (MIS). Tarquini and Favalli (2010) developed such a GIS (geographic information system)-based approach for petrographic analysis. Concerning image classification algorithms, in addition to image segmentation methods (Tarquini and Favalli, 2010; Visalli et al., 2021), significant progress has been made in the field of Machine Learning (ML) and deep learning, especially for petrographic studies. The successful determination of porosity and mineral composition in rock TSs via the classification of microphotographs using, for instance, DA (discriminant analysis), ANNs (artificial neural networks), CNNs (convolutional neural networks), support vector machine, and random forest algorithms has already been demonstrated (Ghiasi-Freez et al., 2012; Naseri and Rezaei Nasab, 2021; Rubo et al., 2019; Tang et al., 2020). So far only microphotographs, small areas of sedimentological TSs, have been promisingly classified using these approaches (Arnay et al., 2021), whereas, to our knowledge, no advances have been made when it comes to the semi-supervised classification of entire TSs using a combination of TL, XPL, and RL red–green–blue (RGB) imagery. By assessing TL, XPL, and RL information, micromorphological constituents or features can be reliably determined (Stoops et al., 2018). Referring to multispectral imagery in remote sensing, gained extended spectral dimensions are beneficial concerning the application of ML-based image classification (Lillesand et al., 2015). However, this requires the processing of large (high-resolution) data sets. GIS, such as the open-source software QGIS 3, is designed to process extensive data. It provides highly efficient image manipulation, classification algorithms, and the opportunity to analyse spatial patterns. Especially at the macroscopic level spatial relationships between features that are important for interpretations are revealed in the TS.

Therefore, we developed the MiGIS toolbox, a geoalgorithm processing chain integrable in QGIS 3 (QGIS Development Team, 2022b), which is tailored to handle TS imagery. Our goal was a straightforward and reproducible workflow (Fig. 4.1) which facilitates GIS integration (Fig. 4.1b), pre-processing, and training for a random forest algorithm-based semi-supervised classification, as well as accuracy assessment and spatial class statistics (Fig. 4.1c).

As an auxiliary tool for the conventional approach described above, it should enable the visualisation, quantification, and analysis of spa-

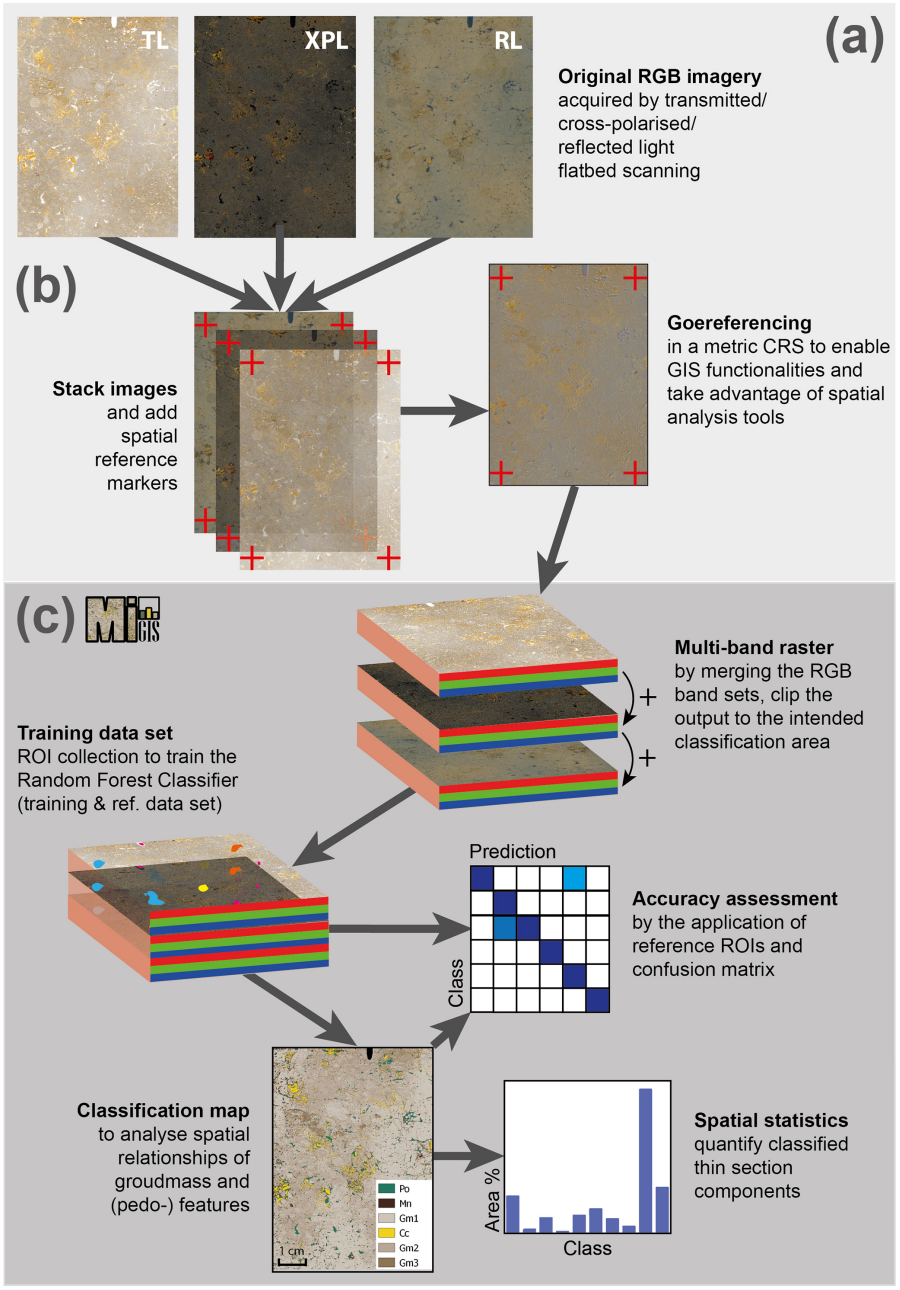

Figure 4.1: Workflow diagram showing digital TS analysis principles and main processing steps. TL: Transmitted light; XPL: Cross-polarised light; RL: Reflected light; CRS: Cooordinate reference system; ROI: Region of interest.

tial relationships of TS constituents. The MiGIS toolbox consists of four Python processing scripts, which can be easily imported to the QGIS processing toolbox.

As a case study, we selected a well-described loess–palaeosol sequence from Rheindahlen in Germany (Kehl et al., 2024). The aim was to classify and quantify the pore space and main micromorphological constituents: four different groundmass types (Gm); coarse constituents, such as medium sand and fine gravel grains (Sg); clay granules (Cg); charred organic material (Ch); and pedofeatures including different clay coating types (Cc, Cci, Ccd) and iron hydroxide (Fe)- and manganese oxide (Mn)-dominated constituents. The methodological advantages of MiGIS are demonstrated using a selection of TSs from Bt horizons.

4.2 MATERIALS AND METHODS

We composed a digital data set of 21 flatbed-scanned TSs from a 6.5 m thick loess–palaeosol sequence sampled at a former brickyard at Rheindahlen (Germany). The TSs were prepared and analysed in stratigraphic order allowing observations on changes in the type and intensities of soil formation with time. These have already been micromorphologically analysed in detail and described using conventional methods in Kehl et al. (2024). The Rheindahlen sediment sequence contains three different palaeosols characterised by pedogenic illuviation of clay (Bt horizons), which were interpreted to have formed during warmer phases (i.e. interglacials) of the Middle and Late Quaternary. These palaeosols are intercalated in diverse loess deposits that are associated with colder and drier phases (glacials) in the past (Kehl et al., 2024). Undisturbed Bt horizons typically contain coatings of oriented clay minerals (clay coatings), whose specifications and distribution are basically of micromorphological interest because they are evidence of the pedogenic process of clay illuviation (Stoops, 2020; IUSS (WRB) WG, 2022). From a micromorphological perspective, the samples contain a modest variation of particles, microstructures, and pedofeatures, thus providing a suitable input for our classification test series. The Rheindahlen loess loam exhibits a distinct groundmass mineral composition, featuring a preponderance of angular, spherical grains of silt-sized quartz and feldspar, in addition to elongated mica particles. All TS data sets were classified with MiGIS and statistically evaluated. To illustrate the advantages of a digital TS analysis in detail, a subset of three thin sections of the above-mentioned Bt horizons was selected. TS A4 originates from the modern Bt horizon sampled at a depth of 113 cm below surface (b.s.), B7 was taken from a second Bt (Erkelenz soil) at a depth of 305 cm b.s., and C5 belongs to the third Bt (Rheindahlen soil) extracted from a depth of 524 cm b.s. (Kehl et al., 2024). Since in some cases individual methods, feature classifications,

or phenomena are more illustrative in other classified TSs from Rheindahlen, some of these additional results (Appendix C.2) appear in the figures.

4.2.1 *Micromorphological samples, analysis, and class definitions*

High-quality uncovered TSs, 60 mm × 80 mm large and 25 μm thick, were produced by Thomas Beckmann (Schwülper-Lagesbüttel, Germany) involving the impregnation of air-dried sediment blocks with polyester resin under vacuum, hardening over several weeks, as well as cutting, grinding, and polishing as described in Beckmann (1997). Conventional micromorphological analysis (as well as the determination and verification of training areas for the semi-supervised image classification) was accomplished using a polarisation microscope at magnifications of 12.5×, 25×, 100×, 200×, or 500×, as well as different illumination techniques (PPL, XPL, and OIL). The micromorphological description was carried out according to the protocol and terminology of Stoops (2020). To differentiate between the various clay coating types, appropriate terms suggested by Brewer (1964) were used. Features considered in the semi-supervised TS image classification using the MiGIS toolbox in this study are listed and described in Table 4.1. The feature classes were established based on material screening and conventional micromorphological analysis under the microscope. Corresponding results and interpretations are described in detail in Kehl et al. (2024).

Pore space as observed in TSs under the microscope is less than the total porosity within a sediment or soil horizon due to geometry-related effects such as the Holmes effect or wedging effects (Stoops, 2020). Usually, fine- to medium-sized pore space cannot be detected under the microscope. Indeed, it is assumed that the image classification approach captures a random selection of larger pore cross sections which results in a minimum pore space proportion.

Regarding the groundmass, the resolution limit (here 25 μm) resulting from the section thickness must be taken into account. Since the fine fraction of the groundmass cannot be differentiated due to the overlapping of the particles (Stoops, 2020), we have specified different groundmass types and accordingly created "mixed" training areas for each class (Table 4.1).

Besides intact clay coatings (Cc), corresponding fragments (clay papules) occur in the sequence and were included in the same class. In addition the class "Fe" represents iron hydroxide.

In general, the colour values of Fe and manganese (Mn) pedofeatures can vary greatly (Vepraskas et al., 2018). In our study, the iron hydroxides appear mainly reddish-brown, whereas manganese-oxide-dominated features appear black under PPL/TL (Stoops, 2020, p. 24). Therefore, we decided to define two separate classes of Fe and Mn

Table 4.1: Micromorphological features observed in thin sections (TSs) from the Rheindahlen loess–palaeosol sequence and class codes for semi-supervised TS image classification.

Feature/type	Class description	Class ID
Pore space	Different types of voids filled with embedding resin	Po
Groundmass	Mineral and organic material composing the matrix of the sediment, at Rheindahlen mainly composed of silt with different shares of fine sand grains, clay minerals, and iron and manganese oxides	
Type 1	Mainly silt grains, redoximorphic loss of iron and manganese oxides ("bleaching"), light beige colour (PPL/TL)	Gm1
Type 2	Mainly silt grains, faint staining due to iron/manganese oxides, medium beige colour (PPL/TL)	Gm2
Type 3	Mainly silt grains, increased staining due to iron/manganese oxide and clay content, strong contrast to the surrounding lighter groundmass, dark beige to brown colour (PPL/TL)	Gm3
Type 4	Lenses of pure silt	Gm4
Type 5	Mainly silt grains, faint staining due to iron/manganese oxides and increased clay content, brown colour under PPL/TL	Gm5
Sand and gravel grains	Medium sand to fine gravel-sized quartz, feldspar, and quartzite grains	Sg
Clay granules	Sand-sized aggregates mainly consisting of clay	Cg
Charred organic material	Charcoal fragments and charred plant material	Ch
Pedofeatures	Group of features indicative of soil formation	
Clay coatings	Limpid intrusive/matrix argillan pedofeature: coated voids, grains, or aggregates, also as clay papules in the matrix	Cc
Impure clay coatings	Intrusive/matrix silt banded argillan pedofeature: coated voids, grains, or aggregates	Cci
Dark clay coatings	Intrusive/matrix ferri-argillan pedofeature: coated voids, grains, or aggregates	Ccd
Iron hydroxide	Nodules, coatings and diffuse impregnations: brown-yellow to reddish-brown colour (PPL/TL), yellowish-green/black colour, and dull or metallic luster (OIL)	Fe
Manganese oxides	Nodules, coatings, and diffuse impregnations: black colour (PPL/TL), black colour and dull luster (OIL)	Mn

pedofeatures depending on their colour under different illumination settings (Table 4.1). For each of the listed classes training data were collected (Sect. 4.2.4). If a certain feature class listed in Table 4.1 was not present in the TS, it was marked with "n/a" (not applicable) in the tabular classification results (Appendix C.2).

4.2.2 *Thin section imagery acquisition and pre-processing*

All TSs were TL scanned (Fig. 4.1a) with the transmitted light unit of Canon's CanoScan 9000F flatbed scanner, which is a relatively cost-efficient approach compared to professional film scanner and microscopy equipment (Haaland et al., 2018). Apart from test scans using 2400 dpi (Sect. 4.3.1), the digital scanning resolution was set to 1200 dpi, which represents the maximum optical resolution of the Canon scanner. The resulting RGB image has an approximate pixel ratio of 2801 × 4194 and a pixel size of 0.02 mm × 0.02 mm.

The captured images of 56.02 mm × 83.88 mm and 24 bit colour depth yield in an uncompressed JPG file size of approximately 8 MB. The identical scan resolution should be applied to each TS (TL, XPL, and

RL) image of the data set. To produce XPL imagery, two orthogonally oriented polarisation films were positioned below and on top of the TS (Arpin et al., 2002). To obtain surface reflection information (RL), a black plastic sheet was added on top of the section and scanned with the regular flatbed unit. A metal frame (e.g. film holder for transmitted light scans) was applied to keep the TS in an exact position and orientation. If necessary and after capturing the image, contrast and brightness can be adjusted using image processing software. For GIS integration, the TL, XPL, and RL images of each TS must be stacked and supplied with spatial reference points (i.e. crosses; Fig. 4.1b). To achieve this, we used the open-source image processing software Inkscape. If the resolution and dimensions of each scan are equal, the individual images can be assigned to layers in Inkscape and accurately positioned on top of each other. However, no exact co-registration of the images on pixel scale is required. An additional layer contains the reference points, which needs to be activated before exporting each aligned image. Since the image properties do not have to be adjusted anymore and with regard to a reduced file size, it is recommended to save the images with 8 bit colour depth before processing them in GIS. Concerning the georeferencing process in QGIS, a metric CRS needs to be applied to the previously aligned images. For instance, EPSG:32634 (WGS84/Universal Transverse Mercator (UTM) zone 34N) was used in this study. This is mandatory to obtain realistic metric dimensions for subsequent spatial analysis in GIS. The spatial resolution of 0.02 mm $\times$ 0.02 mm (pixel) of the imported images results in clearly visible single features of a size down to approximately 0.1 mm. Below this size, the TS constituents have fuzzy boundaries, but for instance fine sand grains can still be distinguished due to their high interference colours.

Related templates for an Inkscape project and a QGIS Georeferencer POINT data set are provided in the MiGIS repository on GitHub ("Code and data availability" section). These can be used for straightforward georeferencing of 60 mm $\times$ 80 mm TS scans with 1200 dpi resolution. Also, detailed instructions on how to stack images and spatial referencing are accessible there.

4.2.3 *Semi-supervised classification of thin section imagery*

ML algorithm-based semi-supervised image classification is often used to process remote sensing data, e.g. to create land surface models and other remote sensing products. Using enhanced multispectral information increases the identification accuracy of different surface types, for instance bare soil versus grassland (Lillesand et al., 2015). The expanded spectral data dimension which provides feature-specific spectral signatures enables the classifier to assign pixels with specific values to discrete classes. MiGIS follows a similar approach by using

bundled RGB information (colour depth) from the TL, XPL, and RL RGB bands, which are composed in a multi-band raster. This raster image thus contains 3 times as much information per pixel as a single image. With only three values (simple RGB image) of, for example, a single TL image, it is likely that the values of different features are too similar in the majority of the channels for a successful division into classes. The extended information in the multi-band raster, on the other hand, allows a clear assignment of a multi-RGB signature for the different features. In Fig. 4.2 this principle is illustrated by randomly selected single-pixel values for different feature classes.

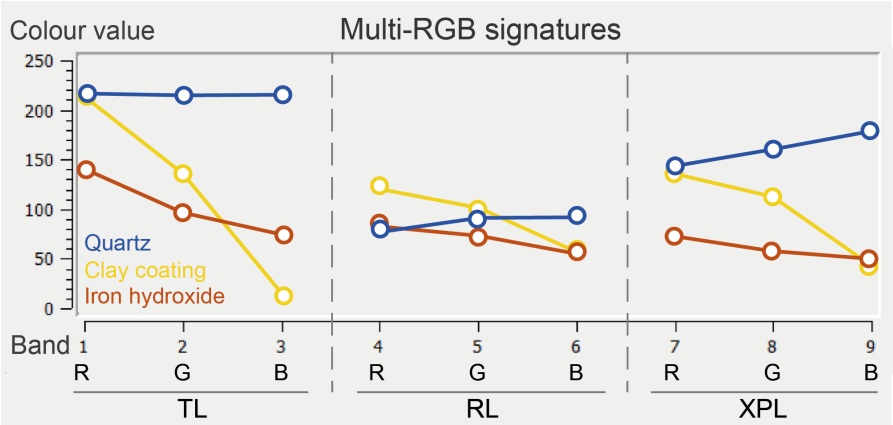

Figure 4.2: Random single-pixel values for different abundant materials in sediment thin sections (TSs) captured from TS A4. The "signatures" of the features are illustrated by artificial lines between the measured pixel values to highlight differences.

To assign pixels to predefined classes (e.g. pore space, clay coating, or manganese) the random forest algorithm needs to be trained by providing a set of regions of interest (ROIs) which cover representative features (pixels) for each class. Based on this data set and using a certain classification scheme, in this case a random forest, the algorithm is able to assign each pixel of the multi-band raster to one of the specified classes.

The implementation of the "Dzetsaka Qgis classification plugin" by Karasiak (2016) in MiGIS enables the use of the random forest classifier of the scikit-learn 1.0.1 Python package (Pedregosa et al., 2011; Scikit-learn developers, 2023) in QGIS 3. The application of feature importance properties and averaging multiple predictions makes the random forest a robust learning method. By default, a fixed number of 100 trees is set, which proved to be a reasonable size to prevent overfitting (Breimann, 2001; Rubo et al., 2019). During the construction each tree is split at every internal node using the square root of the number of features (n):

$$\text{max_features} = \sqrt{(n_\text{features})}. \tag{4.1}$$

The features are determined and randomly selected from the training data (*n*_features): the pixel values defined by the ROIs (regions of interest). The training data set should therefore have a reasonable size. The size depends on the individual data set properties and the desired class number, and there is no standard for this. Nevertheless, it should be taken into account that oversizing can also have negative effects because it will prevent the random forest from learning. The number of samples doubles in each tree level, which results in increased computing time and a fuzzy classification result (Breimann, 2001; Pedregosa et al., 2011; Scikit-learn developers, 2023).

4.2.4 *MiGIS toolbox*

Within the toolbox several automated processing steps are covered, ranging from the creation of a cropped multi-band raster, random forest-based image classification, and calculation of class statistics to the accuracy assessment. Originally, MiGIS was composed using QGIS Graphical Modeler (QGIS Development Team, 2022a). Adaptions and extensions of the processing chain have been carried out in Python. The workflow diagram in Fig. 4.1 illustrates processing steps and the basic principles to apply the presented method. Detailed guidance is available in the MiGIS repository on GitHub ("Code and data availability" section). The four available MiGIS scripts concatenate QGIS 3 (QGIS Development Team, 2022b) and GDAL (GDAL & OGR contributors, 2022) geoalgorithms (both available through the official QGIS 3 repository) in combination with image classification algorithms compiled by Karasiak (2016) within the Dzetsaka Qgis classification plugin. To take advantage of the random forest algorithm in MiGIS the scikit-learn Python package needs to be installed via the QGIS OSGeo4W shell (Windows systems) beforehand ("Code and data availability" section). Detailed references of the applied algorithms are provided in Appendix C.1.

In terms of processing time, the total effort of 1.5 to 2.5 h per TS (Table 4.2) can be considerably reduced after becoming familiar with the software and the various preparation steps. It should be emphasised that digital processing does not replace detailed micromorphological analysis under any circumstance. Instead, it serves as a tool to enhance classical micromorphological analysis with quantitative, statistically viable data. Simultaneously, it offers a convenient method for feature mapping, a capability not found in semi-quantitative approaches such as point-counting (Drees and Ransom, 1994; Murphy et al., 1977) or comparison with estimation charts. Therefore, it significantly improves the presentation and archiving of collected data in a sustainable and illustrative manner.

Table 4.2: MiGIS processing steps and related time expenditure per sample (Intel i7 processor, 32 GB RAM).

Processing step	Time span (approx.)
Total (scan inclusive)	1.5–2.5 h
Familiarisation with the software	0.5–1 h
Preparation (georeferencing, create multi-RGB raster and training data)	0.5 h
MiGIS computation total	10 min
1200 dpi classification	7 min
2400 dpi classification	8 min

Pre-processing georeferenced thin section images

A cropped multi-band raster, containing the target classification area of the TS (sample section) and multi-RGB information of the TL, XPL, and RL bands, is the centrepiece for a successful classification of micromorphological features in TSs. The tool "MiGIS 1 preprocess TS images" ("Code and data availability" section) facilitates the creation of a multi-band raster with six bands (TL and XPL RGB image) or nine bands (TL, XPL, and RL RGB image). The resulting raster data set can be further refined by clipping it to the extent of a custom vector polygon layer (see Appendix C.1). Usually, this is the part of the glass slide covered by the sample. Gaps, such as processing artefacts (e.g. drying cracks, label section), should be omitted from the polygon area (QGIS Development Team, 2022a). In this way, irrelevant image parts can be excluded to obtain precise spatial statistics.

The classification model

In combination with microscopic analysis, the cropped multi-band raster is examined and ROI polygons (separate vector data set for training) are set where they cover specific TS constituents (features), exemplary for each target class (Sect. 4.2.1, Table 4.1). As an input for the tool "MiGIS 2.1 train algorithm", each ROI vector polygon must include an ID (identifier value) and must be assigned to a user-defined class by a unique numerical value. Also, class descriptions (label) can be set.

Every classification process requires at least two classes, each with a minimum of one ROI polygon. The sum of ROI polygons of a specific class determine the number of pixels used to train the random forest algorithm on the specific class. In our study the ROIs covered a total

number of approximately 60–1800 pixels per class to test the optimal training size. After gaining some experience with the material, we were able to lower the ROI number per class to about 14 with about 60 pixels each. Also, the appropriate training data size depends on the TS data set (Sect. 4.2.3). If the feature variation is high or shows increased similarity, the sampling should be increased (e.g. more ROIs per class). In most cases in the analysis, all feature classes are of equal importance because the aim is to determine overall rock or soil composition and structure. To prevent under- or overfitting, each class training set should include an approximately equal number of pixels. By running the tool MiGIS 2.1, which is based on the Dzetsaka QGIS classification plugin (Karasiak, 2016), the generated training data set is applied to the cropped TS multi-band raster, which results in the construction of a random forest (Sect. 4.2.3) classification model.

Optional training data evaluation

Misclassifications may occur where pixel counts of a specific class are too low or the variation in values per class is too high. Using the MiGIS 2.2 tool offers a straightforward option to evaluate the training data set's validity. Based on a spatial query using the ROI geometries, class value bandwidth can be assessed before running the classification and prediction. The tool creates boxplot diagrams out of zonal statistics derived from the multi-band raster (TL–XPL–RL image). The input ROI zones provide information about the pixel value range (mean ROI value) per class and for each raster band. Also, class standard deviation is displayed, which helps to identify outliers (Fig. 4.3). Accordingly, the class width can be narrowed down by adjusting non-representative ROIs that cause values outside the class range (Fig. 4.3).

Classification, accuracy, and spatial analysis

By running "MiGIS 3 classification", the classification map (Fig. 4.1) is generated based on the random forest classification model processed in MiGIS 2.1, and the classification accuracy can be assessed (Sect. 4.3.1) as an indispensable part of the accuracy assessment (Congalton and Green, 2019). This step requires an independently collected ROI reference data set. In remote sensing analysis this would correspond to ground data (field reference). In MiGIS we use the same vector format ROI data set (Sect. 4.2.4) as for the training. In addition, our reference data sets had the same size as the training data sets to avoid a bias due to different weights. With this second ROI data set, reference values for the individual classes are collected and compared to the classification result. Since our case study was conducted with a modest number of fairly well distinguishable materials and classes, the same processor created the reference data set.

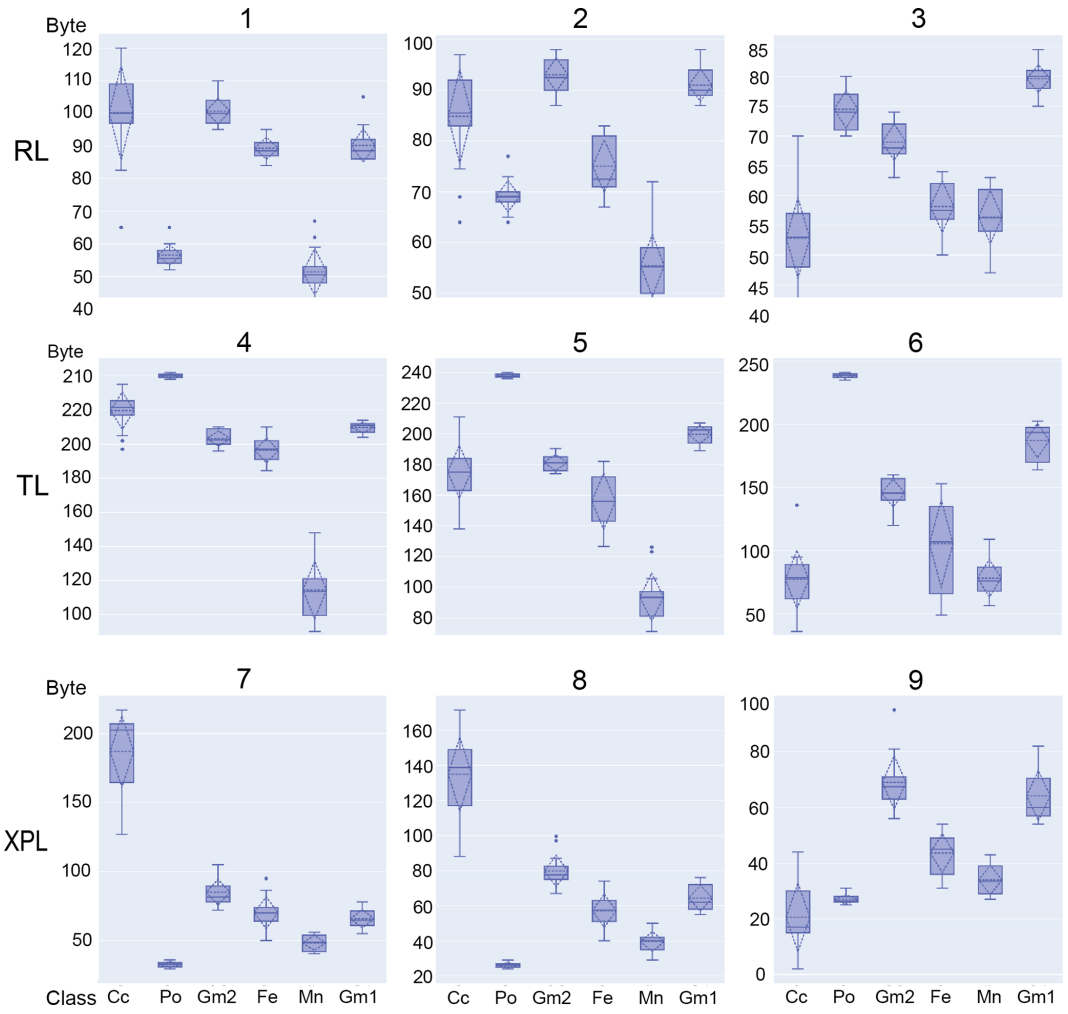

Figure 4.3: MiGIS integrated region of interest (ROI) assessment illustrates training data set validity: class value ranges and standard deviation for each of the reflected light RL, transmitted light TL, and cross-polarised light XPL RGB bands 1–9. Data of TS B7 imagery.

Using the classified and the reference data, a confusion matrix can be calculated and classification accuracy statistics can be derived. The reference data are represented by the columns and the classification result by the rows. Summing all correctly classified pixels (c) divided by the total number of classified pixels (t), the overall accuracy (Eq. 4.2) indicates the percentage of all pixels that were correctly classified.

$$\text{Overall accuracy} = \frac{c_n}{t_n} \times 100 \tag{4.2}$$

$$\text{Producer's accuracy} = \frac{\text{cr}_n}{\text{tr}_n} \times 100 \tag{4.3}$$

$$\text{User's accuracy} = \frac{\text{cc}_n}{\text{tc}_n} \times 100 \tag{4.4}$$

For Eqs. (4.2), (4.3), and (4.4), c is sum of all correctly classified pixels, t is total pixel count of classified pixels, cr is correctly classified pixels in reference data (per class), tr is the sum of all classified pixels in

reference data (per class), cc is the correctly classified pixel in classified data (per class), and tc is the sum of all classified pixels in classified data (per class).

The producer's accuracy (Eq. 4.3) indicates what percentage of the respective class areas was correctly identified as such. The user's accuracy (Eq. 4.4), on the other hand, shows what percentage of the areas assigned to a class is actually part of that class "at ground level" (Congalton and Green, 2019). This allows us to distinguish whether a misclassification (i.e. confusion) occurs due to the training data being inaccurate or because very similar colour properties of two classes evoke increased confusion.

Spatial statistics can be derived from the classification map. If the classification was applied to a cropped image (see Sect. 4.2.4), also the pore space can be quantified. If not, the glass slide rim around the section area would also be included in the pore space's area quantification. Based on the classification map MiGIS 3 calculates feature class-based spatial statistics, which enables the analysis of relative feature quantities in the TS, such as the abundance of a certain feature (e.g. clay coatings). In addition to an output table of pixel areas per class, this can be optionally visualised by running an implemented bar plot function. The classification map itself can be used for further studying distribution patterns in GIS. Classes of interest can be highlighted in colour, whereas other classes can be excluded from the visualisation (see Appendix C.1). Such selective visualisations can be used, for example, to illustrate the distribution of diagnostic features. These derivate maps can easily be exported as scaled image files.

4.3 RESULTS

The semi-supervised image classification with MiGIS yielded 21 classification maps displaying the distribution of classified features (Sect. 4.2.1, Table 4.1) in each TS. Spatial statistics and accuracy assessment results for all TSs of the Rheindahlen sequence are summarised in Appendix C.2. In Sect. 4.3.2 we will describe the produced classification maps and spatial statistics of three selected TSs – A4, B7, and C5 (Appendix C.2) – originating from different Bt horizons of the Rheindahlen sequence (Kehl et al., 2024). This serves to illustrate the classification performance by means of typical micromorphological features, such as pore space (Po), different groundmass types (Gm1/Gm2), quartz sand and gravel grains (Sg), clay coatings (Cc), dark clay coatings (Ccd), iron hydroxide (Fe), and manganese oxides (Mn) pedofeatures. In the following Sect. 4.3.1, we will describe the methodical outcome (Figs. 4.4 and 4.5) and experimental results, conducted to find the most appropriate parameter settings for MiGIS.

4.3.1 *MiGIS classification performance*

A detailed examination of Fig. 4.4 demonstrates that fine linear basic distribution patterns, indicative of disparities in groundmass composition, can be reliably detected, as well as pores, clay coatings, medium to coarse sand and fine gravel grains (quartz), iron hydroxide, and manganese oxide pedofeatures. This outcome underscores the great performance, especially when looking at the clear delimitation of polycrystalline quartz grains from the groundmass and the distinction of finest layer beddings. However, in A7 finer pores are wrongly determined, which may have an influence on the overall porosity; A4 also shows that parts of the sand grain are not recognised, but fine pores are identified as quartz.

Nevertheless, the figure also illustrates the occurrence of misclassifications, especially of fine constituents of the matrix. In the results of TS A7, very fine pores were sometimes classified as groundmass. In A4, however, some small quartz crystals as well as small parts of the larger grain in the middle seem to have been classified as part of the groundmass (Fig. 4.4).

Examining the classification accuracy (Fig. 4.5), it must be considered that B7 was one of the first TS data sets to be classified and C5 one of the last. Note that the confusion matrix of B7 has relatively high pixel counts, and that of A4 is medium and that of C5 is relatively low (Fig. 4.5). This is due to increased confidence in the selection of training and reference data during the test series (Sect. 4.2.4). While the classification of TS A4 achieved an overall accuracy of 100 %, it reaches 97 % accuracy for the classification of TS B7. TS C5 achieves an overall accuracy of only 87 % (Fig. 4.5 and Appendix C.2). Comparing all PA values indicates that the classifier exhibited varying accuracy in identifying the targeted feature classes (Appendix C.2). The same applies for the UA: the training data accuracy varies between classes. Pore space (Po), medium to coarse sand to fine gravel (Sg), and manganese oxide (Mn) could be identified with a precision of 100 %, whereas Groundmass 1 (Gm1), Groundmass 2 (Gm2), and clay coatings (Cc) indicate confusion in some classification runs: Gm1 only reaches 53 % PA in C5, Gm2 reaches between 98 and 89 % in PA and 97 %–80 % in UA, and the class Cc in B7 achieved only 94 % PA (Appendix C.2). Apart from this, all PA and UA values for these classes amount to 100 %. Nevertheless, only about half of Gm1 in TS C5 could be correctly identified (Fig. 4.5). In contrast, the iron-hydroxide-enriched clay coatings (Ccd) in C5 could be identified 100 % of the time. Iron hydroxide (Fe) and class Cc could generally be identified very well, apart from minor confusion regarding Gm2 and Mn in B7. The UA assessment indicates a similar pattern to the PA. The classes Po, Sg, and Mn, with a slight variation for Mn in TS B7 (UA: 99 %), are indeed these features as well. Also, in the classes Cc and Ccd, all targeted features can be assigned to the

different clay coating types. However, some confusion occurs in the classification of Gm1, Gm2, and Fe in TS B7 and C5. Nevertheless, Fe could also be assigned 100 % of the time in TS A4 and B7. The Fe UA value for TS C5, on the other hand, indicates only a very low accuracy of about 25 % for this class.

A comparison of the classified feature areas and class accuracies of a 1200 dpi and a 2400 dpi scanned data set shows no big differences with regard to the classified feature area. A maximum deviation of 4.8 % in area coverage was observed in class Gm1 (Fig. 4.6). Indeed, no significant difference in the effective optical image resolution could be observed in direct comparison of the images, whereas there are few discrepancies when comparing the producer's and user's accuracy of the classes.

We further tested whether a classification model trained on one TS data set can be applied to another data set (Fig. 4.7).

For this purpose, we selected two TSs with maximum classification "overall accuracy" and a similar composition (i.e. with the same feature classes). The sections C7 and C8 were classified once again with the opposite classification model, and the results were compared. It can be seen that the class areas calculated from these differ significantly in most cases (Fig. 4.7). This suggests that the classes in the classification models of C7 and C8 are defined by divergent pixel values. Accordingly the multi-RGB signatures differ.

4.3.2 *Digital micromorphological results*

All recorded micromorphological features of the different Bt horizons in Rheindahlen are described in detail in Kehl et al. (2024). Here we focus on the micromorphological implications of the classification result. The visual comparison of the classification maps in Fig. 4.8 facilitates the identification of distinct differences in the microstructure of the selected TSs.

In A4, vughs, many large channels, and chambers are visible. In contrast, these are smaller and less frequent in B7. Fine planar voids associated with the (sub-) angular blocky microstructure, on the other hand, appear particularly well. These are also found in C5 along with a few channels. In terms of the pore space area, TS B7 and C5 have moderate values between 3.4 % and 2.8 %. In A4, a greater pore space area of 5 % (Po, Fig. 4.9) indicates increased porosity.

In total five different groundmass types were distinguished in all TSs, and Groundmass 1 (Gm1) and Groundmass 2 (Gm2) are present in the three selected TSs. Qualitative analysis of these two groundmass types indicates that the lighter-coloured (bleached) areas represented by Gm1 are characterised by a decrease in the concentration of iron hydroxide and manganese oxides. In contrast the darker-coloured Gm2 shows an increase in diffusely distributed iron hydroxide. The

area ratio of Gm1 and Gm2 is approximately 1 : 2, with values between approximately 25 % (A4 and B7) and 35 % (C5) for Gm1 and values of approximately 57 % (C5), 58 % (B7), and 63 % (A4) for Gm2 (Fig. 4.9). It demonstrates that the two upper Bt horizons reveal a similar groundmass distribution pattern, whereas the Bt of C5 has a higher fraction of bleached zones. However, the PA score is comparatively low for the class Gm1 in the C5 data set (Fig. 4.9). The microstructure becomes particularly clear in the separate map representation of the corresponding feature class (Appendix C.1). These Bt horizons are characterised by subangular blocky (A4 and B7) to angular blocky or weakly developed platy microstructures (C5), with locally small subangular blocky peds with rounded shapes. The subangular blocky microstructure appears especially well in the classification map of B7 (Fig. 4.8). Additionally, A4 is one of a few sections of the sequence that contains medium to coarse sand to fine gravel grains whose distribution in the groundmass is visible in the classification map (Fig. 4.8).

A comparison of all classified pedofeatures indicates distinct spatial distribution patterns, especially when looking at clay coating proportions (Appendix C.2). These are particularly frequent in Bt horizon TSs from the sequence but are also detected in non-Bt horizons. Mostly they include limpid and occasionally layered slightly impure clay coatings (Cc). They are found in pores, on aggregates, or as fragments (clay papules) in the groundmass. In A4 (3.3 %) and C5 (2.7 %) the proportion is increased. Here mostly intact clay coatings are found, but the amount is low in comparison to the classification results of B7 (8 %). However, the classification map of B7 emphasises a different pattern which links the increased Cc proportion to a high number of clay papules in the matrix.

In contrast, class Ccd, which includes dark clay coatings (enriched with iron hydroxide), is unique for C5 and is represented with 0.2 %. The Fe proportion in C5 is slightly increased (2.0 %), but the manganese oxide proportion is comparatively scarce. However, the UA score is comparatively low for the Fe class (Fig. 4.9). Even though there is little iron hydroxide in A4, there is a comparatively high proportion of manganese oxide (1.3 %). With an area fraction of 2.8 %, iron hydroxide is very abundant in B7, compared to manganese oxide amounting to 1.2 %.

4.4 DISCUSSION

4.4.1 *Methodological implications of MiGIS*

At a first glance, it can be observed that all feature classes can effectively be distinguished by the classifier (Figs. 4.4, 4.5, and 4.9 and Appendix C.1). The random forest algorithm proves to be a suitable machine learning method, proficient in handling an expanded number

of classes efficiently. Such high class numbers are usually necessary in micromorphology to encompass internal class variations and the irregular occurrence of features in TSs. Rubo et al. (2019) achieved similarly good results when comparing mineralogical and porosity classification model performance of random forest and artificial neural networks. In addition, limiting the trees to a minimum of 100 was considered to fit this variety and proved to perform well (Rubo et al., 2019).

The overall accuracy of the most imprecise classification result of C5, which was 87 %, achieved satisfactory accuracy with regard to established accuracy standards (Anderson et al., 1976). However, in remote sensing analysis, classification results can be affected by atmospheric effects, such as diffuse radiation or clouds, in the input data (Lillesand et al., 2015; Whitcraft et al., 2015). In contrast, we profit from laboratory conditions for the classification of TSs, which increases classification accuracy (Rubo et al., 2019). Nevertheless, a certain "cloudiness" or level of disturbance cannot be neglected. Depending on the TS quality, air bubbles, cracks, etc. influence the classification results.

The classification result details in Fig. 4.4 illustrate the high accuracy that can be achieved using the random forest algorithm to classify TS scans. By combining the information from three distinct input images (TL, XPL, RL) in the multi-RGB data set, it becomes possible to differentiate features that share similar colour properties in one or even two of the single images. This approach is particularly advantageous when it comes to distinguishing between the Fe and Mn classes. We interpret these classes as predominantly consisting of either iron hydroxides (Fe) or manganese oxides (Mn) (Table 4.1). Depending on the iron oxide content, both can appear blackish in TL/PPL. Indeed, iron hydroxide has a reddish to brown colour when observed under RL, while manganese oxide appears black as well. The same principle applies to quartz and pore space, which are whitish in TL/PPL, but in XPL quartz shows specific interference colours, and pores are isotropic and hence appear black. (Fig. 4.4). However, in the case of predominantly occurring fine sand, it is possible that a significant number of the small quartz grains might be oriented in an extinction position without being realised. In this scenario, the probability of confusion with pore space increases due to the overlapping colour values of both entities in XPL. In the RL image, colour distinctions between the two classes are noticeable, likely contributing to the relatively successful classification. Also confusion with the groundmass occurs that is not detected by the accuracy assessment (Fig. 4.5). This is due to a certain amount of quartz contained in the groundmass. It is conceivable that the classification process might lead to an underestimation of quartz particles in the sand fraction. Consequently, the proportion of sand particles should be considered indicative of minimum values. In contrast, if the interference colours of various occurring mineral grains

differ enough, first classification attempts of TS from other sites show that even small mineral grains can be reliably identified. For instance, this applies to carbonates (e.g. limestone) or mica.

Concerning the producer's accuracy, whereas features which are predominantly monochrome (e.g. Po and Mn) reached 100 % identification accuracy, there were minor misclassifications in other classes with increased colour or intensity variation. A confusion of iron hydroxide (Fe) and Groundmass 2 (Gm2) can be related to the fact that iron hydroxide particles are also present in Gm2 (Fig. 4.4). This illustrates the difficulty of the classifier to properly separate these two classes. Nevertheless, an acceptable classification accuracy of those classes can be yielded, which allows us to estimate the relative distribution of iron hydroxide in the TS.

Regarding the user's accuracy, iron hydroxide could also be assigned 100 % within the classifications of A4 and B7. But the UA for the TS C5, on the other hand, reaches only a very low accuracy of about 25 %. There Fe was largely confused with Gm1, which basically means that some of the created Fe class ROIs must contain pixels that are actually part of the class Gm1. Hence, this training data input should be adjusted.

Initially it is likely that some confusion occurs between feature classes with high similarity in colour such as iron hydroxide and manganese oxides. However, the MiGIS 2.2 tool (Sect. 4.2.4) deals with this issue by visualising the ROI pixel value range per class and band. By a brief examination of the automatically produced boxplot diagrams, it can be investigated whether some ROI positions or their quantity within the respective class would have to be adjusted to improve the classification performance (Sect. 4.2.4). Moreover, it is important to consider all of the presented accuracy assessment parameters (i.e. confusion matrix) when assessing the classification result (Fig. 4.5).

Smaller particles or pedofeatures, such as thin clay coatings, offer few opportunities for setting sufficient training areas and can therefore also cause misclassifications due to the lack of adequate class size and variation.

In this concern, the application of ML instead of colour information classification only could represent a further reasonable adaption, as it combines pixel value classification with segmentation steps (Thierion and Lang, 2018; Visalli et al., 2021). Also, this could be helpful to study geometrical properties of particles, such as single grain rounding and void geometry assessment.

At this stage, we can demonstrate that a classification model trained and applied on an individual TS performs well. However, overfitting can be observed when transferring a created model to another data set. Among others, a successful classification is evoked by representative training data (Vapnik, 2000). Since the colour values of the features

between TSs can differ, depending on the type of manufacture, sample, and imagery, the learning of one model might not cover the variation in another TS data set. To avoid model overfitting (Breimann, 2001), more multi-RGB data (i.e. signatures) could be collected from common materials (e.g. features) in TSs. Intensified training on several TS data sets could be a solution to create representative training data to classify TSs produced using a similar resin, technique, and thickness. Such a combined classification model would possibly increase the classification robustness (Breimann, 2001; Vapnik, 2000). In this regard, providing multi-RGB signatures of different features within the application could prove to be supportive for the creation of representative training data. Similar offers exist for remote sensing products, for example provided by the USGS (Kokaly et al., 2017). Nevertheless, the reproducibility of feature signatures based on multi-RGB imagery in terms of increased variation concerning differing colour values between TS images still needs to be investigated. However, our test results (Fig. 4.7) suggest that great effort is needed to follow this approach, since each TS is a unique product, which implies individual quality characteristics.

In general, a successful classification requires accurately produced TSs. Deviations caused by preparation, such as varying section thickness and embedding resin mixes, air bubbles, and other artefacts, might have a negative effect on the classification result. This is due to the related increased variation in colour of the constituents (i.e. mineral interference colours). Also this limits the transfer of classification models, models which were trained on different TSs (Rubo et al., 2019) and applied to an "untrained" TS data set. Therefore, the application of ML models has so far been broadly limited to the specific TS data set (Sect. 4.3.1, Fig. 4.7). At the moment we suggest constructing separate classification models for each thin section.

Apart from preparation quality, classification errors can also be the consequence of discrepancies in the image acquisition (e.g. skewed images, image distortions). For this study, a flatbed scanner with transmitted light imaging was used. This has the advantage that diffuse ambient radiation is greatly minimised by the closed scanner lid. In contrast, such problems can occur when capturing sections with a single-lens reflex (SLR) camera, in addition to an increased probability of distortion due to the curved lens (Carpentier and Vandermeulen, 2016).

Nevertheless, light refraction effects can occur during scanning due to the highly reflective glass slide (Sect. 4.2.1). At the sample section border they can be excluded during pre-processing in MiGIS 1 (Sect. 4.2.4). Still, light refraction effects can occur at the margins of the pore space. In these transition areas, the embedding resin may not be evenly distributed, which can amplify such effects and consequently cause misclassification. This could possibly be corrected

by post-processing through the application of filter algorithms to remove interfering pixel values, for instance by Gaussian smoothing. A similar approach was implemented in the study of Tang et al. (2020).

In general, optical resolution (i.e. spatial resolution) is a limiting factor because this determines the minimum size of detectable micromorphological constituents. The Canon scanner used for this study should be able to produce high-resolution scans of up to 9600 dpi. TS scans of high quality are already obtained at a resolution of 1200 dpi. TS scans taken at 2400 dpi have a higher digital resolution which means that they appear sharper but do not show significantly more detail. Comparing the classification results of both versions the classified feature area differs only minimally (Sect. 4.3.1, Fig. 4.6). Thus, the 2400 dpi image does not have a higher spatial resolution. Nevertheless, a direct comparison is difficult because separate training data sets are used for the two image data sets due to the different resolution. This results in the deviations observed in the PA and UA values. However, it is probable that the manufacturer's specification of 9600 dpi refers to the merely maximum possible digital resolution, whereas the maximum optical resolution is 1200 dpi. Furthermore, the pixel values will be interpolated when scanning with a higher-resolution setting than 1200 dpi. This will result in increased file size, and the scanned image appears sharper due to increased digital resolution, but the effective optical resolution remains the same.

Professional film scanners, with a usually much higher optical resolution, can possibly increase the image quality significantly. Thus, approaching the overall resolution limit of 25 μm, especially regarding the fine fraction of the groundmass, all features would appear sharper, and light refraction effects might be minimised. In this regard, it would also be possible to increase the minimum size of observable and analysable constituents, which is 0.1 mm using 1200 dpi scans in this study. However, it must be taken into account that such devices are much more cost intensive than transmitted light flatbed scanners (Haaland et al., 2018).

The total processing (Table 4.2) time is not constant but is determined, among other things, by the level of experience in creating training areas. In the initial phase of the test series (first TSs classified), the ROIs contained relatively high numbers of pixels (Appendix C.2). With increasing comprehension of the feature class properties and the algorithm's behaviour, fewer pixels per class were needed to achieve similarly good classification results in later classification runs. Nevertheless, the size of the reference data set used to assess accuracy should correspond to the individual properties (e.g. sample type, resolution, number of classes) of the TS data set (Sect. 4.2.3). Compared to point counting, which also requires considerably more effort than digital image analysis, it is an advantage that the accuracy does not depend so much on the size of the constituents, as the classification is

pixel-based and visual acuity independent (Drees and Ransom, 1994; Murphy et al., 1977).

4.4.2 *Interpretation of the digital micromorphological results*

Though an exhaustive interpretation of sediment and soil formation processes at Rheindahlen exceeds the confines of this paper, we aim to provide illustrative examples of how the derived proportions and distribution patterns of classified constituents can augment the comprehension of conventional micromorphological analyses and to improve the dissemination of the findings.

The visualised microstructure and the determined porosity values (Sect. 4.3.2) can be well assigned to the Bt horizon spectrum (Kehl et al., 2024). Compared to most other samples, the bleached Groundmass 1 (Gm1) is less represented in all analysed TSs, whereas Groundmass 2 (Gm2), characterised by evenly distributed and stronger iron staining, is much more represented. Gm1 identifies parts where iron hydroxide is lacking due to redoximorphic bleaching. This can be easily brought into proportion through the classification and enables an estimation of the relative iron hydroxide content and depletion rates under the assumption that Gm2 represents the pre-depletion state (Sect. 4.3.2 and Kehl et al., 2024).

The uppermost part of the studied profile, including the modern Bt horizon represented by TS A4, contains a notable amount of medium to coarse sand and fine gravel. In silt-dominated loess deposits, inclusion of such grains indicates reworking of the aeolian deposit by overland flow or solifluction. In addition, the patchy distribution pattern of such grains in thin section A7 can be linked to cryoturbation processes (Kehl et al., 2024).

In all presented TSs of the Bt horizons many well-developed clay coatings are preserved (Fig. 4.9), especially in large pores. B7 has the highest proportion of clay coatings in the entire sequence, indicating a particularly intensive and long-term character of soil formation during the related interglacial period (Kehl et al., 2024). The clay coatings of the lower Bt horizons displayed in B7 and C5 are often fragmented, and clay papules are abundant (Sect. 4.3.2). Frost effects are attributed to this mechanical disruption of clay coatings, a phenomenon not observed in the modern Bt horizon of A4.

The abundance of redoximorphic pedofeatures in TS A4 is particularly well displayed in the respective single maps (Appendix C.1). In general, these features indicate the effect of stagnant water conditions. In the presented TSs, they are less than 1 mm in diameter, but also some larger nodules, measuring more than 5 mm, have been observed in some parts, such as in TS A4. However, especially in thin section C5, the increased number of iron hydroxide and manganese oxide nodules, microscopically determined in the lower part of the sequence

(TS C5–C8; Kehl et al., 2024), are not reflected by the classification results. This could be partly attributed to the classification method, which quantifies the aerial percentage of nodules rather than their numerical count.

Nevertheless, the increased confusion with class Gm2, which contains fine-grained iron hydroxide, accompanied by the low UA score, seems to have led to the underestimation of the corresponding classes Fe and Mn (Appendix C.2).

4.4.3 *Implications for micromorphology*

The employment of MiGIS as an auxiliary instrument reveals its efficacy in mapping and quantifying soil and sediment constituents based on their multi-RGB signature (Fig. 4.2), thereby demonstrating the advantageous integration of this supplementary digital dimension into micromorphological analysis. Nevertheless, the MiGIS classification using the random forest algorithm is based on colour values (TL, XPL, and RL) of the TS features. A classification based on shape and size is not included yet. This could possibly be implemented by using Object-Based Image Analysis (OBIA) algorithms through the process of image segmentation (Sect. 4.4.1).

However, the semi-automatic classification approach of MiGIS enables users, e.g. well-trained micromorphologists, to define suitable training data for specific feature classes. This offers the advantages of qualitative control concerning TS imagery, as well as a suitability assessment of colour value differences between constituents. The application of a mask layer to crop the multi-band layer, which is used to select the classification area (sample section) in MiGIS 1, also enables the definition of relevant parts of the sample. Thus, artefact sections such as drying cracks can be excluded. Comparatively fast digital documentation within 1.5–2.5 h processing time (software familiarisation inclusive) per TS enables a straightforward assessment of the overall composition, pore space volume, distribution patterns, and microstructure, in combination with an automated visualisation of these results. Trends and anomalies can thus be highlighted (e.g. by setting a high-contrast colour for a specific feature class), and at the same time feature occurrence can be recorded for statistics without much effort. By classifying entire TSs, feature quantities and spatial patterns can be compared between different TSs (i.e. stratigraphical units). This is of minor interest in digital petrographic analyses, which is mostly focused on the classification of microphotographs (Ghiasi-Freez et al., 2012; Naseri and Rezaei Nasab, 2021; Rubo et al., 2019; Tang et al., 2020), but very innovative for micromorphological analyses. Nevertheless, MiGIS can also be used for the classification of microphotographs. Moreover, it would be conceivable to use the method to verify sedimentological anomalies, for instance, to identify a weakly expressed

archaeological context or feature. Within our working group, MiGIS has already been tested on TSs from archaeological sediments. Even though the material diversity can be significantly higher due to anthropogenic input, the first promising results have already been achieved, e.g. for cave occupation layers and floor contexts in tell sediments. Thus, we plan to evaluate the application of MiGIS to archaeological TSs.

Similar to the studies of Tarquini and Favalli (2010) and Visalli et al. (2021), the GIS environment, which was applied here, is advantageous to survey and query the TS imagery and the classification map within a metric spatial reference system. Thus, realistic spatial measurements, provided by the use of a metric CRS (Sect. 4.2.2), allow native QGIS measurement and spatial analysis tools (QGIS Development Team, 2022a) to be used to capture the dimensions or distribution of micromorphological features. In addition, vectorisation in post-processing of the classification maps enables the use of geometric analysis and further query tools (Visalli et al., 2021). In this sense, the combination of mapping and quantification of constituents in TSs can be gainfully applied for micromorphological analysis and documentation.

However, there are some limitations regarding the significance of measurement results and quantification. Still, a proper classification requires expert microscopic analysis, specifically to assess the individual use of principally underestimated pore space quantification which is obtained by the digital classification approach (Sect. 4.2.1). Nevertheless, by classifying the pore space of an entire TS, the microstructure can be visualised to a high degree of effectiveness. The classification of the groundmass is also an advantage for capturing the respective spatial composition. For instance, this enables the recognition and illustration of bedding features or linear basic distribution patterns, as well as the degree of soil formation (Sect. 4.3.1, Fig. 4.4).

Also, improvements could be made with regard to the misclassifications of manganese oxides and iron hydroxide. Our approach is based on the classification of colour values only, but these can vary not only due to the TS quality, but also in the case of manganese and iron oxide concretions due to the presence of other chemical elements such as phosphorus (Vepraskas et al., 2018). Accordingly, a precise micromorphological analysis is always a prerequisite for the digital analysis, although, referring to Rubo et al. (2019), using chemical or element mapping imagery (micro-XRF) as additional input to improve the classification could be very useful in this concern (Mentzer, 2017; Visalli et al., 2021). Comparing MiGIS classification to element mappings could also provide an independent, detailed compositional reference. For instance, element maps could be used to verify the spatial distribution of specific elements, such as Fe or Mn.

4.5 CONCLUSION

We presented the freely accessible MiGIS toolbox, an innovative tool for digital micromorphological TS analysis based on multi-RGB TS imagery. It can be applied by integrating Python processing scripts ("Code and data availability" section) into the open-source software QGIS 3. The application of a metric CRS enables realistic measurements based on scanned TL, XPL, and RL imagery. The ability to classify TS features using their colour value signature, quantify them, and visualise spatial relationships makes MiGIS a useful supplement to conventional micromorphological analysis (Sect. 4.4.3).

In particular, the visualisation of the spatial distribution of pedofeatures and their quantification could be profitably used for the determination of Bt horizons from the Rheindahlen loess–palaeosol sequence. In this way micromorphological observations become vivid and to a certain extent reproducible. Moreover, the computed spatial statistics enable the quantification of observations (i.e. features) to compare the composition and structure of different samples. Likewise, this could prove to be useful for pedological, sedimentological, and microfacies analyses. However, the achieved classification accuracy depends on the user's academic training level (i.e. in micromorphology or petrography) and the ability to create representative training data. Thus, basic knowledge of the principles of ML-based image classification and GIS functionalities in general are indispensable. Nevertheless, implemented control instances, such as pre-classification ROI evaluation (Sect. 4.2.4) and using a set of independent ROIs for reference, allow for a certain self-control. Further it turned out that a scan resolution of 1200 dpi is sufficient to produce suitable classification results. Also, the random forest algorithm seems to be well-suited for the semi-supervised classification of typically high colour value variation in TS features and high number of classes (Sect. 4.4.2).

The application of element maps (micro-XRF) could serve as a further reference but could also boost the classification accuracy especially of Fe and Mn features (Sect. 4.4.1). Even involving several feature classes (Table 4.1), it turns out that the obtained classification results of a model trained and applied on the same TS are reliable. Nevertheless, the efficiency could still be increased by creating a combined classification model and applying it for a whole sequence, or for micromorphological features in general. Considerable effort is required to establish a comprehensive signature library for micromorphological features in multi-RGB imagery, taking into account the influence of variable TS quality and recording modes as limiting factors. Moreover, a preliminary investigation is essential to determine the reproducibility of multi-RGB signatures for individual features (Sect. 4.4.1). Implementing an OBIA function in individual classification runs could provide the classification result with further detail, for

example to differentiate between geometrical properties of features (Sect. 4.4.1). In general, since MiGIS is based on a Python script, a reasonable next step will be the implementation as an official plugin in the QGIS repository, which would increase accessibility.

ACKNOWLEDGEMENTS

We express our gratitude for the financial backing extended through grant number 408333614 and the coverage of the article processing charge (grant no. 491454339) by the German Research Foundation (DFG). The authors wish to convey their appreciation to Tony Reimann, Stephan Opitz, and Christoph Hütt for their insightful discussions on the results and their assistance in crafting and refining the article. Additionally, we extend our thanks to the reviewers whose valuable comments and guidance substantially enhanced the quality of this paper.

FINANCIAL SUPPORT This research has been supported by the Deutsche Forschungsgemeinschaft (grant nos. 408333614 and 491454339). This open-access publication was funded by Universität zu Köln.

DATA AVAILABILITY All MiGIS toolbox Python processing scripts for QGIS 3 – MiGIS 1 preprocess TS images, MiGIS 2.1 train algorithm, MiGIS 2.2 ROI evaluation (optional), MiGIS 3 classification – and templates are freely available online on GitHub: https://github.com/Mirijamz/MiGIS (last access: 18 January 2024; doi.org/10.5281/zenodo.10527165, Zickel and Gröbner, 2023). In addition to tool scripts and template files, an accompanying toolbox manual (documentation) is available at the above address on GitHub. MiGIS toolbox is based on open-source resources provided by GDAL, Nicolas Karasiak, QGIS, and the Scikit-learn developers. Accordingly, software and underlying code are available on GitHub and Zenodo: GDAL v3.5.1 from https://github.com/OSGeo/gdal (last access: 24 January 2024; doi.org/10.5281/zenodo.6801315, Rouault et al., 2022); Dzetsaka Qgis Classification plugin v3.7 from https://github.com/nkarasiak/dzetsaka/ (last access: 24 January 2024; doi.org/10.5281/zenodo.3463523, Karasiak, 2019); QGIS v3.22 from https://github.com/qgis/QGIS (last access: 24 January 2024; doi.org/10.5281/zenodo.7986774, qgis bot., 2022); and scikit-learn v1.0.1 from https://github.com/scikit-learn/ (last access: 24 January 2024; doi.org/10.5281/zenodo.5596244, Grisel et al., 2021).

DISCLAIMER The contact author has declared that none of the authors has any competing interests. Publisher's note: Copernicus Publications remains neutral with regard to jurisdictional claims made in the text, published maps, institutional affiliations, or any other

geographical representation in this paper. While Copernicus Publications makes every effort to include appropriate place names, the final responsibility lies with the authors.

REVIEW STATEMENT This paper was edited by Christian Zeeden and reviewed by David Brönnimann and Janek Walk.

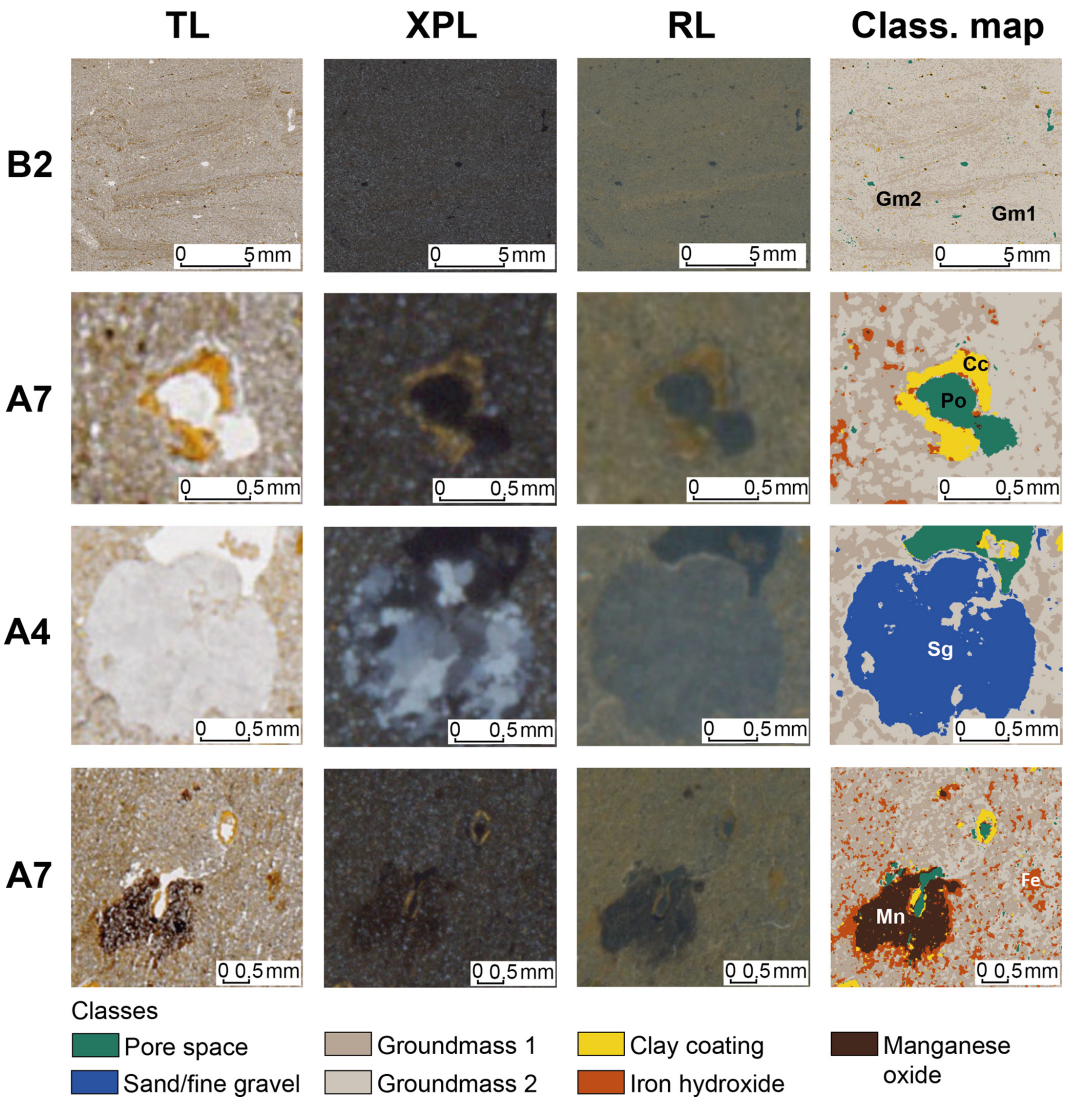

Figure 4.4: Details of selected classification results (Class. map) compared to captures of the transmitted (TL), cross-polarised (XPL), and reflected light (RL) scans of B2: linear basic distribution pattern; A7 (top): clay coating in a vugh; A4: coarse sand grain; A7 (bottom): orthic manganese oxide and iron hydroxide nodule.

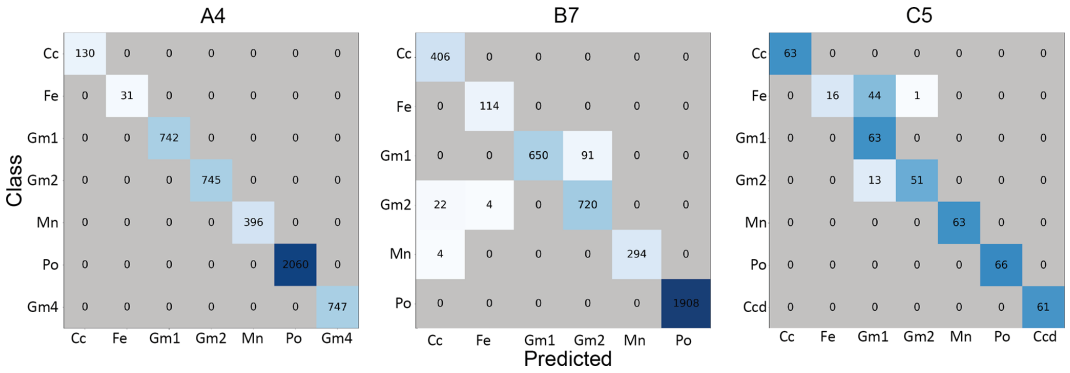

Figure 4.5: Confusion matrices for the classification examples of TS A4 with an overall accuracy of 100 %, B7 with an overall accuracy of 97 %, and C5 with an overall accuracy of 87 %.

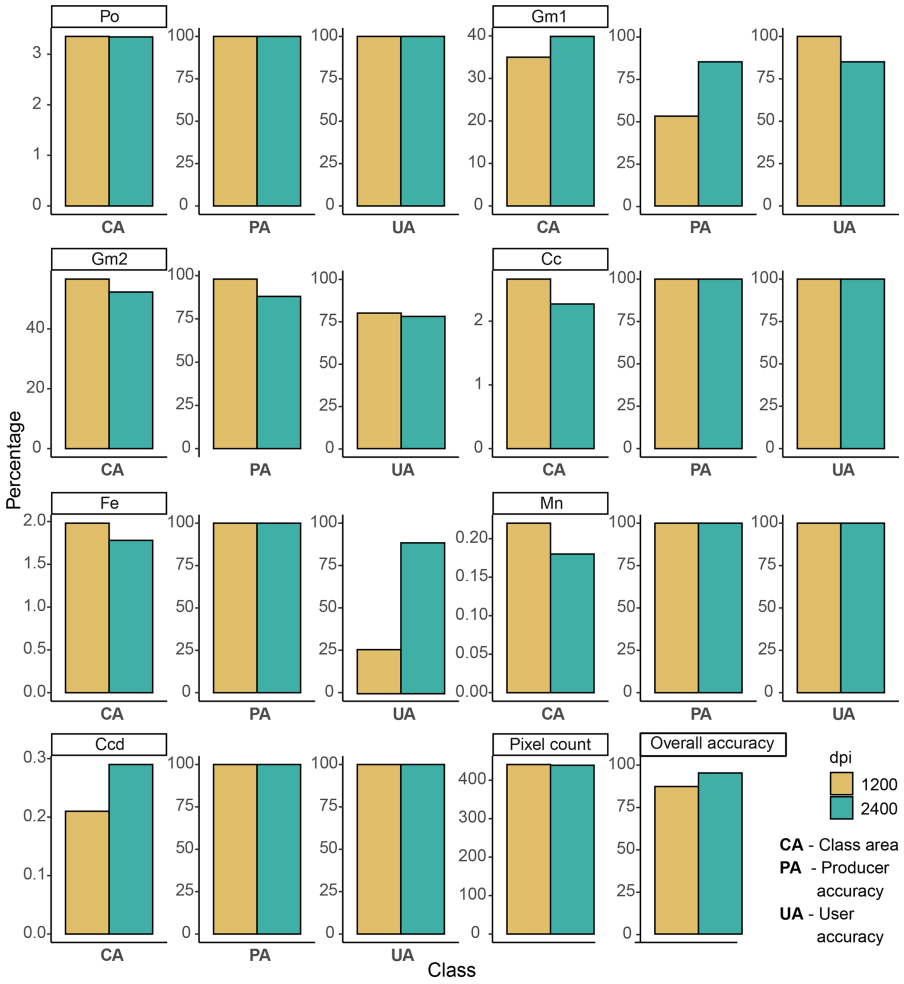

Figure 4.6: Comparison of classified area (CA) proportions and class accuracy parameter (overall, PA, and UA) for thin section (TS) C5, scanned with 1200 and 2400 dpi resolution (data: C.2).

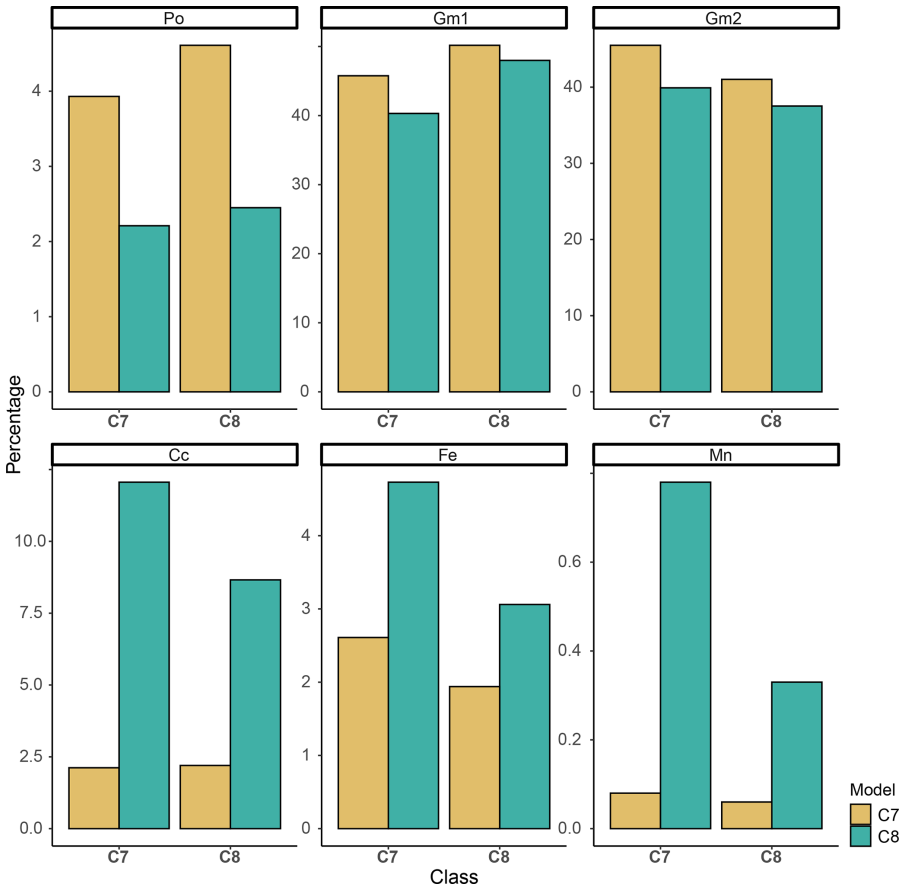

Figure 4.7: Comparison of class area proportions derived from results based on a classification model trained on the same thin section (TS) versus opposite TS. Note the various *y*-axis scale ranges to ensure the illustration of relative differences within the classes.

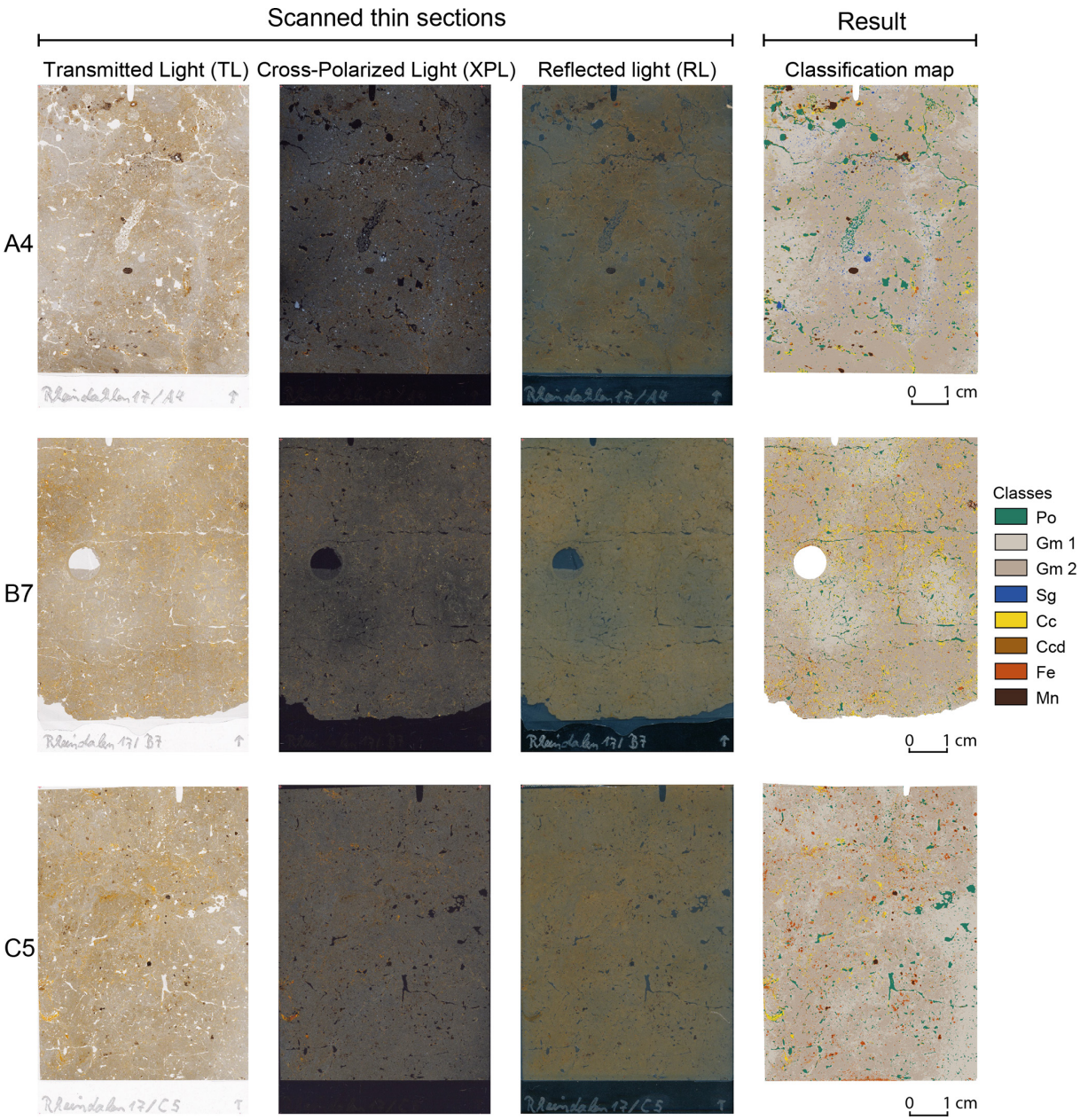

Figure 4.8: Input and output of the image classification of thin section (TS) A4, B7, and C5, which originate from Bt horizons of the Rheindahlen sequence. The classification maps on the right combine the multi-RGB information of the trnsmitted light (TL), cross-polarised light [XPL), and reflected light (RL) input images and visualise the spatial distribution patterns of the micromorphological features.

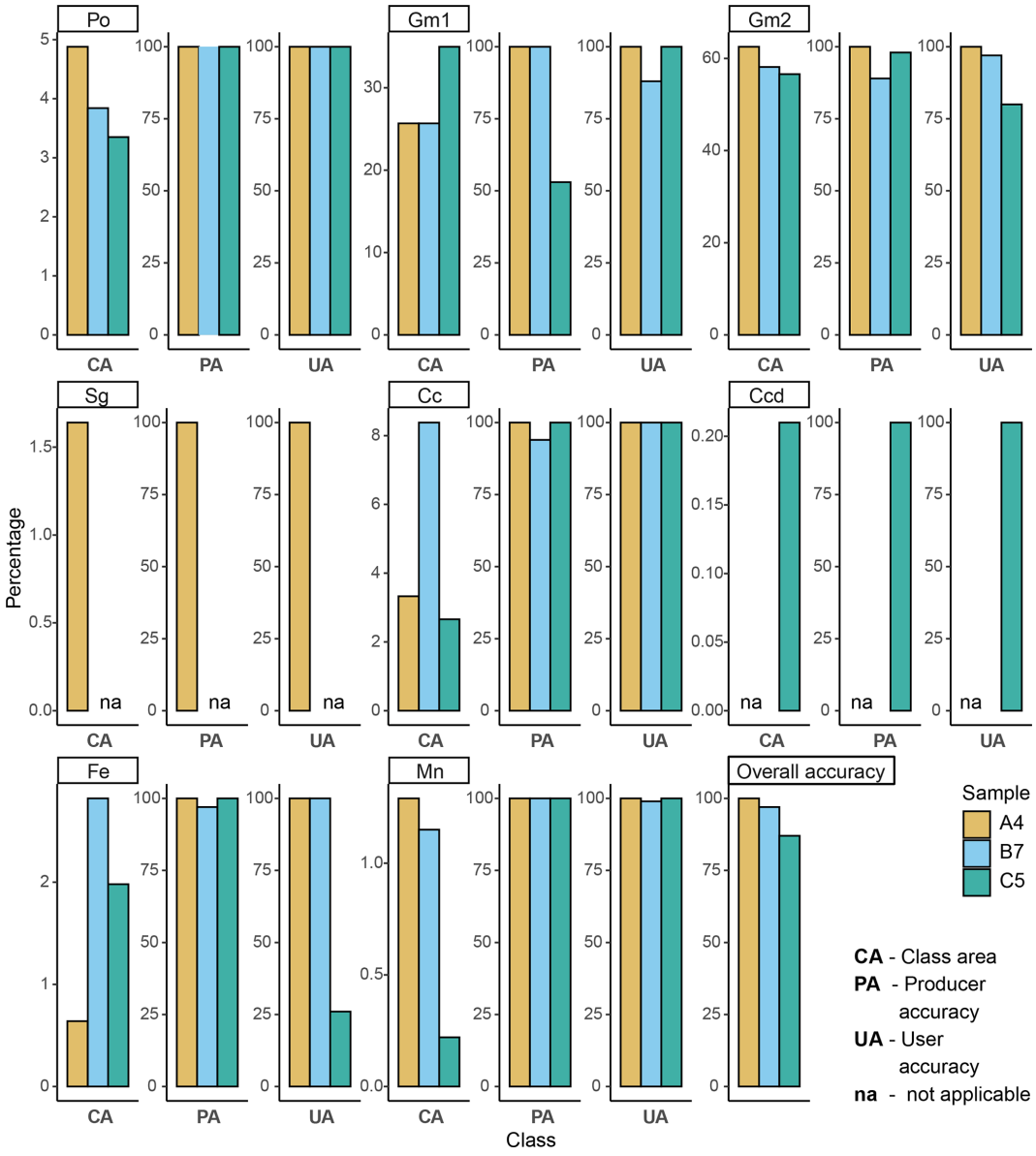

Figure 4.9: Results of the class-based area assessment for thin section A4, B7, and C5. Po: pore space; Gm1: Groundmass 1 (bleached); Gm2: Groundmass 2 (iron hydroxide abundance); Sg: medium and coarse sand and fine gravel; Cc: clay coatings; Ccd: dark clay coatings; Fe: iron hydroxide concretions; Mn: manganese oxide concretions; PA: producer's accuracy; UA: user's accuracy (data: Appendix C.2).

5

MICROMORPHOLOGY AND MICRO-XRF ANALYSIS OF BRONZE AGE HOUSE FLOORS FROM TELL TOBOLIU, ROMANIA

The author contributions are structured by categories, namely: Conceptualization and Methodology, Software and Data Curation, Formal analysis, Investigation, Visualization, Supervision, Project administration, Funding acquisition, Writing –Original Draft, and Writing – Review and Editing. The individual authors' contributions to each category are subsequently listed by their initials.

Conceptualization and Methodology: MZ and AR; Software and Data Curation: MZ and ML; Formal analysis: MZ, AR; Investigation: MZ, AR, ML; Visualization: MZ; Supervision: AR, SO, TR; Project administration and Funding acquisition: AR, TK, TR; Writing – Original Draft: MZ; Writing – Review and Editing: MZ, AR, SO, ML, TR.

Mirijam Zickel[2], Astrid Röpke[1], Stephan Opitz[2], Marian Lie[1], Tobias Kienlin[1], Tony Reimann[2]

Manuscript will be submitted to the Journal *Archaeological and Anthropological Sciences, Springer Nature*

1 Institute of Archaeology, Romanian Academy – Iași Branch

Abstract

The Bronze Age in the eastern Carpathian Basin (CB) was characterised by dense settlement, particularly evident in tell sites, though many have been eroded or altered by later activities, limiting the preservation of archaeological contexts. Among the notable sites is Toboliu in Romania, featuring multiple occupational phases which is among other things recorded in diverse house floor constructions. This study tests an innovative multi-method approach, integrating micromorphological thin-section analysis with Micro-XRF measurements and image analysis to characterise these constructions. High-resolution Micro-XRF point measurements were conducted to improve the micromorphological analysis of house floor microfacies and covering compositions. Simultaneously, mapping of entire thin sections provided information on elemental distributions, facilitating the analysis of spatial relationships among micromorphological phenomena. The findings show that floorings predominantly utilised processed loess-like materials from local deposits, with distinct geochemical signatures. Accordingly, different silty (non-covered) floors, plastered, and wood-covered floors could have been differentiated. This illustrates the significant variability of local construction types employed during the Bronze Age. The tested methodology enhances the understanding of prehistoric construction techniques and material sourcing, offering a reproducible framework for identifying archaeological features, particularly in less well-preserved contexts. The integration of imaging and geochemical analysis holds significant potential for future micromorphological studies of prehistoric settlements.

5.1 INTRODUCTION

House floor characteristics can reflect the relationship between floor types and the cultural, environmental, and material contexts of the respective societies. From the Neolithic to the Middle Ages, a wide range of floor types, from soil and sediment floorings (Macphail and Goldberg, 2018; Lisá et al., 2020; Cereda and Fragnoli, 2021; García-Suárez, 2024; Röpke, A., Kovacs, G., Petö, A., 2024, e.g), plastered floor coverings (Karkanas and Efstratiou, 2009; Friesem et al., 2017; Amadio, 2018), and tempered sediment floorings in Kovács et al. (2024), have been described. As mentioned by Love (2013a) and Love (2013b) and Cereda and Fragnoli (2021), understanding the composition and architectural building materials can provide insights into the construction techniques and cultural practices of past societies. Typically, soil and sediment micromorphology is a valuable tool to identify flooring characteristics (Macphail and Goldberg, 2018). This approach is, however, primarily qualitative, and its reliability is partly contingent on the quality of expert judgment. Micro X-ray fluorescence spectroscopy (Micro-XRF) analysis has the potential to further enhance this technique by offering non-destructive, semi-quantitative insights into the chemical composition of micromorphological features and MF, using the same sample object (thin section). This is essential for comprehending secondary processes in archaeological contexts, such as diagenesis and alteration, as highlighted by Mentzer (2017) and Thorne et al. (2009). Micromorphology combined with Micro-XRF mapping, has also been successfully applied to reconstruct the formation of archaeological deposits, such as hearths and those associated with animal herding (Polisca, 2025). Additionally, it may serve as a valuable tool for identifying and comparing materials and sediment compositions, including those utilised in prehistoric floorings. The archaeological site of Tell Toboliu in Romania (Bihor County) offers a multilayered Bronze Age settlement stratigraphy, providing a rich context to systematically explore the potential of the combined applications of Micromorphology and Micro-XRF analysis. Our primary aim is to assess the effectiveness of this integrated multi-method approach in analysing the material properties and construction techniques of floors within the tell sequence. Our research centres on the micromorphological and geochemical analysis of house floors across different stratigraphic phases of the Toboliu Tell site (Section 5.2), detailly described by (Lie, 2024). This dual approach entails a comprehensive micromorphological analysis of the flooring and covering compositions, emphasizing texture, composition, potential minerogenic and organic tempering, as well as post-depositional processes. This is complemented by Micro-XRF measurements conducted on the same TS, allowing for direct comparisons. Our objective is to identify chemical markers that characterise the flooring and covering construction materials and ascertain their

origins. Accordingly, this approach is being evaluated for its effectiveness in determining the composition of construction materials and identifying their potential sources. Within this context, we examine the construction technique, its spatial utilisation, and the developments or changes that occurred within the tell sequence in the context of archaeological findings. Semi-quantitative Micro-XRF analyses possibly provide an added value for classifying floor types, when combined with qualitative micromorphological data on structure and distribution. This integrated approach could provide more detail and therefore enhance our understanding of socio-cultural factors, including technical knowledge, the significance of flooring, individuality, and the evolution of construction styles over time. Furthermore, this approach has the potential to enhance the reproducibility of micromorphological analyses and establish stronger connections with off-site analysis results obtained through other methods, such as sediment corings.

5.2 SETTING

The site is located in western Romania, in Bihor county. It is situated in a flat landscape at the edge of the CB, characterised by loess derivates (i.e. clayey and sandy loess) and phaeozem soils formed in these deposits (Fig. 5.1a), in the vicinity of the Crișul Repede (HU: *Sebes-Körös*) river. For additional insights into regional landscape evolution (Zickel et al., sub.). The tell consists of a multi-phased Bronze Age settlement, characterised by a mound surrounded by ditches (Fig. 5.1b), with an outer settlement extending beyond (Lie et al., 2019). This structure reflects a probably complex social organisation and settlement pattern typical of the Bronze Age in the eastern CB (Fischl et al., 2015; Gogâltan, 2018; Duffy et al., 2019; Gogâltan et al., 2020; Kienlin, 2020; Găvan and Kienlin, 2021). The occupation last approximately between 3600 and 3880 BP (16th and 19th century Before Common Era (BCE), Lie et al., 2019). Since 2020, interdisciplinary investigations have aimed at reconstructing the settlement's internal organisation.

5.2.1 *Sample context*

Excavation Unit 1 has four profiles (approx. 4m in depth) showing several Bronze Age settlement phases (Lie, 2024). Three profiles were sampled for micromorphology, the western (Fig. 5.2a), northern (Fig. 5.2b), and eastern (Fig. 5.2c) section.

Six micromorphological samples were taken from floor layers across four settlement phases (Table 5.1):

1. Phase 7 represents the oldest house construction, dating back approximately 3560 ± 30 a BP, as determined by radiocarbon dating of a bone fragment. The structure features three compartments and includes two fire hearths or ovens, oriented in an East-West

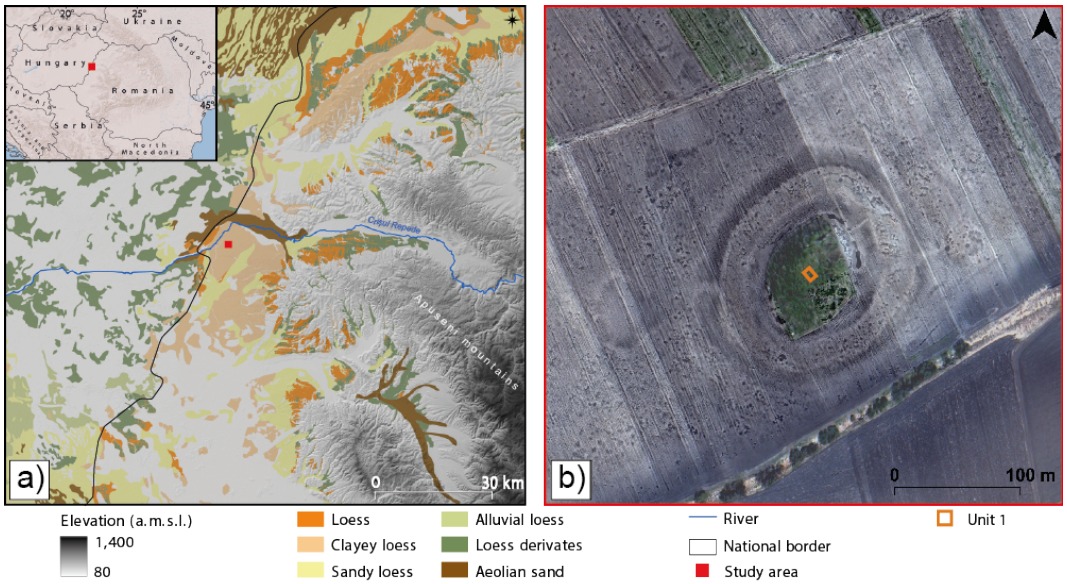

Figure 5.1: a) SRTM digital elevation model (DEM) (USGS - United States Geological Survey, 2009), Loess distribution (Lindner et al., 2017a), Rivers + lake centerlines (Natural-Earth, 2021), edited version of Zickel et al. (sub.) b) Worldview-3 scene from 2021-03-25, (DigitalGlobe, 2021) on magnetographic imagery (Kienlin, 2021) showing the position of excavation Unit 1.

direction. Micromorphological sample Tob.1 was taken from a floor context at the bottom of the tell sequence.

2. The house structure from Phase 5, dating less than 3560 and more 3440 (sandwich context dating) a BP, features a design with three compartments and two fire hearths. It is oriented in a North-South direction. Tob 12 was sampled from a (sub-) flooring context, covered by wooden planks.

3. Phase 4, characterised by a burned house structure, dates to approximately 3415 ± 35 a BP based on dating a seed from a burned cereal mass finding. The structure consists of a house with two compartments and a single fire hearth, oriented in a north-south direction. Tob. 21 (TS 21-1) and Tob. 16 (TS 16) were sampled from distinct flooring contexts and profiles (Fig. 5.2).

4. Phase 3 of the archaeological site reveals a house structure characterised by a wooden floor, dating approximately to 3440 ± 35 a BP. The structure consists of two compartments and features a single fire hearth. The orientation of the house is hypothesised to be North-South. The context is composed of a (sub-) flooring with a calcareous covering which can be found in the area of sample Tob.19 (northern section) only, on top of another wooden plank floor, which is also present in the area of Tob.5 (western section).

Table 5.1: Micromorphological sampling and archaeological context information for the sampled profiles (Fig. 5.2) of Unit 1 (excavation 2017). Dating is provided by uncalibrated radiocarbon ages.

Settlement phase	Context (№)	Sample (Tob)	Depth (∼cm)	Radiocarbon dating (sample)	Archaeological context	Excavated structures	House orientation
7	358, 373, 366	1	330	approx. 3560 ± 30 a BP (bone)	Oldest house structures	3 compartments, 2 fire hearth/oven	East-West
5	312	12	310	<3560/ >3440 a BP	House structures with wooden floor	1 compartment, 2 fire hearth	North-South
4	213, 227	21	240	approx. 3415 ± 35 a BP (plant seed)	Burned house structures	2 compartments, 1 fire hearth?	North-South
	209, 227	16	250				
3	173, 195, 196	5	225	approx. 3440 ± 35 a BP (bone)	House structures with wooden floor	2 compartments, 1 fire hearth	North-South?
	147, 130	19	200				

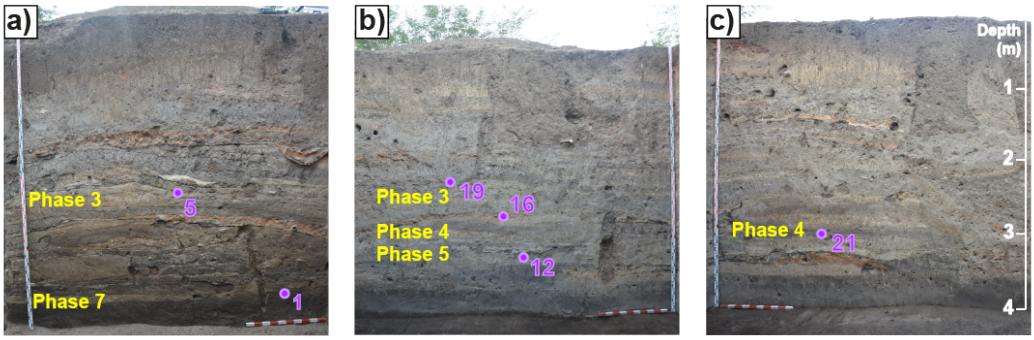

Figure 5.2: Sampled excavation profiles of Unit 1, excavated in the year 2017, and location of the settlement phases: a) western, b) northern, and c) eastern section. The purple dots indicate micromorphological sample positions.

5.3 METHODS

5.3.1 *Micromorphological analysis*

The TSs were prepared from the above-mentioned floors, sampled from different profiles of Unit 1 (previous Section 5.2). High-quality, uncovered TSs measuring 60 mm × 80 mm and 25 µm in thickness were produced by Thomas Beckmann (Schwülper-Lagesbüttel, Germany). This process involved impregnating air-dried sediment blocks with polyester resin under vacuum, allowing for hardening over several weeks, followed by cutting, grinding, and polishing, as detailed in Beckmann (1997). Conventional micromorphological analysis was performed using a polarisation microscope at magnifications of 25×, 100×, 200×, and 400×, employing various illumination techniques: PPL, XPL, and OIL. The micromorphological description is mainly based on terminology established by Stoops (2020) and Nicosia and Stoops (2017). The description of phytoliths in TS is based on the International Code for Phytolith Nomenclature 2.0. (International Committee for Phytolith Taxonomy (ICPT), 2019). The micromorphological description was enhanced by a novel system established by Zickel et al., 2024, which utilises machine learning for the classification of TS scans (PPL, XPL, OIL). The resulting classification maps illustrate the spatial relationships of micromorphological phenomena and microfacies effectively.

5.3.2 *Micro-XRF analysis*

The elemental composition mapping and high-resolution point measurements of each sample, including Al, Ca, Fe, K, Mn, P, S, and Si, were determined using Micro Energy Dispersive X-ray Fluorescence analysis (Micro-EDXRF or Micro-XRF) at the Geo Lab of the Institute for

Geography (University of Cologne). These selected elements are prevalent in mineralogical contexts and are typically found in archaeosediments. Micro-XRF analyses was conducted on polished (uncovered) thin sections with a Bruker M4 Tornado system, equipped with a micro-focused Rh anode (50 kV, 600 µA) and a polycapillary optic (20 µm spot size). The system is equipped with two silicon drift detectors (2-SDD) and element spectra were acquired under vacuum conditions (20 mbar) at 50 kV and 300 µA. To ensure high resolution element mapping the TS were fully mapped at a resolution of 40 µm, resulting in ∼2,500,000 measurement points for sections measuring approximately 50x80 mm (sample area). With a measurement time of 15 ms per point, the entire mapping process could be completed in approximately 11 hours for one TS. We designed a custom sample holder using a Creality Ender 5S 3D printer to maintain a minimum distance of 1 cm from the measurement table. This setup minimises distortion from the semi-permeable (TS) glass slide, which could otherwise affect the X-ray beam target and introduce platform artifacts to the results. The imagery post-processing, which included the generation of element ratio maps to analyse the spatial distribution of element concentrations, was conducted using QGIS 3.38 open-source software. The workflow primarily adhered to the initial step (MiGIS 1 tool) outlined in Zickel et al. (2024). The process involves creating a multiband raster dataset to manually select two to three element maps to display (spatial) element ratios in in RGB mode. For the high-resolution Micro-XRF point measurements (20 µm spot size, , 5 s measurement time), we manually selected two AOIs of the groundmass for each microfacies, ensuring they are representative of the respective microfacies while excluding secondary features (e.g., pedo-features). This also indicates that calcitic concretions (natural or intentionally added) were excluded from microfacies measurement to prevent an over-representation of calcium in the records. Here, we refer to the micromorphological analyses. Each AOI measured approximately 800 x 800 µm and contained a density of 95 to 114 measurement points. To prevent artefacts, we measured (run) two AOIs per microfacies. The collected data was analysed and visualized using the open-source software R and its integrated development environment, RStudio (R Core Team, 2023). This process involved standard scaling, normalization, and PCA. To illustrate the results, we select various element pairings that effectively represent the target microfacies.Si serves as a reliable marker to indicate the relative enrichment of other elements, including Al, Ca, P and Fe. Al can be utilised to demonstrate increased clay content, while Ca aids in identifying carbonates within microfacies. Likewise, Ca, P is frequently enriched in organic materials, and all play a role in the mineralisation process of organic matter (Murphy, 2014; Sidoti et al., 2023).

5.4 RESULTS

5.4.1 *Micromorphology*

The selected TSs (Fig. 5.2, Table 5.1) showcasing house floor layers exemplify well-defined architectural constructions, which facilitate comparative analysis. A thorough micromorphological examination of the TSs suggests significant differences among the various units, as detailed in tabular form in Appendices A-F. The samples are arranged in stratigraphic order, beginning with the lowest layers. Capital letters denote the identified microfacies (Fig. 5.3), high resolution figures with corresponding boundaries on scanned TS and a classification map illustrating the micromorphological findings can also be found in the corresponding Appendix chapter (Appendix D.1- D.6) for each thin section.

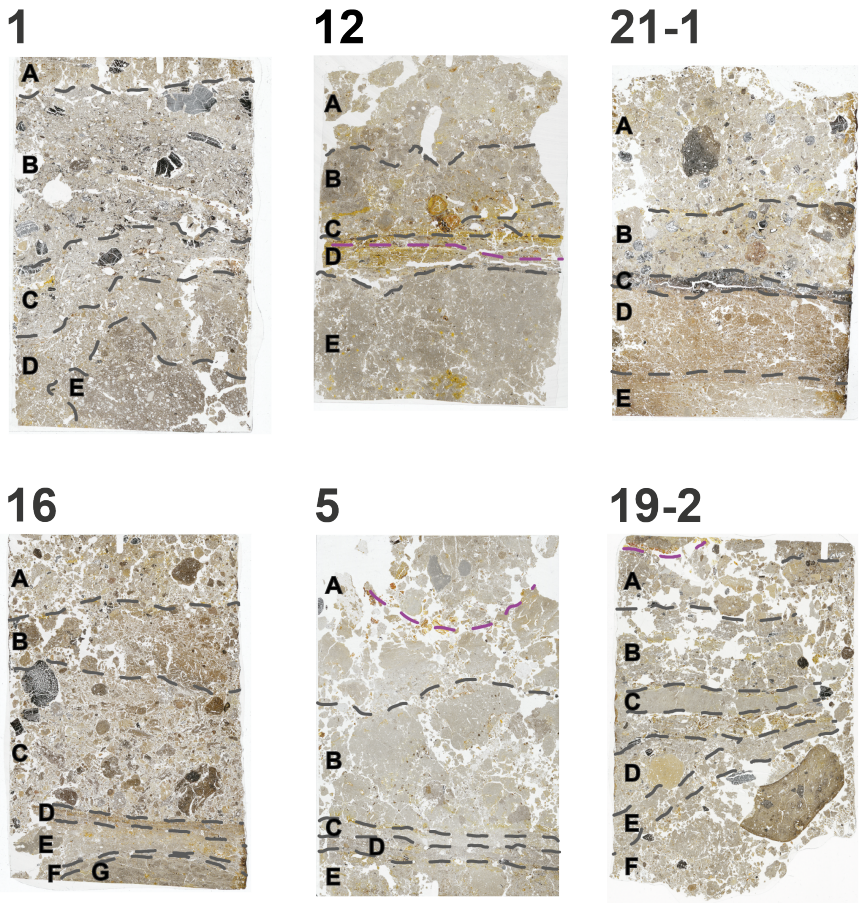

Figure 5.3: Selected thin sections (TS) from the Tell Toboliu stratigraphy. Determined microfacies are labelled with capital letters. Grey lines show microfacies borders and violet lines mark wood fragments.

Thin Section 1

TS 1 (Section D.1) encompasses the first house construction Phase 7. The description focuses on the flooring MF D interrupted by the humic material MF E (Fig. 5.4c/d). The intact parts of the flooring (MF D) are compact and composed of silt including some calcitic fragments (Fig. 5.4a/b) and some accidental intrusion such as macro- and micro plant coal, phytoliths, bone fragments (Fig. 5.4f). Occasionally, secondary calcite coatings and iron nodules are present. The brownish coloured MF E (Fig. 5.3) consists of a coarser texture (sandy silt) and a groundmass enriched in organic matter forming an undifferentiated b fabric (Fig. 5.4c/d). Articulated phytoliths embedded in the organic material (Fig. 5.4e). The presence of charcoal and plant coal fragments point to human disturbance.

Thin Section 12

A compact pure clayey silty floor was built (MF D) with very few accidental intrusions (microscopic plant coal) can be found at the bottom of TS 12 (Appendix D.2). The elevated clay content is shown by a parallel striated and granostriated b-fabric (Fig. 5.5a/b). Iron nodules and secondary phosphate impregnation as well as some multilaminated clay coatings are present (Fig. 5.5c/d). On top of it a use layer (MF C) of fine domestic waste with mostly horizontally orientated macro- and micro plant coal, few bone fragments, phytoliths (some ELONGATE DENDRITIC) and ash has been formed (Fig. 5.5e/f). Within this layer (MF C) wood fragments of whitish-beige appearance (PPL) have been preserved (Fig. 5.5c/d), and articulated cells remain visible (Fig. 5.5g/h). In this case it is not so clear if the clayey silt and the wood formed a constructed unit.

Thin Section 21-1

The lower plant tempered floor (MF E) consists of clayey silt. The b-fabric is complex with a parallel and granostriated b-fabric representing the clay, but also partly calcitic crystallitic and micaceous crystallitic b-fabric occur (Section D.3). It is tempered with cereal-related chaff evidenced by articulated phytoliths (ELONGATE DENTRITIC, ELONGATE DENTATE) in pseudomorphic voids, many of them are oriented horizontally caused by floor making processes (Fig. 5.6a/b). The texture of the following plant tempered floor (MF D) has a distinctly higher clay content and is also tempered with cereal-related chaff created in the same manner as the floor below (Fig. 5.6c/d). The remnants of cereal-related chaff are articulated phytoliths (Fig. 5.6h). The clay content is shown by a mostly parallel striated b-fabric (Fig. 5.6e/f). Higher amounts of mica partly cause a micaceous b-fabric. Rounded clayey aggregates (cf) (Fig. 5.6c/d) as well as calcitic fragments are included (Fig. 5.6g).

Thin Section 16

At the bottom of TS 16 two floor layers, separated by a use layer, are evident (Section D.4). The lower floor (MF G) is composed of a mix of clayey silt (S) and humic (clayey) silty patches (H) (Fig. 5.7a/b), both are partly calcareous. The clay content is shown by a parallel striated b-fabric. Especially, the humic material includes micro plant coal. The use layer (MF F) was sealed by a differently created highly calcareous silty floor with plant temper (MF E) (Fig. 5.7c/d). In most cases the phytoliths of the former plant temper has been dissolved (Fig. 5.7e). Secondary pedofeatures such as iron, calcite and phosphate coatings and impregnations are present in all units.

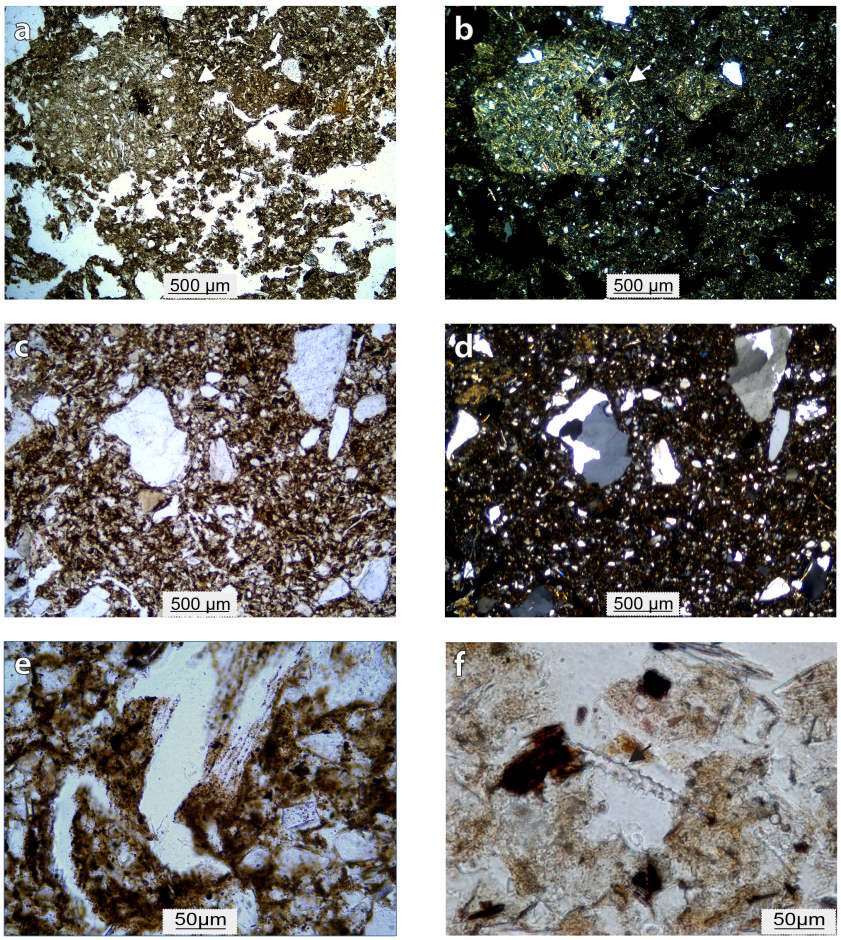

Figure 5.4: Micrographs of TS 1: a) overview of silty sediment of MF 1D, with calcitic silt-sized quartz fragments (arrow) and mica in PPL, b) the same in XPL; c) overview of organic silty material MF 1E with an open porphyric c/f related distribution pattern, coarse fraction sand-sized quartz; d) the same in XPL; g) articulated phytoliths (ELONGATES ENTIRE) in pseudomorphic in MF 1E in PPL h) fine domestic waste within the silty material of MF 1D, isolated ELONGATE DENTATE (white arrow) in PPL.

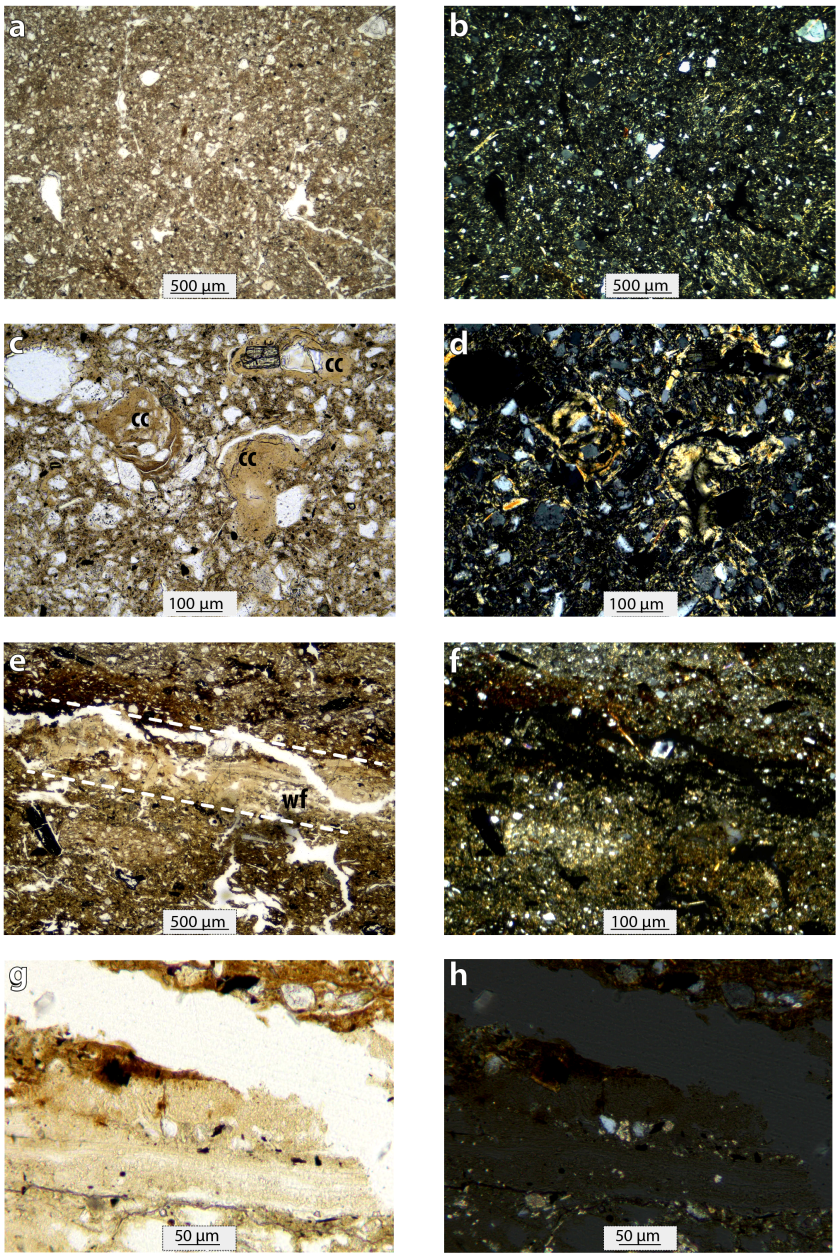

Figure 5.5: Micrographs of TS 12: a) overview of the clayey silt floor (MF 12D) composed of a double spaced porphyric c/f related distribution with a dominant silt-sized coarse fraction and a mostly parallel striated b-fabric in PPL, b) the same in XPL; c) multilaminated limpid clay coatings (cc) in PPL, d) the same in XPL; e) mineralised wood fragments (wf, within dotted white lines) located in a fine use layer in PPL, h) same in XPL; e) detail of the mineralised wood fragment with cell structure, the same in XPL.

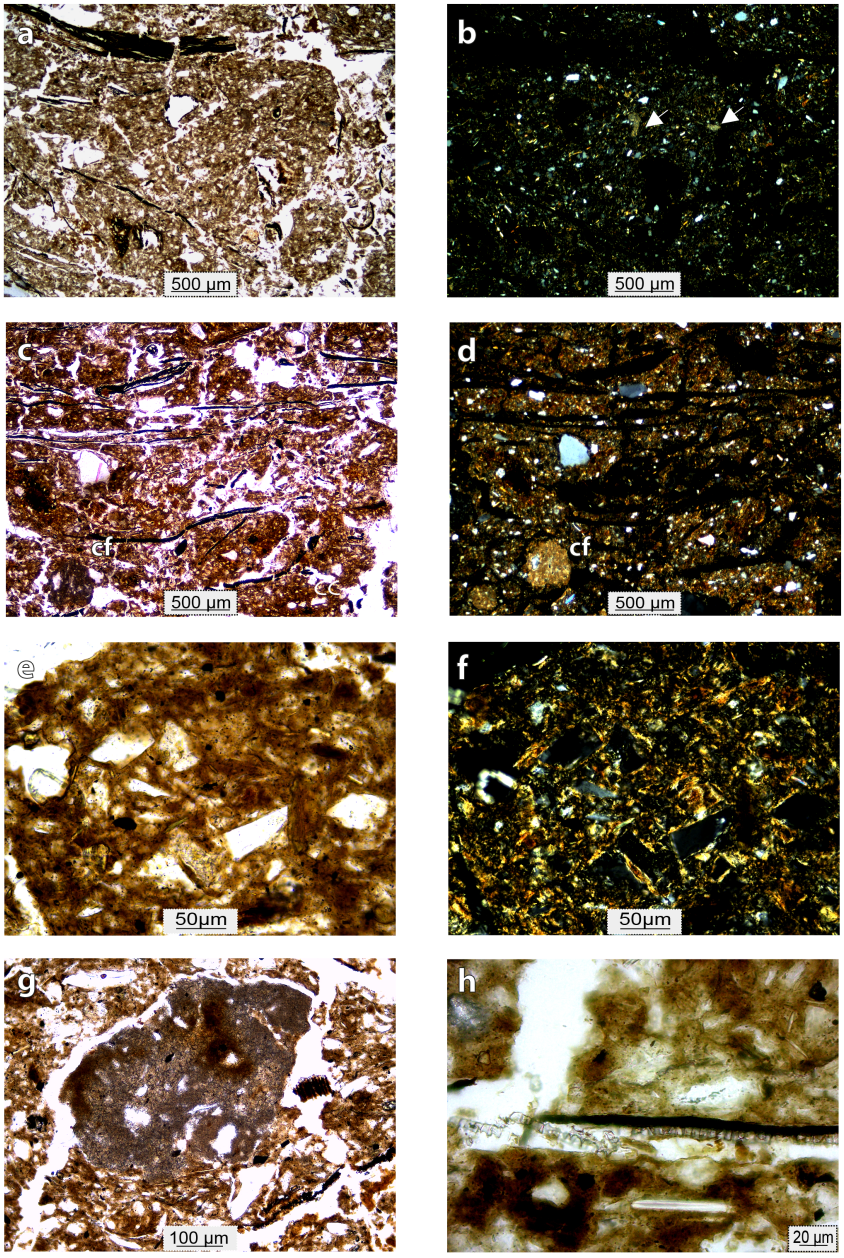

Figure 5.6: Micrographs of TS 21-1: a) overview of MF 21-1E clayey silt floor with horizontally orientated plant temper (cereal chaff) and calcitic fragments (white arrows) in PPL, b) same in XPL; c) overview of MF 21-1D strongly clayey silt floor with horizontally orientated plant temper (cereal chaff) and calcitic fragments (cf) in PPL, d) same in XPL; e) strongly clayey silt of MF 21-1D in PPL f) causing a parallel and granostriated b-fabric in XPL, g) calcitic fragments in MF 21-1D in PPL; h) plant temper of MF 21-1D articulated ELONGATES DENTATE in PPL.

Thin Section 5

The sequence of TS 5 is not intact (Section D.5) because the sample disintegrated into smaller fragments during transport. The floor sequence (MFA/E) begins with MF E at the bottom consisting of clayey silt with a parallel and cross striated b-fabric. Calcitic fragments are present and in certain parts domestic waste has been in-cooperated accidentally. Secondary phosphate, iron and some calcite coatings are evidenced. A use layer developed with a secondary gypsum formation on top. The next flooring (MF C) is disintegrated into smaller fragments and in between domestic waste found its way along cracks after the sampling. Looking at intact parts of MF B, it resembles the clayey silt floor with a higher amount of calcite (calcitic fragments, calcitic areas and secondary calcite coatings) (Fig. 5.7g/h). Mineralised wood fragments with cell structure in MF A (Fig. 5.7f) are scattered disorderly above a subfloor (MF A). It seems very likely that the silty floor (MF B) and the wood formed a floor unit.

Thin Section 19-2

TS 19-2 (Section D.6) comprises two covers (MF C and E) of interest and remnants of a wooden floor (MF 19-2A). MF E is a silty cover laid on a debris of domestic waste (MF F) including a pottery sherd. It is composed of clayey silt with a parallel striated b-fabric. Some calcitic areas are present and charcoal fragments are included accidentally (Fig. 5.8a/b). On top of, it a use layer (MF D) formed which was sealed by the dense calcareous silt cover MF 19-2C (Fig. 5.8c/d). The b-fabric is speckled b-fabric and calcitic-crystallitic and due to increased calcium carbonate content. The c/f ratio is double spaced porphyric with some sand sized quartz and silt sized quartz and mica as coarse fraction. The material is fairly pure, with no accidental intrusions. Few secondary calcite coatings and iron concretions are evident. Remains of a wooden floor (MF A) with similar features as described for MF A in TS 5 are present at the very upper edge.

5.4.2 *Micro-XRF measurements of selected microfacies*

Based on the micromorphological analysis (Section 5.4.1, Table 5.2), we selected AOIs for high resolution point measurement using Micro-XRF (Section 5.3.2) to determine the elemental compositions of various flooring and covering microfacies (Table 5.3). Fig. 5.9 presents a selection of element ratio maps (Section 5.3.2) and illustrates the positions of AOIs for each microfacies across the different TS. Single measurement results (scatter plots) are provided in Appendix D.7. Detailed bi-plots for each selected TS can be found in Appendix D.8 (Fig. D.8 to D.13).

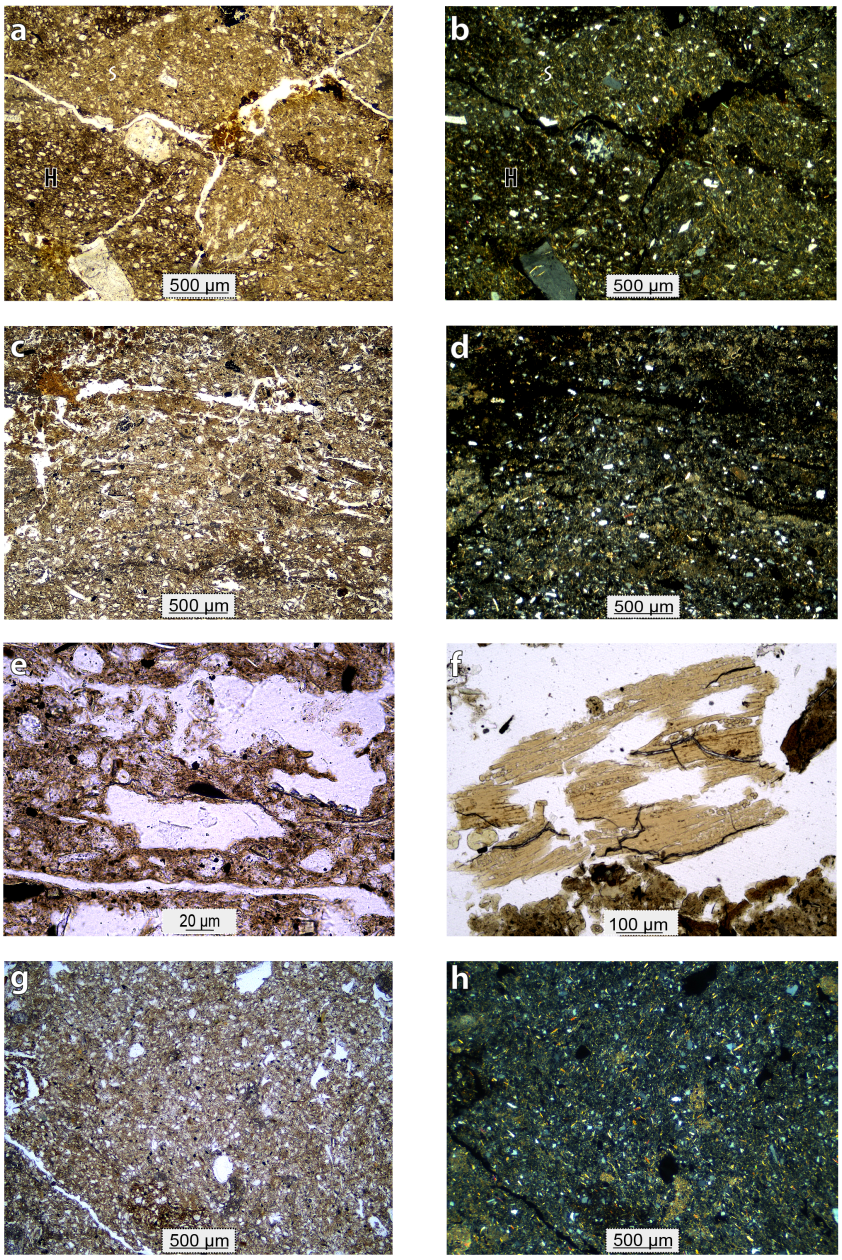

Figure 5.7: Micrographs of TS 16 and TS 5: TS 16 a) overview of MF 16G humic silty patches (H) mixed with clayey silt sediment (S) in PPL, b) same in XPL; c) overview impure calcareous silty sediment (MF 16E), partly layered with horizontally aligned pseudomorphic voids in PPL, d) the same in XPL; e) pseudomorphic voids derived from decayed plant material. TS5 f) mineralised wood fragment with former cell structure (MF 5A) in PPL; g) overview of a calcareous clayey silt floor (MF 5B) in PPL, h) the same in XPL.

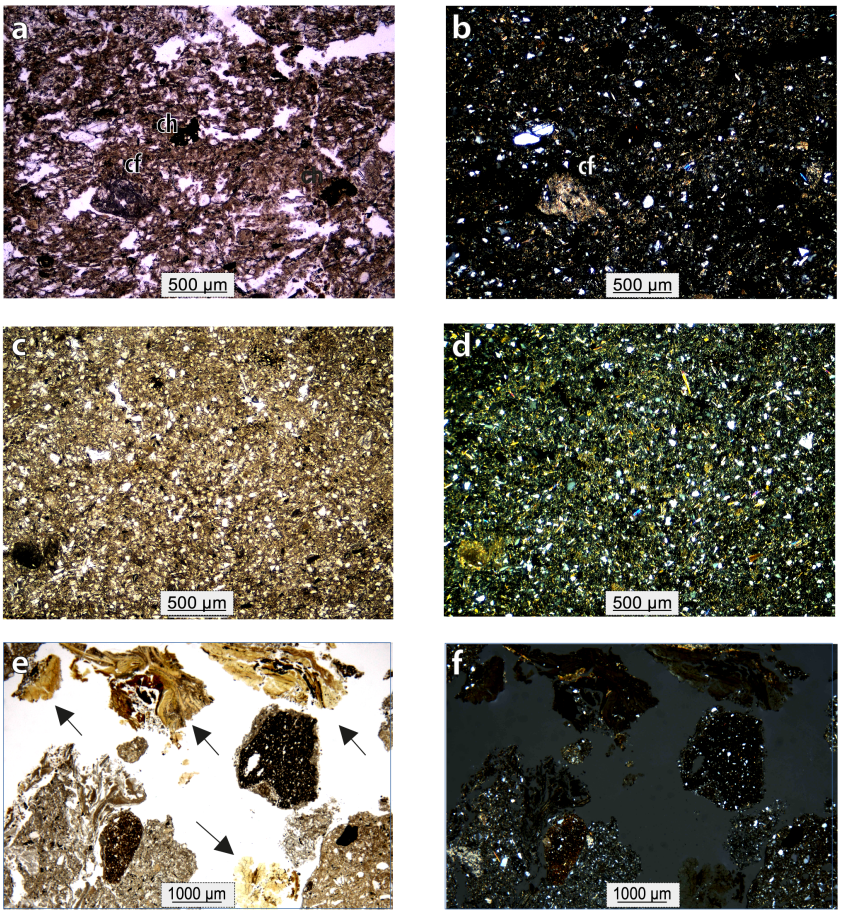

Figure 5.8: Micrographs of TS 19-2: a) overview of MF 19-2E an impure clayey silt cover with micro charcoal (ch) and a calcitic fragments (cf) in PPL, b) the same in XPL; c) overview of a pure calcareous silt cover (MF 19-2C) with d) a calcitic-crystallitic b-fabric in XPL; e) mineralised wood fragments of different colour (white arrows) in A in PPL, f) the same in XPL.

Table 5.2: Overview for the micromorphological results of the selected samples.

Sample	Profile/Phase	Floor type	Additions
1	West/7	E: Krotovina (Phaeozem material, sandy silt) D: Impure silt floor/platform (calcitic)	-
12	North/5	D: remnants of heavily degraded wooden floor E: clayey silt floor/platform	-
21	East/4	D: plant tempered floor, strongly clayey silt E: plant tempered floor, clayey silt	Cereal chaff, calcitic fragments
16	North/4	E: highly calcareous silty floor with plant temper G: mottled floor, clayey silt and humic (clayey) silty patches (calcitic)	Cereal chaff, calcitic fragments
5	West/3	B: Wooden floor A/C/E: impure clayey silt floor (calcitic)	-
19	North/3	A: Wooden floor C: reflooring/plaster (calcitic) E: remnants of a silty cover (calcitic)	-

Table 5.3: Micro-XRF classes based on the selected microfacies.

Class	Thin section (TS)	Microfacies	Settlement phase	Micromorphological description
1E	1	E	7	Sandy silt
12E	12	E	5	Clayey silt
12D	12	D	5	Light wood fragments
21-1D	21-1	E	4	Slilt
21-1E	21-1	D	4	Clayey silt (reddish)
16G-1	16	G	4	Silt
16G-2	16	G	4	Organic silt (dark)
19-2C	19-2	C	3	Calcareous silt cover
5A-1	5	A	3	Light wood fragments
5A-2	5	A	3	Dark wood fragments
19-2A-1	19-2	A	3	Light wood fragments
19-2A-2	19-2	A	3	Dark wood fragments

Sediment floorings and calcareous covering

Based on the mean values of the high resolution Micro-XRF point measurements (Fig. 5.10) within AOIs in Microfacies 1E, the Si-Ca relationship shows comparatively high levels of Si and comparatively low Ca scores. This observation is characterised by moderate scatter and close correspondence between measurement runs. The Si-Al relation indicates a relatively low Al concentration (Fig. 5.10). For P-Ca, very low P values are observed, while Ca remains consistent with low variability. The K-Al relationship also reflects comparatively low K and Al content, with the two measurements runs closely aligned. In MF 12E, the two runs demonstrate close agreement in mean values for all element pairs (Fig. 5.10). The Si-Ca relationship remains fairly stable, with increased Si and very low Ca levels and narrow scatter ranges. The Si-Al pairing features increased Al content with high Si and comparatively tight scatter. P is low to moderate, while Ca stays in the mid-range with small variability in the P-Ca relationship and low scatter. The K-Al pairing shows moderate K levels and increased Al values, with wider scatter. In MF 21-1D, Si is stable at mid-range level, while Ca levels are relatively low, however minimal scatter in the Si-Ca relationship can be observed. The Si-Al pairing features increased Al and moderate Si values, with consistent runs. P remains very low. Both, P and Ca show very small scatter (Fig. 5.10). The K-Alrelationship shows relatively high K and high Al, with agreeing runs. MF 21-1E exhibits moderate Si levels, with increased Ca and low scatter in the Si-Ca relationship (Fig. 5.10). The Si-Al pairing shows mid-range to low Al and steady Si, with modest scatter. P values are increased, showing some scattering (Section D.7) and Ca is comparatively increased in the P-Ca relationship. The K-Al relationship indicates relatively low K and midrange Al levels, with some Al induced difference between the runs. In MF 16G-1, Si levels are stable, while scattering is observed for the slightly increased Ca levels, also between both measurement runs. The Si-Al relationship maintains mid-range Si and Al, with some scatter spread (Fig. 5.10). Also, P remains low, and Ca shows moderate variability in the P-Ca pairing. The K-Al relationship indicates comparatively moderate K and slightly increased Al levels, and consistent results for both runs. MF 16G-2 presents runs that cluster around similar mid-range Si and Ca levels, with low scatter ranges (Section D.7) in the Si-Ca relationship. The Si-Al pairing shows slightly elevated Al with moderate Si and a tighter scatter (Fig. 5.10). P values are low, but with a comparatively wide scatter. Ca is slightly increased with minimal scatter in the P-Ca relationship. The K-Al pairing reflects moderate K and Al values, the results were consistent across both runs. MF 19-2C reveals low Si and very high Ca levels, with runs overlapping well and modest scatter in the Si-Ca relationship (Fig. 5.10). The Si-Al pairing shows very low Al and a high Si induced scatter. P is very high, alike Ca, with modest spread in the P but increased scattering induced by Ca (Section D.7).

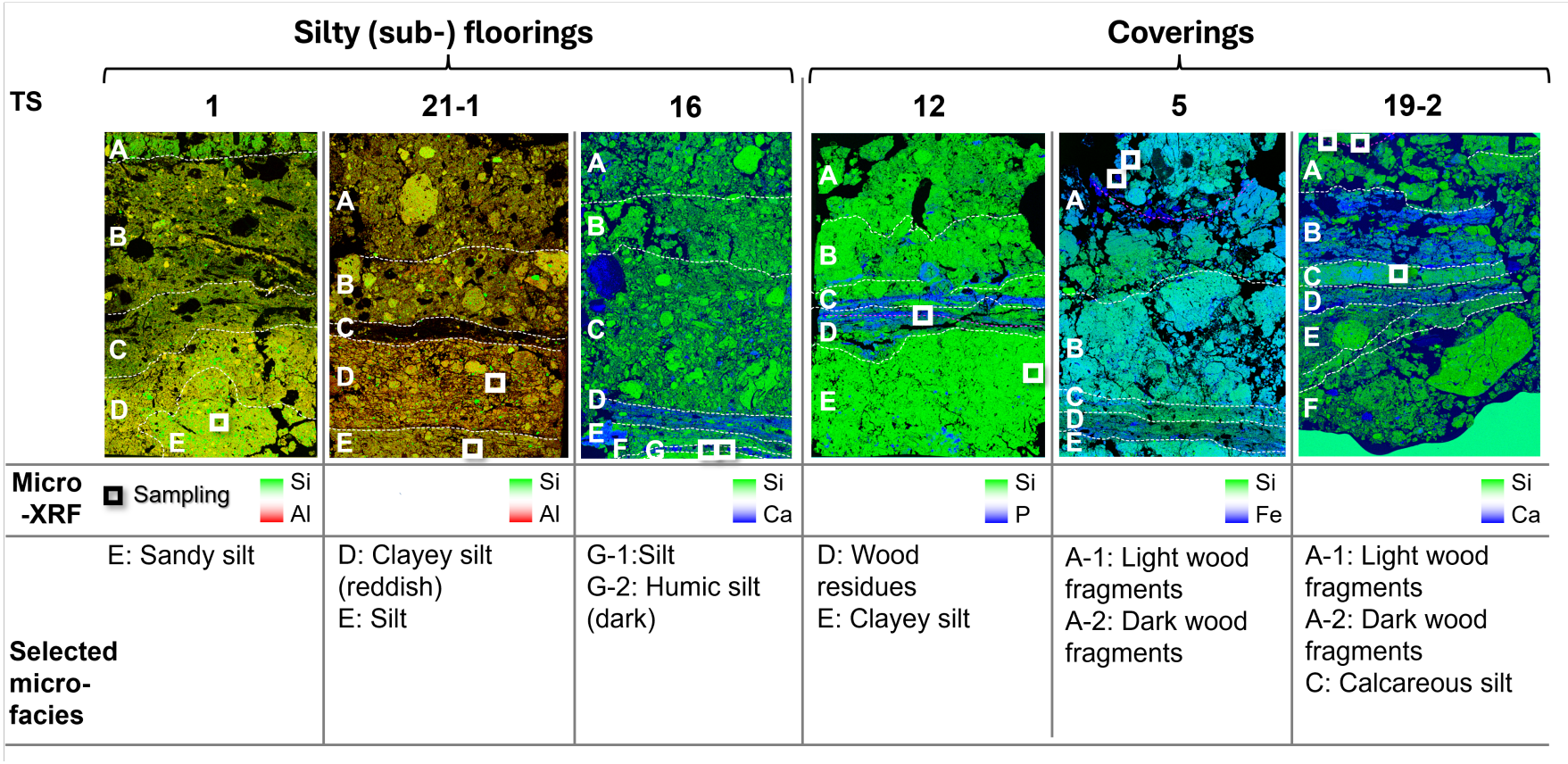

Figure 5.9: Elemental mappings sourced from Micro-XRF of all thin sections (TS)s, post processed as described in Section. 5.3.2 Capital letters label the determined microfacies (Table 5.3), white squares indicate the centre points of measured AOIs for each microfacies.

The K-Al relationship indicates very low K levels in comparison to Al, with modest scatter. The point measurements of 21-1E and 1E (Table 5.3) exhibit greater variability in Si and Al, with 1E displaying higher Si levels (Fig. 5.9). Both have low Ca scores (Fig. 5.10). The microfacies 1E, 21-1E, 16G-1, 16-G2, and 12E show a similar pattern with relatively balanced scores. They are characterised by comparatively high Ca and Si values alongside reduced Al scores, especially in 1E. Low Ca and high Al scores can be observed in 21-1D. In these terms 21-1E, 16G-1, 16-G2, and 12E occupy an intermediate composition between 21-1D and 1E. 19-2C contains elevated Ca levels and comparatively high P scores which separate them from the other microfacies (1E, 21-1E, 16G-1, 16-G2, and 12E). The PCA reduces the complex chemical data of the Micro-XRF point measurements into two principal components (PC1=77 % and PC2=19 %), capturing 96 % of total variance in the data set and reflects compositional differences (Fig. 5.11). Here 21-1E and 1E cluster separately due to varying Si, Al, and K contents. 19-2C appears distinctly separated due to high Ca and low Si/Al. Moreover, the microfacies 12D, 5A-1, 5A-2, 19-2A-1, 19-2A-2 measurements are clearly different from the silt/plaster microfacies, due to elevated P and partly high Fe (19-2A-2, 5A-2) and Ca (12D, 19-2A-1, 5A-1) signals.

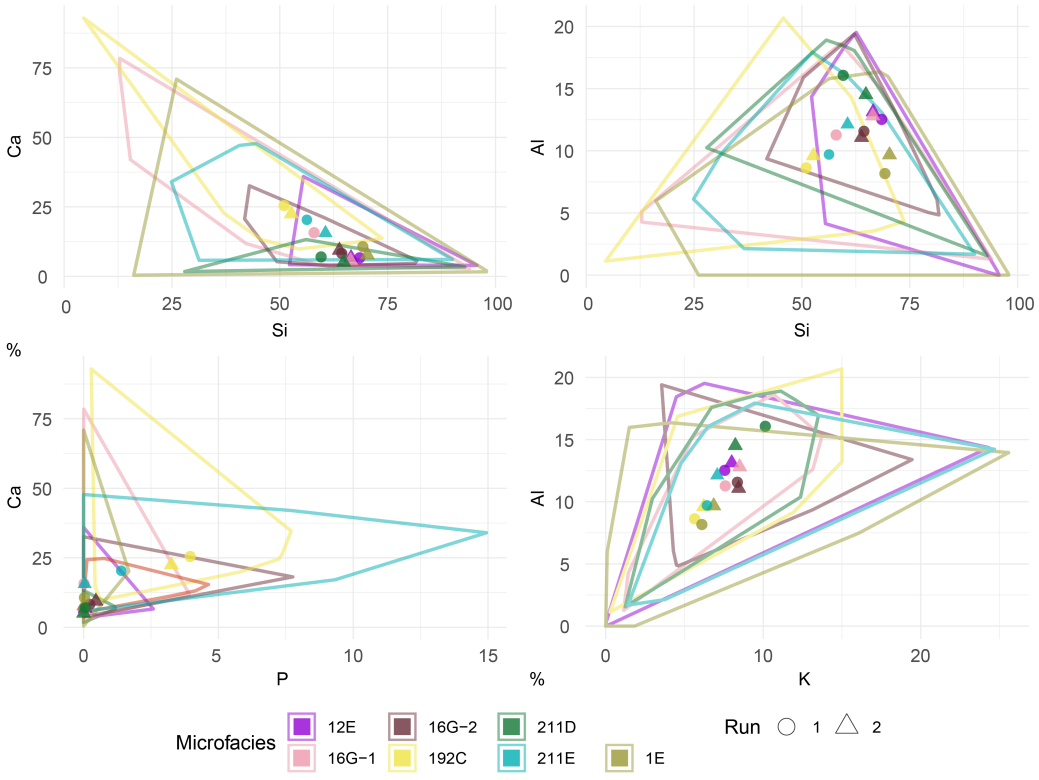

Figure 5.10: Mean (dots) and scatter (polygon area) of Micro-XRF element point measurements per sediment flooring microfacies.

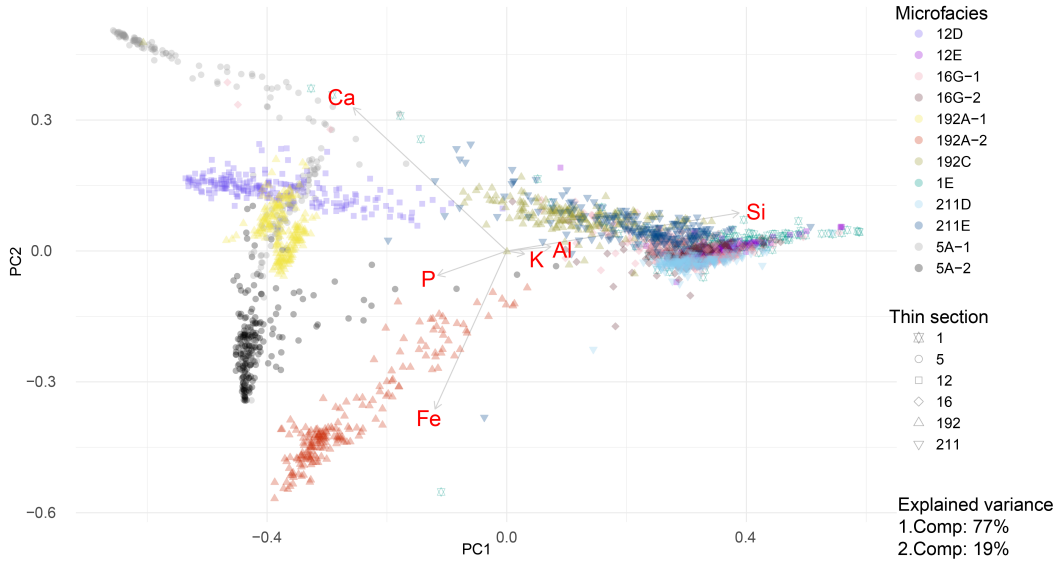

Figure 5.11: Results of a principal component analysis (PCA), based on Micro-XRF element point measurements.

Wooden floor coverings

In Microfacies 12D, the Ca-Fe relationship shows both elements at moderate levels (Fig. 5.12), with moderate scatter (Ca-driven), compared to the other MFs. The P-Fe pairing maintains stable for both P and Fe, exhibiting moderate scatter that is slightly elongated along the Fe axis. In the P-Ca relationship, P values range from low to moderate, while Ca remains moderate, with scatter slightly tighter than that observed in the Ca-Fe pairing. In Microfacies 5A-1, moderate Ca levels are observed, while Fe shows slight variability, resulting in moderate scatter with a gentle spread along the Fe axis in the Ca-Fe relationship (Fig. 5.12). The P-Fe pairing indicates low P and moderate Fe, with small scatter. In the P-Ca relationship, P is low, Ca is stable, and the scatter is narrow and consistent. Microfacies 5A-2 exhibits both elements at comparatively moderate levels in the Ca-Fe relationship, although the scatter is slightly more elongated along the Ca axis (Fig. 5.12). The P-Fe pairing shows P values that are low to moderate, with stable Fe and minimal scatter. In the P-Ca relationship, P remains low, Ca is moderate, and the scatter is very tight, indicating stable measurement runs. In Microfacies 19-2A-1, moderate levels of Ca are noted, while Fe is moderate to slightly higher (Fig. 9), with relatively tight scatter in the Ca-Fe relationship. The P-Fe pairing shows P values that are low to moderate, with steady Fe and small scatter. In the P-Ca relationship, P is moderate, Ca is steady, and the scatter is minimal, indicating consistent results between measurements. Finally, Microfacies 19-2A-2 presents moderate levels of both Ca and Fe, with narrow scatter that is balanced along both axes in the Ca-Fe relationship (Fig. 5.12). The P-Fe pairing shows moderate P and consistent Fe, with tight scatter.

In the P-Ca relationship, P values are low to moderate, while Ca remains stable, with narrow scatter. Similar to 19-2C, the PCA results show a clear separation of the MF measurement results in microfacies 12D, 19-2A-1, 19-2A-2, 5A-1 and 5A-2 compared to the previously described sediment flooring microfacies (Fig. 5.11). Most of the microfacies show high P scores, with Fe scores differentiating 19-2A-2, and 5A-2 (dark wood fragments) from 12D, 19-2A-1, and 5A-1 (light wood fragments). The dark wood residue microfacies are consistently higher in Fe (Fig. 5.12). Wider spread in plots, especially P vs. Fe, the wood residue microfacies show lower elemental concentrations in general, with tighter clusters in all three plots and high Ca and P scores.

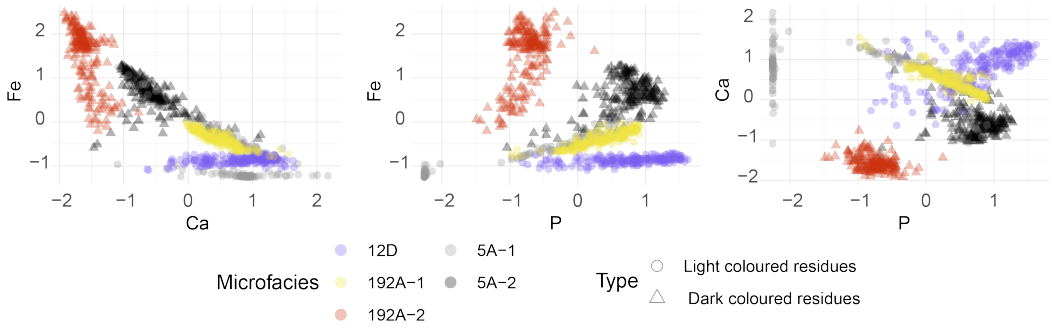

Figure 5.12: Micro-XRF element point measurement results of wood residue samples, normalised and scaled values.

5.5 DISCUSSION

5.5.1 *Synthesis and characterisation of the flooring units*

The micromorphological description allowed to distinguish different floorings as well as debris/waste, and use layers could have been identified in the TSs (Appendix D.1- D.6). Furthermore, horizontally oriented wood residues and compact calcareous layers occur as floor coverings in the upper part of the profiles of excavation Unit 1 (Fig. 5.2), in Phase 5 and 3. The Micro-XRF results provide geochemical fingerprints for the floorings and covering MF. The floorings and a calcareous covering in 19-2 (C) exhibit varying concentrations of Si, Al, K, Ca and P. Whereas, the wood residues are mineralised and demonstrate elevated levels of Fe, P, and Ca. The integration of micromorphological analysis (Section 5.4.1) and Micro-XRF point measurement and mapping results (Section 5.4.2) enriches the microscopical observations with geochemical data, enabling a more detailed characterisation of the different flooring MFs. This approach allowed us to differentiate and compare distinct flooring compositions which originate from different house floor construction types. By combining micromorphological and Micro-XRF analyses of the same samples, we could differentiate the silt

dominated minerogenic construction material of the tell sequence of Toboliu.

Microfacies 1E, which extends into the covering floor 1D, could be differentiated from typical floorings due to its intermixed character and its elevated Si scores (Fig. 5.11) associated with sand-sized quartz components (Section D.1). Low P values might indicate minor human impact. Nevertheless, the heterogenous matrix is dominated by silt and finely dispersed organic matter and phytoliths. The organic matter content, observed under the microscope, is not represented by the Micro-XRF results, because carbon cannot be measured using this method (Flude et al., 2017). The inability to measure carbon also accounts for the lack of discernible differences between the lighter (16G-1) and darker patches (16G-2) in TS 16. 16G-1 exhibits slightly elevated Ca and Al scores, with the latter indicating a partially parallel striated b-fabric; however, it does not contain a significant amount of organic matter. Both samples have the typical moderate Si values in the used pairings and display an intermediate composition, from a geochemical perspective, between 21-1D (high Al) and 1E (high Si), thus being typical loess like sediment, but MF 16-G2 consists of soil material. The most common group of used sediments consists of clayey silt. 21-1D, 12E exhibit typically high Si scores, linked to dominant silt-sized quartz observed under the microscope. They differ by elevated to high Al scores, low to slightly increased Ca values (21-1E), and increased to high K values (21-1D, 12E) which can be linked to the increased clay content observed under the microscope. This is also reflected by a distinctly striated b-fabric in the micromorphological record of both microfacies. The mixed character of the groundmass in 21-1E which was observed under the microscope (Section D.3) is only partially represented in the Micro-XRF results, which are based on punctual microfacies samples (point measurements). The elevated Ca scores likely indicate the presence of a crystallitic b-fabric with micritic calcite. However, the observed micaceous crystallitic b-fabric is not reflected by the Micro-XRF results. K, which is typically elevated in mica (Brigatti and Guggenheim, 2002), was not measured above average in this microfacies. Moreover, as the Micro-XRF measurements are based on the mean fine material of the groundmass, phenomena such as clay coated grains (granostriated b-fabric) might not be recorded. Apart from clay, calcium carbonate is a reliable parameter for distinguishing between different building materials which is reflected by the Ca/Si ratio. The finely dispersed micritic calcium carbonate is well represented by increased Ca scores in 19-2C, whereas the clayey silt of 12E and 21-1D is low in Ca values in the fine material. In the case of 21-1 D calcitic fragments were identified in thin section which might be interpreted as intentionally added. Particularly 19-2C has a more calcareous character, with strongly elevated Ca values in the Micro XRF measurements (Fig. 5.10 and Fig. 5.11). Notably, microfacies 19-2B

(Section D.6) shows higher Ca values in the element mapping (Fig. 5.9). However, the elevated Ca scores determined by the high-resolution point measurements (Section 5.3.2) in 19-2C are supported micromorphologically by a calcitic crystallitic b-fabric. In contrast, the elevated P values in 19-2C cannot be confirmed microscopically; only minor secondary phosphate is observable which may be, apart from that, being finely dispersed in the groundmass. Overall, the P scores in the minerogenic building material appear notably low, suggesting a minimal anthropogenic waste content. Overall, the P scores in the minerogenic building material are notably low, which suggests either a minimal content of anthropogenic waste or a low phosphorus concentration in the carbonate source material. Micro-XRF analysis of samples 12D, 5A, and 19-2A from the wooden floors indicates significant variations in the chemical composition and high Ca, P and Fe values of the remnants, which micromorphological analysis cannot ascertain. However, the plant cell structure can still be recognised microscopically (Fig. 5.5c/d). The compositional differences are particularly evident when compared to the sediment floorings (Fig. 5.11). The light wood residue microfacies (12D, 19-2A-1, and 5A-1) exhibit high P and Ca scores, indicating significant calcium-phosphate mineralisation. They demonstrate low concentrations overall, with tighter clusters across all three plots, indicating better preservation or less mineralisation. In contrast, the dark wood residues (19-2A-2 and 5A-2) show high Fe scores and a wider scattering in bi-plots, particularly in the P versus Fe analysis (Fig. 5.10). Both suggest alteration under varying conditions.

5.5.2 *Origin and alteration of the construction materials*

The presented flooring microfacies 1E, 12E, 21-1D and 21-1E, 16G-1, 16G-2, as well as further only microscopically analysed floorings (5B, 5E, 19-2B and 19-2E) indicate a loess derivate composition, which is composed of mainly silt fraction. The mostly silt dominated flooring microfacies with varying clay and carbonate content exhibit a pattern similar to the loess derivate deposits in the surroundings of the Bronze Age tell (Lie et al., 2024; Zickel et al., sub.). Our integrated analyses suggest that, in all instances, floorings are constructed from materials, likely sourced from the local environment. These findings aligns well with numerous other studies, which demonstrate that the availability of local materials and environmental conditions significantly influence floor construction (Friesem et al., 2017; Goldberg, 1979; Kovács et al., 2024; Macphail and Goldberg, 2007).The use of pure loess for flooring has also been documented in other archaeological tell settlements such as Szazhalombatta-Foldvar (Kovács et al., 2024) and Vésztő-Mágor (Parkinson et al., 2018). Additionally, the floors 21-1D, 12E exhibit a higher clay content resemble the clayey, decalcified loess derivates from Marine Isotope Stage 2 (MIS2) in the surroundings

of the tell (Zickel et al., sub.). Furthermore, both microfacies exhibit low Ca and P concentrations (Fig. 5.10 and Fig. 5.11)- Low Ca point to decalcification, as observed in the parent (loess) material of the local Phaeozem. Inconspicuous P may indicate that pure loess was extracted avoiding contamination with waste materials. Microfacies 1E can be characterised as being silty and humic, but with a strongly increased sand content. This material at the bottom of the excavation profile (Fig. 5.2) may have been introduced into the initial tell layers through bioturbation (krotovina) and likely originates from the underlying layers. However, the presence of increased organic matter, along with grass phytoliths visible in TS, indicates that the soil material is derived from Phaeozem soil, which is characteristic of the region (Zickel et al., sub. Lie et al., 2024). Microfacies 16G exhibits a mottled flooring, predominantly consisting of clayey silt. The humic-silty patches of 16G-2 resemble microfacies 1E, possibly derived from local Phaeozems (Zickel et al., sub. Lie et al., 2024). However, microfacies 16G represents the only case where organic material was incorporated (mottled) in a flooring. Microfacies 19-2C differs significantly from other flooring materials by its highly calcareous character. The clayey loess, derived from more than one meter below the surface in the vicinity of the tell, contains carbonate concretions (Zickel et al., sub.), which may serve as a raw material source for plastering. Such calcareous nodules (Osteocols/ Lösskindel) contain a high portion of 30 to 70% of $CaCO_3$ as mentioned by Li et al. (2018) and where eventually collected during the exploitation of the loess derivate deposit. The clayey loess, derived from more than one meter below the surface in the vicinity of the tell, contains carbonate concretions (Zickel et al., sub.), which may serve as a raw material source for plastering. The observed mineralisation of the wood is a well-known form of macro-botanical remain mineralisation in the archaeological record. Calcium phosphate, which derives from remains such as bones, teeth and dung, replaces the original organic substance (e.g. (Jacomet and Kreuz, 1999; Murphy, 2014). Moreover, the high Fe scores (dark wood residues: 5A-2 and 19-2A-2) can be associated with post-depositional alterations, such as charring or degradation of organic matter (Stemmler and Berthelin, 2003), possibly under alternating aerobic and anaerobic conditions.

5.5.3 *Bronze Age flooring techniques*

In Toboliu, a variety of local resources were utilised for the installation of floors and coverings, employing adapted techniques (Fig. 5.13). We identified several types of silt (sub-) floorings (Fig. 5.13), across four settlement phases (Section 5.2.1). The mineralised residues can be associated with wooden planks (**lie2024tell**), while 19-2C from the latest settlement phase (Phase 3) provided evidence of floor plastering.

Silt floorings

The predominant flooring material is (clayey) loess derivate, with variations in clay and carbonate content, all of them are present within the local environment of the settlements. The (clayey) loess derivate like composition (i.e. 12E, 21-1D, and 21-1E) suggests that these regionally abundant deposits were utilised as primary construction materials for floorings. The resource was likely exploited during the Bronze Age for various construction activities, including the excavation of deep ditches, cutting such layers, surrounding the tell (Lie et al., 2019; Zickel et al., sub.). Mostly the sediment was utilised without prior treatment and likely handled with care, as evidenced by the absence of waste content. The use of untreated loess for flooring has been documented in other Bronze Age tell settlements throughout the CB (Parkinson et al., 2018; Kovács et al., 2024). Typically, calcareous sediment is considered a favourable flooring material due to its binding properties in floor construction (Thiemeyer and Fritzsch, 2011; Uzdurum et al., 2023). However, in our case, reddish, strongly clayey silt was also employed, though it required tempering for flooring purposes.

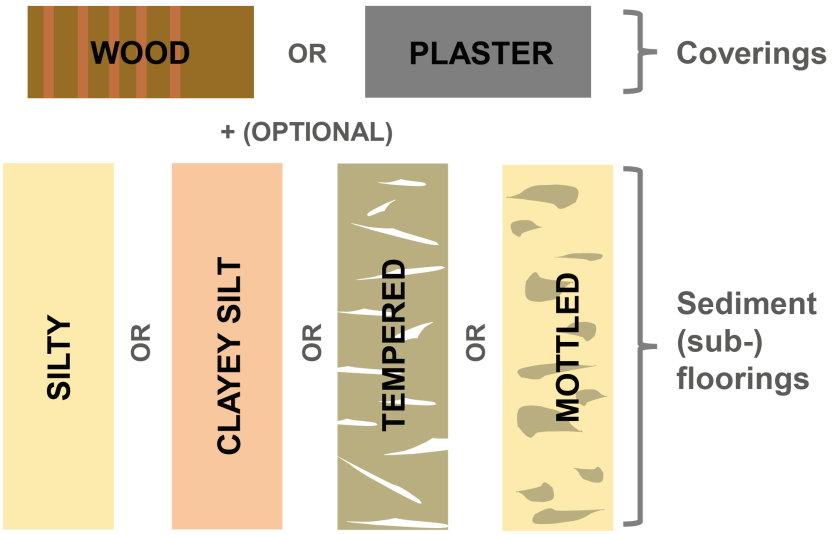

Figure 5.13: Scheme of (sub-) floorings and coverings found in the Tell Toboliu stratigraphy. Different (sub-) flooring types could have been determined in the following microfacies (MF). Silty: 1E; Clayey silt: 12E; Tempered (and silty/clayey): 21-1D, 21-1E; Mottled: 16G. Wood coverings can be found in 12D, 5A and 19-2A. 19-2C represents a plastered covering.

Tempered floorings

In contrast to the previously mentioned pure silt floors of Phase 4 and 5, the presented floors 21-1D, 21-1E, and 16E (described in Section

D.4only) were plant tempered. While the organic plant temper decayed or was burnt, so-called pseudomorphic plant voids remain (Matthews, 1995; Shillito, 2011). In the case of 21-1D and E, phytolith morphotypes such as ELONGATE DENDRITIC and ELONGATE DENTATE remain. This combination indicates the presence of cereal chaff (Shillito, 2011; Vrydaghs et al., 2017; Macphail and Goldberg, 2018; Macphail and Goldberg, 2018; International Committee for Phytolith Taxonomy (ICPT), 2019; Out et al., 2024). Cereal-related chaff tempering of clayey silt floors has also been found at the Bronze Age tell Borsodivánka in Hungary (Fischl et al., 2025; Röpke, A., Kovacs, G., Petö, A., 2024). In contrast to the floor in Borsodivanka, which has a random distribution of pseudomorphic voids, the ones of 21-1D and E are horizontally orientated, reminiscent of a smoothing technique used for plasters or ceramics. However, as microscopically observed, this is associated with the tempering of cereal chaff, eventually to prevent desiccation cracks induced by the increased clay content (Tang et al., 2021). The chaff fibres can serve as a stabiliser to reduce cracking. Furthermore, calcitic fragments were observed in the decalcified raw material, which may suggest additional intentional tempering. Such minerogenic temper was used for wall material at other tell sites (Fischl et al., 2025). Additionally, the abundance of pseudomorphic plant voids in another calcareous floor (16E, not presented in detail) suggests the former presence of plant material. However, due to the dissolution and mineralisation of organic matter as well as the phytoliths, identification is no longer possible (Jacomet and Kreuz, 1999; Shillito, 2011; Murphy, 2014).

The mottled floor

In microfacies 16G, a mixture of pure silty (16G-1) and soil (16G-2) patches correspond to a mottled silt floor, further highlighting the variability in silty floorings. This was not observed on another occasion, and no reference to other sites can be made. It cannot be compared to a beaten floor, as the mixed materials remain clearly visible (Banerjea et al., 2015; Macphail and Goldberg, 2018). It may be coincidental, as it is conceivable that the material composition is linked to the exploitation of nearby sediment deposits. Portions of the topsoil likely mixed with underlying loess derivate during excavation, processing or this might be related to a levelling (preflooring) layer.

Plastered covering

Micrfoacies 19.2C likely reflects a more selective flooring method by opting for or preparing a 'plaster-like' covering, as described by Amadio (2018) as well as Karkanas and Efstratiou (2009). Regarding plastered coverings in general, it is noteworthy that 19-2C exhibits lower Ca and P scores than expected (Section D.6). However, as Karkanas

(2007) points out, plasters are rarely pure; they typically consist of a mixture of soft lime (burned lime) and debris, which may account for such additives. In Toboliu's case the calcareous material might consist of processed (ground) loess noduels. Karkanas and Efstratiou (2009) mention that informal floor surfaces were often constructed using recycled materials, while more formal floors, rich in plaster, were regularly re-laid. The micromorphological evidence for an earlier plastered floor beneath the thick layer (19-2C) supports this notion.

Wooden coverings

Concerning wooden coverings, significant mineralisation of the remnants could have been determined by analysing microfacies 12D, 19-2A, and 5A, although they display differences in micromorphology and elemental concentration, which may be attributed to varying degrees (irregular) mineralisation. Unfortunately, the cell structures are either destroyed or poorly preserved, hindering the determination of tree species, as noted by Schweingruber (1978). Nevertheless, the mineralised wood residues witness the presence of a formal floor in Phase 3.

Kovács et al. (2024) suggest that floor types may have been influenced by both functional and cultural factors. Variations in raw material selection and construction style may reflect technological or social shifts. The changing orientation of houses where different floors were found indicates that construction culture may have evolved between Phase 7 (TS 1) and Phase 5 (TS 12), as well as between Phase 4 (TS 16 and 21-1) and Phase 3 (TS 5 and 19-2). While local materials served as the foundation for the earliest settlement in Phase 7, a pure silty subflooring with an initial wooden covering was identified in Phase 5. Subsequently, mottling and tempering were introduced in Phase 4, followed by a more clayey flooring in 21-1E. A strong inclination towards coverings is evidenced by the wooden planks discovered in Phase 3.

5.5.4 *Potential and limits of combined Micro XRF and micromorphological analyses*

Micro-XRF analysis offers significant advantages in micromorphological and archaeological contexts due to its rapid and non-destructive nature. This technique enables geochemical examination of samples, as previously demonstrated in studies like Mentzer (2017). Moreover, Micro-XRF measurements highlight small differences in micromorphologically similar microfacies, such as silty sediments with slightly different geochemical (mineral) composition of the fine fraction, through variations in elemental concentration. This is particularly useful for assessing certain features/remnants of unclear origin such as the mineralised wooden floor. Without Micro-XRF a clear determination

would not be possible. Evaluating variations in clay or carbonate content among microfacies by analysing geochemical concentrations such as of Al, Si, and Ca in the groundmass provides an additional, semi-quantitative parameter for direct comparison of different floor microfacies. Our results show, that Micro-XRF data are suitable for a semi-quantitative approach, effectively representing relative differences in microfacies, although there are limitations. Both methods complement each other; for instance, Micro-XRF is unsuitable to measure carbon (Flude et al., 2017), but micromorphologically, high carbon content can be eventually identified as degraded or charred organic matter (amorphous, isotropic-opaque appearance), such as in MF 16G. Conversely, minerals with similar optical properties can be excluded through increased elemental concentrations (e.g. Fe in magnetite) using Micro-XRF analysis. A significant advantage is the ability to identify mineralisation and the associated chemical elements in organic (residue) structures, such as wooden floors (MF 12C, 5A, and 19-2A). However, challenges arise regarding spatial resolution. When measuring elemental concentration over a large area, a resolution must be set that is manageable within a reasonable timeframe. For element mappings of whole TS (∼50 x 80 mm) we applied a spatial resolution of 40 µm (∼2,500,000 measurement points) which takes about 11 hours (Section 5.3.2). Components smaller than 40 µm may be underrepresented, such as phytoliths found in the floor sediment of TS 21-1. Additionally, simply mapping individual elements with Micro-XRF is often impractical, as the presence of specific elements can be overestimated. Based on our experience it is more effective to represent area-wide element ratios (Fig. 5.9), showing the local enrichment of certain elements relative to those present throughout the area. However, this requires more complex post-processing of the output element maps (Section 5.3.2). Nevertheless, the overestimation of certain elements, for example Ca, may still arise due to methodological factors, such as grain size or matrix effects (Böning et al., 2007). The observation that microfacies 19-2B (use layer) exhibits higher Ca values in the element mapping compared to plaster-like covering of 19-2C (Fig. 5.9) is not corroborated by the micromorphological results, which are illustrated in the classified imagery (Section D.6). However, increased ash content in the use layers was observed under the microscope. Significant differences between the microfacies are evident especially in terms of density which may be associated with the effects described by Böning et al. (2007). Point measurements can achieve higher accuracy (resolution) for smaller areas, but limiting factors exist. For instance, grain size in the selected area should not vary excessively; large sand grains in the matrix can lead to an overrepresentation of Si content. Moreover, these measurements only capture a small section (Section 5.3.2), which may not be representative of the exact sediment composition. Minor variations, observable under the

microscope as distinct b-fabrics, as described for microfacies 21-1E (Section 5.5.1), are likely not represented. Therefore, AOIs should be selected carefully. Overall, our results indicate that both micromorphological and Micro-XRF analyses yield similar conclusions regarding the sediment composition of floors. Using this integrated multi-proxy oriented approach, micromorphological findings can be effectively backed by Micro-XRF results. The quantitative nature of these results enhances the reproducibility of micromorphological observations.

5.6 CONCLUSION

The integration of micromorphology and Micro-XRF significantly enhances our understanding of floor construction practices, not only during the Bronze Age in the eastern CB but potentially across various archaeological periods. In Toboliu's case, sediment floorings evolved from locally sourced, unprocessed silt layers to more complex compositions involving tempering and coverings. The calcareous cover in Tob.19-2 may represent plaster, while remnants of wooden floor coverings highlight previously under recognised organic construction strategies in tell settlements. Additionally, Micro-XRF analyses revealed that the wood planks were entirely mineralised, with various types of mineralization identified. Evidence suggests a transition in construction styles, likely linked to local cultural changes, reflecting a sophisticated knowledge of construction materials and techniques. This combined approach offers new perspectives on domestic architecture and resource use during the Bronze Age in the eastern CB and beyond. The integrated analysis illustrates diverse construction styles and proves beneficial for distinguishing materials and house floor compositions, detecting plant tempering, and identifying post-depositional alterations, such as mineralisation of organic components.

ACKNOWLEDGMENTS

The authors wish to express their gratitude to the other founders and team members of the project: Dr. Alexandra Găvan, Dr. Tanja Zerl, and Dr. Nadine Nolde from the Institute of Prehistoric Archaeology, University of Cologne in Germany. We also appreciate the support provided by numerous undergraduate and graduate students during fieldwork. The project 'Living Together or Apart? Unravelling the Development, Internal Organization, and Social Structure of a Complex Bronze Age Tell Settlement at Toboliu, Western Romania' was funded by the Deutsche Forschungsgemeinschaft (DFG, German Research Foundation) – project number 436834905. Living in the Bronze Age tell settlements. Moreover, Excavations at Tell Toboliu were supported by the Romanian Ministry of National Education through the project titled "A Study of Settlement Archaeology at the Eastern Frontier of

the Carpathian Basin". This open-access publication is supported by the University of Cologne, Germany (DEAL agreement).

Part III

DISCUSSION

6 DISCUSSION

The primary objective of this thesis is to achieve a comprehensive integration of geoscientific and archaeological data, spanning from the macro to the microscale. This integration aims to enhance geoarchaeological and landscape reconstruction methodologies, particularly in relation to the case study in Toboliu, Romania. The methodological framework is significantly shaped by the advancements in Digital Geoarchaeology as outlined by Siart et al. (2018b) (Section 1.4). Each subsection of the discussion addresses a specific research focus as outlined in the research objectives (Section 1.2). Section 6.1 focuses on landscape reconstruction aspects and the integration from macro- and mesoscale data. In Section 6.2 the role of innovative methods in micromorphology in linking information across micro and meso scale will be discussed. This corresponds to the thesis structure and order of integrated manuscripts and publications presented in Section 1.5.

6.1 LANDSCAPE RECONSTRUCTION METHODS

As outlined in Section 1.2, the effectiveness of applying site selection analysis on a macro scale was evaluated in Chapter 2 for the southern Levant in the Eastern Mediterranean. The outcome will be discussed in Section 6.1.1. Additionally, Section 6.1.1 will address the significance of integrating data from both the macro- and meso scale, drawing on insights from the case study in Toboliu (Chapter 2), for site catchment analysis. Both approaches provided novel insights, from distinct perspectives, into the integration of multi scale (palaeo-) geographical information for analysing the spatial distribution and catchment of archaeological sites, following concepts of Digital Geoarchaeology after Siart et al. (2018b) (Section 1.4).

6.1.1 *Macro scale - landscape analysis (objective 1.1)*

The first study concerning Upper Palaeolithic site distribution (Chapter 2) underscores the potential but also the inherent difficulties in conducting predictive modelling over extensive and geographically diverse areas, such as across the Southern Levant (Section 2.2). It shows, that gathering diverse (palaeo-) geographical data, in combination with DEM derived information and archaeological site distribution can be used to identify areas of high potential for Upper Palaeolithic site occurrence, on the macro scale. Further, it was possible to reference these findings by meso scale data from a well studied area with high

archaeological site occurrence, the Wadi Sabra region. The distribution of archaeological sites, and consequently areas with a high potential for discovering new sites, can be understood as a function of prehistoric human preferences, preservation conditions, accessibility, and archaeological survey bias. In the southern Levant site locations are often found along regions with major aquifers, being productive since the Pleistocene, likely linked to water availability for early humans. The presence of karst systems and a general influence of geomorphology on site preservation are important factors (Holting and Coldewey, 2009), which can be illustrated by the results. Site preservation is further influenced by slope and terrain, with open-air sites being more likely to be found in areas with gentle slopes, while cave sites are often located in steep escarpments. Palaeoclimate and vegetation reconstruction data, suggest that habitable conditions likely prevailed across much of the study area, accordingly these are not seen as restricting factors (Hayes et al., 1999; Rohling, 2013; Torfstein et al., 2013; Torfstein and Enzel, 2017). However, present vegetation types (Miebach, 2016) can affect site visibility and discovery. Densely vegetated areas, such as Mediterranean forest, hinder archaeological surveys, leading to a bias in site distribution data. While such studies are relatively rare, they can provide valuable insights into archaeological site distribution (Kondo et al., 2012; Luo et al., 2014). The presented study enables that specific underrecognised regions, including the north-eastern Galilee and parts of the Jordan Highland Escarpment, have been identified as promising new candidates for future, more detailed archaeological investigations. However, MCDA is noted for slightly overestimating site potential due to coarse geomorphological data. Other methods like logistic regression have been successfully applied in the region, indicating a need for further testing of the MCDA approach (Wachtel et al., 2018). The precision of published archaeological site coordinates and historical research biases can be discussed as significant factors affecting data quality. Also a dominance of site clusters induced by a spatial research bias in certain areas, which can skew predictive outputs and emphasises the importance of a reliable dataset for reproducibility (Marks, 1976; Nir, 1978; Goldberg and Brimer, 1983) is highlighted. Future geoarchaeological fieldwork will further assess the accuracy of this predictive approach. Utilising more precise site location data (e.g. coordinates) and high-resolution land cover data, will eventually contribute to a more refined model of Upper Palaeolithic occupation in the Southern Levant.

6.1.2 *Meso scale - landscape analysis (objective 1.2)*

A comprehensive site catchment analysis approach is presented for the case study in Toboliu. It combines chronostratigraphic and geospatial data from various scales (Chapter 3). In this study, a local geomorpho-

logical phenomenon was investigated by connecting local observations to the regional context. It was clarified that several CDs near the Bronze Age tell are likely not a result of loam exploitation associated with the settlement, but rather are part of natural Pleistocene landscape evolution. This is derived from integrated chronostratigraphical findings based on sediment core drilling and spatial analysis utilising Worldview-3 satellite imagery, historical topographic maps, as well as digital elevation and geomagnetic data. Through this multi scale approach, an elongated basin was identified as a palaeochannel segment, likely associated with increased Palaeo-Körös fluvial activity during MIS-2 (Nádor et al., 2007; Nádor et al., 2011; Kiss et al., 2015). In this tectonically active zone fluvial erosion partially affected the loess derivate covered region between the Apuseni Mountains and the CB. Also, the palaeochannel incises older MIS-6 drainage channels, which are discernible through distinct CIR and DEM signatures and were identified in the core samples. These older structures are interpreted as silted fluvial channels or oxbow lakes, corresponding to the abundance of CDs. By studying the location, shape, size, and distinct digital elevation and geomagnetic patterns related to the CDs and palaeoenvironmental data from the CB (Lehmkuhl et al., 2020; Lehmkuhl et al., 2021), their formation were placed within a periglacial context. In conjunction with a limnic bottom unit found in the thoroughly investigated CD2 (Core 13), these landforms can be identified as pingo ruins (Kluiving et al., 2010). Furthermore, as this unit exhibits a minimum age of 9,910-10,200 cal a BP and Early Holocene pollen, the presence of a pond during this period is indicated. Backfilling (colluviation) of the depression commenced approximately 5.1 ± 0.2 ka years ago, preceding the onset of the Bronze Age (~3880 BP) in the region (Section 1.3). However, the depth of the partly backfilled CDs likely facilitated moisture retention, thereby creating niches. This suggests a ceetain potential for land-use diversification (e.g. used for fish ponds, troughs). However, phaeozem soils, which were found to be dominant in Toboliu through the presented soil analysis, likely played a more significant role in attracting Bronze Age settlers due to their high potential for field crop production. The results underscore the importance of integrating multiple data sources and methods. In this case, the approach allows for the combination of high temporal/depth resolution data with a multilayered, high spatial coverage, and regional contexts, enabling landscape reconstruction even in such a scientific data-scarce area such as the Eastern CB. Even if the initial question regarding a potential anthropogenic origin of the CDs has been clarified, numerous new issues emerged during investigations. These issues, building upon the established foundation (Chapter 3), should be addressed in future fieldwork. The discovery of remarkably well-preserved pollen (Section 1.3) within the bottom unit of the CDs indicates that these landforms serve as valuable palaeoenvironmental

archives, which are scarce in the CB (Magyari et al., 2010), and thus warrant further exploration. While the outcome that the CDs represent pingo ruins or periglacial relict forms is supported by coring data and geospatial analysis, their precise morphology should be determined through field-based profile sections of several CDs (Kluiving et al., 2010). Additionally, it is crucial to investigate whether this phenomenon is localised or if similar forms occur in comparable terrain positions along the Eastern Carpathians (Section 1.1), for instance, near MIS-2 palaeochannels. Further, the palaeochannel in Toboliu needs to be further investigated in detail, for example with sediment core drillings. If it was water-filled during the Bronze Age it could have represented an important water source for the settlement.

6.2 MICROMORPHOLOGICAL ADVANCES

The second research focus, which addresses the integration of qualitative micromorphological information with site context (e.g. landscape) analysis, will be subsequently discussed. Relating to the framework of Digital Geoarcharchaeology (Siart et al., 2018b), the methodological achievements in quantifying, characterising, and mapping micromorphological phenomena are paramount to this objective (Section 1.4). Section 6.2.1 is based on the findings presented in Chapter 4, which applies machine learning for thin section image classification, using an example of a well-studied LPS in Rheindahlen (Germany). The application potential of this innovative approach to complex Bronze Age archaeosediments from the Toboliu case study, particularly the enhancement achieved through Micro-XRF measurements, was presented in Chapter 5 and will be further explored in this section.

6.2.1 *Micromorphology and image classification (objective 2.1)*

The developed MiGIS toolbox (Zickel and Gröbner, 2023) facilitates the mapping and quantification of soil and sediment constituents from thin section scans. By employing a set of thin section scans captured in TL, XPL, and RL modes, along with the Random Forest ML algorithm (Scikit-learn developers, 2023), micromorphological features can be successfully classified across entire TSs. The study illustrates that GIS proved to be a suitable environment by utilising a metric spatial reference system in QGIS (QGIS Development Team, 2022d). GIS also enables accurate area measurements on TSs for spatial analysis and quantification. This offers a direct approach for investigating the spatial distribution of micromorphological (micro scale) phenomena, which helps to identify sediment composition patterns and delineate microfacies. The semi-automatic classification approach allows users to define training data, thereby offering qualitative control, which remains crucial in micromorphology. However, the optical resolution of

the thin section scans using flatbed scanning restricts the minimum detectable size of constituents (Carpentier and Vandermeulen, 2016). This limitation could potentially be overcome by enhanced image acquisition methods; automated digital microscope mappings might achieve higher resolution, thus enabling the detection of smaller sediment constituents (e.g. microcharcoal). Also, deviations in TS preparation, such as variations in thickness, embedding resin, or the presence of air bubbles, negatively impact classification accuracy and might hinder the transferability of classification models. Overfitting remains a challenge when transferring models to different datasets (Breimann, 2001; Rubo et al., 2019), primarily due to variations in feature interference colours caused by thin section processing. To enhance model robustness, representative training data, potentially sourced from heterogeneous thin section datasets, is necessary. Additionally, OBIA, which incorporates object size and shape, could address these issues and improve classification accuracy (Thierion and Lang, 2018; Visalli et al., 2021). The resulting micromorphological classification maps, which illustrate the distribution of groundmass, pedofeatures, or archaeological components across entire thin sections, support the reproducibility of micromorphological observations. This approach also makes the results accessible to non-experts in the interdisciplinary environment. Furthermore, it provides the capability to compare sediment composition (microfacies) within or between stratigraphical profiles, thereby offering an additional proxy for landscape evolution when applied to sequences like the Rheindahlen LPS (Kehl et al., 2024). Furthermore, integrating geochemical mappings (e.g. Micro-XRF) could further refine this innovative micro-geospatial approach, particularly for distinguishing minerals and the fine fraction of sediments (Mentzer, 2017). Moreover, obtaining geochemical signatures for microfacies could strengthen the integration of micromorphological results with site catchment analysis on the macro scale.

6.2.2 *Micromorphology and Micro-XRF (objective 2.2)*

Micro-XRF analysis, when integrated with micromorphological techniques, offers substantial benefits in geoarchaeological contexts due to its non-destructive nature. The presented method (Chapter 5) facilitates the geochemical examination of samples, highlighting subtle differences in micromorphologically similar microfacies through variations in elemental concentrations. For instance, in this study, it aided in assessing features of ambiguous composition, such as mineralised wood residues, and in evaluating variations in clay or carbonate content by the use of element ratios (e.g. Si/Ca, or Si/Ca). By adapting the methodologies outlined in the previously discussed study (Section 6.2.1), this approach enabled the characterisation of distinct flooring units within the Bronze Age tell sediments of the case study

(Chapter 1.3). However, while Micro-XRF data provides valuable semi-quantitative insights into relative differences between microfacies, it has limitations. It cannot detect light elements such as carbon (Flude et al., 2017), which micromorphology can identify as degraded or charred organic matter. Conversely, Micro-XRF can differentiate minerals with similar optical properties by detecting elevated elemental concentrations (e.g. Fe in isotropic/ opaque magnetite). Another significant advantage is its capacity to identify mineralisation and associated chemical elements (e.g. Fe, P, and Ca) within organic residues. Challenges include spatial resolution and the time required for element mapping. Components smaller than the applicable resolution (e.g. 40 µm for a 50x80 mm sample) may still be under-represented as mentioned before (Section 6.2.1). Simply using individual element maps can lead to overestimation; therefore, using element ratios, such as Si/Ca to determine carbonate concentration in microfacies, is found to be more effective, though it necessitates more complex multiband raster post-processing as described in Section 4. Nevertheless, morphological factors like grain size or matrix effects can also cause overestimation of certain elements, particularly in the case of Ca (Böning et al., 2007). High-resolution point measurements using Micro-XRF offer sufficient accuracy. However, measurement areas must be selected carefully, or a sufficient number of AOI per microfacies should be analysed. Otherwise, minor grain size variations or local matrix impregnations (Stoops, 2020) can lead to similar overestimating effects as described above, negatively impacting the representativeness of the overall sediment composition. Overall, the integration of micromorphological and Micro-XRF analyses represents a comprehensive step forward in supporting interdisciplinary micromorphological research. Its quantitative nature further enhances the reproducibility of micromorphological observations. By combining micromorphology with geochemical information, detailed insights into sediment composition and post-depositional processes can be gained, which can be readily illustrated and integrated with the results of mesoscale analysis approaches. In this specific case, findings from the local landscape reconstruction (Chapter 3 and Section 6.1.2) could have been compared to the micromorphological/Micro-XRF results from this study. It was determined that the house floors of the Bronze Age tell settlement were constructed using variations of local sediments (loess derivates) with different additives, such as soil material or cereal chaff tempering, which are valuable aspects for further site catchment analysis. As the CDs investigated in Chapter 3 are found to be not the product of loam exploitation, a probable source for minerogenic construction materials may be sediment extracted during the construction or maintenance of the two concentric ditches around the tell (Chapter 1.3). This could be a future focus of geoarchaeological work in the study area.

Part IV

CONCLUSION

7

CONCLUSION

Collectively, these studies emphasise the critical role of multi scale approaches. The integration of diverse data in advancing geoarchaeological and palaeoenvironmental investigations (Chapter 1.4) is crucial for focussed field work, cultural heritage protection, and reproducibility. From macro scale predictive modelling (Chapter 2) to meso scale landscape reconstruction (Chapter 3), and integrative (micro scale) micromorphological analyses (Chapter 4 and 5), the findings highlight the linkage of human-environment interactions across various temporal and spatial scales.

The predictive modelling approach integrates diverse (palaeo-) geographical data and effectively identifies high-potential areas for archaeological sites, such as for the Upper Palaeolithic in the southern Levant (Section 2). However, the accuracy of the model relies on data quality and careful consideration of factors like human preferences, preservation, and survey biases should be taken into account (Chapter 6.1.1). Meso scale studies, exemplified by the Toboliu case (Chapter 3), demonstrate how combining local observations with regional contexts can resolve specific questions, such as the origin of the CDs, which were identified as pingo ruins instead of Bronze Age loam extraction pits (Section 6.1.2). This integration of macro- and meso scale data allows for the validation of observations and the refinement of areas for in-depth geoarchaeological research.

Furthermore, advancements in micro scale analytical techniques, including the MiGIS toolbox (Chapter 4) for micromorphological mapping and the integration of Micro-XRF (Chapter 5), provide unprecedented detail of sediment composition and post-depositional processes which can be linked to the site catchment (Chapter 3). These tools enhance the reproducibility and interdisciplinary applicability of findings, offering new proxies for on-site analysis and landscape reconstruction, thereby enriching the understanding of site formation processes and environmental contexts at broader scales (Section 6.2).

In conclusion, these studies offer significant methodological contributions to understanding prehistoric human-environment relationships across different scales. While significant progress has been achieved, as thoroughly presented and discussed in the results chapters of this thesis, the findings consistently underscore the necessity for continuous methodological refinement, enhanced data precision, and additional fieldwork. This is crucial for validating aspects such as remote sensing observations or predictive models, and for addressing complex research questions in site catchment on-site anal-

ysis. The identified potential for methodological innovation within Digital Geoarchaeology, particularly in integrating field and spatial data, promises to enhance comprehensive geoarchaeological work and landscape reconstruction, ultimately facilitating reproducibility, collaboration, and knowledge transfer in this interdisciplinary field.

Part V

APPENDIX

A

SUPPLEMENTARY TO **UPPER PALAEOLITHIC SITES AND WHERE TO FIND THEM: A PREDICTIVE MODELLING APPROACH TO ASSESS SITE EXPECTANCY IN THE SOUTHERN LEVANT**

A.1 METHODS

A.1.1 *Pre-processing*

Data collection

One data basis of the study consists of historical, analogue maps that were freely available as scanned images or documents. The maps were first georeferenced and manually digitized. After this process, spatially registered geomorphological (Nir, 1978), hydrogeological (Schöler et al., 1990), and vegetational (Zohary, 1973) information was available in digitalized form for the study area. The legend information from the maps was then assigned a number to facilitate later rasterization and classification of the vector layers.

DEM preparation

As a basis for the terrain analysis, the SRTM 30 M (USGS - United States Geological Survey, 2009) was chosen. It is a digital elevation model with a spatial resolution of one arc second which corresponds to about 30 m. It belongs to the freely available global DEM products with the highest resolution and a relatively low height error; thus, it was considered suitable for this analysis. Aside from the use of the elevation model itself, the following DEM derivates were computed: Aspect, Slope, and the Terrain Ruggedness Index (TRI). The values of the Aspect represent the cardinal points in degrees. The pixel values in the Slope raster show the terrain inclination and are also given in degrees. In case of the TRI, the individual pixel values represent the change in elevation for a pixel window of 3x3, i.e. for each pixel and its 8 surrounding cells (QGIS Development Team, 2022c). All DEM processing steps were performed using the UTM CRS and WGS84 reference ellipsoid. UTM provides metric units for latitude, longitude, and altitude, which simplifies the application of terrain analysis algorithms.

Archaeological site database

The archaeological site database was first converted into geodata format (point vector layer) and the accuracy of the mapping was

checked on a random sample base. As mentioned above, the accuracy of site coordinates plays a major role, as even an inaccuracy of a few meters in the following may result in deviations in the pixel value query. Nevertheless, errors cannot be ruled out especially for sites recorded before the widespread availability of GPS devices. This dataset consists of 92 archaeological sites forming the criteria sample size.

A.1.2 *Processing*

Study area

The exact extent of the computational study area was determined by the maximum extend of each discontinuous thematic vector layer respectively their overlapping area. Accordingly, the expansions of the continuous raster layers (DEM and derivates) as well as the archaeological site database layer, were reduced to this extend. The result is a study area covering a large part of the coastal Southern Levant including the present coastline.

Drainage system

The HydroRIVERS vector data set (Lehner et al., 2008) was evaluated and the individual riverbed sections (starting from the potential spring area) compared to the spatial distribution of the sites. This quickly revealed a certain dependence of the sites on the upper reaches. Most of the sites are located within a 5 km radius of the first 22 river kilometres upstream.

Harmonisation

First, as the different data sources provided different CRSs, they were all initially adapted to the UTM WGS84 system. Except the sample dataset (archaeological sites) all vector datasets were then rasterized. Additionally, and on the basis of the observation mentioned above, the original HydroRIVERS vector dataset was first rasterized and then processed into a proximity raster with a maximum distance of 5 km with intervals of 1 km. In total this resulted in an eight-criteria raster layer.

A.1.3 *Analysis*

Data acquisition

The cells (pixel values) of all eight previously created criteria datasets were queried with the point sample dataset (archaeological sites point layer). The resulting matrix then provided the basis for the creation of

histograms. Frequently used in image classification of remotely sensed data, histograms are a basic graphical method to show the frequency distribution of query values. It is helpful to identify individual classes using a layer-related but uniform class width (equal intervals). In case of the former vector datasets, the number of bins was created according to the number of different types. The original classes could then be ranked by frequency and normalized by using the same value range, a maximum of 8 classes, for each of the eight datasets. The grids were then reclassified on this basis. It should be noted that highly frequented classes received a higher score. With a value of 8, the most frequented class would thus be the class with the highest score. This resulted in eight thematic normalized layers with classified areas, rescaled according to the probability of archaeological site occurrence. To obtain an overview of the distributional situation of the individual classified and ranked criteria layers, each was mapped with a corresponding colour scale (see the figures in supplementary material S2).

Suitability analysis

Based on heuristics, a suitability map was created according to the principle presented in the handbook of Malczewski and Rinner (2015). Central to the approach is the implementation of a MCDA in GIS. This is a process where '*a set of areas that fulfil several dozen criteria (e.g. type or proximity) can be identified and their relative importance can be taken into account* [...].' (Lloyd, 2010, p. 71). The case study combines geographical and archaeological data to target the identification of areas with a high site preservation probability. Accordingly, a '*weighted summation decision rule approach transforms and combines geographical data and value judgements to obtain information for decision making.* [...]' was applied (Malczewski, 2006, p. 703). Briefly, the criteria layer, in this case the eight classified and ranked raster datasets, are summarized. In accordance with this, an additional weight can be assigned to each criteria layer and added to the function. An alternate expression for the process later described is a weighted overlay function and can be implemented in a GIS raster calculator:

$$\text{Suitability map} = \text{Criteria}_{\text{Grid A}} \cdot x_A + \text{Criteria}_{\text{Grid B}} \cdot x_B + \text{Criteria}_{\text{Grid C}} \cdot x_C \tag{A.1}$$

Figure A.1: Weighted overlay function for suitability map calculation. x is the weight assigned to the specific raster dataset (criteria grid)

In consequence, grid cells (pixel values) of the criteria input are grouped using the individual ranking and assigned an index value representing a suitability score of the specific area (pixel group). Most

suitable areas, where a high probability of preserved sites is expected, have high scores (index values), whereas unsuitable areas are assigned low values (Malczewski and Rinner, 2015) or are even not represented in the map, indicated as "no data pixel". In this sense, the identification of territories involving the chosen criteria, the specified elevation, aspect, slope, TRI, vegetation type, hydrogeology type, geomorphology type and river proximity intervals, is enabled.

Accuracy assessment

As the information used for decision making is based on several different data sources, the application of an accuracy assessment is especially suitable. Environmental datasets can correlate, a problem that Congalton and Green (2009) discuss as well as the choice of a meaningful method for an accuracy assessment. Exemplifying the problem of parameter equidirectionality, local vegetation patterns can be a consequence of geomorphology and/or aspect (cardinal point) of the specific terrain position. Moreover, interpolation or generalisation can play a role in the digitized environmental information maps and it has to be kept in mind, that the archaeological site database consists of data collected over years and by different surveyors. These points are therefore difficult to judge statistically. In principle, the best approach in the case of this study would be an extensive field survey, i.e. the collection of standardized field data that could serve as realistic sample size (ground truth) in the accuracy assessment. However, for the moment, the use of another archaeological site database as a reference dataset was considered the best validation method. Since the original criteria sample dataset consists of 92 data points, the sample size of the reference site dataset was chosen in the same size. These 92 sites comprise single reported findspots resulting from a query of Upper Palaeolithic entries from the online Survey Database of the Israel Antiquities Authority (Authority, 2020). The same processing steps were performed as described in the sections above. In a next step, the accuracy of the original MCDA classification can be described by the deviation of the result from the reference dataset. For this purpose, an error- or confusion matrix of the original and the reference result map can be calculated. As a result, consistencies and deviations within the individual preservation condition classes can be displayed based on the number of pixels. In addition, the overall accuracy value indicates the percentage of total agreement between the original classification and the reference (Congalton and Green, 2009). In order to get an impression of the spatial distribution of the differences between the two result datasets, a change detection grid was calculated. This algorithm calculates and quantifies the numerical difference between two pixels with the same geolocation, which allows the quantification of positive (loss) and negative (gain) deviations from the original dataset. As mentioned above, optimally, the reference data set should

consist of standardized and systematic field observations. In the case of the study this value should not be overestimated, since the reference is a dataset including quality restrictions.

Landform Classification Wadi Sabra

For the study area of the Wadi Sabra the analysis bases mainly on the evaluation of the DEM data. Here, a DEM calculated out of stereo-data shot by the Pleiades satellites (Airbus Defence and Space) was used, consisting of two satellite photos calculated into an DEM by Andreas Bolten, Project Z2, CRC 806, with the DEM Extraction Module of ENVI 5.3. One of the photos is taken in plane view, the other in an angle to the ground. The resulting DEM has a resolution of 0.5m. First, the straight satellite image was used to visually map the extent of the top of the sediment remnant in the Upper Wadi Sabra. Likewise, the transition from the upper, bare parts of the stratigraphy to the detritic cones covering the lower part of the stratigraphy was mapped. Then the DEM was used to calculate the slope inclination with the tools Slope and Curvature of ArcGIS 10.3.1. A landform classification was calculated for the Pleiades DEM using the TPI first presented by Weiss (2001). The TPI is calculated with a computational algorithm by (Jenness, 2006b)with a freeware toolbox extension of ArcGIS (Dilts, 2015). It determines the elevation of a raster cell in relation to the average elevation of its surrounding cells. Positive values indicate a higher elevation in comparison to the surrounding and negative ones a lower elevation. The position of the raster cell on the slope is defined by the extend of this difference. For near-zero values the slope inclination of the cell is used to distinguish a flat area from a mid-slope (Jenness, 2006a, p.4,). As the TPI is strongly scale dependent, two different sets of TPI are calculated to distinguish the location of the cell in the micro and meso-topography, called large and small neighbourhoods. Annular – ring-shaped – neighbourhoods are chosen for this study. The small neighbourhood is described by a ring with the inner radius of 25 m and an outer radius of 30 m, the large neighbourhood by a ring with the inner radius of 195 m and the outer radius of 200 m. The width of the rings is the ten-fold value of the raster cell and the outer radius values confirm to the Micro- and Meso-relief classified by Leser (1977) and Manner (2004).

Table A.1: GIS processing and analysis tools of the QGIS environment (QGIS Development Team, 2022c) that were applied in the workflow.

Software version: QGIS 3.14 "Pi"		**CRS: EPSG 32636 UTM zone 36N**	
Tool (algorithm)	**Purpose**	**Provider**	**Documentation**
Aspect	Terrain analysis: Compute aspect of the SRTM 30M DEM	(QGIS Development Team, 2022c)	https://docs.qgis.org/3.10/en/docs/user_manual/processing_algs/qgis/rasterterrainanalysis.html
Clip raster by mask layer	Clip raster datasets to footprint extend	(contributors, 2020)	https://docs.qgis.org/3.10/en/docs/user_manual/working_with_raster/raster_analysis.html
Clip (vector)	Clip vector datasets to footprint extend	(QGIS Development Team, 2022c)	https://docs.qgis.org/3.10/en/docs/user_manual/processing_algs/qgis/vectoroverlay.html
Editing toolbox	Digitise analogue maps	(QGIS Development Team, 2022c)	https://docs.qgis.org/3.10/en/docs/user_manual/working_with_vector/editing_geometry_attributes.html
Georeferencer Plugin	Georeference analogue maps	(QGIS Development Team, 2022c)	https://docs.qgis.org/3.10/en/docs/user_manual/plugins/core_plugins/plugins_georeferencer.html
Hillshade	Terrain analysis: Compute hillshade of the SRTM 30M DEM	(QGIS Development Team, 2022c)	https://docs.qgis.org/3.10/en/docs/user_manual/processing_algs/qgis/rasterterrainanalysis.html#hillshade
Change Detection	Multivariate Alteration Detector OTB 6.6.1	(Team, 2018)	https://www.orfeo-toolbox.org/CookBook/Applications/
Point sampling tool	Query raster data with the archaeological site database	(Jurgiel, 2020)	https://plugins.qgis.org/plugins/pointsamplingtool/
Proximity (raster distance)	Create 5km zones of the HydroRIVERS raster	(contributors, 2020)	https://docs.qgis.org/3.10/en/docs/user_manual/processing_algs/gdal/rasteranalysis.html?highlight=proximity#proximity-raster-distance
Raster calculator	Calculate weighted overlay of the reclassified raster data	(QGIS Development Team, 2022c)	https://docs.qgis.org/3.10/en/docs/user_manual/processing_algs/qgis/rasteranalysis.html#raster-calculator
Rasterize	Conversion of vector data (digitised maps) to raster data	(contributors, 2020)	https://docs.qgis.org/3.10/en/docs/user_manual/processing_algs/gdal/vectorconversion.html?highlight=rasterize#rasterize-vector-to-raster
Raster layer unique values report	Calculate area statistics of the reclassified raster data	(QGIS Development Team, 2022c)	https://docs.qgis.org/3.4/en/docs/user_manual/processing_algs/qgis/rasteranalysis.html
Reproject layer	Harmonise vector CRS	(QGIS Development Team, 2022c)	https://docs.qgis.org/3.10/en/docs/user_manual/processing_algs/qgis/vectorgeneral.html#reproject-layer
r.reclass	Reclassify integer raster values	(GRASS Development Team, 2020)	https://grass.osgeo.org/grass76/manuals/r.reclasshtml
r.recode	Reclassify float raster values	(GRASS Development Team, 2020)	https://grass.osgeo.org/grass76/manuals/r.recode.html
Ruggedness index (TR)	Terrain analysis: Compute TRI of the SRTM 30M DEM	(QGIS Development Team, 2022c)	https://docs.qgis.org/3.10/en/docs/user_manual/processing_algs/qgis/rasterterrainanalysis.html#ruggedness-index
Slope	Terrain analysis: Compute slope of the SRTM 30M DEM	(QGIS Development Team, 2022c)	https://docs.qgis.org/3.10/en/docs/user_manual/processing_algs/qgis/rasterterrainanalysis.html#slope
Warp (reproject)	Harmonise raster CRS	(contributors, 2020)	https://docs.qgis.org/3.10/en/docs/user_manual/processing_algs/gdal/rasterprojections.html#warp-reproject

A.2 RESULTS

A.2.1 *Area statistics*

Table A.2: **Geomorphology**; Count: No. of polygons, m^2: Total area of class, Frequency: No of sites in class

Class	Class Name	count	m^2	Freq. Original	Freq. Reference
1	Rocky basement	14831073	13347965700	57	26
2	Reg / rocky basement	5186287	4667658300	9	0
3	Limestone sediments	10476200	9428580000	9	23
4	Hamada / limestone sediments	5842221	5257998900	7	7
5	Reg / limestone sediments	965921	869328900	4	0
6	Hamada / rocky basement	684308	615877200	3	0
7	Crescentic dunes / alluvial sediments	775855	698269500	2	13
8	Calcerous crust	277935	250141500	1	0
9	Holocene Alluvial sediments	11840477	10656429300		
10	Calcerous crust / limestone sediments	1494251	1344825900	0	13
11	Calcerous crust/ Pleistocene alluvial sediments	46583	41924700		
12	Crescentic dunes	509445	458500500	0	1
13	Hamada	193506	174155400		
14	Hamada/ Pleistocene tertiary conglomerates	14919	13427100		
15	Hills of red sand in Coastal Plain	200562	180505800		
16	Hills of red sand in coastal plain/ Pleistocene alluvial sediments	382051	343845900		
17	Hills of red sand in coastal plain/ rocky basement	2951	2655900		
18	Kurkar ridges in coastal plain/ rocky basement	315915	284323500		
19	Playa	168295	151465500		
20	Pleistocene alluvial Sediments	74600	67140000		
21	Pleistocene tertiary conglomerates	220892	198802800	0	9
22	Reg	608873	547985700		
23	Reg/ Pleistocene alluvial sediments	4853	4367700		
24	Reg/ Pleistocene tertiary conglomerates	12465	11218500		
25	Reg/ Pleistocene tertiary conglomerates	35367	31830300		
26	Sand fields/ limestone sediments	1534285	1380856500		
27	Sand fields/ rocky basement	416072	374464800		
28	Serir	159002	143101800		
29	Serir/ limestone sediments	5346	4811400		
30	Serir/ Pleistocene alluvial sediments	35288	31759200		
31	Serir/ Pleistocene tertiary conglomerates	2551697	2296527300		
32	Serir/ rocky basement	16264	14637600		

Table A.3: **Drainages**; Count: No. of polygons, m^2: Total area of class, Frequency: No of sites in class

Interval	to (km)	Class	count	m^2	Freq. Original	Freq. Reference
0	22	1	433828	97611300	83	46
22.1	42	2	212811	47882475	6	33
42.1	62	3	60625	13640625	1	3
62.1	82	4	18293	4115925	2	1
82.1	102	5	9188	2067300	0	9
102.1	122	6	8870	1995750	0	0
122.1	142	7	6961	1566225	0	0
142.1	162	8	6903	1553175	0	0
162.1	182	9	5442	1224450	0	0
182.1	202	10	3710	834750	0	0
202.1	222	11	2115	475875	0	0
222.1	242	12	1969	443025	0	0
242.1	262	13	2741	616725	0	0
262.1	282	14	2276	512100	0	0
282.1	302	15	1573	353925	0	0
302.1	322	16	2102	472950	0	0

Table A.4: **Hydrogeology**; Count: No. of polygons, m^2: Total area of class, Frequency: No of sites in class

Class	Class name	count	m^2	Freq. Original	Freq. Reference
1	Intergranular aquifers: extensive and highly productive	9308326	8377493400	3	36
2	Intergranular aquifers: local or discontinous productive	827062	744355800	2	12
3	Fissured/ karstic aquifers: extensive and highly productive	2238996	2015096400	0	0
4	Fissured/ karstic aquifers: local or discontinous productive aquifers	31800588	28620529200	12	30
5	Strata with local and limited groundwater resources	13801708	12421537200	75	14
6	Strata with essentially no groundwater resources	682459	614213100	0	0
10	Depleted zone of important aquifers	1069361	962424900	0	0

Table A.5: **Vegetation**; Count: No. of polygons, m^2: Total area of class, Frequency: No of sites in class

Class	Class name	count	m^2	Freq. Original	Freq. Reference
1	Mediterranean woodland	20569169	18512252100	9	44
3	Irano-Turanian	9183988	8265589200	15	18
4	Saharo-Arabian	19519244	17567319600	60	26
5	Sudanian and Sub-Sudanian	7155041	6439536900	6	0
6	Halo- and Hydrophytic	794286	714857400	2	1

Table A.6: **Elevation**; Count: No. of polygons, m^2: Total area of class, Frequency: No of sites in class

Interval	to (km)	Classes	count	m^2	Freq. Original	Freq. Reference
-100	100	1	7761722	7126674260	2	23
100.1	300	2	10685883	9811586568	11	46
300.1	500	3	11018337	10116839882	12	9
500.1	700	4	9382009	8614392791	13	1
700.1	900	5	6327473	5809772491	39	5
900.1	1100	6	4808710	4415271480	15	5
1100.1	1300	7	2801420	2572213718	0	3
1300.1	1500	8	1199508	1101366783	0	0
1500.1	1700	9	408116	374724808.8	0	0
1700.1	1900	10	3673	3372482.879	0	0
-300	-100.1	11	2313815	2124503532	0	0
-500	-300.1	12	1973149	1811710106	0	0

Table A.7: Confusion matrix for the reference dataset

Preservation								
	Reference							
Original data	cat#	Very bad 1	2	3	4	5	Very good 6	Row Sum
	Very bad 1	140	2380	1571	376	0	0	4467
	2	7530	107351	258066	149353	42286	4418	569004
	3	21247	508389	1487985	1435944	640739	56584	4150888
	4	9703	573202	2378073	3336301	1494335	122864	7914478
	5	661	208896	1376151	2298375	1164404	102586	5151073
	Very good 6	0	660	45872	318372	365386	13308	743598
	Col Sum	39281	1400878	5547718	7538721	3707150	299760	18533508

Detailed maps

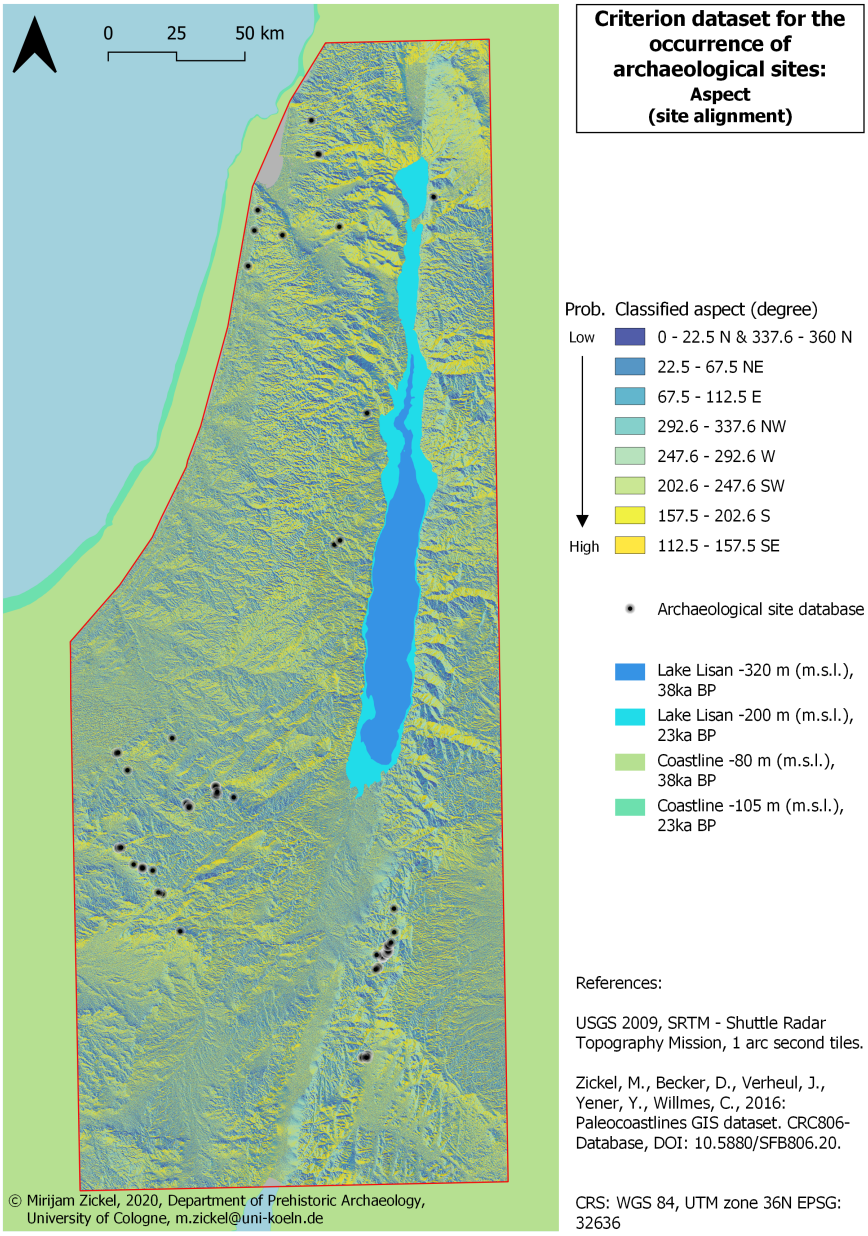

Figure A.2: Aspect.

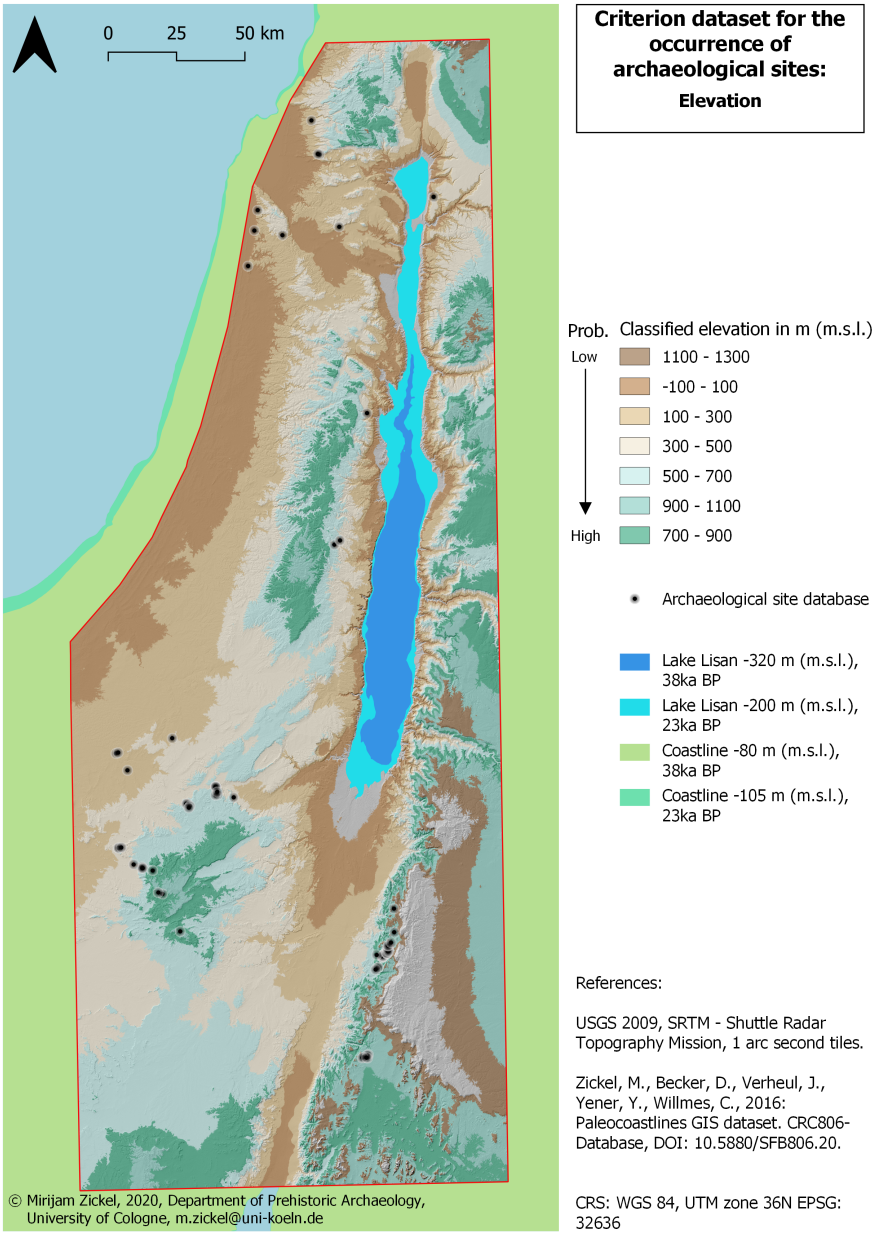

Figure A.3: Elevation.

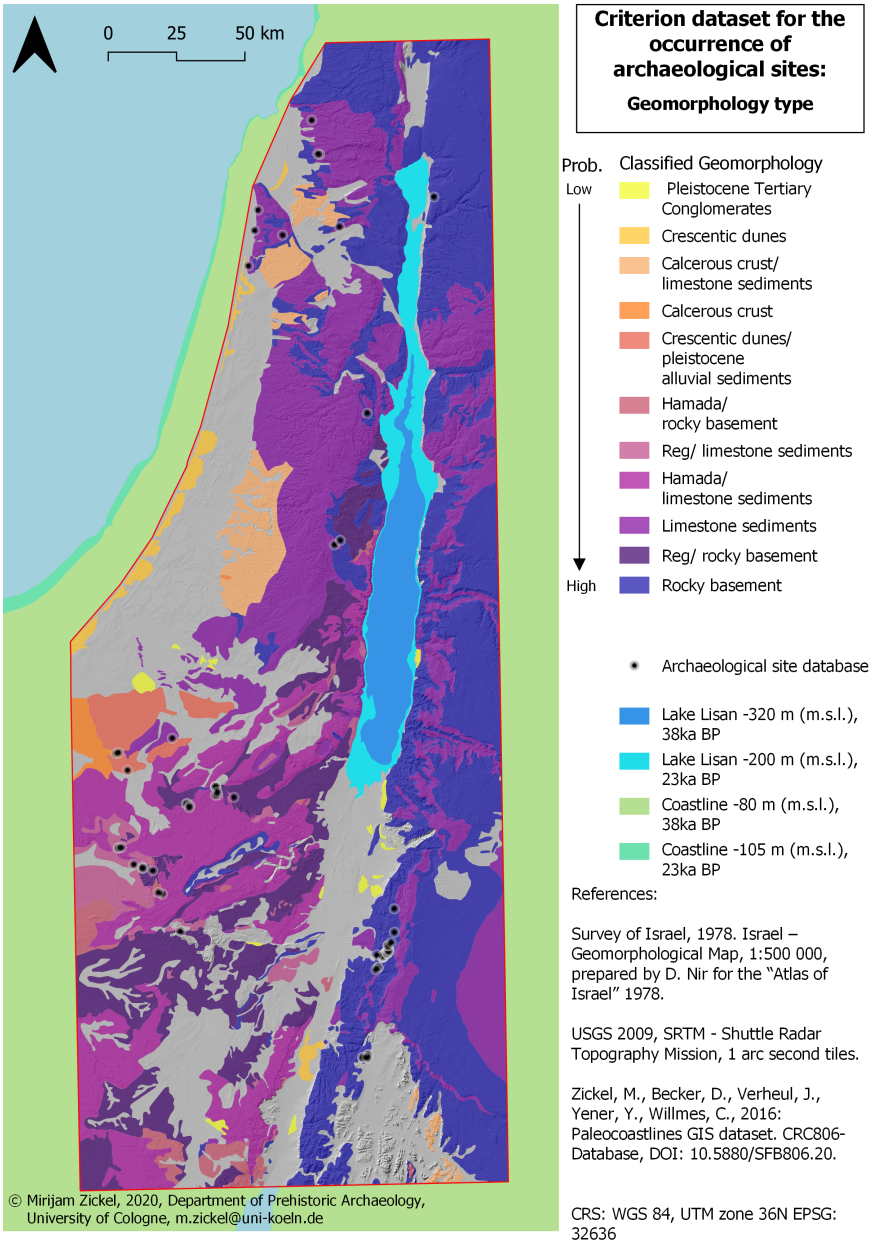

Figure A.4: Geomorphology.

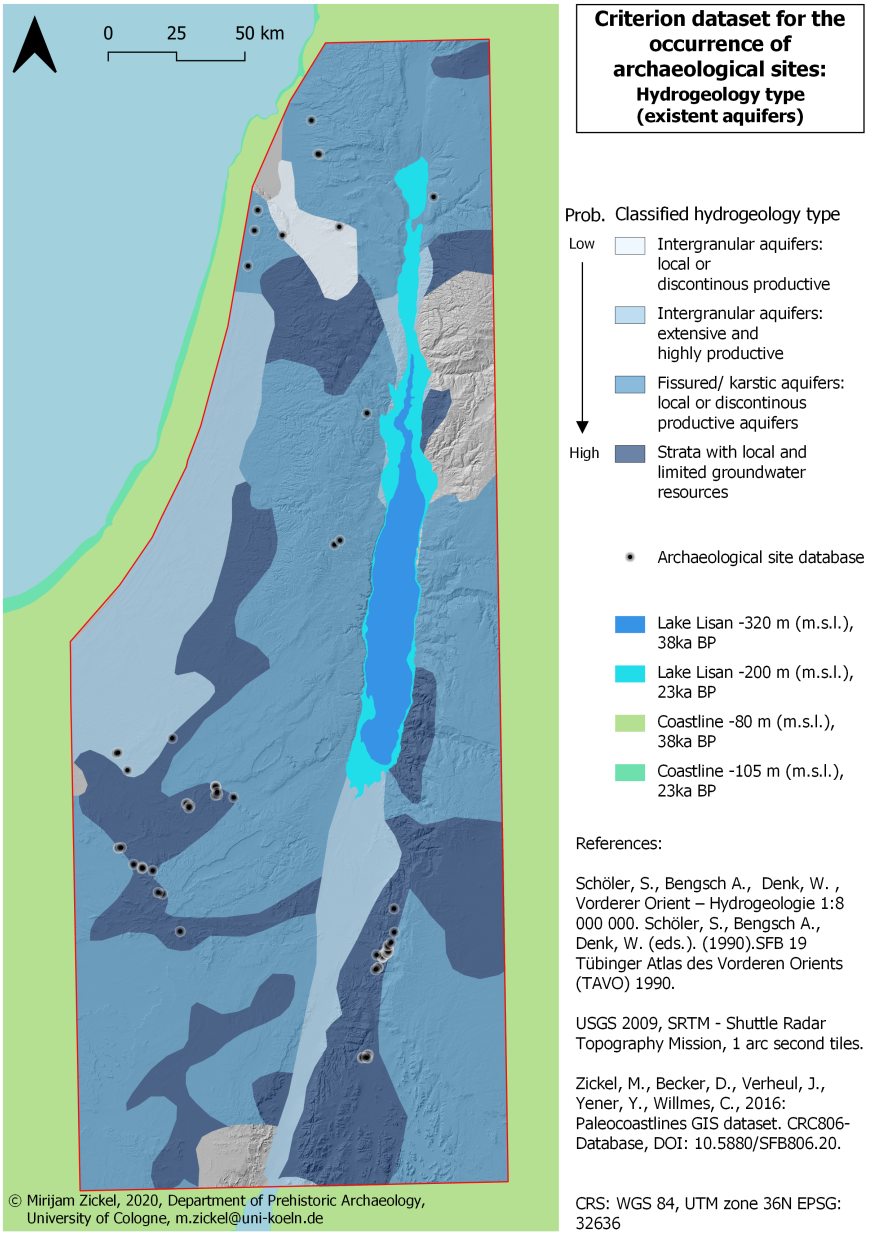

Figure A.5: Hydrogeology.

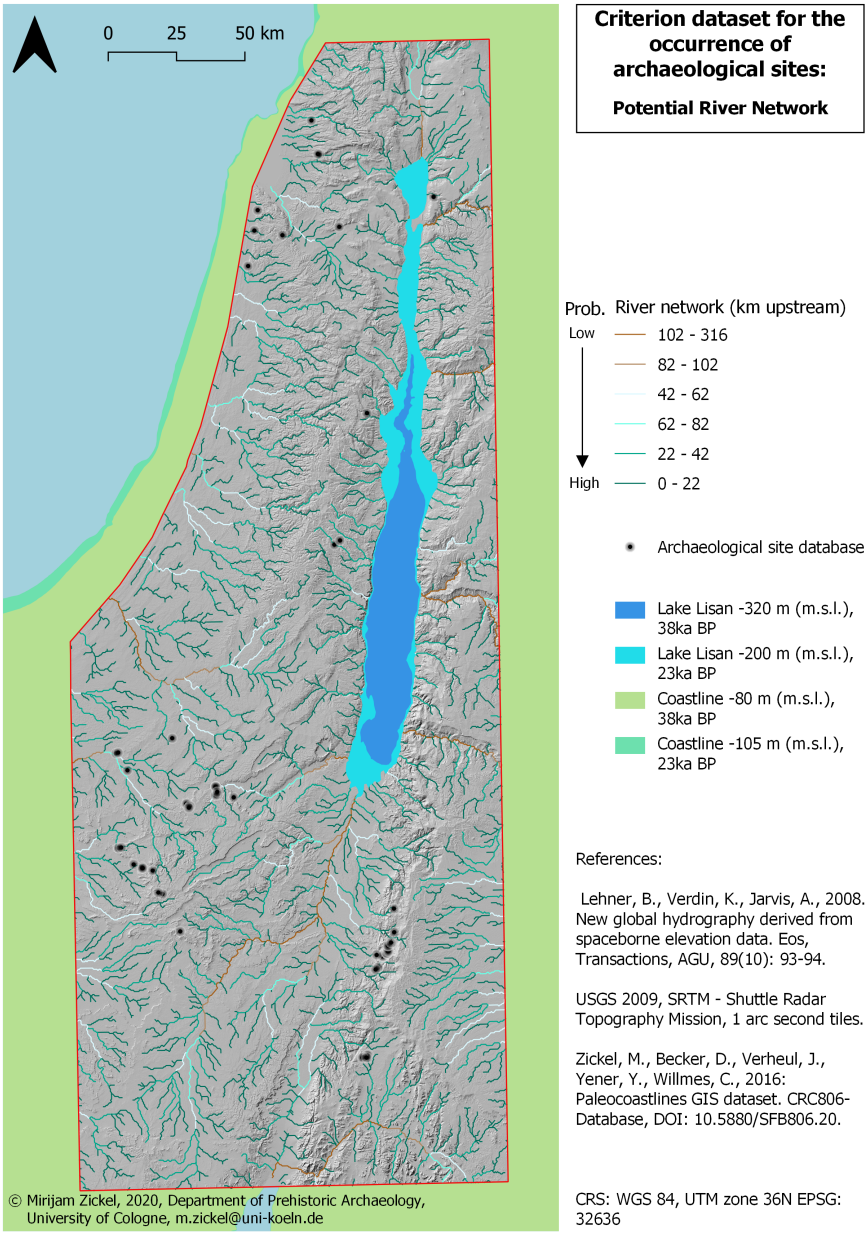

Figure A.6: Potential river network.

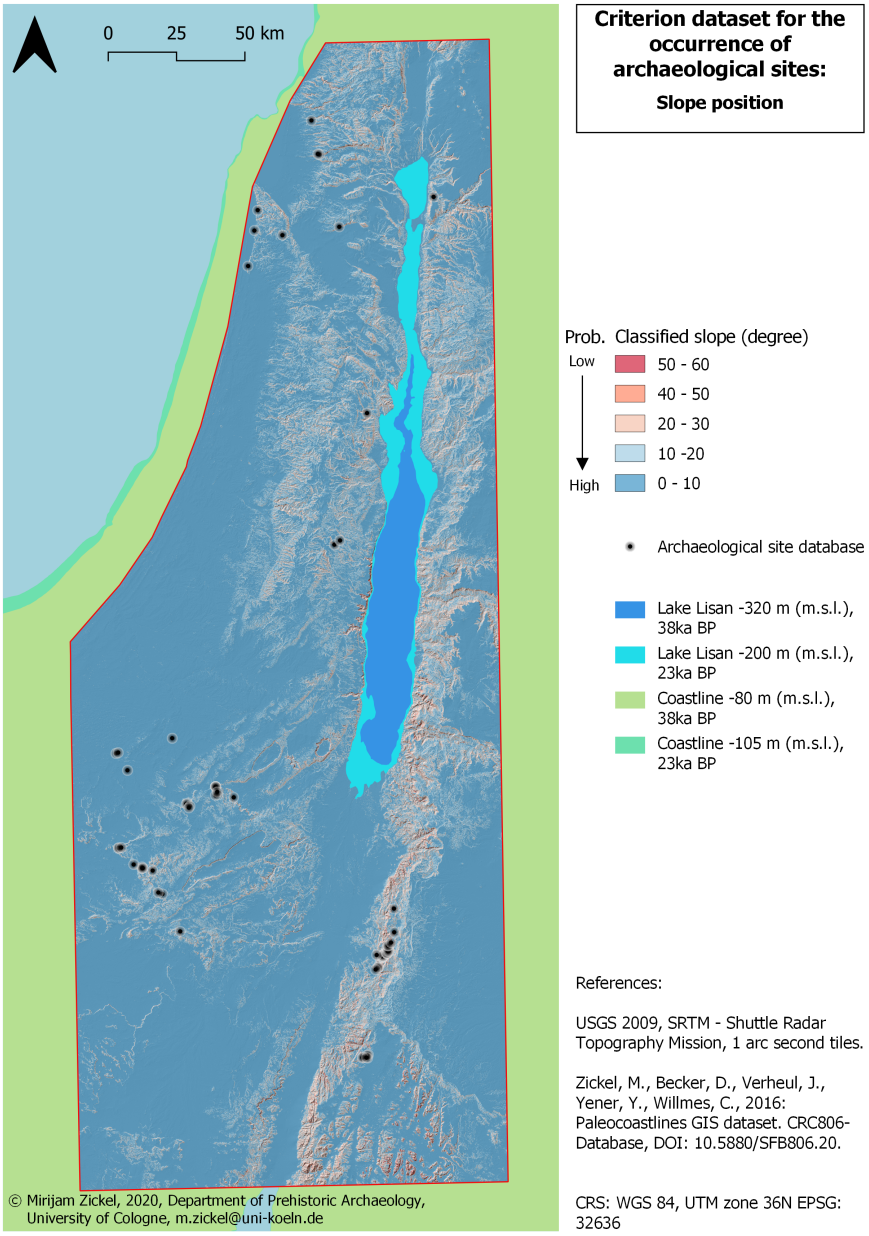

Figure A.7: Slope.

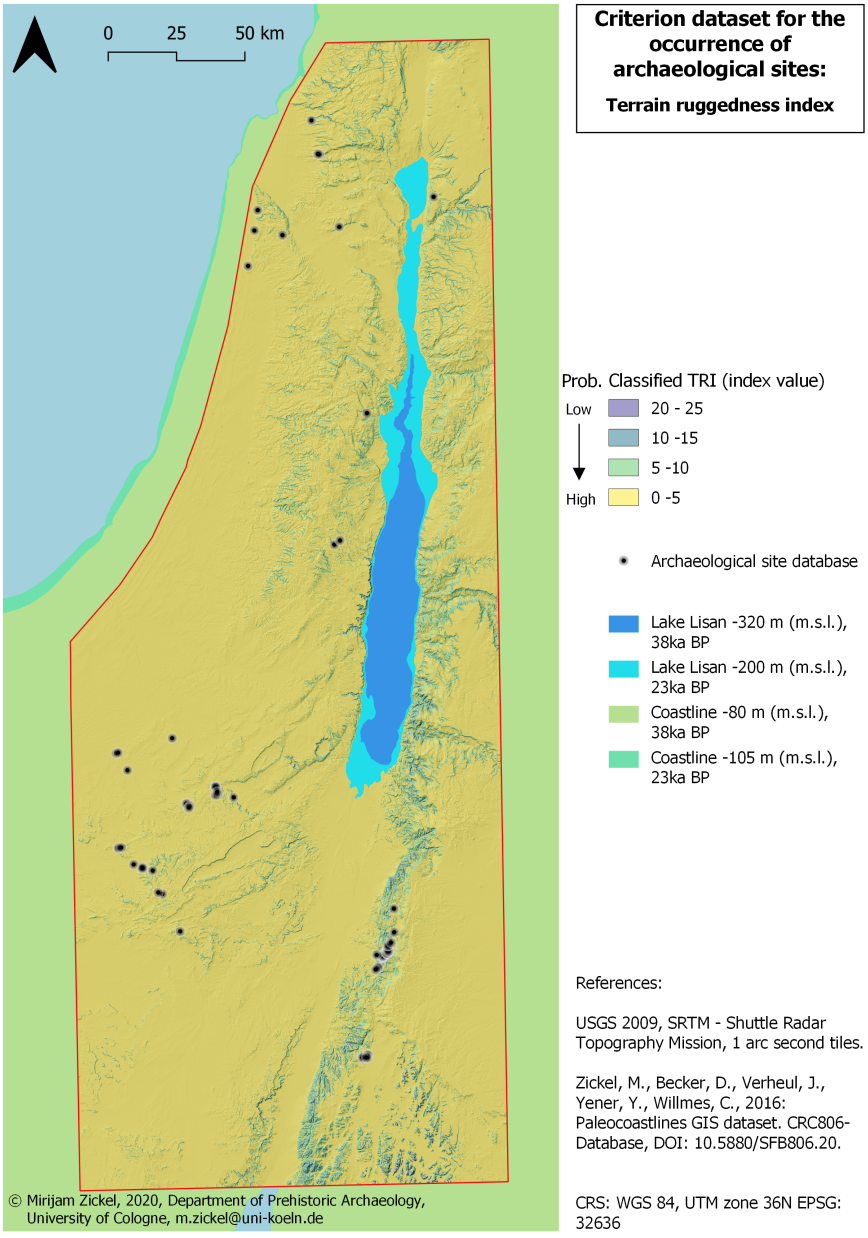

Figure A.8: Terrain Ruggedness Index (TRI).

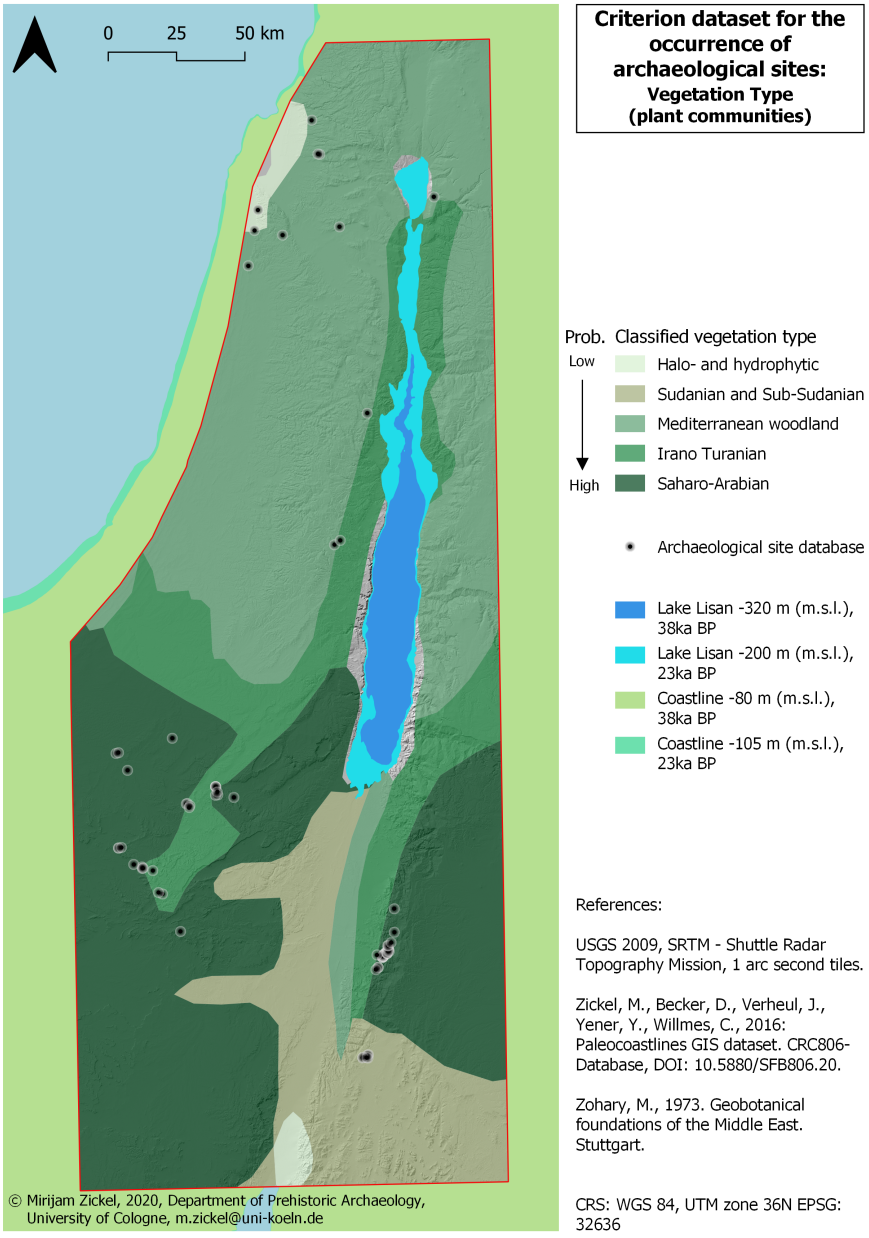

Figure A.9: Vegetation.

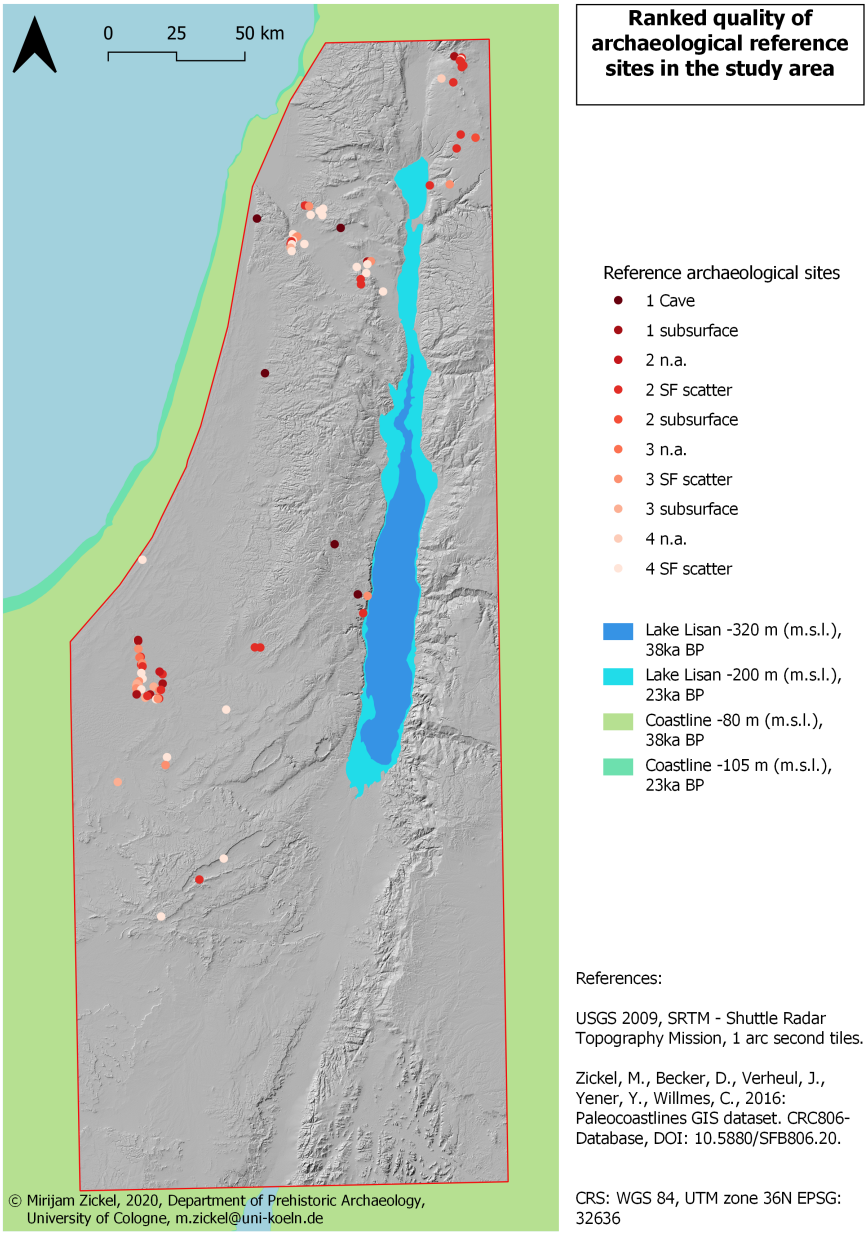

Figure A.10: Reference site ranking.

A.3 DATA

Table A.8: Original sites; only the original dataset is referred to by number on the maps. This is a copy of the supplementary data, which can be found on the Quaternary International journal webpage. (*Continued on next page*)

Dataset	OBJECTID	Site	Site_Type	periods	WGS84_x	WGS84_y	RiV_up_km	Veg_Label	Veg_TYPE	Hygeo_Label	Hygeo_TYPE	LAND_FORM	TYPE	Lform_Sedi	Geomorph_TYPE	DEM	TRI	Slope	Aspect
Original	14	Meged Rockshelter	Rockshelter	single	35.22413639	32.92164156	11.6	Mediterranean woodland	1	Fissured/karstic aquifers: local or discontinous productive aquifers	4		LST_SED	Limestone sediments	3	230	2.49627	8.65009	310.60129
Original	16	Ein Qadis III	Open Air	single	34.49078836	30.57937776	7.9	Irano Turanian	3	Strata with local and limited groundwater resources	5	RG	ROCK	Reg/ rocky basement	2	518	1.75979	3.02403	38.65981
Original	17	Ein Qadis V	Open Air	single	34.49175315	30.57550141	7.9	Irano Turanian	3	Strata with local and limited groundwater resources	5	RG	ROCK	Reg/ rocky basement	2	624	0.67515	1.37792	210.96375
Original	18	Ein Quadis IV	Open Air	single	34.49409118	30.57597876	11.9	Irano Turanian	3	Strata with local and limited groundwater resources	5	RG	ROCK	Reg/ rocky basement	2	621	3.87961	13.01581	34.82449
Original	19	Nahal Nizzana XIII	Open Air	single	34.44041191	30.89974938	60.6	Saharo-Arabian	4	Intergranular aquifers: extensive and highly productive	1	CD	PLEIS_AL_SED	Crescentic dunes/ pleistocene alluvial sediments	7	231	0.71644	1.9483	14.03625
Original	20	Rumilah IV	Open Air	single	34.4595971	30.58828697	15.7	Saharo-Arabian	4	Strata with local and limited groundwater resources	5	RG	LST_SED	Reg/ limestone sediments	5	445	4.22294	15.33663	226.21887
Original	21	Sde Divshon D27B	Open Air	single	34.78427639	30.81383125	33.6	Saharo-Arabian	4	Strata with local and limited groundwater resources	5	HD	LST_SED	Hamada/ limestone sediments	4	519	0.75813	3.30532	0
Original	26	Azariq IV	Open Air	single	34.39702762	30.95613961	66.7	Saharo-Arabian	4	Intergranular aquifers: extensive and highly productive	1	CC		Calcerous crust	8	188	0.39809	1.79945	66.80141
Original	27	Azariq VI	Open Air	single	34.40603536	30.95860416	66.7	Saharo-Arabian	4	Intergranular aquifers: extensive and highly productive	1	CD	PLEIS_AL_SED	Crescentic dunes/ pleistocene alluvial sediments	7	196	0.36135	0.33426	225
Original	28	Boker A	Open Air	single	34.77623279	30.84136947	20.6	Irano Turanian	3	Strata with local and limited groundwater resources	5	RG	ROCK	Reg/ rocky basement	2	369	2.20679	7.64231	135
Original	29	Boker BE	Open Air	single	34.77623279	30.84136947	20.6	Irano Turanian	3	Strata with local and limited groundwater resources	5	RG	ROCK	Reg/ rocky basement	2	369	2.20679	7.64231	135
Original	30	Boker C	Open Air	single	34.77623279	30.84136947	20.6	Irano Turanian	3	Strata with local and limited groundwater resources	5	RG	ROCK	Reg/ rocky basement	2	369	2.20679	7.64231	135
Original	31	Boker Tachtit	Open Air	single	34.77738105	30.84070418	20.6	Irano Turanian	3	Strata with local and limited groundwater resources	5	RG	ROCK	Reg/ rocky basement	2	374	2.05483	7.97723	317.38593
Original	32	D22 Arkov	Open Air	single	34.77609752	30.81290029	33.6	Saharo-Arabian	4	Strata with local and limited groundwater resources	5	HD	LST_SED	Hamada/ limestone sediments	4	531	0.82092	3.40477	326.30994
Original	33	D27A	Open Air	single	34.7829446	30.82426342	33.6	Saharo-Arabian	4	Strata with local and limited groundwater resources	5	HD	LST_SED	Hamada/ limestone sediments	4	512	0.61244	1.79945	336.80139
Original	34	Ein Aqev D31	Open Air	single	34.84564045	30.80524496	20.6	Saharo-Arabian	4	Strata with local and limited groundwater resources	5	RG	ROCK	Reg/ rocky basement	2	403	5.39359	20.91685	122.66091
Original	35	El Khiam	Open Air	single	35.25008843	31.6332031	11.8	Mediterranean woodland	1	Fissured/karstic aquifers: local or discontinous productive aquifers	4		LST_SED	Limestone sediments	3	460	6.13465	23.23763	98.2858
Original	36	Erq el Ahmar	Cave	single	35.2723896	31.64668827	24.8	Irano Turanian	3	Fissured/karstic aquifers: local or discontinous productive aquifers	4		ROCK	Rocky basement	1	383	1.71805	3.40477	123.69006
Original	37	G11	Open Air	single	34.56777114	30.48970253	18.8	Irano Turanian	3	Strata with local and limited groundwater resources	5	HD	ROCK	Hamada/ rocky basement	6	877	2.81565	11.01857	126.38435
Original	38	Har Horesha I	Open Air	single	34.53194463	30.56747237	11.9	Irano Turanian	3	Strata with local and limited groundwater resources	5	HD	ROCK	Hamada/ rocky basement	6	876	3.88897	15.46821	169.69516
Original	39	Har Lavan IV	Open Air	single	34.66747322	30.78667308	10	Irano Turanian	3	Strata with local and limited groundwater resources	5	HD	LST_SED	Hamada/ limestone sediments	4	642	3.31021	10.0986	346.60751
Original	40	Har Lavan V	Open Air	single	34.66383116	30.78640259	10	Saharo-Arabian	4	Strata with local and limited groundwater resources	5	HD	LST_SED	Hamada/ limestone sediments	4	602	6.08236	24.06508	295.14478
Original	41	Har Saggi I	Open Air	single	34.63356199	30.36531592	9.7	Saharo-Arabian	4	Strata with local and limited groundwater resources	5	RG	ROCK	Reg/ rocky basement	2	886	3.27635	11.93185	51.34019
Original	42	J440	Rockshelter	single	35.31712963	29.93741902	12.5	Sudanian and Sub-Sudanian	5	Strata with local and limited groundwater resources	5		ROCK	Rocky basement	1	1004	5.4088	16.92878	57.17146
Original	43	Jebel Humeima (J412)	Rockshelter	single	35.33953679	29.94715411	12.5	Sudanian and Sub-Sudanian	5	Strata with local and limited groundwater resources	5		ROCK	Rocky basement	1	962	2.1039	7.43229	145.30484
Original	44	K9A	Open Air	single	34.55230516	30.49475742	18.8	Irano Turanian	3	Strata with local and limited groundwater resources	5	HD	ROCK	Hamada/ rocky basement	6	941	3.36576	4.85523	119.0546
Original	54	Madamagh	Cave	double	35.44802292	30.34979982	8.5	Saharo-Arabian	4	Strata with local and limited groundwater resources	5		ROCK	Rocky basement	1	982	4.67582	13.52492	174.09386
Original	55	Qadesh Barnea 601	Open Air	single	34.40235454	30.64307447	6.5	Saharo-Arabian	4	Fissured/karstic aquifers: local or discontinous productive aquifers	4	RG	LST_SED	Reg/ limestone sediments	5	348	1.39021	5.17498	239.93141
Original	56	Qadesh Barnea 602	Open Air	single	34.40260752	30.64382953	6.5	Saharo-Arabian	4	Fissured/karstic aquifers: local or discontinous productive aquifers	4	RG	LST_SED	Reg/ limestone sediments	5	355	1.21325	4.00458	225
Original	57	Qadesh Barnea 9	Open Air	single	34.41315994	30.64493506	8.8	Saharo-Arabian	4	Strata with local and limited groundwater resources	5	RG	LST_SED	Reg/ limestone sediments	5	367	1.03132	4.05963	144.46233
Original	58	Ramat Matred I	Open Air	single	34.67761585	30.77936302	10	Irano Turanian	3	Strata with local and limited groundwater resources	5	HD	LST_SED	Hamada/ limestone sediments	4	633	0.4749	2.03237	324.46231
Original	59	Ramat Matred IV	Open Air	single	34.67347608	30.77345122	10	Irano Turanian	3	Strata with local and limited groundwater resources	5	HD	LST_SED	Hamada/ limestone sediments	4	642	0.91723	3.40477	213.69006
Original	60	Sabra 4 Palmview 1	Open Air	single	35.4049319	30.27183515	20.7	Saharo-Arabian	4	Strata with local and limited groundwater resources	5		ROCK	Rocky basement	1	802	5.15557	20.62469	116.00334
Original	61	Sabra 4 Palmview 3	Open Air	single	35.40458883	30.27225639	20.7	Saharo-Arabian	4	Strata with local and limited groundwater resources	5		ROCK	Rocky basement	1	816	3.77952	13.93908	105.42216
Original	62	Shunera XVI	Open Air	single	34.61362593	31.00372702	8.1	Saharo-Arabian	4	Strata with local and limited groundwater resources	5		LST_SED	Limestone sediments	3	309	0.38453	0.94534	180
Original	63	Siq Umm al-Alda 1	Open Air	single	35.4490627	30.42774941	23.8	Saharo-Arabian	4	Strata with local and limited groundwater resources	5		ROCK	Rocky basement	1	1000	4.03566	15.20035	210.06857
Original	65	Tor Aeid (J432)	Rockshelter	single	35.33747809	29.93658272	13.6	Sudanian and Sub-Sudanian	5	Strata with local and limited groundwater resources	5		ROCK	Rocky basement	1	972	3.98875	15.09632	156.5713
Original	66	Tor Fawaz (J403)	Rockshelter	single	35.33656023	29.94590289	12.5	Sudanian and Sub-Sudanian	5	Strata with local and limited groundwater resources	5		ROCK	Rocky basement	1	965	0.79508	2.67213	135
Original	67	Tor Hamar (J431)	Rockshelter	single	35.3192625	29.93923737	12.5	Sudanian and Sub-Sudanian	5	Strata with local and limited groundwater resources	5		ROCK	Rocky basement	1	1019	5.44135	20.89457	276.20343
Original	70	Wadi Aghar (J433)	Rockshelter	single	35.33311274	29.9376155	13.6	Sudanian and Sub-Sudanian	5	Strata with local and limited groundwater resources	5		ROCK	Rocky basement	1	984	6.21769	24.1685	161.23193
Original	74	El Wad Cave	Cave	Multi	34.96368899	32.67499348	17.7	Halo- and hydrophytic	6	Fissured/karstic aquifers: local or discontinous productive aquifers	4		LST_SED	Limestone sediments	3	31	0.67688	2.40896	258.69006
Original	75	Fazael Site IX	Open Air	single	35.38740227	32.065088	14.8	Mediterranean woodland	1	Fissured/karstic aquifers: local or discontinous productive aquifers	4		ROCK	Rocky basement	1	220	7.24976	25.56725	44.3013

Original	76	Hayonim Cave	Cave	Multi	35.21751604	32.92361131	11.6	Mediterranean woodland	1	Fissured/karstic aquifers: local or discontinous productive aquifers	4	LST_SED	Limestone sediments	3	224	5.37122	20.66774	174.35175
Original	77	Iraq El-Baroud/Sefunim	Cave	Multi	34.97825224	32.74224492	16.1	Halo- and hydrophytic	6	Fissured/karstic aquifers: local or discontinous productive aquifers	4	LST_SED	Limestone sediments	3	192	1.38154	5.49582	300.96375
Original	78	Kebara	Cave	Multi	34.93685836	32.55841747	25.5	Mediterranean woodland	1	Fissured/karstic aquifers: local or discontinous productive aquifers	4	LST_SED	Limestone sediments	3	47	4.93749	20.89457	276.20343
Original	80	Manot Cave	Cave	Multi	35.19516167	33.03489078	10.9	Mediterranean woodland	1	Fissured/karstic aquifers: local or discontinous productive aquifers	4	LST_SED	Limestone sediments	3	208	3.28003	13.1115	202.9321
Original	81	Nahal Ein Gev I	Open Air	double	35.66607521	32.77318057	9.1	Mediterranean woodland	1	Fissured/karstic aquifers: local or discontinous productive aquifers	4	ROCK	Rocky basement	1	101	5.582	17.89943	24.92847
Original	82	Qafzeh	Cave	Multi	35.29529666	32.68177953	17.3	Mediterranean woodland	1	Intergranular aquifers: extensive and highly productive	2	LST_SED	Limestone sediments	3	291	5.45461	20.66774	264.35175
Original	83	Raqefet	Cave	Multi	35.0727609	32.65804738	17.7	Mediterranean woodland	1	Intergranular aquifers: extensive and highly productive	2	ROCK	Rocky basement	1	227	6.10055	18.23173	247.9321
Original	85	Ansab 1	Open Air	single	35.38332996	30.23412835	9.9	Saharo-Arabian	4	Strata with local and limited groundwater resources	5	ROCK	Rocky basement	1	606	2.93989	13.07969	186.11551
Original	86	Absab 2	Open Air	single	35.38361098	30.2343622	9.9	Saharo-Arabian	4	Strata with local and limited groundwater resources	5	ROCK	Rocky basement	1	614	3.27408	6.03131	231.34019
Original	87	Sabra 3 Centre	Open Air	single	35.40094949	30.26697179	20.7	Saharo-Arabian	4	Strata with local and limited groundwater resources	5	ROCK	Rocky basement	1	788	2.2692	7.17787	121.6075
Original	88	Sabra 3 Nord	Open Air	single	35.40103577	30.26719231	20.7	Saharo-Arabian	4	Strata with local and limited groundwater resources	5	ROCK	Rocky basement	1	788	1.41776	4.77478	122.90524
Original	91	Sabra 4 PV 2	Open Air	single	35.40478581	30.27181077	20.7	Saharo-Arabian	4	Strata with local and limited groundwater resources	5	ROCK	Rocky basement	1	802	5.15557	20.62469	116.00334
Original	92	Sabra 4 PV 4	Open Air	single	35.40500385	30.27265468	20.7	Saharo-Arabian	4	Strata with local and limited groundwater resources	5	ROCK	Rocky basement	1	807	4.10522	16.19072	112.55725
Original	93	Sabra 4 PV 5	Open Air	single	35.40399135	30.27289879	20.7	Saharo-Arabian	4	Strata with local and limited groundwater resources	5	ROCK	Rocky basement	1	819	1.46444	5.20691	275.19443
Original	94	Sabra 10	Open Air	single	35.40577115	30.27513919	20.7	Saharo-Arabian	4	Strata with local and limited groundwater resources	5	ROCK	Rocky basement	1	826	2.41858	9.55202	101.30994
Original	95	2010-1	Open Air	single	35.40499593	30.27233009	20.7	Saharo-Arabian	4	Strata with local and limited groundwater resources	5	ROCK	Rocky basement	1	805	4.39752	17.60105	102.77124
Original	96	2010-2	Open Air	single	35.40503056	30.27289773	20.7	Saharo-Arabian	4	Strata with local and limited groundwater resources	5	ROCK	Rocky basement	1	811	3.51111	13.93908	111.44774
Original	97	2010-3	Open Air	single	35.40493773	30.2729265	20.7	Saharo-Arabian	4	Strata with local and limited groundwater resources	5	ROCK	Rocky basement	1	811	3.51111	13.93908	111.44774
Original	98	2010-4	Open Air	single	35.40581113	30.27337048	20.7	Saharo-Arabian	4	Strata with local and limited groundwater resources	5	ROCK	Rocky basement	1	811	3.64533	12.01982	125.53767
Original	99	2010-5	Open Air	single	35.40138483	30.27212579	20.7	Saharo-Arabian	4	Strata with local and limited groundwater resources	5	ROCK	Rocky basement	1	814	1.70201	5.37395	164.74487
Original	100	2010-6	Rockshelter	single	35.40284643	30.27026784	20.7	Saharo-Arabian	4	Strata with local and limited groundwater resources	5	ROCK	Rocky basement	1	803	5.18936	19.94469	130.38934
Original	101	2010-7	Open Air	single	35.40462105	30.27272485	20.7	Saharo-Arabian	4	Strata with local and limited groundwater resources	5	ROCK	Rocky basement	1	819	3.72855	14.343	107.85032
Original	102	2010-8	Open Air	single	35.40580404	30.27350592	20.7	Saharo-Arabian	4	Strata with local and limited groundwater resources	5	ROCK	Rocky basement	1	811	3.64533	12.01982	125.53767
Original	103	2010-9	Open Air	single	35.40780255	30.27746515	20.7	Saharo-Arabian	4	Strata with local and limited groundwater resources	5	ROCK	Rocky basement	1	841	3.0364	9.95421	203.55226
Original	104	2010-10	Open Air	single	35.41206614	30.28181558	20.7	Saharo-Arabian	4	Strata with local and limited groundwater resources	5	ROCK	Rocky basement	1	874	2.8645	9.35257	202.0679
Original	105	2010-11	Open Air	single	35.41335301	30.28131377	20.7	Saharo-Arabian	4	Strata with local and limited groundwater resources	5	ROCK	Rocky basement	1	857	4.14002	15.46821	153.43495
Original	106	2010-12	Open Air	single	35.41331787	30.28115206	20.7	Saharo-Arabian	4	Strata with local and limited groundwater resources	5	ROCK	Rocky basement	1	857	4.14002	15.46821	153.43495
Original	107	2010-13	Open Air	single	35.40054868	30.26851497	20.7	Saharo-Arabian	4	Strata with local and limited groundwater resources	5	ROCK	Rocky basement	1	796	1.29436	4.53691	188.97263
Original	108	2010-15	Open Air	single	35.40363153	30.2713539	20.7	Saharo-Arabian	4	Strata with local and limited groundwater resources	5	ROCK	Rocky basement	1	804	2.99409	11.38804	124.99202
Original	109	2010-16	Open Air	single	35.4041038	30.27154367	20.7	Saharo-Arabian	4	Strata with local and limited groundwater resources	5	ROCK	Rocky basement	1	804	3.55806	14.2604	166.86597
Original	110	2010-17	Open Air	single	35.40354139	30.27106691	20.7	Saharo-Arabian	4	Strata with local and limited groundwater resources	5	ROCK	Rocky basement	1	800	3.74982	14.74095	131.18593
Original	111	2010-18	Open Air	single	35.42420335	30.29313714	9.8	Saharo-Arabian	4	Strata with local and limited groundwater resources	5	ROCK	Rocky basement	1	868	2.28864	7.29875	194.93143
Original	112	2010-19	Open Air	single	35.41447277	30.28077896	20.7	Saharo-Arabian	4	Strata with local and limited groundwater resources	5	ROCK	Rocky basement	1	817	3.50348	12.85451	130.60129
Original	113	2010-20	Open Air	single	35.41756768	30.28365339	20.7	Saharo-Arabian	4	Strata with local and limited groundwater resources	5	ROCK	Rocky basement	1	832	3.3362	12.18502	133.45184
Original	114	2010-21	Open Air	single	35.40499448	30.27525269	20.7	Saharo-Arabian	4	Strata with local and limited groundwater resources	5	ROCK	Rocky basement	1	835	2.21706	8.37613	191.30994
Original	115	2010-22	Open Air	single	35.40072756	30.27202059	20.7	Saharo-Arabian	4	Strata with local and limited groundwater resources	5	ROCK	Rocky basement	1	818	3.01087	12.83418	137.93567
Original	116	2010-23	Open Air	single	35.42091525	30.28749725	20.7	Saharo-Arabian	4	Strata with local and limited groundwater resources	5	ROCK	Rocky basement	1	839	1.89753	6.53862	120.25644
Original	117	2010-24	Open Air	single	35.42474023	30.29467867	9.8	Saharo-Arabian	4	Strata with local and limited groundwater resources	5	ROCK	Rocky basement	1	877	2.77155	12.21947	72.25533
Original	118	2010-25	Open Air	single	35.41918203	30.28040333	20.7	Saharo-Arabian	4	Strata with local and limited groundwater resources	5	ROCK	Rocky basement	1	930	20.47709	55.23666	339.90479
Original	119	2010-26	Open Air	single	35.41846457	30.28038953	20.7	Saharo-Arabian	4	Strata with local and limited groundwater resources	5	ROCK	Rocky basement	1	880	13.87944	45.26429	332.49231
Original	120	2010-27	Open Air	single	35.41792792	30.28139167	20.7	Saharo-Arabian	4	Strata with local and limited groundwater resources	5	ROCK	Rocky basement	1	830	2.52448	9.28313	280.17551
Original	121	2010-28	Open Air	single	35.42409565	30.29256185	9.8	Saharo-Arabian	4	Strata with local and limited groundwater resources	5	ROCK	Rocky basement	1	866	1.68519	6.03131	141.34019
Original	122	2010-29	Open Air	single	35.42137164	30.29718555	10.1	Saharo-Arabian	4	Strata with local and limited groundwater resources	5	ROCK	Rocky basement	1	1020	13.89707	41.77062	115.14478
Original	123	2010-30	Open Air	single	35.42641951	30.28773805	9.8	Saharo-Arabian	4	Strata with local and limited groundwater resources	5	ROCK	Rocky basement	1	913	2.92696	11.82977	302.125
Original	124	2010-31	Open Air	single	35.42231842	30.28707439	20.7	Saharo-Arabian	4	Strata with local and limited groundwater resources	5	ROCK	Rocky basement	1	866	4.63601	10.75458	267.51044
Original	125	Abu Shaher	Open Air	single	35.37960047	30.27591538	20.7	Irano Turanian	3	Strata with local and limited groundwater resources	5	ROCK	Rocky basement	1	716	7.36568	29.83587	125.63349
Original	126	Al-Halla 1	Open Air	single	35.42256101	30.3058139	10.1	Saharo-Arabian	4	Strata with local and limited groundwater resources	5	ROCK	Rocky basement	1	978	2.13415	8.89691	198.43495
Original	127	Al-Halla 2	Open Air	single	35.42350921	30.30548063	10.1	Saharo-Arabian	4	Strata with local and limited groundwater resources	5	ROCK	Rocky basement	1	977	1.55783	3.54868	273.81409
Original	128	Al Anbat Coffeeshop	Open Air	single	35.43491343	30.31599377	10.1	Saharo-Arabian	4	Strata with local and limited groundwater resources	5	ROCK	Rocky basement	1	1018	3.90524	12.11577	2.2026
Original	129	Al Takhir	Open Air	single	35.37417434	30.22793508	9.9	Saharo-Arabian	4	Strata with local and limited groundwater resources	5	ROCK	Rocky basement	1	611	2.88914	8.56191	350.53769

Table A.9: Reference sites, only the original dataset is referred to by number on the maps. This is a copy of the supplementary data, which can be found on the Quaternary International journal webpage.(*Continued on next page*)

Dataset	OBJECTID	Site	Site_Type	periods	WGS84_x	WGS84_y	RiV_up_km	Veg_Label	Veg_TYPE	Hygeo_Label	Hygeo_TYPE	LAND_FORM	TYPE	Lform_Sedi	Geomorph_TYPE	DEM	TRI	Slope	Aspect
Original	14	Meged Rockshelter	Rockshelter	single	35.22413639	32.92164156	11.6	Mediterranean woodland	1	Fissured/karstic aquifers: local or discontinous productive aquifers	4		LST_SED	Limestone sediments	3	230	2.49627	8.65009	310.60129
Original	16	Ein Qadis III	Open Air	single	34.49078836	30.57937776	7.9	Irano Turanian	3	Strata with local and limited groundwater resources	5	RG	ROCK	Reg/ rocky basement	2	518	1.75979	3.02403	38.65981
Original	17	Ein Qadis V	Open Air	single	34.49175315	30.57550141	7.9	Irano Turanian	3	Strata with local and limited groundwater resources	5	RG	ROCK	Reg/ rocky basement	2	624	0.67515	1.37792	210.96375
Original	18	Ein Quadis IV	Open Air	single	34.49409118	30.57597876	11.9	Irano Turanian	3	Strata with local and limited groundwater resources	5	RG	ROCK	Reg/ rocky basement	2	621	3.87961	13.01581	34.82449
Original	19	Nahal Nizzana XIII	Open Air	single	34.44041191	30.89974938	60.6	Saharo-Arabian	4	Intergranular aquifers: extensive and highly productive	1	CD	PLEIS_AL_SED	Crescentic dunes/ pleistocene alluvial sediments	7	231	0.71644	1.9483	14.03625
Original	20	Rumilah IV	Open Air	single	34.4595971	30.58828697	15.7	Saharo-Arabian	4	Strata with local and limited groundwater resources	5	RG	LST_SED	Reg/ limestone sediments	5	445	4.22294	15.33663	226.21887
Original	21	Sde Divshon D27B	Open Air	single	34.78427639	30.81383125	33.6	Saharo-Arabian	4	Strata with local and limited groundwater resources	5	HD	LST_SED	Hamada/ limestone sediments	4	519	0.75813	3.30532	0
Original	26	Azariq IV	Open Air	single	34.39702762	30.95613961	66.7	Saharo-Arabian	4	Intergranular aquifers: extensive and highly productive	1	CC		Calcerous crust	8	188	0.39809	1.79945	66.80141
Original	27	Azariq VI	Open Air	single	34.40603536	30.95860416	66.7	Saharo-Arabian	4	Intergranular aquifers: extensive and highly productive	1	CD	PLEIS_AL_SED	Crescentic dunes/ pleistocene alluvial sediments	7	196	0.36135	0.33426	225
Original	28	Boker A	Open Air	single	34.77623279	30.84136947	20.6	Irano Turanian	3	Strata with local and limited groundwater resources	5	RG	ROCK	Reg/ rocky basement	2	369	2.20679	7.64231	135
Original	29	Boker BE	Open Air	single	34.77623279	30.84136947	20.6	Irano Turanian	3	Strata with local and limited groundwater resources	5	RG	ROCK	Reg/ rocky basement	2	369	2.20679	7.64231	135
Original	30	Boker C	Open Air	single	34.77623279	30.84136947	20.6	Irano Turanian	3	Strata with local and limited groundwater resources	5	RG	ROCK	Reg/ rocky basement	2	369	2.20679	7.64231	135
Original	31	Boker Tachtit	Open Air	single	34.77738105	30.84070418	20.6	Irano Turanian	3	Strata with local and limited groundwater resources	5	RG	ROCK	Reg/ rocky basement	2	374	2.05483	7.97723	317.38593
Original	32	D22 Arkov	Open Air	single	34.77609752	30.81290029	33.6	Saharo-Arabian	4	Strata with local and limited groundwater resources	5	HD	LST_SED	Hamada/ limestone sediments	4	531	0.82092	3.40477	326.30994
Original	33	D27A	Open Air	single	34.7829446	30.82426342	33.6	Saharo-Arabian	4	Strata with local and limited groundwater resources	5	HD	LST_SED	Hamada/ limestone sediments	4	512	0.61244	1.79945	336.80139
Original	34	Ein Aqev D31	Open Air	single	34.84564045	30.80524496	20.6	Saharo-Arabian	4	Strata with local and limited groundwater resources	5	RG	ROCK	Reg/ rocky basement	2	403	5.39359	20.91685	122.66091
Original	35	El Khiam	Open Air	single	35.22500843	31.6332031	11.8	Mediterranean woodland	1	Fissured/karstic aquifers: local or discontinous productive aquifers	4		LST_SED	Limestone sediments	3	460	6.13465	23.23763	98.2858
Original	36	Erq el Ahmar	Cave	single	35.2723896	31.64668827	24.8	Irano Turanian	3	Fissured/karstic aquifers: local or discontinous productive aquifers	4		ROCK	Rocky basement	1	383	1.71805	3.40477	123.69006
Original	37	G11	Open Air	single	34.56777114	30.48970253	18.8	Irano Turanian	3	Strata with local and limited groundwater resources	5	HD	ROCK	Hamada/ rocky basement	6	877	2.81565	11.01857	126.38435
Original	38	Har Horesha I	Open Air	single	34.53194463	30.56747237	11.9	Irano Turanian	3	Strata with local and limited groundwater resources	5	HD	ROCK	Hamada/ rocky basement	6	876	3.88897	15.46821	169.69516
Original	39	Har Lavan IV	Open Air	single	34.66747322	30.78667308	10	Irano Turanian	3	Strata with local and limited groundwater resources	5	HD	LST_SED	Hamada/ limestone sediments	4	642	3.31021	10.0986	346.60751
Original	40	Har Lavan V	Open Air	single	34.66383116	30.78640259	10	Saharo-Arabian	4	Strata with local and limited groundwater resources	5	HD	LST_SED	Hamada/ limestone sediments	4	602	6.08236	24.06508	295.14478
Original	41	Har Saggi I	Open Air	single	34.63356199	30.36531592	9.7	Saharo-Arabian	4	Strata with local and limited groundwater resources	5	RG	ROCK	Reg/ rocky basement	2	886	3.27635	11.93185	51.34019
Original	42	J440	Rockshelter	single	35.31712963	29.93741902	12.5	Sudanian and Sub-Sudanian	5	Strata with local and limited groundwater resources	5		ROCK	Rocky basement	1	1004	5.4088	16.92878	57.17146
Original	43	Jebel Humeima (J412)	Rockshelter	single	35.33953679	29.94715411	12.5	Sudanian and Sub-Sudanian	5	Strata with local and limited groundwater resources	5		ROCK	Rocky basement	1	962	2.1039	7.43229	145.30484
Original	44	K9A	Open Air	single	34.55230516	30.49475742	18.8	Irano Turanian	3	Strata with local and limited groundwater resources	5	HD	ROCK	Hamada/ rocky basement	6	941	3.36576	4.85523	119.0546
Original	54	Madamagh	Cave	double	35.44802292	30.34979982	8.5	Saharo-Arabian	4	Strata with local and limited groundwater resources	5		ROCK	Rocky basement	1	982	4.67582	13.52492	174.09386
Original	55	Qadesh Barnea 601	Open Air	single	34.40235454	30.64307447	6.5	Saharo-Arabian	4	Fissured/karstic aquifers: local or discontinous productive aquifers	4	RG	LST_SED	Reg/ limestone sediments	5	348	1.39021	5.17498	239.93141
Original	56	Qadesh Barnea 602	Open Air	single	34.40260752	30.64382953	6.5	Saharo-Arabian	4	Fissured/karstic aquifers: local or discontinous productive aquifers	4	RG	LST_SED	Reg/ limestone sediments	5	355	1.21325	4.00458	225
Original	57	Qadesh Barnea 9	Open Air	single	34.41315994	30.64493506	8.8	Saharo-Arabian	4	Strata with local and limited groundwater resources	5	RG	LST_SED	Reg/ limestone sediments	5	367	1.03132	4.05963	144.46233
Original	58	Ramat Matred I	Open Air	single	34.67761585	30.77936302	10	Irano Turanian	3	Strata with local and limited groundwater resources	5	HD	LST_SED	Hamada/ limestone sediments	4	633	0.4749	2.03237	324.46231
Original	59	Ramat Matred IV	Open Air	single	34.67347608	30.77345122	10	Irano Turanian	3	Strata with local and limited groundwater resources	5	HD	LST_SED	Hamada/ limestone sediments	4	642	0.91723	3.40477	213.69006
Original	60	Sabra 4 Palmview 1	Open Air	single	35.4049319	30.27183515	20.7	Saharo-Arabian	4	Strata with local and limited groundwater resources	5		ROCK	Rocky basement	1	802	5.15557	20.62469	116.00334
Original	61	Sabra 4 Palmview 3	Open Air	single	35.40458883	30.27225639	20.7	Saharo-Arabian	4	Strata with local and limited groundwater resources	5		ROCK	Rocky basement	1	816	3.77952	13.93908	105.42216
Original	62	Shunera XVI	Open Air	single	34.61362593	31.00372702	8.1	Saharo-Arabian	4	Strata with local and limited groundwater resources	5		LST_SED	Limestone sediments	3	309	0.38453	0.94534	180
Original	63	Siq Umm al-Alda 1	Open Air	single	35.4490627	30.42774941	23.8	Saharo-Arabian	4	Strata with local and limited groundwater resources	5		ROCK	Rocky basement	1	1000	4.03566	15.20035	210.06857
Original	65	Tor Aeid (J432)	Rockshelter	single	35.33747809	29.93658272	13.6	Sudanian and Sub-Sudanian	5	Strata with local and limited groundwater resources	5		ROCK	Rocky basement	1	972	3.98875	15.09632	156.5713
Original	66	Tor Fawaz (J403)	Rockshelter	single	35.33656023	29.94590289	12.5	Sudanian and Sub-Sudanian	5	Strata with local and limited groundwater resources	5		ROCK	Rocky basement	1	965	0.79508	2.67213	135
Original	67	Tor Hamar (J431)	Rockshelter	single	35.3192625	29.93923737	12.5	Sudanian and Sub-Sudanian	5	Strata with local and limited groundwater resources	5		ROCK	Rocky basement	1	1019	5.44135	20.89457	276.20343
Original	70	Wadi Aghar (J433)	Rockshelter	single	35.33311274	29.9376155	13.6	Sudanian and Sub-Sudanian	5	Strata with local and limited groundwater resources	5		ROCK	Rocky basement	1	984	6.21769	24.1685	161.23193
Original	74	El Wad Cave	Cave	Multi	34.96368899	32.67499348	17.7	Halo- and hydrophytic	6	Fissured/karstic aquifers: local or discontinous productive aquifers	4		LST_SED	Limestone sediments	3	31	0.67688	2.40896	258.69006
Original	75	Fazael Site IX	Open Air	single	35.38740227	32.065088	14.8	Mediterranean woodland	1	Fissured/karstic aquifers: local or discontinous productive aquifers	4		ROCK	Rocky basement	1	220	7.24976	25.56725	44.3013

Original	76	Hayonim Cave	Cave	Multi	35.21751604	32.92361131	11.6	Mediterranean woodland	1	Fissured/karstic aquifers: local or discontinous productive aquifers	4	LST_SED	Limestone sediments	3	224	5.37122	20.66774	174.35175
Original	77	Iraq El-Baroud/Sefunim	Cave	Multi	34.97825224	32.74224492	16.1	Halo- and hydrophytic	6	Fissured/karstic aquifers: local or discontinous productive aquifers	4	LST_SED	Limestone sediments	3	192	1.38154	5.49582	300.96375
Original	78	Kebara	Cave	Multi	34.93685836	32.55841747	25.5	Mediterranean woodland	1	Fissured/karstic aquifers: local or discontinous productive aquifers	4	LST_SED	Limestone sediments	3	47	4.93749	20.89457	276.20343
Original	80	Manot Cave	Cave	Multi	35.19516167	33.03489078	10.9	Mediterranean woodland	1	Fissured/karstic aquifers: local or discontinous productive aquifers	4	LST_SED	Limestone sediments	3	208	3.28003	13.1115	202.9321
Original	81	Nahal Ein Gev I	Open Air	double	35.66607521	32.77318057	9.1	Mediterranean woodland	1	Fissured/karstic aquifers: local or discontinous productive aquifers	4	ROCK	Rocky basement	1	101	5.582	17.89943	24.92847
Original	82	Qafzeh	Cave	Multi	35.29529666	32.68177953	17.3	Mediterranean woodland	1	Intergranular aquifers: extensive and highly productive	2	LST_SED	Limestone sediments	3	291	5.45461	20.66774	264.35175
Original	83	Raqefet	Cave	Multi	35.0727609	32.65804738	17.7	Mediterranean woodland	1	Intergranular aquifers: extensive and highly productive	2	ROCK	Rocky basement	1	227	6.10055	18.23173	247.9321
Original	85	Ansab 1	Open Air	single	35.38332996	30.23412835	9.9	Saharo-Arabian	4	Strata with local and limited groundwater resources	5	ROCK	Rocky basement	1	606	2.93989	13.07969	186.11551
Original	86	Absab 2	Open Air	single	35.38361098	30.2343622	9.9	Saharo-Arabian	4	Strata with local and limited groundwater resources	5	ROCK	Rocky basement	1	614	3.27408	6.03131	231.34019
Original	87	Sabra 3 Centre	Open Air	single	35.40094949	30.26697179	20.7	Saharo-Arabian	4	Strata with local and limited groundwater resources	5	ROCK	Rocky basement	1	788	2.2692	7.17787	121.6075
Original	88	Sabra 3 Nord	Open Air	single	35.40103577	30.26719231	20.7	Saharo-Arabian	4	Strata with local and limited groundwater resources	5	ROCK	Rocky basement	1	788	1.41776	4.77478	122.90524
Original	91	Sabra 4 PV 2	Open Air	single	35.40478581	30.27181077	20.7	Saharo-Arabian	4	Strata with local and limited groundwater resources	5	ROCK	Rocky basement	1	802	5.15557	20.62469	116.00334
Original	92	Sabra 4 PV 4	Open Air	single	35.40500385	30.27265468	20.7	Saharo-Arabian	4	Strata with local and limited groundwater resources	5	ROCK	Rocky basement	1	807	4.10522	16.19072	112.55725
Original	93	Sabra 4 PV 5	Open Air	single	35.40399135	30.27289879	20.7	Saharo-Arabian	4	Strata with local and limited groundwater resources	5	ROCK	Rocky basement	1	819	1.46444	5.20691	275.19443
Original	94	Sabra 10	Open Air	single	35.40577115	30.27513919	20.7	Saharo-Arabian	4	Strata with local and limited groundwater resources	5	ROCK	Rocky basement	1	826	2.41858	9.55202	101.30994
Original	95	2010-1	Open Air	single	35.40499593	30.27233009	20.7	Saharo-Arabian	4	Strata with local and limited groundwater resources	5	ROCK	Rocky basement	1	805	4.39752	17.60105	102.77124
Original	96	2010-2	Open Air	single	35.40503056	30.27289773	20.7	Saharo-Arabian	4	Strata with local and limited groundwater resources	5	ROCK	Rocky basement	1	811	3.51111	13.93908	111.44774
Original	97	2010-3	Open Air	single	35.40493773	30.2729265	20.7	Saharo-Arabian	4	Strata with local and limited groundwater resources	5	ROCK	Rocky basement	1	811	3.51111	13.93908	111.44774
Original	98	2010-4	Open Air	single	35.40581113	30.27337048	20.7	Saharo-Arabian	4	Strata with local and limited groundwater resources	5	ROCK	Rocky basement	1	811	3.64533	12.01982	125.53767
Original	99	2010-5	Open Air	single	35.40138483	30.27212579	20.7	Saharo-Arabian	4	Strata with local and limited groundwater resources	5	ROCK	Rocky basement	1	814	1.70201	5.37395	164.74487
Original	100	2010-6	Rockshelter	single	35.40284643	30.27026784	20.7	Saharo-Arabian	4	Strata with local and limited groundwater resources	5	ROCK	Rocky basement	1	803	5.18936	19.94469	130.38934
Original	101	2010-7	Open Air	single	35.40462105	30.27272485	20.7	Saharo-Arabian	4	Strata with local and limited groundwater resources	5	ROCK	Rocky basement	1	819	3.72855	14.343	107.85032
Original	102	2010-8	Open Air	single	35.40580404	30.27350592	20.7	Saharo-Arabian	4	Strata with local and limited groundwater resources	5	ROCK	Rocky basement	1	811	3.64533	12.01982	125.53767
Original	103	2010-9	Open Air	single	35.40780255	30.27746515	20.7	Saharo-Arabian	4	Strata with local and limited groundwater resources	5	ROCK	Rocky basement	1	841	3.0364	9.95421	203.55226
Original	104	2010-10	Open Air	single	35.41206614	30.28181558	20.7	Saharo-Arabian	4	Strata with local and limited groundwater resources	5	ROCK	Rocky basement	1	874	2.8645	9.35257	202.0679
Original	105	2010-11	Open Air	single	35.41335301	30.28131377	20.7	Saharo-Arabian	4	Strata with local and limited groundwater resources	5	ROCK	Rocky basement	1	857	4.14002	15.46821	153.43495
Original	106	2010-12	Open Air	single	35.41331787	30.28115206	20.7	Saharo-Arabian	4	Strata with local and limited groundwater resources	5	ROCK	Rocky basement	1	857	4.14002	15.46821	153.43495
Original	107	2010-13	Open Air	single	35.40054868	30.26851497	20.7	Saharo-Arabian	4	Strata with local and limited groundwater resources	5	ROCK	Rocky basement	1	796	1.29436	4.53691	188.97263
Original	108	2010-15	Open Air	single	35.40363153	30.2713539	20.7	Saharo-Arabian	4	Strata with local and limited groundwater resources	5	ROCK	Rocky basement	1	804	2.99409	11.38804	124.99202
Original	109	2010-16	Open Air	single	35.4041038	30.27154367	20.7	Saharo-Arabian	4	Strata with local and limited groundwater resources	5	ROCK	Rocky basement	1	804	3.55806	14.2604	166.86597
Original	110	2010-17	Open Air	single	35.40354139	30.27106691	20.7	Saharo-Arabian	4	Strata with local and limited groundwater resources	5	ROCK	Rocky basement	1	800	3.74982	14.74095	131.18593
Original	111	2010-18	Open Air	single	35.42420335	30.29313714	9.8	Saharo-Arabian	4	Strata with local and limited groundwater resources	5	ROCK	Rocky basement	1	868	2.28864	7.29875	194.93143
Original	112	2010-19	Open Air	single	35.41447277	30.28077896	20.7	Saharo-Arabian	4	Strata with local and limited groundwater resources	5	ROCK	Rocky basement	1	817	3.50348	12.85451	130.60129
Original	113	2010-20	Open Air	single	35.41756768	30.28365339	20.7	Saharo-Arabian	4	Strata with local and limited groundwater resources	5	ROCK	Rocky basement	1	832	3.3362	12.18502	133.45184
Original	114	2010-21	Open Air	single	35.40499448	30.27525269	20.7	Saharo-Arabian	4	Strata with local and limited groundwater resources	5	ROCK	Rocky basement	1	835	2.21706	8.37613	191.30994
Original	115	2010-22	Open Air	single	35.40072756	30.27202059	20.7	Saharo-Arabian	4	Strata with local and limited groundwater resources	5	ROCK	Rocky basement	1	818	3.01087	12.83418	137.93567
Original	116	2010-23	Open Air	single	35.42091525	30.28749725	20.7	Saharo-Arabian	4	Strata with local and limited groundwater resources	5	ROCK	Rocky basement	1	839	1.89753	6.53862	120.25644
Original	117	2010-24	Open Air	single	35.42474023	30.29467867	9.8	Saharo-Arabian	4	Strata with local and limited groundwater resources	5	ROCK	Rocky basement	1	877	2.77155	12.21947	72.25533
Original	118	2010-25	Open Air	single	35.41918203	30.28040333	20.7	Saharo-Arabian	4	Strata with local and limited groundwater resources	5	ROCK	Rocky basement	1	930	20.47709	55.23666	339.90479
Original	119	2010-26	Open Air	single	35.41846457	30.28038953	20.7	Saharo-Arabian	4	Strata with local and limited groundwater resources	5	ROCK	Rocky basement	1	880	13.87944	45.26429	332.49231
Original	120	2010-27	Open Air	single	35.41792792	30.28139167	20.7	Saharo-Arabian	4	Strata with local and limited groundwater resources	5	ROCK	Rocky basement	1	830	2.52448	9.28313	280.17551
Original	121	2010-28	Open Air	single	35.42409565	30.29256185	9.8	Saharo-Arabian	4	Strata with local and limited groundwater resources	5	ROCK	Rocky basement	1	866	1.68519	6.03131	141.34019
Original	122	2010-29	Open Air	single	35.42137164	30.29718555	10.1	Saharo-Arabian	4	Strata with local and limited groundwater resources	5	ROCK	Rocky basement	1	1020	13.89707	41.77062	115.14478
Original	123	2010-30	Open Air	single	35.42641951	30.28773805	9.8	Saharo-Arabian	4	Strata with local and limited groundwater resources	5	ROCK	Rocky basement	1	913	2.92696	11.82977	302.125
Original	124	2010-31	Open Air	single	35.42231842	30.28707439	20.7	Saharo-Arabian	4	Strata with local and limited groundwater resources	5	ROCK	Rocky basement	1	866	4.63601	10.75458	267.51044
Original	125	Abu Shaher	Open Air	single	35.37960047	30.27591538	20.7	Irano Turanian	3	Strata with local and limited groundwater resources	5	ROCK	Rocky basement	1	716	7.36568	29.83587	125.63349
Original	126	Al-Halla 1	Open Air	single	35.42256101	30.3058139	10.1	Saharo-Arabian	4	Strata with local and limited groundwater resources	5	ROCK	Rocky basement	1	978	2.13415	8.89691	198.43495
Original	127	Al-Halla 2	Open Air	single	35.42350921	30.30548063	10.1	Saharo-Arabian	4	Strata with local and limited groundwater resources	5	ROCK	Rocky basement	1	977	1.55783	3.54868	273.81409
Original	128	Al Anbat Coffeeshop	Open Air	single	35.43491343	30.31599377	10.1	Saharo-Arabian	4	Strata with local and limited groundwater resources	5	ROCK	Rocky basement	1	1018	3.90524	12.11577	2.2026
Original	129	Al Takhir	Open Air	single	35.37417434	30.22793508	9.9	Saharo-Arabian	4	Strata with local and limited groundwater resources	5	ROCK	Rocky basement	1	611	2.88914	8.56191	350.53769

B

SUPPLEMENTARY TO **PLEISTOCENE-HOLOCENE LANDSCAPE EVOLUTION AND CLOSED DEPRESSIONS AT THE EASTERN CARPATHIAN BASIN (TOBOLIU, ROMANIA)**

B.1 TDZ22 CORINGS

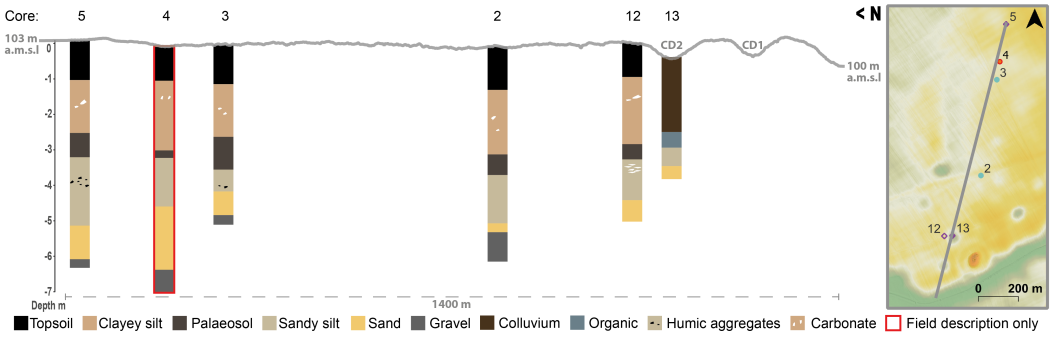

Figure B.1: Exemplary coring transect scheme for the NE to SE section. Core 4 was drilled in a low terrain position (channel-like elevation feature/soil mark) and documented during field work only. The position of Core 12 lies beyond the transect, but was adjusted for illustrative reasons in this figure.

B.2 FIELD WORK AND SURVEYING

All corings were conducted using an Atlas Copco Cobra Pro breaker drilling set. The maximum coring depth reached approximately seven meters below surface level. Groundwater influence was observed at a depth of ∼four metres. All coring profiles were logged, and detailed records of the sequences were established and stratigraphically linked. Distinct sediment layers were carefully characterised in the field using a range of standard parameters, such as grain size, sediment/soil colour (Munsell soil colour chart), humus, carbonate, iron, and manganese oxide content. Special attention was paid to the documentation of post-sedimentary features, including those resulting from pedogenetic processes (e.g. hydromorphy), archaeological findings, botanical macro-remains, and other organic matter indicating pollen preservation. For soil characterisation we used the classification system outlined by the Food and Agriculture Organization of the United Nations (FAO), following the guidelines set forth by (IUSS (WRB) WG, 2015). Positioning and altimetry of the corings were conducted using a total station (Trimble M3 DR 1) with a precision of < 3

cm. Georeferencing of the local tachymetric system was done using a DGPS (KQ GEO M8) with network RTK which provides a positioning accuracy of ±2 -3 cm based on the Romanian Position Determination System (ROMPOS). The received Pulkovo 1942(58), Stereo70/ European Terrestrial Reference System 1989 (ETRS89) coordinates were transformed to UTM zone 34N/ World Geodetic System 1984 (WGS84). GIS analysis was conducted using the open-source software QGIS 3.28 (QGIS Development Team, 2022d).

B.3 GEOSPATIAL IMAGERY

B.3.1 *LiDAR imagery acquisition, ANCPI 2009-2014)*

Sensing was done using the RIEGL Q780 scanner mounted on an MP42 Diamond DA-42 Twin Star 42 aircraft. Aerial surveys were carried out with UltraCam Eagle Mark 2 and UltraCam digital cameras with high precision for areas with high flood risk on the border between Romania and Hungary in Arad and Bihor counties (10,000 km 2, with a density of 8 points/m2). The resulting high-resolution DEM provides detailed information about slight elevation differences in the study area.

B.3.2 *WorldView-3 satellite imagery*

Multispectral WorldView- 3 provided by European Space Imaging GmbH – ESA (DigitalGlobe, 2021) has an original spatial resolution (pixel size) of 1.24 x 1.24 m (pansharpening produced a resolution of 31 x 31 cm) and provides spectral surface reflectance data from 400 to 954 nm (shortwave blue to near infrared wavelength). This enables the processing of CIR (colour-infrared), using the bands 7, 5, and 3 for the red, green, and blue (RGB) channels. This visualisation is particularly useful for investigating vegetation cover and determining soil moisture patterns.

B.3.3 *Geomagnetic imagery*

A five-sensor Sensys gradiometer system with a line spacing of 0.5 m and a sampling interval of 0.05 m was used for the geomagnetic survey of $\sim$0.6 km^2. The grayscale imagery shows the standard ±10 nT plots. Thus, positive anomalies are displayed in dark grey to black colour and negative anomalies show light grey to white colour (Kienlin, 2021; Lie et al., 2024).

B.4 LABORATORY ANALYSIS, ELEMENT RATIOS, AND STATISTICS

B.4.1 *D.1 Sample preprocessing*

All samples were air-dried at 35 °C, aggregates were carefully disintegrated using a mortar, and organic macro-remains and anthropogenic material were separated in the same step. Subsequently, the material was sieved to retrieve grain-sizes less than 2 mm.

B.4.2 *Grain size analysis*

Prior to the measurements, the organic content was dissolved by 15% hydrogen peroxide. In addition, carbonates were dissolved by hydrochloric acid (5%). To avoid coagulations, the samples were extensively washed, centrifuged, and dispersed with sodium pyrophosphate (40 g/l) and mixed using an overhead shaker for about 24 hours (Schulte et al. 2016). After triple measurement using the Fraunhofer optical diffraction model, the GSD data was analysed using the method of Folk and Ward (1957) and Blott and Pye (2001).

B.4.3 *Carbon analysis*

To determine the total carbon (TC), total organic carbon (TOC), and total inorganic carbon (TIC) concentrations in sediment samples, a DIMATOC 2000 carbon analyser was used, based on thermocatalytic oxidation with subsequent NDIR detection. The entire analysis procedure generally adheres to the DIN 'TOC suspension 15936' standard, with adaptations made by Nicole Mantke (Institute of Geology and Mineralogy, University of Cologne, Germany). Accordingly, the TC and TIC were determined using the suspension method. In this process, 30 mg of the sample was suspended in 10 mL of RO water using an ultrasonic disperser. The TC content was measured as the CO^2 emitted after combustion at 900 °C. The TIC content was analysed by treating the dispersed material with 40% phosphoric acid ($H3PO4$) and then incinerating it at 160 °C. The TOC content was calculated by subtracting the TIC from the TC. Measurements results are given in percentage of sample weight.

B.4.4 *Element concentrations*

Before analysis the sieved samples were grounded in a ball mill grinder (Retsch MM 400) for both methods (Carbon and XPL analysis). Elemental composition was analysed by energy dispersive x-ray fluorescence analysis (EDXRF) using an Spectro Xepos P spectrometer (SPECTRO Analytical Instruments Ltd.). Dual measurements and a helium gas atmosphere were applied. For the analysis, 5 g of the fine-grained sedi-

ment samples mixed with 1 g of Fluxana Cereox wax were pressed into 3 cm diameter pellets using a hydraulic press. The concentration of all elements from sodium to uranium were simultaneously measured and adjusted to sample weight.

B.4.5 *Geochemical ratios, statistics, and data visualisation*

For producing GSD plots, standard libraries of the Python programming language were utilised. Statistical analyses, including Principal Component Analysis (PCA), and graphical representations were generated using the R programming language (R Core Team, 2023). For explorative data analysis, we used various element ratios. Al/Ca can be used to identify authigenic carbonate deposition. In combination withFe/acMn andFe/S, which are proxies for reducing (an-/suboxic) conditions, these ratios can indicate limnic conditions (Boyle, 2001; Davies et al., 2015; Sheldon and Tabor, 2009). P/Si is useful to identify phases of phosphorous enrichment (Boyle, 2001) within the sediment sequence, considering silicon as an immobile reference (Buggle et al., 2011). Often, phosphorus concentrations in sediments were linked to early agricultural activity (Lubos et al., 2013; Ottaway and Matthews, 1988; Ruttenberg and Goñi, 1997; Smeck, 1985). Furthermore, theRb/Sr ratio serves as an indicator for assessing weathering and reworking processes inLPS. It also reflects post-sedimentary calcium substitution. In contrast, the CPA acts as a carbonate-independent indicator for soil formation, as noted by Buggle et al. (2011). The CPA is based on the CIW' (Chemical Index of Weathering' = molecular [Al2O3/(Al2O3+Na2O)]x100) of Cullers (2000) CPA/CIW' is useful to investigate weathering intensity, in terms of plagioclase and K-feldspar weathering in the LPS. Moreover, oxide biplots of selected elements were prepared to potentially identify differences in dust sources of the loess derivate deposits (Appendix B.6, Fig. B.4). Additionally, we followed a multivariate approach usingPCA as suggested by Davies et al. (2015).

B.5 CHRONOLOGY - OPTICAL STIMULATED LUMINESCENCE DATING

The eight samples for equivalent dose (D_e) determination were taken from 10 cm intervals, while the corresponding dosimetric samples were taken from the surrounding material. The water content was determined for both sample sets after drying. Following a four-week storage period to compensate for radon loss, radionuclide concentrations (uranium, thorium, potassium) were determined by gamma-ray spectrometry. For the D_e samples, organic matter, carbonates, and clays were removed using HCl, H2O2, and Na2C2O4. The fine grain fraction (4-11 µm) and the 100-200 µm coarse grain fraction were retrieved and

further density separated to extract FSP) and Qz minerals. Parts of both Q grain size fractions were etched using 34% hexafluorosilicic acid (4-11 µm) and 40% hydrofluoric acid (100-200 µm) to further purify the quartz extracts. In general, aliquots with D_e errors >20%, recuperation >5%, and recycling ratios > 10% were rejected. Initial coarse grain measurements were performed on 1 mm aliquots and further measurements were done on 4 mm aliquots to obtain stronger signals and thus better counting statistics. For luminescence measurement various protocols and steps according to different grain and mineral fraction were undertaken (Table B.1). Preliminary measurements included dose recovery tests, whose results are depicted in Figure B.2. All sample D_es were calculated based on the arithmetic mean and standard error of the corresponding D_e distributions. Examples of OSL signals and dose response curves are shown in Figure B.3. Water contents as determined in the laboratory (± 5%) were used for age calculation. Total dose rates and final ages calculation (DRAC, v. 1.2 Durcan et al. (2015) assume 0.5±0.2 m of total topsoil erosion for the samples from Core 5. For Core 13, which is situated in a CD erosion was not considered. Fine-grained quartz OSL samples show a fast component-dominated decay curve, a satisfying dose response curve fit and generally suitable luminescence properties (Appendix B.5, Fig. B.3.2). The preheat plateau test (plateau between 180 and 280 °C) and the dose recovery tests (recovered/given ratios of 1.05±0.00 and 0.97±0.01, Appendix B.5 Fig. B.2) confirm the suitability of the used protocol. Both coarse-grained quartz samples (C-L5379 and C-L5380, Appendix, Table B.2), however, showed poor recycling ratios, strongly varying test dose behaviour throughout the SAR cycle and clear indications of OSL signal saturation. As these results illustrate that the coarse-grained quartz samples cannot be dated reliably with the tested protocol, we refrained from further analyses. Almost all aliquots were accepted for the coarse-grain feldspar OSL measurements, showing strong signals and well-fitted dose response curves (Appendix B.5, Fig. B.3). Only sample C-L5378 had a higher amount of rejected aliquots as some of the sensitivity-corrected natural signals are situated in the flattened part of the dose-response curve resulting in D_e errors >20%. Dose recovery tests were performed on C-L5377 with a ratio of 1.09±0.03 (n=3) and on C-L5379 with a higher ratio 1.14±0.14 (n=3), which can be attributed to one high outlier of 1.49±0.23 (see Appendix B.5, Fig. B.2. Nevertheless, within error, the dose recovery ratios are within the acceptable range, underlining the suitability of the protocol for our samples. The reliability of the FSP dating results can be confirmed considering their stratigraphical position.

Table B.1: Different luminescence measurement protocols used in this study, following Murray and Wintle (2003) and Murray and Wintle (2000), Thomsen et al. (2008), and Kars et al. (2012).

Step	Quartz (4-11 µm)	Quartz (100-200 µm), 4 mm	FSP (100-200 µm)
2 mm			
1	Give dose, Di	Give dose, Di	Give dose, Di
2	Preheat 240 °C	Preheat 240 °C	Preheat 250 °C
3a	Stimulate for 50s at 125 °C	Stimulate for 40s at 125 °C	Stimulate for 200s at 50 °C
3b			Stimulate for 300s at 225 °C
3c			Stimulate for 300s at 225 °C
4	Give test dose (11Gy), Dt	Give test dose (4Gy), Dt	Give test dose, Dt (22/74Gy)
5	Preheat 220 °C	Preheat 220 °C	Preheat 250 °C
6a	Stimulate for 50s at 125 °C	Stimulate for 40s at 125 °C	Stimulate for 200s at 50 °C
6b			Stimulate for 300s at 225 °C
7		Stimulate for 40s at 250 °C	Stimulate for 300s at 225 °C
	Return to 1	Return to 1	Return to 1

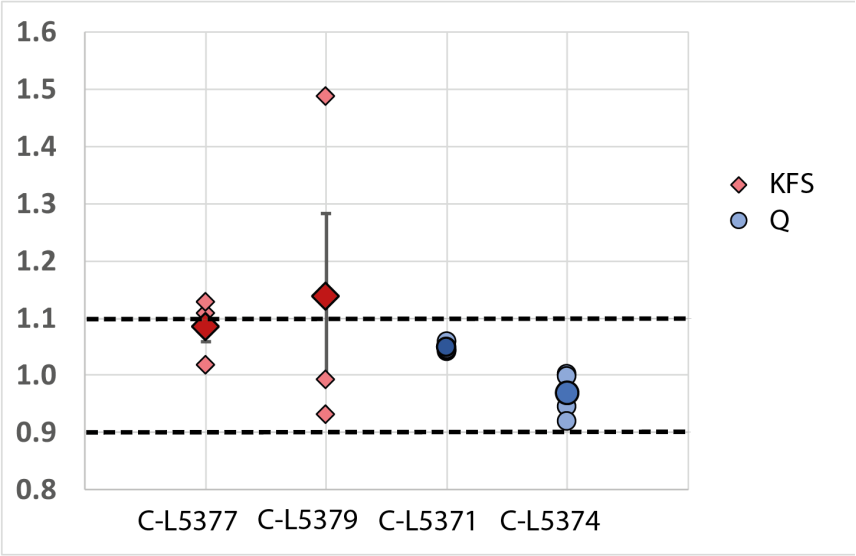

Figure B.2: Results of the dose recovery tests on samples C-L5377 (100-200 µm FSP, 2mm aliquots, n=3), C-L5379 (100-200 µm FSP, 2mm aliquots, n=3), C-L5371 (4-11 µm Q, n=5) and C-L5374 (4-11 µm Q, n=5). Quartz measurements are shown as blue circles, while feldspar Post-Infrared Infrared Stimulated Luminescence (pIRIR) measurements are shown in red diamonds. The results of the single aliquots are indicated in lighter colours, while the means incl. standard errors are shown in stronger colours. Errors of Q are so small that they vanish behind the symbols. The acceptable recovered/given dose ratio of 1.0±0.1 is indicated with the dashed lines.

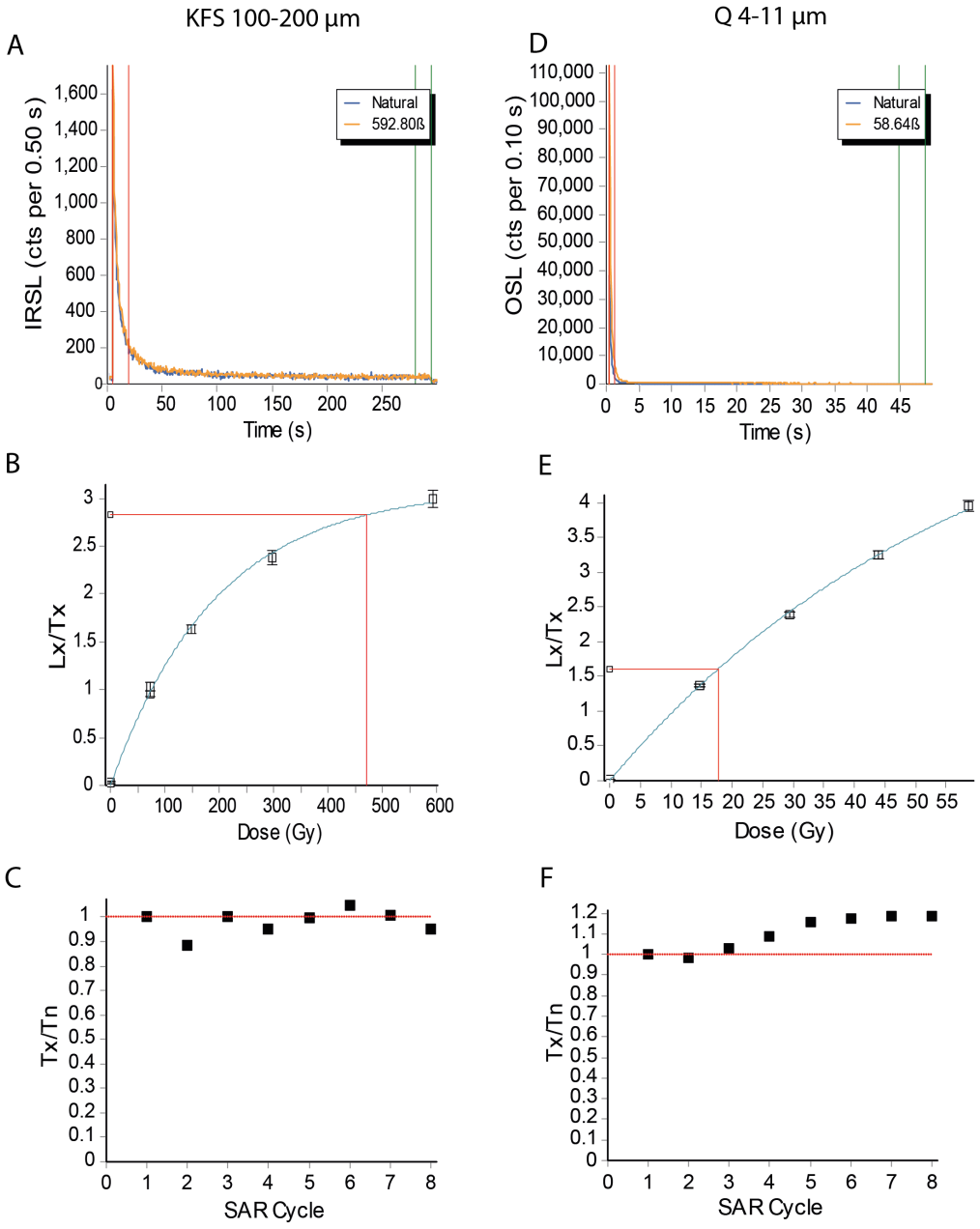

Figure B.3: Exemplary OSL signals (A, D), dose response curves (B, E) and Tx/Tn plots (C, F) of a FSP sample (left) and a quartz sample (right).

Table B.2: Detailed OSL measurement data, giving the depth in metre above mean sea level (Depth m a.m.s.l.), grain size range, water content (W), accepted/measured aliquots (n/N), recycling ratios, concentrations of U, Th, and K, average D_e, dose rate and age.

Lab code	Depth (m a.m.s.l)	Core	S.№	Mineral	Grain size (µm)	U (ppm)	Th (ppm)	K (%)	W (%)	n/N	$\bar{x}$ D_e (Gy)	Dose rate (Gy/ka)	Age (ka)
C-L5374	100.6	5	1	FSP	100-200	2.88 ± 0.20	14.91 ± 1.04	1.71 ± 0.05	17.86 ± 5	7/9	127.0 ± 8.3	3.9 ± 0.2	32.7 ± 2.9
C-L5374				QZ	4-11	2.88 ± 0.20	14.91 ± 1.04	1.71 ± 0.05	17.86 ± 5	4/4	138.2 ± 4.7	3.7 ± 0.1	37.0 ± 1.9
C-L5375	100	5	2	FSP	100-200	2.77 ± 0.19	14.51 ± 1.02	1.76 ± 0.05	18.54 ± 5	7/9	178.0 ± 2.9	3.8 ± 0.2	46.3 ± 2.9
C-L5375				QZ	4-11	2.77 ± 0.19	14.51 ± 1.02	1.76 ± 0.05	18.54 ± 5	3/3	177.5 ± 1.1	3.7 ± 0.1	48.2 ± 1.8
C-L5376	99.6	5	3	FSP	100-200	2.76 ± 0.19	14.21 ± 0.99	1.77 ± 0.05	19.49 ± 5	8/9	331.6 ± 20.5	3.8 ± 0.2	87.3 ± 7.6
C-L5377	99	5	4	FSP	100-200	2.91 ± 0.21	15.79 ± 1.11	2.1 ± 0.06	22.26 ± 5	9/9	516.7 ± 34.5	4.1 ± 0.2	126 ± 11
C-L5378	98.1	5	5	FSP	100-200	2.99 ± 0.21	16.83 ± 1.18	2.55 ± 0.07	22.95 ± 5	3/9	624.1 ± 72.6	4.5 ± 0.3	138 ± 18
C-L5379	97.9	5	6	FSP	100-200	2.34 ± 0.17	13.11 ± 0.92	2.11 ± 0.06	19.96 ± 5	9/9	549.3 ± 33.0	3.9 ± 0.2	142 ± 12
C-L5380	97	5	7	FSP	100-200	1.53 ± 0.11	7.40 ± 0.52	1.56 ± 0.04	11.75 ± 5	9/9	452.6 ± 61.7	3.0 ± 0.2	150 ± 23
C-L5371	99.19	13	2	QZ	4-11	2.38 ± 0.17	12.9 ±						
0.9	1.94 ± 0.05	22.49 ± 5	7/7	18.3 ± 0.3	3.6 ± 0.1	5.1 ± 0.2							

B.6 DUST SOURCE INDICATORS

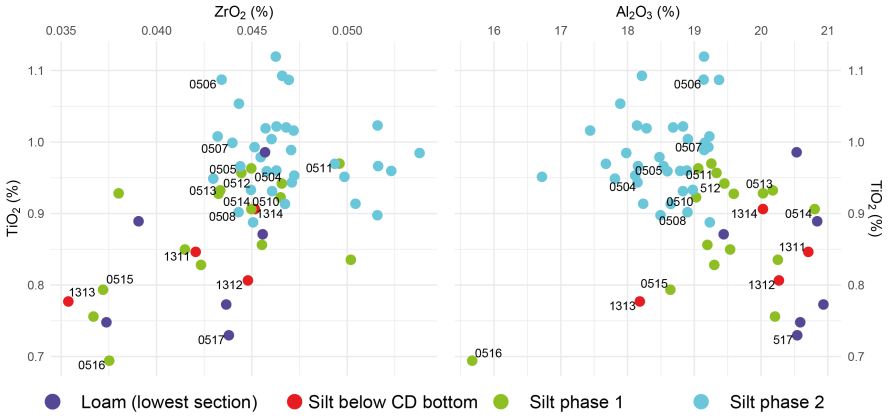

Figure B.4: Bi-plots of common element oxides used for dust source determination in LPS. The displayed data set contains loess unit measurement values of eight analysed cores (this study).

B.7 CORE 12 DATA AND MAIN CHRONOSTRATIGRAPHIC UNITS

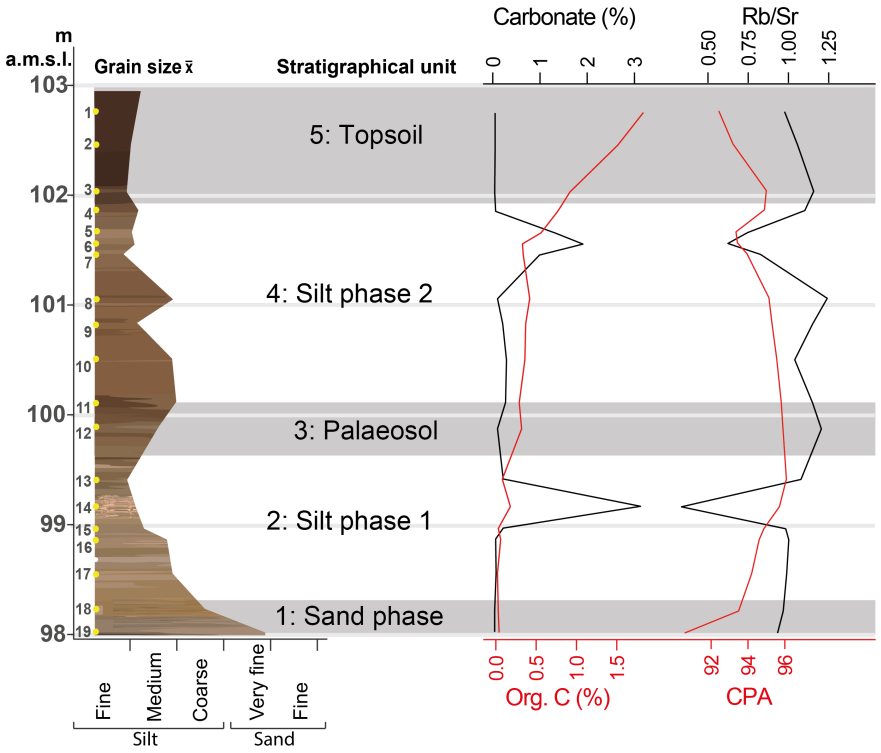

Figure B.5: Core 12 data and main stratigraphic units. Depth is given in metres above mean sea level (a.m.s.l.), sample depth and numbers are highlighted by yellow points. Mean grain size ($\bar{x}$) is displayed by the core plot. Carbonate and Organic carbon (Org. C) contents (percentage of sample weight), as well as the Rb/Sr ratio to illustrate weathering intensity and the Chemical Proxy of Alteration (CPA) as weathering/pedogenesis proxies are displayed. Proxy details can be found in Appendix B.4.

B.8 GRAIN SIZE FREQUENCY PLOTS OF CORES 5, 12, AND 13

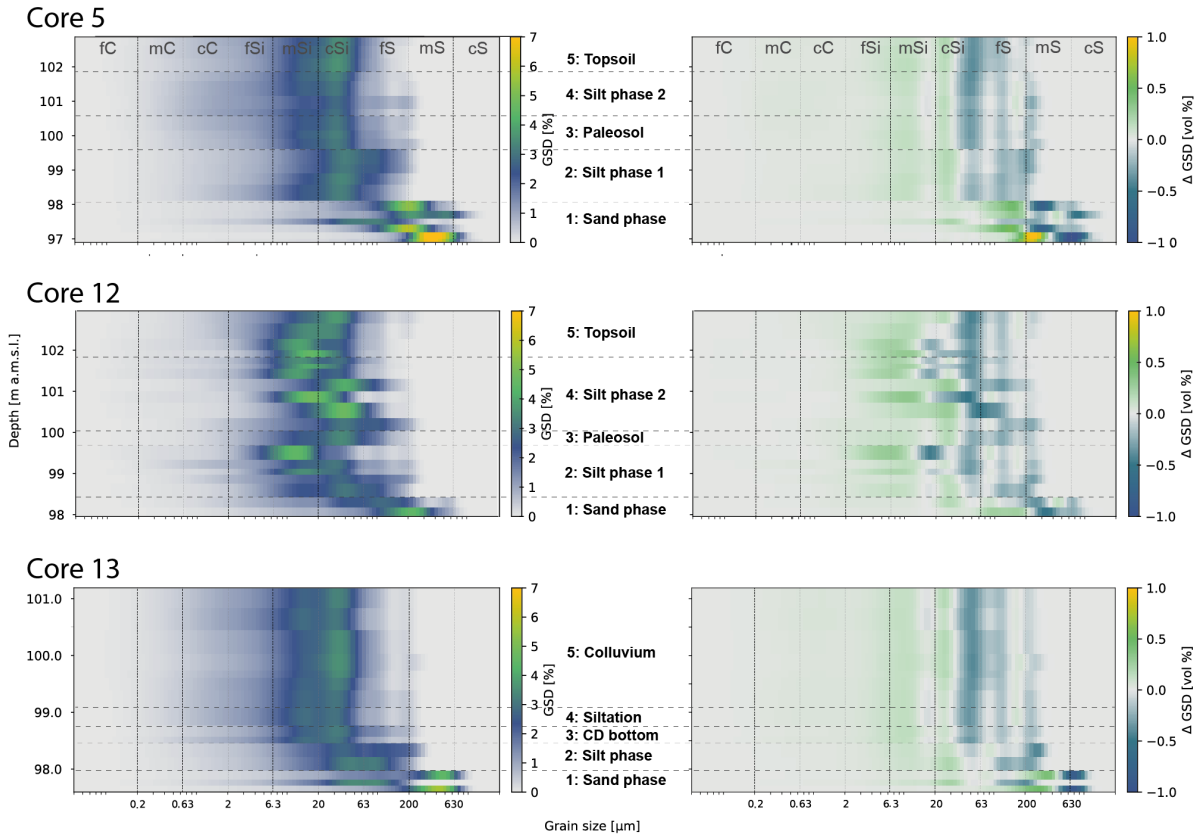

Figure B.6: Intra-profile grain size frequencies and derivates for Cores 5, 12, and 13 after Schulte et al. (2018).

B.9 CORE 15 DATA AND MAIN CHRONOSTRATIGRAPHIC UNITS

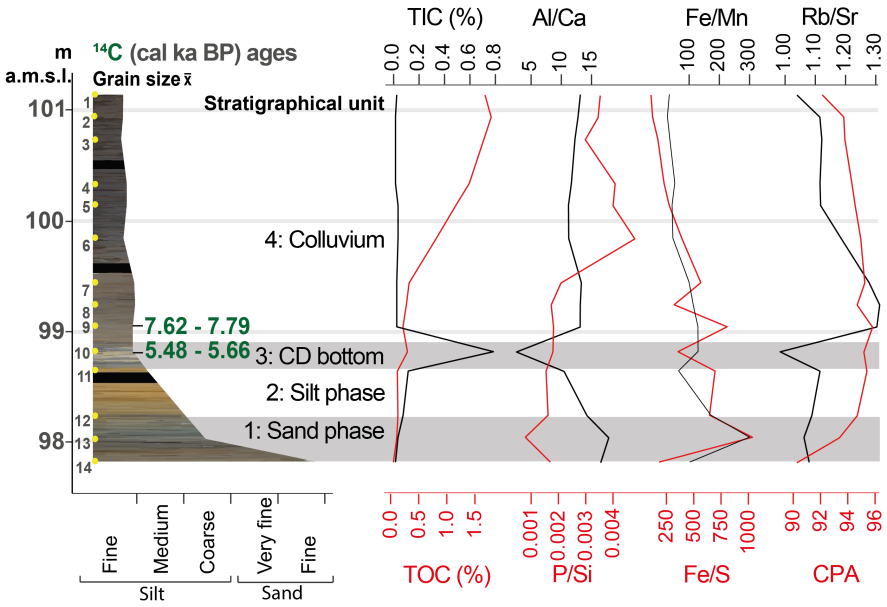

Figure B.7: Core 15 data and main chronostratigraphic units. Depth is given in metres above mean sea level (a.m.s.l.), sample depth and numbers are highlighted by yellow points. Mean grain size ($\bar{x}$) is displayed by the core plot. Black boxes show areas of core loss. Dating results are listed in cal a before present (BP), reference year 1950). Carbonate and organic carbon contents (percentage of sample weight), as well as theRb/ Sr ratio to illustrate weathering intensity and the Chemical Proxy of Alteration (CPA) as weathering/pedogenesis proxies are displayed.Al/Ca, and Fe/Mn, andFe/S ratio highlight hydromorphic modes. P/Si ratio is used as indicator for biological/agricultural activity.

C

SUPPLEMENTARY TO **MIGIS: MICROMORPHOLOGICAL SOIL AND SEDIMENT THIN SECTION ANALYSIS USING AN OPEN-SOURCE GIS AND MACHINE LEARNING APPROACH**

C.1 IMPLEMENTED GEOALGORITHMS IN QGIS 3

Table C.1: Implemented geoalgorithms in MiGIS toolbox with references.

Tool	Label	Function	Geoalgorithm	Reference
MiGIS 1	Merge (TS multi-band raster)	Create multi-band raster: stack georeferenced thin section images (TL, XPL, RL)	Merge	GDAL & OGR contributors (2022)
MiGIS 1	TS multi-band image clip	Clip merged multi-band raster	Clip raster by mask layer	GDAL & OGR contributors (2022)
MiGIS 2.1	Train random forest algorithm	Train random forest algorithm with vector ROI data	Train algorithm	Karasiak (2016)
MiGIS 2.2	Band: ROI pixel statistics (mean, SD)	ROI evaluation: query the multi-band raster using the ROI data set – pixel values (mean) per ROI and σ	Zonal statistics	QGIS Development Team (2022a)
MiGIS 2.2	Unite single-band statistics	Merge single-band zonal statistics to one CSV table	Merge vector layers	QGIS Development Team (2022a)
MiGIS 2.2	Box plot band	Plot single-band zonal statistics	Box plot	QGIS Development Team (2022a)
MiGIS 3	TS classification	Classify multi-band raster based on the training	Predict model (classification map)	Karasiak (2016)
MiGIS 3	Assess classification accuracy (vector reference)	Query the generated classification map using a reference ROI vector data set	Zonal histogram	QGIS Development Team (2022a)
MiGIS 3	Dissolve class	Sum zonal histogram pixel counts per class (classification map) and output CSV table	Dissolve	QGIS Development Team (2022a)
MiGIS 3	Spatial statistics	Count pixel per class (classification map) and calculate class areas	Raster layer unique values report	QGIS Development Team (2022a)
MiGIS 3	Refactor fields	Convert the class field double format (raster layer unique values report) to integer	Refactor fields	QGIS Development Team (2022a)
MiGIS 3	Join attributes by field value	Add class label field to the spatial statistics CSV table	Join attributes by field value	QGIS Development Team (2022a)
MiGIS 3	Bar plot	Plot class area statistics	Bar plot	QGIS Development Team (2022a)

C.2 CLASSIFICATION RESULTS AND ACCURACY FOR THE RHEINDAHLEN THIN SECTIONS

Table C.2: Total thin section (TS) classification results for the Rheindahlen stratigraphy. TS image classifications presented in Sect. 4.3 are highlighted. OA; producer's accuracy (PA); user's accuracy (UA); n/a: respective constituent (feature class) not present in the TS. Quality criteria: 100 %–90 % class accuracy – very good; * 90 %–80 % class accuracy – good; ** < 80 % class accuracy – poor.

S. no.	Horizon	Depth cm	DPI	Po	Po PA %	Po UA %	Gm5	Gm5 PA %	Gm5 UA %	Gm1	Gm1 PA %	Gm1 UA %	Gm2	Gm2 PA %	Gm2 UA %	Gm3	Gm3 PA %	Gm3 UA %	Gm4	Gm4 PA %	Gm4 UA %	Pixel total	OA %
A1	M	56	1200	6.0	100	100	n/a	n/a	n/a	57.4	100	100	33.2	100	100	n/a	n/a	n/a	n/a	n/a	n/a	375	100
A2	MBtg	74	1200	8.6	100	100	86.6	100	100	n/a	n/a	n/a	n/a	n/a	n/a	n/a	n/a	n/a	n/a	n/a	n/a	6727	99.0
A3	Bt1	96	1200	5.2	100	100	n/a	n/a	n/a	31.0	100	100	59.2	100	100	n/a	n/a	n/a	n/a	n/a	n/a	8212	99.7
A4	**Bt2**	**113**	**1200**	**4.9**	**100**	**100**	**n/a**	**n/a**	**n/a**	**25.7**	**100**	**100**	**62.5**	**100**	**100**	**n/a**	**n/a**	**n/a**	**n/a**	**n/a**	**n/a**	**4851**	**100**
A5	BCt	132	1200	6.3	100	100	n/a	n/a	n/a	47.5	100	100	43.4	99.9	99.7	n/a	n/a	n/a	n/a	n/a	n/a	8209	99.9
A6	BC(t)1	153	1200	1.8	100	100	n/a	n/a	n/a	73.9	100	100	18.9	100	100	n/a	n/a	n/a	n/a	n/a	n/a	444	99.0
A7	BC(t)2	184	1200	2.3	100	100	n/a	n/a	n/a	59.9	100	97.0	30.9	97.0	93.0	n/a	n/a	n/a	n/a	n/a	n/a	944	98.0
B2	BC1	217	1200	1.5	100	100	n/a	n/a	n/a	70.2	100	100	26.1	100	100	n/a	n/a	n/a	n/a	n/a	n/a	255	100
B4	BC3	251	1200	1.5	100	100	n/a	n/a	n/a	40.2	100	100	56.9	100	100	n/a	n/a	n/a	n/a	n/a	n/a	317	100
B5	E1	266	1200	2.3	100	100	n/a	n/a	n/a	51.6*	89.0	100	43.3*	100	87.0	n/a	n/a	n/a	n/a	n/a	n/a	1041	97.0
B6	E+Bt	284	1200	1.1	100	100	n/a	n/a	n/a	15.6	100	100	71.5	100	100	9.7	100	100	n/a	n/a	n/a	441	100
B7	**Bt1**	**305**	**1200**	**3.8**	**100**	**100**	**n/a**	**n/a**	**n/a**	**25.7***	**100**	**88.0**	**58.1**	**89.0**	**97.0**	**n/a**	**n/a**	**n/a**	**n/a**	**n/a**	**n/a**	**4092**	**97.0**
B8	Bt2	325	1200	3.5	100	100	n/a	n/a	n/a	49.2	94.0	91.0	31.7*	89.0	93.0	7.7	100	95.0	n/a	n/a	n/a	12 207	98.0
C1	BCt	375	1200	4.2	100	100	n/a	n/a	n/a	49.4	100	100	43.7	100	100	n/a	n/a	n/a	n/a	n/a	n/a	311	100
C2	BC1	420	1200	5.4	100	100	n/a	n/a	n/a	39.7*	95.0	85.0	39.9	100	100	n/a	n/a	n/a	12.1*	87.0	95.0	444	97.0
C3	BC2	449	1200	2.8	100	100	n/a	n/a	n/a	60.0	100	100	34.1	100	100	n/a	n/a	n/a	n/a	n/a	n/a	373	100
C4	E1	482	1200	2.4	100	100	n/a	n/a	n/a	50.6*	85.0	100	42.6*	100	82.0	n/a	n/a	n/a	n/a	n/a	n/a	376	92.0
C5	**Btg**	**524**	**1200**	**3.4**	**100**	**100**	**n/a**	**n/a**	**n/a**	**35.0****	**53.0**	**100**	**56.6***	**98.0**	**80.0**	**n/a**	**n/a**	**n/a**	**n/a**	**n/a**	**n/a**	**441**	**87.0**
C5	Btg	524	2400	3.3	100	100	n/a	n/a	n/a	39.9*	85.0	85.0	52.3**	88.0	78.0	n/a	n/a	n/a	n/a	n/a	n/a	439	95.0
C6	BCg(t)	557	1200	5.0	100	100	n/a	n/a	n/a	31.2	100	100	60.7	100	100	n/a	n/a	n/a	n/a	n/a	n/a	382	86.0
C7	Bwg(t)	594	1200	3.9	100	100	n/a	n/a	n/a	45.8	100	100	45.5	100	100	n/a	n/a	n/a	n/a	n/a	n/a	380	100
C8	Bwg(t)	644	1200	2.5	100	100	n/a	n/a	n/a	48.0	100	100	37.5	100	100	n/a	n/a	n/a	n/a	n/a	n/a	377	100

Table C.3: Total thin section (TS) classification results for the Rheindahlen stratigraphy. TS image classifications presented in Sect. 4.3 are highlighted. OA; producer's accuracy (PA); user's accuracy (UA); n/a: respective constituent (feature class) not present in the TS. Quality criteria: 100 %–90 % class accuracy – very good; * 90 %–80 % class accuracy – good; ** < 80 % class accuracy – poor.

S.	Horizon	Depth	DPI	Sg	Sg	Sg	Cc	Cc	Cc	Cg	Cg	Cg	Cci	Cci	Cci	Ccd	Ccd	Ccd	Fe	Fe	Fe	Mn	Mn	Mn	Ch	Ch	Ch
no.		cm			PA %	UA %		PA %	UA %		PA %	UA %		PA %	UA %		PA %	UA %		PA %	UA %		PA %	UA %		PA %	UA %
A1	M	56	1200	1.9	100	100	n/a	n/a	n/a	n/a	n/a	n/a	n/a	n/a	n/a	n/a	n/a	n/a	1.4	100	100	n/a	n/a	0.0	0.3	100	100
A2	MBtg	74	1200	n/a	n/a	n/a	2.3*	81.0	98.0	n/a	n/a	n/a	n/a	n/a	n/a	n/a	n/a	n/a	1.0	0.0	0.0	1.6	100	100	n/a	n/a	n/a
A	Bt1	96	1200	n/a	n/a	n/a	2.5	100	100	n/a	n/a	n/a	n/a	n/a	n/a	n/a	n/a	n/a	0.9	100	62.0	1.2	97.0	100	n/a	n/a	n/a
A4	**Bt2**	**113**	**1200**	**1.6**	**100**	**100**	**3.3**	**100**	**100**	**n/a**	**n/a**	**n/a**	**n/a**	**n/a**	**n/a**	**n/a**	**n/a**	**n/a**	**0.6**	**100**	**100**	**1.3**	**100**	**100**	**n/a**	**n/a**	**n/a**
A5	BCt	132	1200	n/a	n/a	n/a	1.1	100	100	n/a	n/a	n/a	n/a	n/a	n/a	n/a	n/a	n/a	1.0	93.0	98.0	0.6	100	100	n/a	n/a	n/a
A6	BC(t)1	153	1200	4.0	100	100	0.6	100	100	n/a	n/a	n/a	n/a	n/a	n/a	n/a	n/a	n/a	0.8	100	94.0	0.2	94.0	100	n/a	n/a	n/a
A7	BC(t)2	184	1200	n/a	n/a	n/a	1.4	100	100	n/a	n/a	n/a	n/a	n/a	n/a	n/a	n/a	n/a	5.1*	86.0	86.0	0.4	100	100	n/a	n/a	n/a
B2	BC1	217	1200	n/a	n/a	n/a	0.2	100	100	1.7	100	100	n/a	n/a	n/a	n/a	n/a	n/a	n/a	n/a	n/a	0.4	100	100	n/a	n/a	n/a
B4	BC3	251	1200	n/a	n/a	n/a	n/a	n/a	n/a	n/a	n/a	n/a	n/a	n/a	n/a	n/a	n/a	n/a	1.1	100	100	0.4	100	100	n/a	n/a	n/a
B5	E1	266	1200	n/a	n/a	n/a	n/a	n/a	n/a	n/a	n/a	n/a	n/a	n/a	n/a	n/a	n/a	n/a	2.3	100	100	0.5	100	100	n/a	n/a	n/a
B6	E+Bt	284	1200	n/a	n/a	n/a	0.3	100	100	n/a	n/a	n/a	n/a	n/a	n/a	n/a	n/a	n/a	1.6	100	100	0.2	100	100	n/a	n/a	n/a
B7	**Bt1**	**305**	**1200**	**n/a**	**n/a**	**n/a**	**8.4**	**94.0**	**100**	**n/a**	**n/a**	**n/a**	**n/a**	**n/a**	**n/a**	**n/a**	**n/a**	**n/a**	**2.8**	**97.0**	**100**	**1.2**	**100**	**99.0**	**n/a**	**n/a**	**n/a**
B8	Bt2	325	1200	n/a	n/a	n/a	3.1	100	100	n/a	n/a	n/a	n/a	n/a	n/a	n/a	n/a	n/a	n/a	n/a	n/a	4.7	95.0	100	n/a	n/a	n/a
C1	BCt	375	1200	n/a	n/a	n/a	2.6	100	100	n/a	n/a	n/a	n/a	n/a	n/a	n/a	n/a	n/a	n/a	n/a	n/a	0.2	100	100	n/a	n/a	n/a
C2	BC1	420	1200	n/a	n/a	n/a	1.7	100	100	n/a	n/a	n/a	n/a	n/a	n/a	n/a	n/a	n/a	1.2	100	100	0.1	100	100	n/a	n/a	n/a
C3	BC2	449	1200	n/a	n/a	n/a	n/a	n/a	n/a	n/a	n/a	n/a	1.5	100	100	n/a	n/a	n/a	1.4	100	100	0.2	100	100	n/a	n/a	n/a
C4	E1	482	1200	n/a	n/a	n/a	2.4	100	100	n/a	n/a	n/a	n/a	n/a	n/a	n/a	n/a	n/a	1.6**	100	72.0	0.3**	78.0	100	n/a	n/a	n/a
C5	**Btg**	**524**	**1200**	**n/a**	**n/a**	**n/a**	**2.7**	**100**	**100**	**n/a**	**n/a**	**n/a**	**n/a**	**n/a**	**n/a**	**0.2**	**100**	**100**	**2.0****	**100**	**26.0**	**0.2**	**100**	**100**	**n/a**	**n/a**	**n/a**
C5	Btg	524	2400	n/a	n/a	n/a	2.3	100	100	n/a	n/a	n/a	n/a	n/a	n/a	0.3	100	100	1.8	100	89.0	0.2	100	100	n/a	n/a	n/a
C6	BCg(t)	557	1200	n/a	n/a	n/a	1.8	100	100	n/a	n/a	n/a	n/a	n/a	n/a	n/a	n/a	n/a	0.9**	68.0	33.0	0.5**	57.0	85.0	n/a	n/a	n/a
C7	Bwg(t)	594	1200	n/a	n/a	n/a	2.1	100	100	n/a	n/a	n/a	n/a	n/a	n/a	n/a	n/a	n/a	2.6	100	100	0.1	100	100	n/a	n/a	n/a
C8	Bwg(t)	644	1200	n/a	n/a	n/a	8.7	100	100	n/a	n/a	n/a	n/a	n/a	n/a	n/a	n/a	n/a	3.1	100	100	0.3	100	100	n/a	n/a	n/a

C.3 EXEMPLARY INDIVIDUAL FEATURE CLASS VISUALISATION

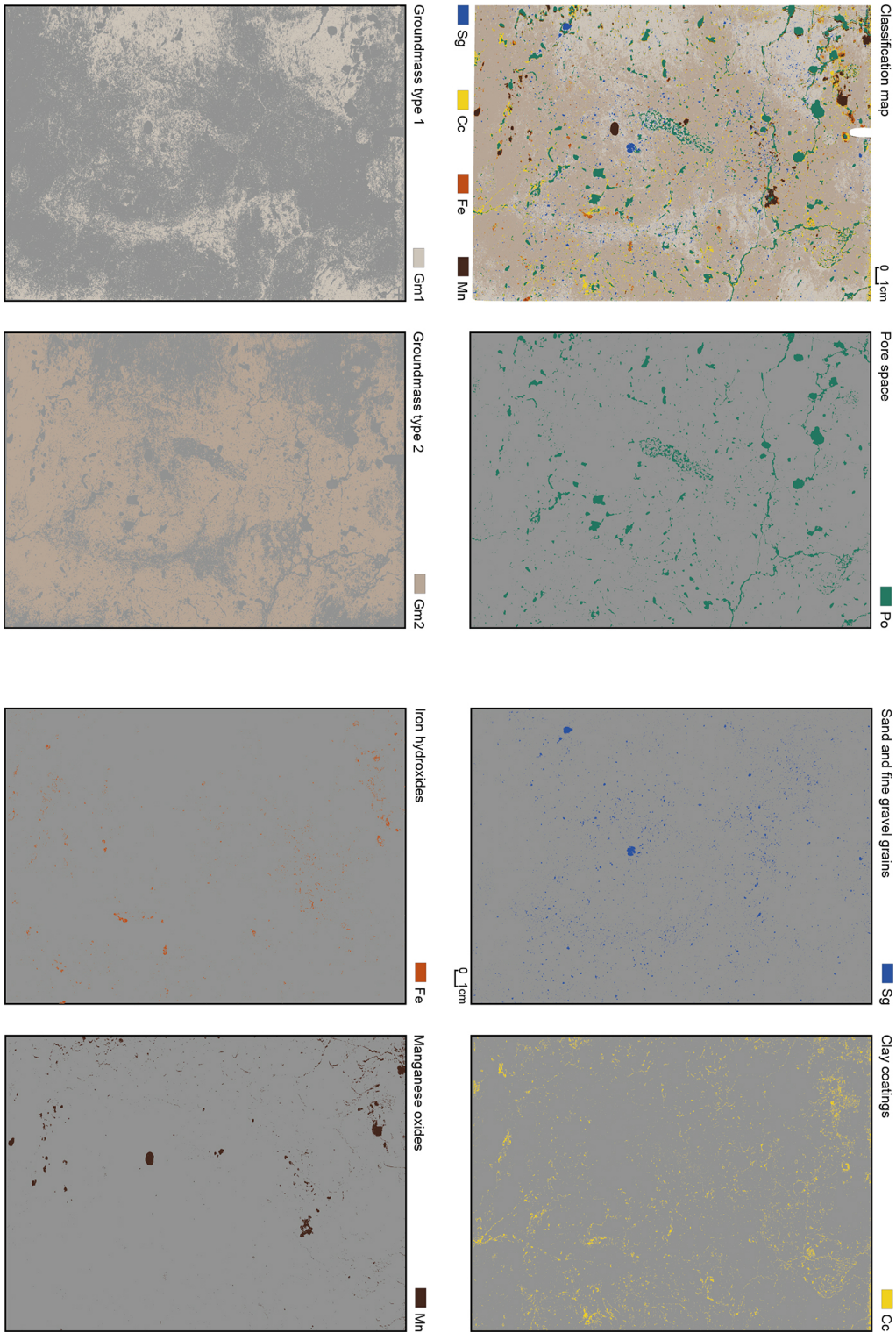

Figure C.1: Individual visualisation of classified feature classes, derived from the classification map of thin section A4.

D

SUPPLEMENTARY TO **INTEGRATED MICROMORPHOLOGICAL AND MICRO-XRF ANALYSIS OF BRONZE AGE HOUSE FLOORS AT TELL TOBOLIU, ROMANIA**

D.1 TS 1, MICROMORPHOLOGICAL SAMPLE DESCRIPTION

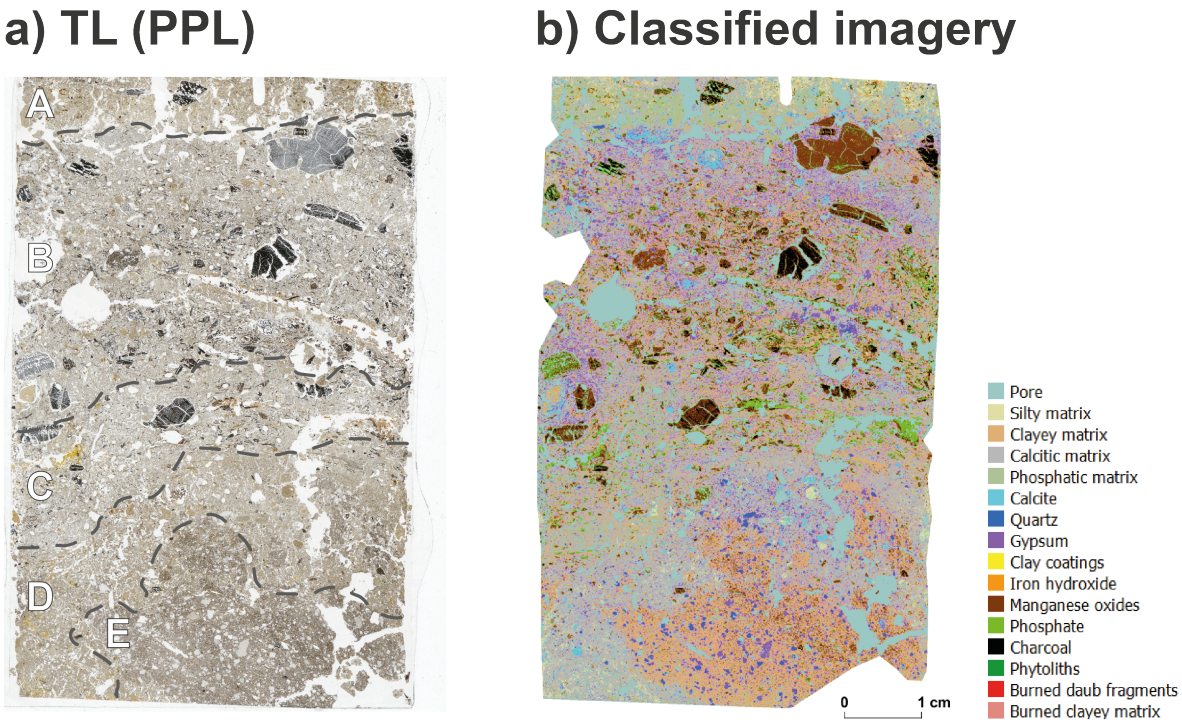

Figure D.1: Thin section Tob 1: a) Transmitted (TL), equivalent to plane polarised light (PPL), scanned thin section image and mapped microfacies labels. b) Sample composition classification based on TL, cross-polarised light (XPL), and reflected light (RL) scanned imagery and Random Forest Algorithm (Zickel et al., 2024).

Table D.1: Detailed micromorphological characterisation of sample TS 1: Microstructure, pores, groundmass properties, archaeological materials, and pedofeatures.

Unit	Microstructure and porosity	Groundmass		Anthropogenic/ organic components	Pedofeatures	Interpretation
		b-fabric	C/f ratio; minerogenic components			
A	Compact; some voids, chambers	Complex, stipple speckled, partly crystallitic b-fabric	Double spaced porphyric coarse fraction: few sand-sized angular-subangular quartz,few mica, few feldspar; fine fraction: silt sized quartz and clay, calcite (micritic)	Some macro- and micro charcoal/plant coal, phytoliths, ash	Some secondary calcite (hypo)-coatings, iron nodules	Highly carbonatic layer
B	Complex; vesicles, Chambers, channels, pseudomorphic voids	Complex, mainly crystallitic b-fabric	Complex, mostly porphyric coarse fraction: few sand-sized angular-subangular quartz, few mica, few feldspar; fine fraction: silt sized quartz and clay, calcite (micritic)	Various domestic waste: large pieces of charcoal (with visible tree rings), charred cereal grains, bone fragments, phytoliths (some ELONGATE DENDRITIC) , ash	Secondary calcite (hypo)-coatings, iron depletion, phosphate, gypsum bioturbation	Debris, domestic waste layer
C	Complex; vesicles, chambers, channels, pseudomorphic voids	Complex, stipple speckled, undifferentiated, crystallitic b-fabric	Complex, mostly porphyric coarse fraction: few sand-sized angular-subangular quartz, few mica, few feldspar; fine fraction: silt sized quartz and clay, some calcite (micritic)	All kinds of domestic waste: large pieces of charcoal (with visible tree rings), charred cereal grains, bone fragments, phytoliths (some ELONGATE DENDRITIC)	Some secondary phospate, calcite (hypo)-coatings, iron nodules	Mixed silty sediment and domestic waste
D	Compact; with areas of vesicles, chambers and vughes	Complex, stipple speckled, partly crystallitic b-fabric	Double spaced porphyric, coarse fraction: few sand-sized angular-subangular quartz, few mica, few feldspar; fine fraction: silt sized quartz and clay, micritic calcite	Some macro- and micro plant coal, phytoliths, bone fragments	Some secondary calcite (hypo)-coatings, iron nodules	Disturbed impure silt floor/platform (calcitic silt, calcite fragments)
E	Compact; aggregates, some chambers and planes	Undifferentiated b-fabric	Single spaced porphyric, coarse fraction: sand-sized angular-subangular quartz, few mica, few feldspar; fine fraction: silt sized quartz, calcitic fragments	Some micro and macro plant coal, isolated weathered phytoliths, high amount of amorphous organic fine material	Some secondary calcite coatings, iron nodules	Krotovina filled with Phaeozeme/ colluvial material

D.2 TS 12, MICROMORPHOLOGICAL SAMPLE DESCRIPTION

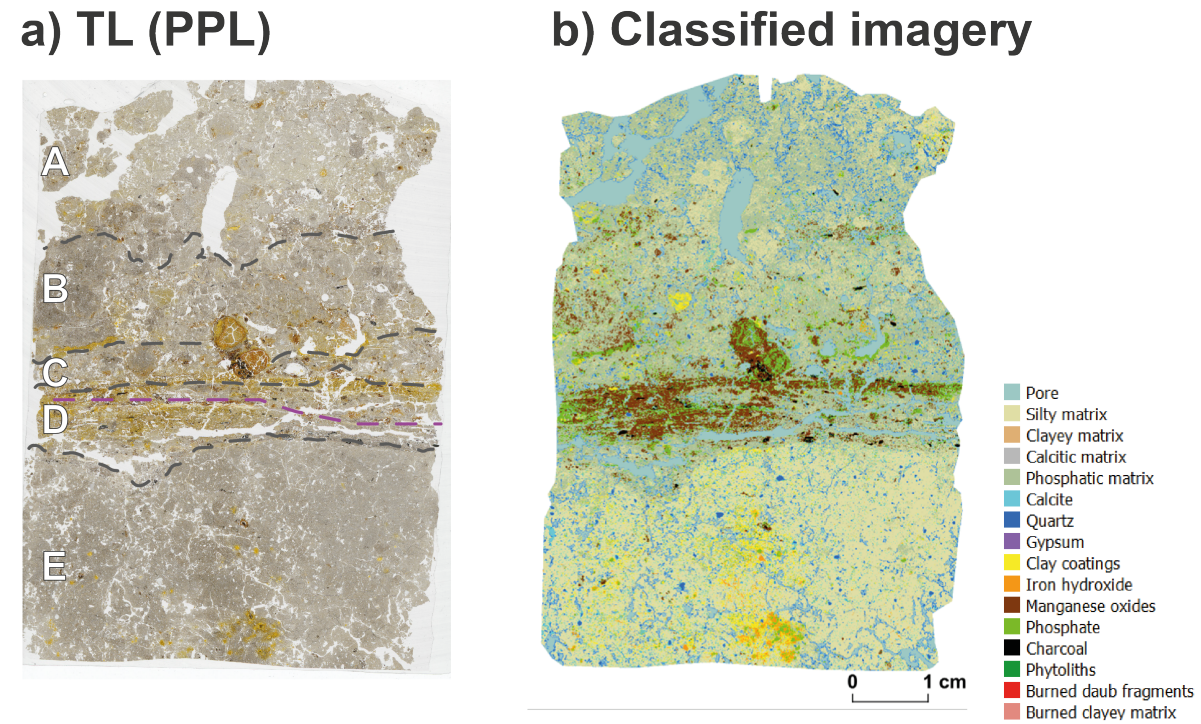

Figure D.2: Thin section Tob 12: a) Transmitted light (TL), equivalent to plane polarised light (PPL), scanned thin section image and mapped microfacies labels. b) Sample composition classification based on TL, cross-polarised light (XPL), and reflected light (RL) scanned imagery and Random Forest Algorithm (Zickel et al., 2024).

Table D.2: Detailed micromorphological characterisation of sample TS 12: Microstructure, pores, groundmass properties, archaeological materials, and pedofeatures.

Unit	Microstructure and porosity	Groundmass		Anthropogenic/ organic components	Pedofeatures	Interpretation
		b-fabric	C/f ratio; minerogenic components			
A	Complex, partly compact, all kind of voids	Complex, micaceous - crystallitic b-fabric, partly calcitic crystallitic b-fabric	Mostly double spaced porphyric coarse fraction: some angular to subangular sand-sized quartz, mainly silt sized quartz, mica, few feldspar; fine fraction: clay, calcitic fragments	Mosaic of silty sediments with some micro domestic waste (mostly plant coal, phytoliths), some humic aggregates	Mosaic of Iron, manganese impregnation as well as some phosphatic areas, calcite (hypo) coatings	Silt floor/platforms (rich in mica, calcitic fragments)
B	Complex, partly compact, all kind of voids	Complex, partly stipple speckled, calcitic crystallitic b-fabric	Mostly double spaced porphyric coarse fraction: some angular to subangular sand-sized quartz, mainly silt sized quartz, mica, few feldspar; fine fraction: clay, calcitic areas	Mosaic of silty sediments with domestic waste (mostly plant coal, phytoliths) and humic aggregates	Mosaic of Iron, manganese impregnation as well as some phosphatic areas	Impure silt floor/platform (clayey silt, humic parts, domestic waste)
C	Compact, some chambers and vughes	Complex, calcitic crystallitic b-fabric partly stipple speckled	Mostly double spaced porphyric coarse fraction: some angular to subangular sand-sized quartz, mainly silt sized quartz, mica, few feldspar; fine fraction: clay, calcitic	Some domestic waste (mostly plant coal, phytoliths)	Iron, manganese impregnation as well as some phosphatic areas	Silty sediment cover (partly calcitic)
D	Complex, partly planar, all kind of voids, also pseudomorphic voids	Complex, partly undifferentiated, calcitic crystallitic b-fabric	Complex, partly double spaced porphyric coarse fraction: mainly silt sized quartz, mica, few feldspar; fine fraction: clay	Finely dispersed domestic waste: horizontally orientated macro- and micro plant coal, few bone fragments, phytoliths (some ELONGATE DENDRITIC), ash, fragments of the wooden floor	Iron, manganese impregnation as well as phosphate	Directly above the clayey silt floor, a use layer of fine domestic waste on top of remnants of a heavily degraded wooden floor, followed by layered domestic waste
E	Compact, some chambers and vughs	Mainly parallel striated, granostriated and stipple speckled b-fabric, few areas calcitic crystallitic b-fabric	Double spaced porphyric coarse fraction: some angular to subangular sand-sized quartz, mainly silt sized quartz, mica, few feldspar, manganese; fine fraction: clay, some calcitic areas	Very few plant coal	iron nodules and impregnation, phosphate, some clay coatings	Clayey silt floor/foundation (low in calcium carbonate)

D.3 TS 21-1, MICROMORPHOLOGICAL SAMPLE DESCRIPTION

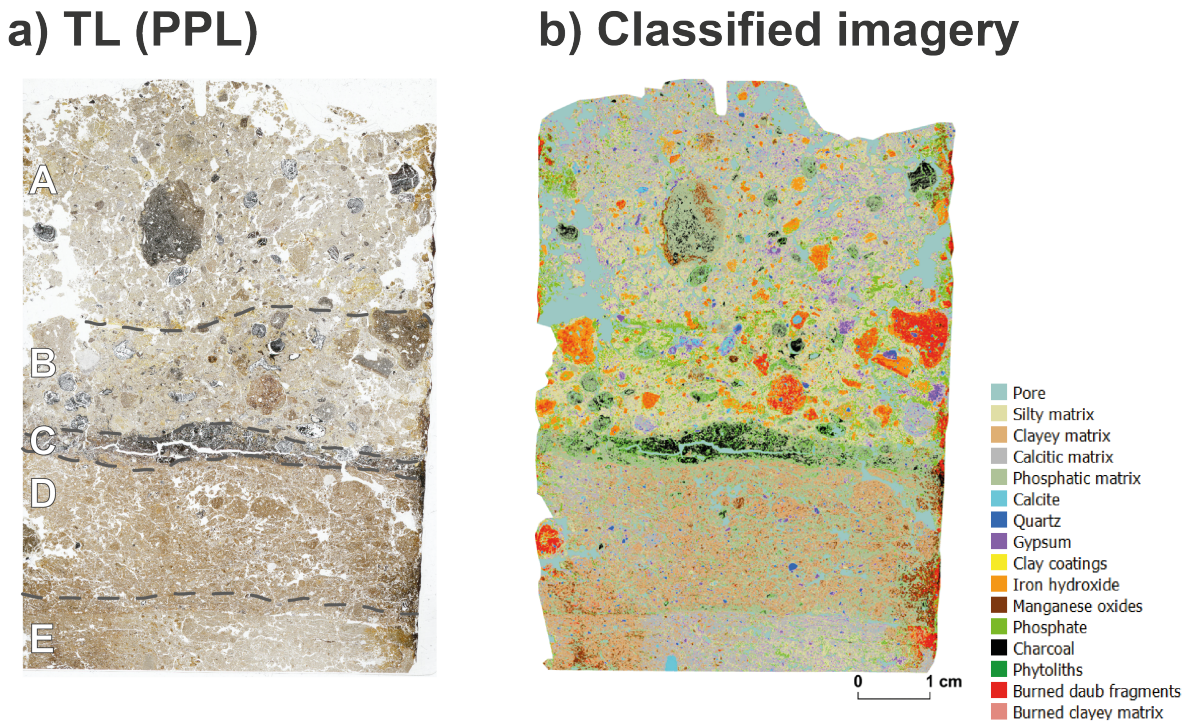

Figure D.3: Thin section Tob 21-1: a) Transmitted light (TL), equivalent to plane polarised light (PPL), scanned thin section image and mapped microfacies labels. b) Sample composition classification based on TL, cross-polarised light (XPL), and reflected light (RL) scanned imagery and Random Forest Algorithm (Zickel et al., 2024).

Table D.3: Detailed micromorphological characterisation of sample TS 21-1: Microstructure, pores, groundmass properties, archaeological materials, and pedofeatures.

Unit	Microstructure and porosity	Groundmass		Anthropogenic/ organic components	Pedofeatures	Interpretation
		b-fabric	C/f ratio; minerogenic components			
A	Complex, heterogeneous, all kinds of voids	Complex speckled, partly crystallitic b-fabric	Double spaced porphyric coarse fraction: sand, silt sized quartz, mica, few feldspar; fine fraction: silt and clay, calcite (micritic)	Charred cereal seeds, charcoal, differently heated daub fragments, ash, secondary iron, secondary calcite (hypo)-coatings	Debris, domestic waste (charred cereal grains, daub)	
B	Compact, heterogeneous composition, high amount of domestic waste (pottery sherds, articulated phytoliths, also ELONGATE DENDRITIC), ash	Complex speckled, undifferentiated, some areas calcitic crystallitic b-fabric	Double spaced porphyric coarse fraction: sand and silt sized quartz, mica, few feldspar; fine fraction: clay, calcite (micritic)	Charred cereal seeds, burnt daub	Secondary phosphate, calcite (hypo)-coatings, secondary iron	Debris, domestic waste (charred cereal grains, high amount of daub)
C	Complex, partly compact, partly layered, all kind of voids, also pseudomorphic voids	Complex, mainly undifferentiated, calcitic crystallitic b-fabric	Minerogenic areas: double spaced porphyric coarse fraction: mainly silt sized quartz, mica, few feldspar; fine fraction: silt and clay	Macro and micro charcoal/plant coal, phytoliths (also ELONGATE DENDRITIC), faecal spherulites, ash	Secondary calcite (hypo)-coatings, secondary iron	Charcoal/plant coal layer
D	Compact, pseudomorphic voids	Complex, parallel and granostriated b-fabric	Double spaced to open porphyric coarse fraction: few sand, but mainly silt sized quartz, mica, few feldspar, rounded soil/sediment fragments; fine fraction: clay, few calcitic fragments	Plant temper: chaff (articulated phytoliths, also ELONGATE DENDRITIC) horizontally orientated by preparation technique, ferruginized macro and micro charcoal and other plant coal, calcitic fragments, rounded clayey aggregates, Crysophyceae	Few dusty clay coatings, secondary calcite (hypo)-coatings, distinct iron impregnations	Plant tempered floor, strongly clayey silt
E	Compact, pseudomorphic voids	Complex speckled, parallel and granostriated b-fabric, partly calcitic crystallitic and micaceous crystallitic b-fabric	Double spaced porphyric coarse fraction: mainly silt sized quartz, mica, few feldspar; fine fraction: clay, calcitic fragments	Plant temper: chaff (articulated phytoliths, also ELONGATE DENDRITIC) horizontally orientated by preparation technique, some ferruginized macro and micro charcoal and other plant coal, angular calcitic fragments, rounded clayey aggregates	Few dusty clay coatings, secondary calcite (hypo-) coatings, secondary gypsum, secondary iron depletion	Plant tempered floor, clayey silt, calcitic fragments

D.4 TS 16, MICROMORPHOLOGICAL SAMPLE DESCRIPTION

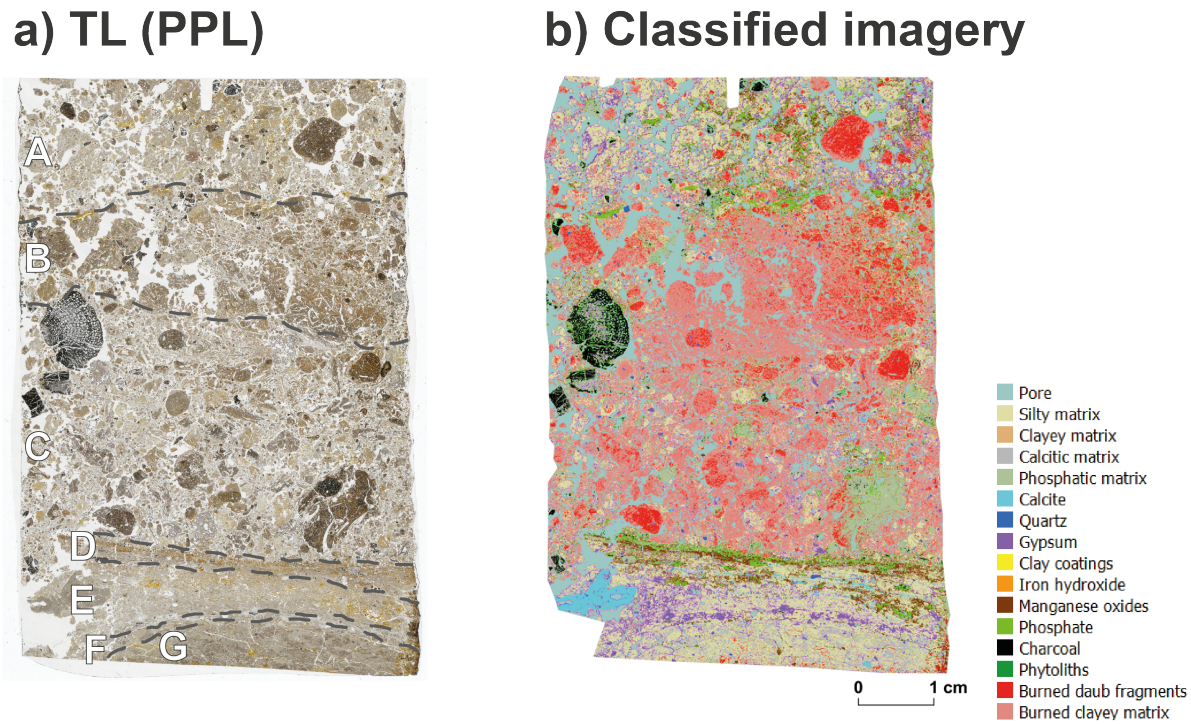

Figure D.4: Thin section Tob 16: a) Transmitted light (TL), equivalent to plane polarised light (PPL), scanned thin section image and mapped microfacies labels. b) Sample composition classification based on TL, cross-polarised light (XPL), and reflected light (RL) scanned imagery and Random Forest Algorithm (Zickel et al., 2024).

Table D.4: Detailed micromorphological characterisation of sample TS 16: Microstructure, pores, groundmass properties, archaeological materials, and pedofeatures.

Unit	Microstructure and porosity	Groundmass b-fabric	C/f ratio; minerogenic components	Anthropogenic/ organic components	Pedofeatures	Interpretation
A	Complex, loose, different kinds of voids, pseudomorphic voids	Complex, speckled and calcitic crystallitic b-fabric	Partly double spaced porphyric; mainly silt sized quartz, mica, few feldspar; fine fraction: clay, calcite (micritic)	Randomly distributed fragmented domestic waste (charred seed, charcoal, bone), ceramic fragments, daub fragments, ash	Secondary calcite, secondary iron and phosphate depletion	Debris layer, all kinds of waste (domestic and construction material, ceramics)
B	Complex, partly compact, different kinds of voids, pseudomorphic voids	Complex, speckled and calcitic crystallitic b-fabric	Complex, partly double spaced porphyric coarse fraction: sand sized quartz, mica, few feldspar; fine fraction: silt and clay, calcite (micritic)	Reddened daub with plant tempered (chaff) pieces, macro- and microscopic charcoal, glassy phytolith slags, heat deformed phytoliths and intact ELONGATE DENDRITIC, ash	Secondary iron nodules, secondary calcite	Debris layer, dominated by burnt daub
C	Complex, different kinds of voids, pseudomorphic voids	Complex, undifferentiated, speckled and calcitic crystallitic b-fabric	Complex, partly double spaced porphyric coarse fraction: sand sized quartz, mica, few feldspar; fine fraction: silt and clay, calcite (micritic)	Randomly distributed differently heated daub (reddening, partly molten) with plant tempered (chaff) pieces, ceramic fragments some plant tempered, macro- and microscopic charcoal, glassy phytolith slags, heat deformed phytoliths and intact ELONGATE DENDRITIC, bone fragments, ash	Secondary calcite, secondary iron and phosphate depletion	Burnt debris layer, all kinds of heat altered material (construction material, ceramics, domestic waste)
D	Complex, partly planar, all kinds of voids, also pseudomorphic voids	Complex, undifferentiated and calcitic crystallitic b-fabric	Complex, partly double spaced porphyric coarse fraction: mainly silt sized quartz, mica, few feldspar; fine fraction: clay, calcite (micritic)	Burnt layered domestic waste: horizontally orientated mostly charred organic material, bone fragments, phytoliths (also ELONGATES DENDRITIC), ash, faecal spherulites	Secondary calcite, secondary iron nodules and depletion	Use layer
E	Complex, partly compact, partly planar, all kinds of voids, pseudomorphic voids; compact layer on top	Complex speckled and calcitic crystallitic b-fabric	Double spaced porphyric coarse fraction: mainly silt sized quartz, mica, few feldspar; fine fraction: clay, micritic calcite	Top layer: calcite (micritic, partly micro plant coal); some domestic waste (macro and micro charcoal/plant coal, bone fragments) and plant temper (only few articulated phytoliths left in pseudomorphic voids), ash	Secondary calcite, secondary iron and phosphate depletion	Plant tempered silt floor, highly calcareous including fragments of domestic waste
F	Compact, microstructure dominated by secondary gypsum, some chambers and planes	Complex, mostly calcitic crystallitic b-fabric	Partly double spaced porphyric; mainly silt sized quartz, mica, few feldspar; fine fraction: clay, calcite (micritic)	Domestic waste: macro and micro charcoal horizontally orientated, small bone fragments, few isolated phytoliths, large micritic calcite fragment	Secondary gypsum, secondary calcite coatings, secondary iron	Use layer
G	Compact, aggregates, some chambers and planes	Complex, undifferentiated, speckled, parallel striated and calcitic crystallitic b-fabric	Double spaced porphyric coarse fraction: some sand-sized quartz, mainly silt sized quartz, mica, few feldspar; fine fraction: clay, calcitic areas	Mixing of different materials, more humic silty material with calcitic silty sediments	Some secondary calcite coatings, iron nodules	Mottled silt floor composed of mixed materials (clayey silt and humic clayey silty material)

D.5 TS 5, MICROMORPHOLOGICAL SAMPLE DESCRIPTION

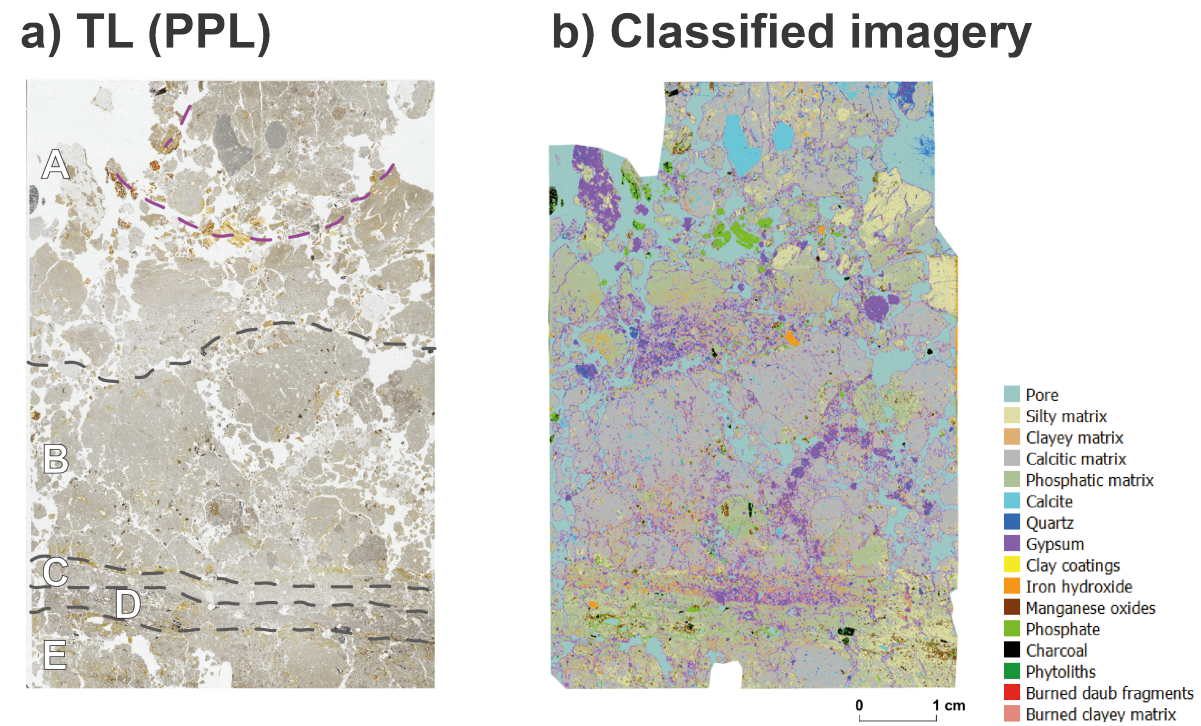

Figure D.5: Thin section Tob 5: a) Transmitted light (TL), equivalent to plane polarised light (PPL), scanned thin section image and mapped microfacies labels. b) Sample composition classification based on TL, cross-polarised light (XPL), and reflected light (RL) scanned imagery and Random Forest Algorithm (Zickel et al., 2024).

Table D.5: Detailed micromorphological characterisation of sample TS 5: Microstructure, pores, groundmass properties, archaeological materials, and pedofeatures.

Unit	Microstructure and porosity	Groundmass		Anthropogenic/ organic components	Pedofeatures	Interpretation
		b-fabric	C/f ratio; minerogenic components			
A	Complex, heterogeneous, all kinds of voids	Complex speckled, partly crystallitic b-fabric	Double spaced porphyric coarse fraction: sand, silt sized quartz, mica, few feldspar; fine fraction: silt and clay, calcite (micritic)	Charred cereal seeds, charcoal, differently heated daub fragments, ash	Secondary iron, secondary calcite (hypo) coatings	Debris, domestic waste (charred cereal grains, daub)
B	Compact, heterogeneous composition	Complex speckled, undifferentiated, some areas calcitic crystallitic b-fabric	Double spaced porphyric coarse fraction: sand and silt sized quartz, mica, few feldspar; fine fraction: clay, calcite (micritic)	Charred cereal seeds, burnt daub, high amount of domestic waste (pottery sherds, articulated phytoliths, also ELONGATE DENDRITIC), ash	Secondary phosphate, calcite (hypo)-coatings, secondary iron	Debris, domestic waste (charred cereal grains, high amount of daub)
C	Complex, partly compact, partly layered, all kinds of voids, also pseudomorphic voids	Complex, mainly undifferentiated, calcitic crystallitic b-fabric	Minerogenic areas: double spaced porphyric coarse fraction: mainly silt sized quartz, mica, few feldspar; fine fraction: silt and clay	Macro and micro charcoal/plant coal, phytoliths (also ELONGATE DENDRITIC), faecal spherulites, ash	Secondary calcite (hypo)-coatings, secondary iron	Charcoal/plant coal layer
D	Compact, pseudomorphic voids	Complex, parallel and granostriated b-fabric	Double spaced to open porphyric coarse fraction: few sand, mainly silt sized quartz, mica, few feldspar, rounded soil/sediment fragments; fine fraction: clay, few calcitic fragments	Plant temper: chaff (articulated phytoliths, also ELONGATE DENDRITIC), horizontally orientated by preparation technique, ferruginized macro and micro charcoal and other plant coal, calcitic fragments, rounded clayey aggregates, Crysophyceae	Few dusty clay coatings, secondary calcite (hypo)-coatings, distinct iron impregnations	Plant tempered floor, strongly clayey silt
E	Compact, pseudomorphic voids	Complex speckled, parallel and granostriated b-fabric, partly calcitic crystallitic and micaceous crystallitic b-fabric	Double spaced porphyric coarse fraction: mainly silt sized quartz, mica, few feldspar; fine fraction: clay, calcitic fragments	Plant temper: chaff (articulated phytoliths also ELONGATE DENDRITIC), horizontally orientated by preparation technique, some ferruginized macro and micro charcoal and other plant coal, angular calcitic fragments, rounded clayey aggregates	Few dusty clay coatings, secondary calcite (hypo-) coatings, secondary gypsum, secondary iron depletion	Plant tempered floor, clayey silt, calcitic fragments

D.6 TS 19-2, MICROMORPHOLOGICAL SAMPLE DESCRIPTION

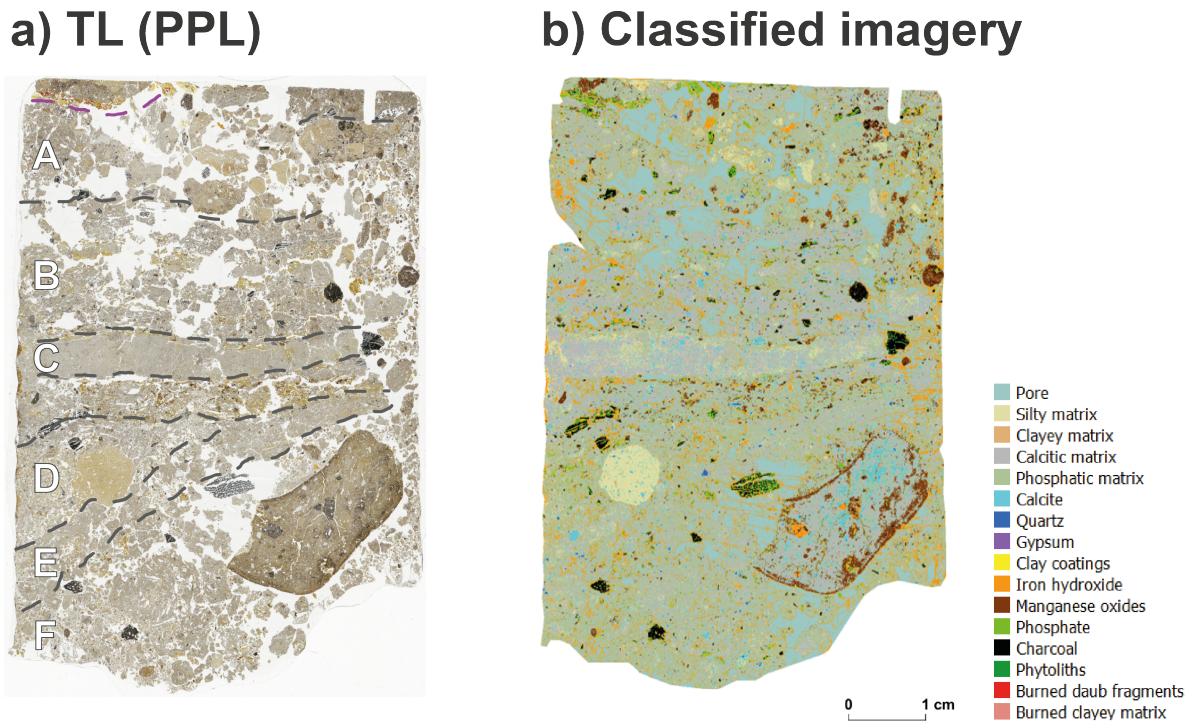

Figure D.6: Thin section Tob 19-2: a) Transmitted light (TL), equivalent to plane polarised light (PPL), scanned thin section image and mapped microfacies labels. b) Sample composition classification based on TL, cross-polarised light (XPL), and reflected light (RL) scanned imagery and Random Forest Algorithm (Zickel et al., 2024).

Table D.6: Detailed micromorphological characterisation of sample TS 19-2: Microstructure, pores, groundmass properties, archaeological materials, and pedofeatures.

Unit	Microstructure and porosity	Groundmass		Anthropogenic/ organic components	Pedofeatures	Interpretation
		b-fabric	C/f ratio			
A	-	-	-	Remnants of wood	secondary iron, calcite and phosphate depletion	remnants of a wooden floor (see micro XRF)
B	Complex, partly compact; planes and voids, partly not intact (due to transport)	Complex, calcitic crystallitic and speckled b-fabric	Double spaced porphyric coarse fraction: mainly silt sized quartz, mica, few feldspar; fine fraction: clay and silt, micritic calcite	All kinds of domestic waste, partly layered: macro and micro charcoal, bone fragments, ash, articulated phytoliths, ELONGATE DENDRITIC	Secondary iron, calcite and phosphate depletion	Debris, domestic waste; possibly silty cover on top (not intact sample preservation)
C	Compact, some voids	Mainly calcitic crystallitic b-fabric	Partly double spaced porphyric, mainly silt sized quartz, few feldspar, very few mica; fine fraction: clay, micritic calcite	Almost no accidental waste residues	Secondary calcite, secondary iron	Calcareous cover (reflooring, plaster?)
D	Compact, aggregates, some chambers and planes	Complex, calcitic crystallitic and speckled b-fabric	Double spaced porphyric coarse fraction: some sand-sized quartz, mainly silt sized quartz, mica, few feldspar; fine fraction: clay	Domestic waste: horizontally layered macro and micro charcoal/plant coal, few bone fragments, ash, articulated phytoliths, ELONGATE DENDRITIC	Some secondary calcite, iron depletion (upper part)	Use layer with partly orientated fine domestic waste
E	Partly compact, partly not intact	Parallel striated b-fabric, some areas calcitic crystallitic b-fabric	Double spaced porphyric coarse fraction: some sand-sized quartz, mainly silt sized quartz; fine fraction: clay, micritic calcite	Some horizontally orientated microscopic plant coal	Few secondary iron and calcite	Remnants of a silty cover/finish
F	Complex, aggregates, (pseudomorphic) voids, chambers	Complex, undifferentiated, speckled and calcitic crystallitic b-fabric	Complex, partly double spaced porphyric; coarse fraction: sand sized quartz, mica, few feldspar; fine fraction: silt and clay, micritic calcite	Randomly orientated domestic waste: pottery sherd (l.: 2.5 cm), loessic chunk, macro- and microscopic charcoal, phytoliths, bone fragments, glassy phytolith slags	Secondary iron, some secondary calcite and phosphate	Debris, domestic waste with a pottery sherd (high in clay), possibly forming a platform

D.7 SINGLE VALUES OF THE MICRO-XRF MEASUREMENTS IN SELECTED FLOORING MICROFACIES

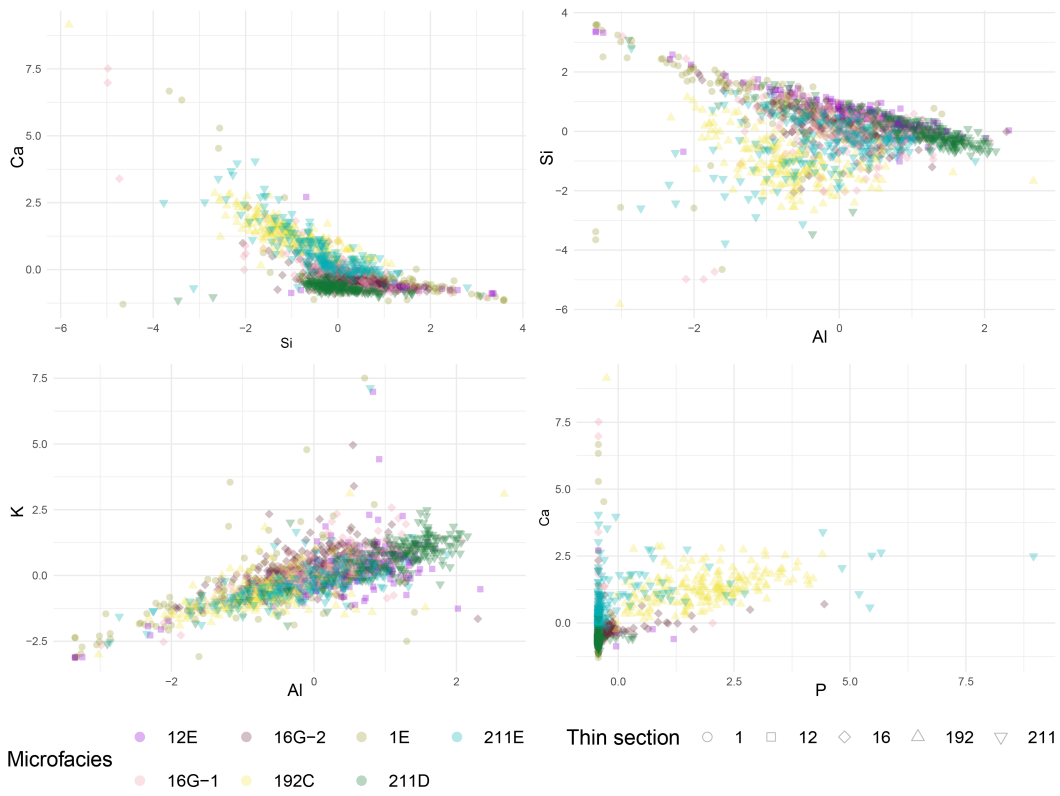

Figure D.7: Micro-XRF point measurements (single value scatter) on thin sections for the sediment flooring and calcareous covering classes, normalised and scaled values.

D.8 MICRO-XRF MEASUREMENT RESULTS PER THIN SECTION



Figure D.8: Micro-XRF measurements of microfacies E in thin section 1.

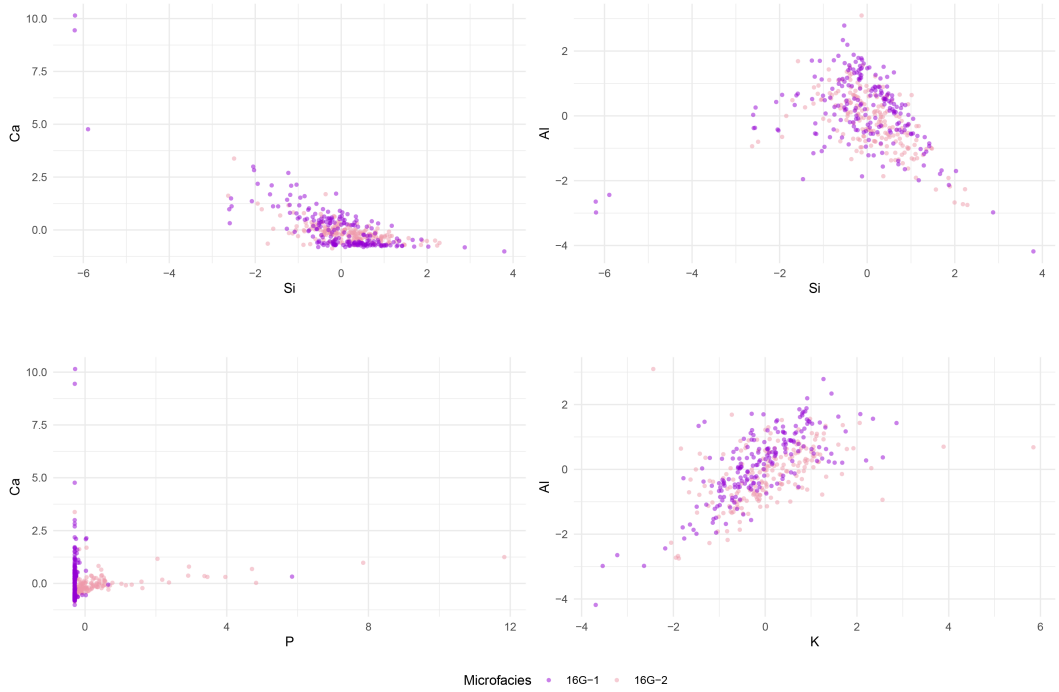

Figure D.9: Micro-XRF measurements of microfacies G in thin section 16.

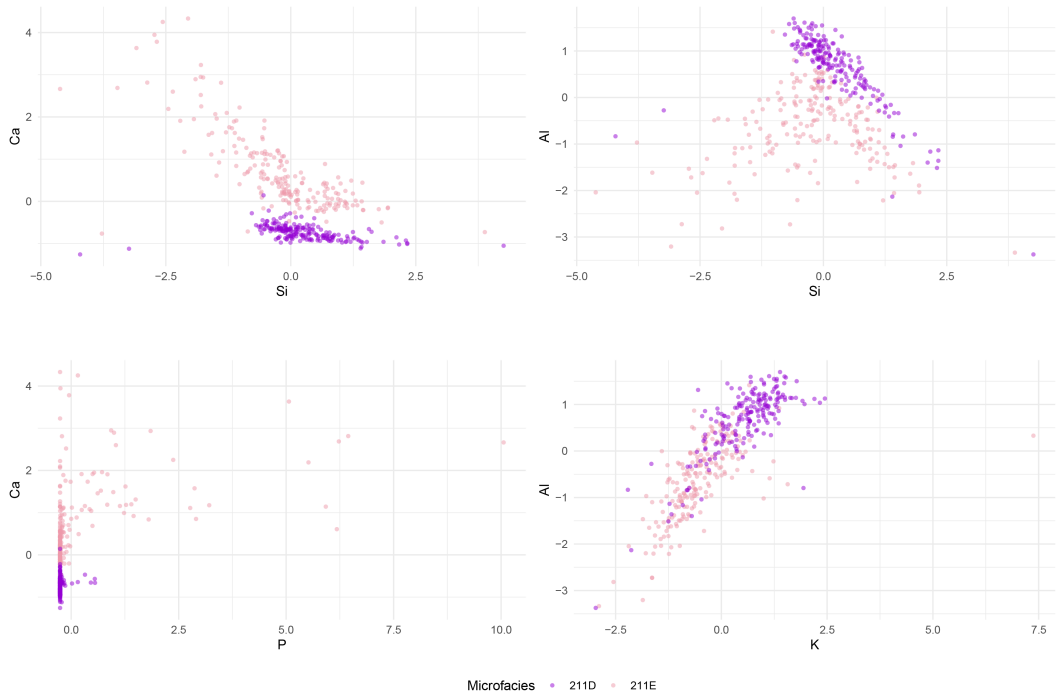

Figure D.10: Micro-XRF measurements of microfacies D and E in thin section 21-1.

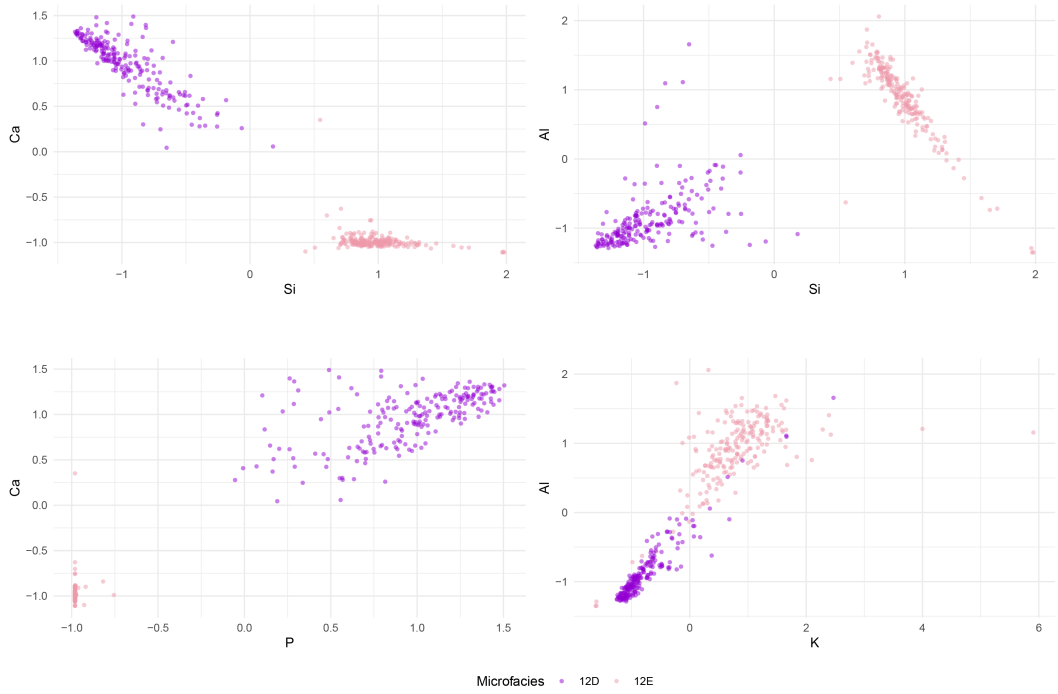

Figure D.11: Micro-XRF measurements of the wooden residues in microfacies D and E in thin section 12.

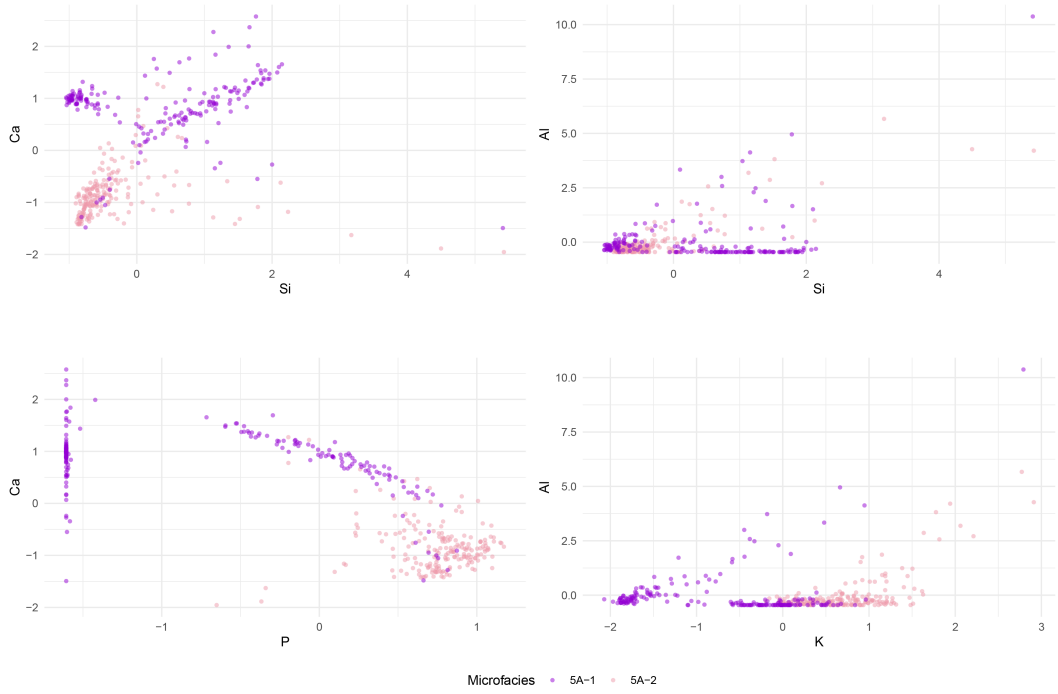

Figure D.12: Micro-XRF measurements of the wooden residues in microfacies A in thin section 5.

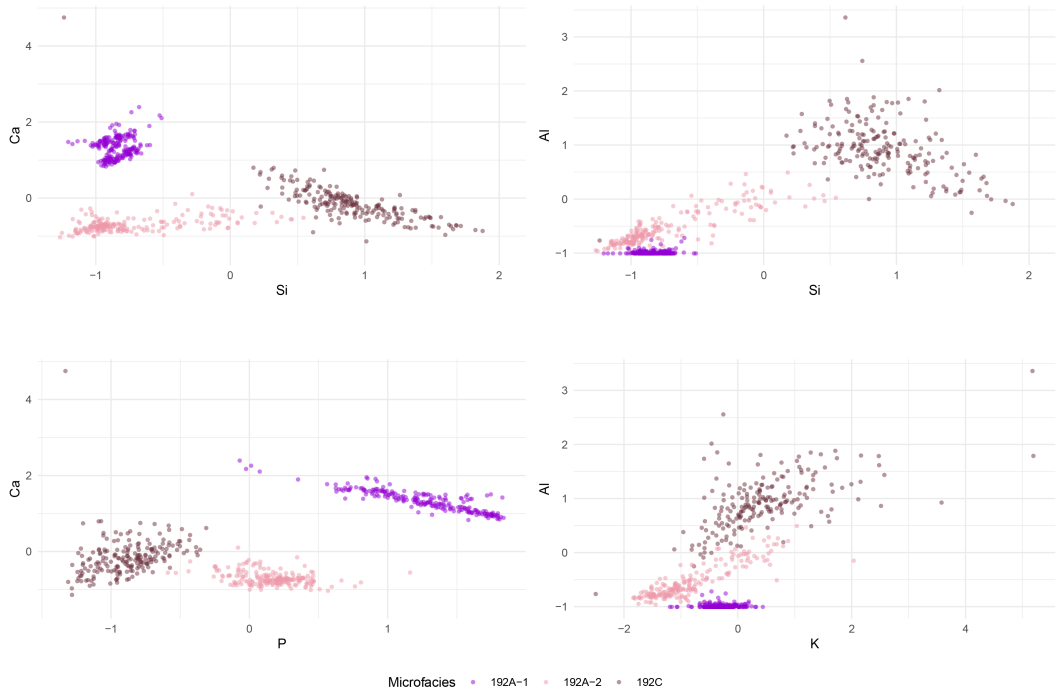

Figure D.13: Micro-XRF measurements of the wooden residues in microfacies A and the calcareous flooring in C in thin section 19-2.

Abulafia, T. (2018). "Post-depositional Processes in the Upper Paleolithic Period; A Typotechnological Case Study from Manot Cave Area C". MA thesis. Beer Sheva: Ben Gurion University of the Negev (cit. on p. 51).

Abulafia, T., M. Goder-Goldberger, F. Berna, O. Barzilai, and O. Marder (2019). "A techno-typological analysis of the Ahmarian and Levantine Aurignacian assemblages from Manot Cave (Area C) and the interrelation with site formation processes". In: *J. Hum. Evol.* (cit. on p. 51).

Alex, B., O. Barzilai, I. Hershkovitz, O. Marder, F. Berna, V. Caracuta, T. Abulafia, L. Davis, M. Goder-Goldberger, R. Lavi, et al. (2017). "Radiocarbon chronology of Manot cave, Israel and upper paleolithic dispersals". In: *Science advances* 3.11, e1701450 (cit. on pp. 51, 52).

Amadio, M. (2018). "From deposits to social practices: Integrated micromorphological analysis of floor sequences at Middle Bronze Age Erimi-Laonin tou Porakou, Cyprus". In: *Journal of Archaeological Science: Reports* 21, pp. 433–449. DOI: https://doi.org/10.1016/j.jasrep.2018.07.023 (cit. on pp. 152, 176).

Anderson, J. R., E. E. Hardy, J. T. Roach, and R. E. Witmer (1976). *A land use and land cover classification system for use with remote sensor data*. Tech. rep. Professional Paper 964. Reston, USA: USGS Publications Warehouse. DOI: 10.3133/pp964 (cit. on p. 134).

Antoine, P., D.-D. Rousseau, M. Fuchs, C. Hatté, C. Gauthier, S. B. Marković, M. Jovanović, T. Gaudenyi, O. Moine, and J. Rossignol (2009). "High-resolution record of the last climatic cycle in the southern Carpathian Basin (Surduk, Vojvodina, Serbia)". In: *Quaternary International* 198.1. Loess in the Danube Region and Surrounding Loess Provinces: The Marsigli Memorial Volume, pp. 19–36. DOI: 10.1016/j.quaint.2008.12.008 (cit. on pp. 85, 105, 107).

Arnay, R., J. Hernández-Aceituno, and C. Mallol (2021). "Soil micromorphological image classification using deep learning: The porosity parameter". In: *Applied Soft Computing* 102, p. 107093. DOI: 10.1016/j.asoc.2021.107093 (cit. on p. 119).

Arpin, T. L., C. Mallol, and P. Goldberg (2002). "Short contribution: A new method of analyzing and documenting micromorphological thin sections using flatbed scanners: Applications in geoarchaeological studies". In: *Geoarchaeology* 17, pp. 305–313. DOI: 10.1002/gea.10014 (cit. on pp. 119, 124).

Authority, I. A. (2020). *The archaeological survey of Israel*. Accessed 1 December 2020. URL: http://survey.antiquities.org.il/index_Eng.html#/ (cit. on pp. 61, 198).

Avni, Y. (2017). "Tectonic and physiographic settings of the levant". In: *Quaternary of the Levant*. Ed. by Y. Enzel and O. Bar-Yosef. Cambridge University Press, pp. 3–16 (cit. on pp. 53, 55, 56).

Azoury, I. (1986). *Ksar Akil, Lebanon: A Technological and Typological Analysis of the Transitional and Early Upper Paleolithic Levels of Ksar Akil and Abu Halka Volume I: Levels XXV-XII*. Vol. 289. BAR International Series. Oxford: B.A.R, p. 477 (cit. on pp. 51, 52).

Bailey, S., T. Weaver, and J.-J. Hublin (2009). "Who made the Aurignacian and other early Upper Paleolithic industries?" In: *J. Hum. Evol.* 57.1, pp. 11–26 (cit. on p. 52).

Banerjea, R. Y., M. Bell, W. Matthews, and A. Brown (2015). "Applications of micromorphology to understanding activity areas and site formation processes in experimental hut floors". In: *Archaeological and Anthropological Sciences* 7, pp. 89–112. URL: https://api.semanticscholar.org/CorpusID:129857003 (cit. on p. 176).

Bánffy, E. and O. Books (2019). *First Farmers of the Carpathian Basin: Changing Patterns in Subsistence, Ritual and Monumental Figurines*. Prehistoric Society Research Paper. Philadelphia, USA: Oxbow Books. URL: https://books.google.com/books?id=zBs4zgEACAAJ (cit. on p. 84).

Bar-Yosef, O. and A. Belfer-Cohen (1996). "Another look at the levantine aurignacian". In: *The Upper Palaeolithic. Colloquium XI: the Late Aurignacian*. Ed. by A. Montet-White, A. Palma de Cesnola, and K. Valoch. Forli, Italy: A.B.A.C.O, pp. 8–14 (cit. on p. 52).

Bar-Yosef, O. and A. Belfer-Cohen (2004). "The Qafzeh upper paleolithic assemblages: 70 Years later". In: *Eurasian Prehistory* 2.1, pp. 145–180 (cit. on p. 51).

Bar-Yosef, O. and A. Belfer-Cohen (2010). "The levantine upper palaeolithic and epipalaeolithic". In: *South-eastern Mediterranean Peoples between 130,000 and 10,000 Years Ago*. Ed. by E. Garcea. Oxford, Oakville CT: Oxbow Books, pp. 144–167 (cit. on p. 52).

Bar-Yosef, O. and A. Belfer-Cohen (2019). "The upper paleolithic industries of Kebara cave". In: *Kebara Cave, Mt. Carmel, Israel. The Middle and Upper Paleolithic Archaeology*. Ed. by L. Meignen and O. Bar-Yosef. Vol. 51. Peabody Museum of Archaeology and Ethnology, Harvard University, Cambridge, Massachusetts: American School of Prehistoric Research Bulletin, pp. 309–400 (cit. on p. 51).

Bar-Yosef, O., B. Vandermeersch, and I. U. for Quaternary Research (1972). "The stratigraphical and cultural problems of the passage from Middle to Upper Palaeolithic in Palestinian caves". In: *Symposium on Environmental Changes and the Origin of Homo Sapiens. The Origin of homo Sapiens: Proceedings of the Paris Symposium*. Ed. by F. Bordes. Paris: UNESCO, pp. 221–225 (cit. on p. 78).

Barjous, M. (2003). "The Geology of Petra and the Wadi Al-Lahyana area, map sheets No. 3050-I and 3050-IV". In: *1:50 000 Geological Mapping Series*. Amman: Geological Bulletin No. 56 (cit. on p. 56).

Barzilai, O., I. Hershkovitz, and O. Marder (2016). "The early upper paleolithic period at Manot cave, western galilee, Israel". In: *Hum. Evol.* 31.1–2, pp. 85–100 (cit. on pp. 51, 52).

Barzilai, O., I. Hershkovitz, O. Marder, A. Ayalon, M. Bar-Matthews, G. Bar-Oz, E. Boaretto, F. Berna, A. Frumkin, H. Khalaily, et al. (2012). "Manot cave". In: *Hadashot Arkheologiyot* 124 (cit. on pp. 52, 60).

Barzilai, O., O. Marder, and I. Hershkovitz (2014). "Manot cave, seasons 2011–2012". In: *Hadashot Arkheologiyot* 126 (cit. on p. 52).

Becker, D., M. d. Andrés-Herrero, C. Willmes, G.-C. Weniger, and G. Bareth (2017). "Investigating the influence of different DEMs on GIS-based cost distance modeling for site catchment analysis of prehistoric sites in andalusia". In: *IJGI* 6.2, p. 36 (cit. on p. 74).

Beckman Coulter, Inc. (2011). *LS 13 320 Laser Diffraction Particle Size Analyzer. Instruction for use*. Ed. by Beckman Coulter, Inc. URL: https://www.mybeckman.nl/particle-size-analyzers/ls-13-320-xr (cit. on p. 89).

Beckmann, T. (1997). "Präparation bodenkundlicher Dünnschliffe für mikromorphologische Untersuchungen". In: *Hohenheimer Bodenkundliche Hefte* 55, pp. 31–40 (cit. on pp. 122, 156).

Belfer-Cohen, A. and O. Bar-Yosef (1973). "Nahal ein gev I, preliminary report". In: *Journal of the Israel Prehistoric Society*, pp. 1–7 (cit. on pp. 52, 60).

Belfer-Cohen, A. and O. Bar-Yosef (1981). "The aurignacian at Hayonim cave". In: *Paleorient* 7.2, pp. 19–42 (cit. on p. 52).

Belfer-Cohen, A. and O. Bar-Yosef (2015). "Paleolithic recycling: the example of Aurignacian artifacts from Kebara and Hayonim caves". In: *Quat. Int.* 361, pp. 256–259 (cit. on p. 51).

Belfer-Cohen, A., A. Davidzon, A. Goring-Morris, D. Lieberman, and M. Spiers (2004). "Nahal ein gev I: a late upper palaeolithic site by the sea of galilee, Israel". In: *Paleorient* 30.1, pp. 25–46 (cit. on p. 52).

Belfer-Cohen, A. and A. Goring-Morris (1986). "Har horesha I: an upper paleolithic occupation in the western Negev highlands". In: *Journal of the Israel Prehistoric Society* 19, pp. 43–57 (cit. on p. 60).

Belfer-Cohen, A. and A. Goring-Morris (2003). "Current issues in levantine upper palaeolithic research". In: *More than Meets the Eye. Studies on Upper Palaeolithic Diversity in the Near East*. Ed. by A. Goring-Morris and A. Belfer-Cohen. Oxford, Oakville: Oxbow Books, pp. 1–12 (cit. on pp. 51, 52).

Belfer-Cohen, A. and A. Goring-Morris (2014). "On the rebound - a levantine view of upper palaeolithic dynamics". In: *Modes de contacts et de d´eplacements au Paleolithique eurasiatique*. Ed. by M. Otte. Actes du colloque international de la Commission 8´ (Paleolithique Su´ p´erieur) de l'UISPP, Universit´e de Liege, pp. 27–36 (cit. on p. 51).

Bell, W. (1980). "Alpha dose attenuation in quartz grains for thermoluminescence dating." In: *Ancient TL* 12, pp. 4–8 (cit. on p. 90).

Bergman, C., J. Williams, K. Douka, and D. Schyle (2017). "The palaeolithic sequence of ksar 'Akil, Lebanon". In: *Quaternary of the Levant*. Ed. by Y. Enzel and O. Bar-Yosef. Cambridge University Press, pp. 267–276 (cit. on pp. 51, 52).

Bergman, C. (1987). *Ksar Akil, Lebanon: A Technological and Typological Analysis of the Later Palaeolithic Levels of Ksar Akil. Volume II: Levels XIII-VI*. Vol. 329. Oxford, UK: BAR International Series (cit. on p. 51).

Berna, F. (2019). "Geoarchaeology: The Human-Environmental Approach". In: *The Holocene* 29.6, pp. 1105–1106. DOI: \\newline10.1177/0959683619837034 (cit. on pp. 34, 41).

Bertrams, M. (2013). "Late quaternary landscape evolution in the wadi Sabra (Jordan) based on sedimentological and geochemical investigations". In: *Aachener Geographische Arbeiten*. Vol. 49. RWTH Aachen, Geographisches Institut (cit. on pp. 56, 68).

Beyin, A., J. Hall, and C. Day (2019). "A least cost path model for hominin dispersal routes out of the east African Rift region (Ethiopia) into the levant". In: *J. Archaeol. Sci.: Report* 23, pp. 763–772 (cit. on p. 72).

Blott, S. J. and K. Pye (2001). "GRADISTAT: a grain size distribution and statistics package for the analysis of unconsolidated sediments". In: *Earth Surface Processes and Landforms* 26.11, pp. 1237–1248. DOI: 10.1002/esp.261. eprint: https://onlinelibrary.wiley.com/doi/pdf/10.1002/esp.261 (cit. on pp. 89, 221).

Böning, P., E. Bard, and J. Rose (May 2007). "Toward direct, micron-scale XRF elemental maps and quantitative profiles of wet marine sediments". In: *Geochemistry, Geophysics, Geosystems* 8.5, p. 5004. DOI: 10.1029/2006gc001480 (cit. on pp. 178, 188).

Bösken, J. J., I. Obreht, C. Zeeden, N. Klasen, U. Hambach, P. Sümegi, and F. Lehmkuhl (2019). "High-resolution paleoclimatic proxy data from the MIS3/2 transition recorded in northeastern Hungarian loess". In: *Quaternary International*. DOI: 10.1016/j.quaint.2017.12.008 (cit. on pp. 85, 105, 107).

Boyle, J. F. (2001). "Inorganic Geochemical Methods in Palaeolimnology". In: *Tracking Environmental Change Using Lake Sediments: Physical and Geochemical Methods*. Ed. by W. M. Last and J. P. Smol. Dordrecht: Springer Netherlands, pp. 83–141. DOI: 10.1007/0-306-47670-3_5 (cit. on pp. 89, 222).

Breimann, L. (2001). "Random Forests". In: *Machine Learning* 45, pp. 5–32. DOI: 10.1023/A:1010933404324 (cit. on pp. 125, 126, 136, 187).

Brennan, B. (2003). "Beta doses to spherical grains". In: *Radiation Measurements* 37.4. Proceedings of the 10th international Conference on Luminescence and Electron-Spin Resonance Dating (LED 2002), pp. 299–303. DOI: 10.1016/S1350-4487(03)00011-8 (cit. on p. 90).

Brewer, R. (1964). *Fabric and mineral analysis of soils*. New York, USA: John Wiley & Sons (cit. on p. 122).

Brigatti, M. F. and S. Guggenheim (2002). "Mica Crystal Chemistry and the Influence of Pressure, Temperature, and Solid Solution on Atomistic Models". In: *Reviews in Mineralogy and Geochemistry* 46.1, pp. 1–97. DOI: 10.2138/rmg.2002.46.01 (cit. on p. 172).

Bronk Ramsey, C. (2009). "Bayesian Analysis of Radiocarbon Dates". In: *Radiocarbon* 51.1, pp. 337–360. DOI: 10.1017/S0033822200033865 (cit. on p. 90).

Brönnimann, D., B. Röder, N. Spichtig, H. Rissanen, G. Lassau, and P. Rentzel (2020). "The Hidden Midden: Geoarchaeological investigation of sedimentation processes, waste disposal practices, and resource management at the La Tène settlement of Basel-Gasfabrik (Switzerland)". In: *Geoarchaeology* 35, pp. 522–544. DOI: 10.1002/gea.21787 (cit. on p. 118).

Brooks, G. R. (2003). "Alluvial deposits of a mud-dominated stream: the Red River, Manitoba, Canada". In: *Sedimentology* 50.3, pp. 441–458. DOI: 10.1046/j.1365-3091.2003.00559.x. eprint: https://onlinelibrary.wiley.com/doi/pdf/10.1046/j.1365-3091.2003.00559.x (cit. on pp. 102, 105).

Buggle, B., B. Glaser, U. Hambach, N. P. Gerasimenko, and S. B. Marković (2011). "An evaluation of geochemical weathering indices in loess-paleosol studies". In: *Quaternary International* 240, pp. 12–21. URL: https://api.semanticscholar.org/CorpusID:128838789 (cit. on pp. 89, 222).

Buggle, B., B. Glaser, L. Zöller, U. Hambach, S. Marković, I. Glaser, and N. Gerasimenko (2008). "Geochemical characterization and origin of Southeastern and Eastern European loesses (Serbia, Romania, Ukraine)". In: *Quaternary Science Reviews* 27.9, pp. 1058–1075. DOI: 10.1016/j.quascirev.2008.01.018 (cit. on p. 105).

Bullock, P. and I. S. of Soil Science (1985). *Handbook for Soil Thin Section Description*. Albrighton, UK: Waine Research (cit. on p. 118).

Canti, M. and D. J. Huisman (2015). "Scientific advances in geoarchaeology during the last twenty years". In: *Journal of Archaeological Science* 56, pp. 96–108. DOI: 10.1016/j.jas.2015.02.024 (cit. on p. 118).

Carpentier, F. and B. Vandermeulen (2016). "High-Resolution Photography for Soil Micromorphology Slide Documentation". In: *Geoarchaeology* 31, pp. 603–607. DOI: 10.1002/gea.21563 (cit. on pp. 136, 187).

Cereda, S. and P. Fragnoli (May 2021). "Petrography and Micromorphology Face-to-Face: the Potential of Multivocality in the Study of Earth-Based Archaeological Materials". In: *Interdisciplinaria Archaeologica, Natural Sciences in Archaeology* XII.1, pp. 9–18. DOI: 10.24916/iansa.2021.1.1 (cit. on p. 152).

Chazan, M. (2001). "Bladelet production in the aurignacian of Hayonim cave, Israel". In: *Paleorient* 27.1, pp. 81–88 (cit. on p. 52).

Coeli, L., F. S. d. Oliveira, M. J. Rodet, and R. C. Valadão (2024). "Geomorphology, Geoarchaeology and their multiscalar approaches". In: *Revista Brasileira de Geomorfologia* 25.4. DOI: 10.20502/rbg.v25i4.2573 (cit. on p. 41).

Cohen, H. and J. Laronne (2005). "High rates of sediment transport by flashfloods in the Southern Judean Desert, Israel". In: *Hydrol. Process.* 19.8, pp. 1687–1702 (cit. on p. 55).

Coinman, N. (1993). "WHS 618 - Ain el-buheira: an upper paleolithic site in the wadi Hasa, west-Central Jordan". In: *Paleorient* 19.2, pp. 17–37 (cit. on p. 61).

Coinman, N. (2003). "The upper palaeolithic of Jordan: new data from the wadi al-hasa". In: *More than Meets the Eye. Studies on Upper Palaeolithic Diversity in the Near East*. Ed. by A. Goring-Morris and A. Belfer-Cohen. Oxford, Oakville: Oxbow Books, pp. 151–170 (cit. on p. 61).

Coinman, N. (2005). "Subsistence and technology in the late levantine upper paleolithic". In: *Journal of the Israel Prehistoric Society* 35, pp. 159–177 (cit. on p. 61).

Coinman, N. ((1998). *The Archaeology of the Wadi Hasa, West-Central Jordan: Volume 1: Surveys, Settlement Patterns and Paleoenvironments*. Tempe, USA: University Anthropological Research Papers (cit. on pp. 52, 61).

Congalton, R. G. and K. Green (2019). *Assessing the Accuracy of Remotely Sensed Data – Principles and Practices Third edition*. 3rd. Boca Raton, USA: CRC Press, Taylor & Francis Group. DOI: 10.1201/9780429052729 (cit. on pp. 128, 130).

Congalton, R. and K. Green (2009). *Assessing the Accuracy of Remotely Sensed Data - Principles and Practices*. second. Boca Raton: CRC Press, Taylor & Francis Group (cit. on pp. 60, 198).

Constantin, D., J. Mason, D. Veres, U. Hambach, C. Panaiotu, C. Zeeden, L. Zhou, S. Marković, N. Gerasimenko, A. Avram, et al. (2021). "OSL-dating of the Pleistocene-Holocene climatic transition in loess from China, Europe and North America, and evidence for accretionary pedogenesis". In: *Earth-Science Reviews* 221, p. 103769. DOI: 10.1016/j.earscirev.2021.103769 (cit. on pp. 85, 108).

contributors, G. (2020). *GDAL/OGR Geospatial Data Abstraction Library*. DOI: 10.5281/zenodo.5884351. URL: https://gdal.org (cit. on p. 200).

Cordova, C. E. (2017). "Geoamorphology". In: *Encyclopedia of Geoarchaeology*. Ed. by A. S. Gilbert. Springer Netherlands, pp. 314–323. DOI: 10.1007/978-1-4020-4409-0_10 (cit. on p. 41).

Courty, M. A., P. Goldberg, and R. I. MacPhail (1989). *Soils and Micromorphology in Archaeology*. Cambridge, UK: Cambridge University Press (cit. on p. 118).

Crocetti, L., M. Forkel, M. Fischer, F. Jurečka, A. Grlj, A. Salentinig, M. Trnka, M. Anderson, W.-T. Ng, Ž. Kokalj, et al. (2020). "Earth

Observation for agricultural drought monitoring in the Pannonian Basin (southeastern Europe): current state and future directions". In: *Regional Environmental Change* 20, pp. 1–17. DOI: 10.1007/s10113-020-01710-w (cit. on pp. 38, 86).

Crouvi, O., R. Amit, M. Ben Israel, and Y. Enzel (2017). "Loess in the Negev desert: sources, loessial soils, palaeosols, and palaeoclimatic implications". In: *Quaternary of the Levant*. Ed. by Y. Enzel and O. Bar-Yosef. Cambridge University Press, pp. 471–482 (cit. on p. 56).

Crouvi, O., R. Amit, Y. Enzel, N. Porat, and A. Sandler (2008). "Sand dunes as a major proximal dust source for late Pleistocene loess in the Negev Desert, Israel". In: *Quat. Res.* 70.2, pp. 275–282 (cit. on p. 56).

Cullers, R. L. (2000). "The geochemistry of shales, siltstones and sandstones of Pennsylvanian–Permian age, Colorado, USA: implications for provenance and metamorphic studies". In: *Lithos* 51.3, pp. 181–203. DOI: 10.1016/S0024-4937(99)00063-8 (cit. on p. 222).

Dan, Y., Z. Raz, D. Yaalon, and Koyumdijisky (1975). *Soil Map of Israel*. Ministry of Agriculture, Agricultural Research Organisation & Soil Conservation and Drainage Department (cit. on pp. 55, 56).

Davidzon, A. and A. Goring-Morris (2003). "Sealed in stone: the upper palaeolithic early ahmarian knapping method in the light of refitting studies at nahal Nizzana XIII, western Negev, Israel". In: *Journal of the Israel Prehistoric Society* 33, pp. 75–205 (cit. on p. 51).

Davies, S. J., H. F. Lamb, and R. Sj (2015). "Micro-xrf core scanning in palaeolimnology: recent developments". In: *Micro-XRF Studies of Sediment Cores*, pp. 189–226. DOI: 10.1007/978-94-017-9849-5_7 (cit. on pp. 89, 222).

Demidenko, Y. and T. Hauck (2017). "Yabrud II rock-shelter archaeological sequence (Syria) and possible Proto-Aurignacian origin in the Levant". In: *Vocation pr´ehistoire. Hommage a Jean-Marie Le Tensorer*. Ed. by D. Wojtczak. Vol. 148. Liège: ERAUL, pp. 87–98 (cit. on p. 52).

Diez-Martín, F. (2010). "Evaluating the effect of plowing on the archaeological record: the early middle palaeolithic in the river Duero basin plateaus (north-central Spain)". In: *Quat. Int.* 214.1–2, pp. 30–43 (cit. on p. 50).

DigitalGlobe (2021). *WorldView-3 satellite mission 2014 - ongoing, Scene: 21MAR25093915*. Version 28.4. European Space Imaging (ESA)GmbH/Space Imaging Middle East and DigitalGlobe, Inc. URL: https://dg-cms-uploads-production.s3.amazonaws.com/uploads/document/file/95/DG2017_WorldView-3_DS.pdf (visited on 04/29/2019) (cit. on pp. 13, 15, 17, 39, 88, 92, 104, 154, 220).

Dilts, T. (2015). *Topography Tools for ArcGIS 10.3 and earlier*. http://www.arcgis.com/home/item.html?id=arcgis-topography-tools (cit. on p. 199).

Dischamps, E., F. Bachellerie, M. Baillet, and L. Sitzia (2019). "The use of spatial taphonomy for interpreting Pleistocene palimpsests: an interdisciplinary approach to the chatelperronian and carnivore occupations at cassenade (dordogne, France)". In: *PaleoAnthropology*, pp. 362–388 (cit. on p. 50).

Dóka, K. (1997). *A Körös és Berettyó vízrendszer szabályozása a 18-19. században*. Vol. 7. Közlemények Békés megye és környéke történetéből. Gyula, Hungary: Erdmann (cit. on pp. 38, 86).

Domínguez-Solera, S. (2010). "An experiment on the vertical migration of archaeological materials in clay deposits". In: *Journal of Taphonomy* 8.1, pp. 69–74 (cit. on p. 50).

Douka, K., C. Bergman, R. Hedges, F. Wesselingh, and T. Higham (2013). "Chronology of Ksar Akil (Lebanon) and implications for the colonization of Europe by anatomically modern humans". In: *PloS One* 8.9, e72931 (cit. on p. 51).

Drees, L. R. and M. D. Ransom (1994). "Light Microscopic Techniques". In: *Quantitative Methods in Soil Mineralogy*. Ed. by J. E. A. Chair and J. W. Stucki. John Wiley & Sons, Ltd, pp. 137–176. DOI: 10.2136/1994.quantitativemethods.c5 (cit. on pp. 118, 126, 138).

Duffy, P. R., G. M. Parditka, J. I. Giblin, and L. Paja (2019). "The problem with tells: lessons learned from absolute dating of Bronze Age mortuary ceramics in Hungary". In: *Antiquity* 93.367, pp. 63–79. DOI: 10.15184/aqy.2018.179 (cit. on pp. 84, 153).

Durcan, J. A., G. E. King, and G. A. Duller (2015). "DRAC: Dose Rate and Age Calculator for trapped charge dating". In: *Quaternary Geochronology* 28, pp. 54–61. DOI: 10.1016/j.quageo.2015.03.012 (cit. on pp. 90, 223).

Erel, Y., S. Goldstein, A. Torfstein, D. Palchan, M. Israel, and M. Stein (2017). "Isotopic tracers of dust and loess in the levant". In: *Quaternary of the Levant*. Ed. by Y. Enzel and O. Bar-Yosef. Cambridge University Press, pp. 483–492 (cit. on p. 55).

Eren, M., A. Boehm, B. Morgan, R. Anderson, and B. Andrews (2011). "Flaked stone taphonomy: a controlled experimental study on the effects of sediment consolidation on flake edge morphology". In: *Journal of Taphonomy* 9.3, pp. 201–217 (cit. on p. 50).

ESRI (2019). *World Shaded Relief, ID: 9c5370d0b54f4de1b48a3792d7377ff2*. URL: https://services.arcgisonline.com/ArcGIS/rest/services/World_Shaded_Relief/MapServer (visited on 10/03/2021) (cit. on pp. 12, 87).

Faegri, K. I. and J. Iversen (1989). *J. 1989. Text book of pollenan alysis*. John Wiley and Son, Chichester, NewYork, Brisbane, Toronto, Singpore (cit. on p. 90).

FAO & IIASA (2023). *Harmonized World Soil Database Version 2.0*. Tech. rep. Rome (Italy) and Laxenburg (Austria): FAO & IIASA. DOI: 10.4060/cc3823en. (Visited on 06/01/2024) (cit. on p. 108).

Feurdean, A., A. Perşoiu, I. Tanţău, T. Stevens, E. Magyari, B. Onac, S. Marković, M. Andrič, S. Connor, S. Fărcaş, et al. (2014). "Climate variability and associated vegetation response throughout Central and Eastern Europe (CEE) between 60 and 8 ka". In: *Quaternary Science Reviews* 106. Dating, Synthesis, and Interpretation of Palaeoclimatic Records and Model-data Integration: Advances of the INTIMATE project(INTegration of Ice core, Marine and TErrestrial records, COST Action ES0907), pp. 206–224. DOI: 10.1016/j.quascirev.2014.06.003 (cit. on p. 107).

Feurdean, A., C. Parr, I. Tanţău, S. Fărcaş, E. Marinova, and I. Perşoiu (Feb. 20, 2013). "Biodiversity variability across elevations in the Carpathians: Parallel change with landscape openness and land use". In: *The Holocene* 23.6, pp. 869–881. DOI: 10.1177/0959683612474482 (cit. on p. 107).

Fischl, K., T. Kienlin, B. Tugya, and T. Múzeum (2015). "BRONZE AGE SETTLEMENT RESEARCH IN NORTH-EASTERN HUNGARY - BRONZKORI TELEPÜLÉSKUTATÁSOK ÉSZAKKELET MAGYARORSZÁGON". In: *Archeometriai Mühely* XII./2<0, pp. 117–135 (cit. on p. 153).

Fischl, K. P., T. Pusztai, M. Buzás, A. K. Röpke, E. Drunagel, J. Anvari, L. Gucsi, Á. Balázs, and T. L. Kienlin (2025). "Reconstructing two buildings and architectural decorations on the Bronze Age Tell of Borsodivánka-Nagyhalom (Northeastern Hungary)". In: *Acta Archaeologica Academiae Scientiarum Hungaricae* 76.1, pp. 55–81. DOI: 10.1556/072.2025.00030 (cit. on p. 176).

Fitchett, J. M., S. W. Grab, M. K. Bamford, and A. W. Mackay (2016). "Multi-disciplinary review of late Quaternary palaeoclimates and environments for Lesotho". In: *South African Journal of Science* 112, p. 9. DOI: 10.17159/sajs.2016/20160045 (cit. on p. 33).

FitzPatrick, E. A. (2012). *Micromorphology of Soils*. 2nd. London: Springer Science & Business Media (cit. on p. 118).

Flude, S., M. Haschke, and M. Storey (2017). "Application of benchtop micro-XRF to geological materials". In: *Mineralogical Magazine* 81.4, pp. 923–948. DOI: 10.1180/minmag.2016.080.150 (cit. on pp. 172, 178, 188).

Folk, R. L. and W. C. Ward (1957). "Brazos River bar [Texas]; a study in the significance of grain size parameters". In: *Journal of sedimentary research* 27.1, pp. 3–26 (cit. on pp. 89, 221).

Frahm, E. and T. Hauck (2017). "Origin of an obsidian scraper at yabroud rockshelter II (Syria): implications for near eastern social networks in the early upper palaeolithic". In: *J. Archaeol. Sci.: Report* 13, pp. 415–427 (cit. on p. 52).

French, J. (2015). "The demography of the Upper Palaeolithic hunter–gatherers of Southwestern France: a multi-proxy approach using archaeological data". In: *J. Anthropol. Archaeol.* 39, pp. 193–209 (cit. on p. 50).

Friesem, D., J. Wattez, and M. Onfray (Aug. 2017). "Earth Construction Materials". In: *Archaeological soil and sediment micromorphology*. Ed.

by S. G. Nicosia C. Hoboken: Wiley, pp. 99–110. DOI: 10.1002/9781118941065.ch10 (cit. on pp. 152, 173).

Frumkin, A., B. Langford, and R. Porat (2017). "The Judean desert - the major hyogene cave region of the southern levant". In: *Hypogene Karst Regions and Caves of the World*. Ed. by A. Klimchouk, A. Palmer, J. de Waele, A. S. Auler, and P. Audra. Cham: Springer International Publishing, pp. 463–477 (cit. on pp. 11, 53–55).

Gábris, G. and A. Nádor (2007). "Long-term fluvial archives in Hungary: response of the Danube and Tisza rivers to tectonic movements and climatic changes during the Quaternary: a review and new synthesis". In: *Quaternary Science Reviews* 26.22. Global correlation of Late Cenozoic fluvial deposits: IGCP Project No. 449, pp. 2758–2782. DOI: 10.1016/j.quascirev.2007.06.030 (cit. on pp. 84–86, 102, 103, 105, 109, 112).

García-Suárez, A. (2024). "From settled villages to mega-sites:a micromorphological approach towardsunderstanding the origins of urbanism in Anatolia". In: *Urban Geoarchaeology*. Ed. by Q. BORDERIE and F. SALOMON. Paris, France: CNRS Éditions. Chap. Urban Geoarchaeology (cit. on p. 152).

Garfunkel, Z. (1981). "Internal structure of the Dead Sea leaky transform (rift) in relation to plate kinematics". In: *Tectonophysics* 80.1–4, pp. 81–108 (cit. on p. 53).

Garrod, D. (1937). *The Stone Age of Mount Carmel: Report of the Joint Expedition of the British School of Archaeology in Jerusalem and the American School of Prehistoric Research, 1929-1934*. 1 online resource (2 volumes). New York: AMS Press (cit. on p. 52).

Gavan, A., L. Marian, T. Kienlin, and L. Marian (2024). "Preliminary report on the 2022 and 2023 excavation seasons at Toboliu". In: *CRISIA* LIV, pp. 51–67 (cit. on p. 40).

Găvan, A. and T. Kienlin (2021). "Introduction: Bronze Age Settlements in North-Western Romania". In: ed. by T. L. K. Găvan. Vol. 364. Bonn: Habelt, pp. 9–20 (cit. on p. 153).

Găvan, A., T. Kienlin, A. Röpke, N. Nolde, T. Zerl, M. Zickel, M. Lie, G. Fazecaș, and F. Gogâltan (2021). "Living together or apart? Unravelling the development, internal organization and social structure of a complex Bronze Age tell settlement at Toboliu, western Romania". In: *Crisia* 51, pp. 59–76 (cit. on p. 84).

Găvan, A., M.-A. Lie, N. Nolde, T. Zerl, A. Röpke, M. Zickel, T. Kienlin, and G. Fazecaș (2022). "Preliminary Report On The 2021 Excavation Season At Toboliu". In: *Crisia* LII, pp. 65–84. URL: https://crisia.mtariicrisurilor.ro/wp-content/uploads/2023/02/Alexandra-Gavan-2022.pdf (cit. on pp. 84, 86, 112).

GDAL & OGR contributors (2022). *GDAL & OGR Geospatial Data Abstraction software Library*. release 3, last access: 18 January 2024. URL: https://gdal.org/ (cit. on pp. 126, 231).

Gerlach, R. (2001). "Keinsfalls Ausnahmen: materialentnahmegruben als Befundzerstorer:¨ außmaß im Rheinland und Erkennbarkeit". In: *Archaologische Informationen* 24.1, pp. 29–38 (cit. on p. 51).

Gerlach, R. (2003). "Geoarchaologie - ein arc¨ haologisches Desiderat oder "There could be¨ no real archaeology without Geology". In: *Archaologische Informationen* 26.1, pp. 9–15 (cit. on p. 51).

Gerlach, R. and E. Eckmeier (2012). "Prehistoric land use and its impact on soil formation since early neolithic. Examples from the lower rhine area". In: *Landscape Archaeology. Proceedings of the International Conference Held in Berlin, 6th-8th June 2012*. Ed. by W. Bebermeier, R. Hebenstreit, E. Kaiser, and J. Krause. eTopoi - Journal for Ancient Studies, Special, pp. 11–16 (cit. on p. 51).

Gerlach, R., H. Baumewerd-Schmidt, K. van den Borg, E. Eckmeier, and M. W. I. Schmidt (2006). "Prehistoric alteration of soil in the Lower Rhine Basin, Northwest Germany—archaeological, 14C and geochemical evidence". In: *Geoderma* 136, pp. 38–50. DOI: 10.1016/j.geoderma.2006.01.011 (cit. on pp. 85, 110).

Ghiasi-Freez, J., I. Soleimanpour, A. Kadkhodaie-Ilkhchi, M. Ziaii, M. Sedighi, and A. Hatampour (2012). "Semi-automated porosity identification from thin section images using image analysis and intelligent discriminant classifiers". In: *Computers and Geosciences* 45, pp. 36–45. DOI: 10.1016/j.cageo.2012.03.006 (cit. on pp. 119, 139).

Ghilardi, M. (2021). "Geoarchaeology: Where Geosciences Meet the Humanities to Reconstruct Past Human–Environment Interactions. An Application to the Coastal Areas of the Largest Mediterranean Islands". In: *Applied Sciences* 11.10, p. 4480. DOI: 10.3390/app11104480 (cit. on p. 34).

Gilead, I. (1981). "The Upper Palaeolithic in Sinai and the Negev: Sites in Gebel Maghara Kadesh Barnea and Nahal Zin". PhD thesis. Hebrew University of Jerusalem, p. 431 (cit. on pp. 51, 60, 62).

Gilead, I. (1991). "The upper paleolithic period in the levant". In: *J. World PreHistory* 5.2, pp. 105–154 (cit. on p. 52).

Gilead, I. (1993). "Upper palaeolithic sites in the ramat matred area". In: *Palest. Explor. Q.* 1.125, pp. 19–42 (cit. on pp. 52, 60).

Gladfelter, B. G. (1977). "Geoarchaeology: The Geomorphologist and Archaeology". In: *American Antiquity* 42.4, pp. 519–538. DOI: 10.2307/278926 (cit. on pp. 34, 41).

Glatz, C. and J. Casana (2016). "Of highland-lowland borderlands: Local societies and foreign power in the Zagros-Mesopotamian interface". In: *Journal of Anthropological Archaeology* 44, pp. 127–147. DOI: 10.1016/j.jaa.2016.09.001 (cit. on p. 84).

Goder-Goldberger, M., R. Lavi, L. Kolska Horwitz, D. Bar-Yosef Mayer, and L. Edeltin (2019). "The besor basin prehistoric survey: initial results". In: *Journal of the Israel Prehistoric Society* 49, pp. 63–79 (cit. on pp. 62, 77).

Gogâltan, F. (Feb. 2018). "THE BRONZE AGE MULTILAYERED SETTLEMENTS IN THE CARPATHIAN BASIN (CCA. 2500-1600/1500 BC). AN OLD CATALOGUE AND SOME CHRONOLOGICAL PROBLEMS." In: *JOURNAL OF ANCIENT HISTORY AND ARCHAEOLOGY* 4.4. DOI: 10.14795/j.v4i4.284 (cit. on pp. 40, 153).

Gogâltan, F., A. Găvan, M. Lie, G. Fazecaș, C. Cordoș, and T. Kienlin (Nov. 2020). "Exploring the Bronze Age Tells and Tell-like Settlements from the Eastern Carpathian Basin. Results of a Research Project". In: *Current Approaches to Tells in the Prehistoric Old World*. Ed. by A. B.-G.
bibinitperiod T. L. KIENLIN. Oxbow Books, pp. 73–96. DOI: 10.2307/j.ctv13pk5j9.8 (cit. on p. 153).

Goldberg, P. and B. Brimer (1983). "Late Pleistocene geomorphic surfaces and environmental history of Avdat/Havarim area, Nahal Zin". In: *Prehistory and Paleoenvironments in the Central Negev, Israel. Volume III the Avdat/Aqev Area, Part 3*. Ed. by A. Marks. Dallas: Southern Methodist University Press, pp. 1–14 (cit. on pp. 74, 184).

Goldberg, P. and R. Macphail (2006). *Practical and Theoretical Geoarchaeology*. Malden, Mass.: Blackwell, p. 454 (cit. on pp. 42, 50, 74).

Goldberg, P. (Mar. 1979). "Geology of Late Bronze Age Mudbrick from Tel Lachish". In: *Tel Aviv* 6.1-2, pp. 60–67. DOI: 10.1179/033443579788497478 (cit. on p. 173).

Goring-Morris, A. (1980a). "Late Quaternary Sites in Wadi Fazael, Lower Jordan Valley". MA thesis. Hebrew University of Jerusalem, p. 143 (cit. on p. 60).

Goring-Morris, A. (1980b). "Upper Palaeolithic sites from Wadi Fazael, Lower Jordan Valley". In: *Paleorient* 6, pp. 173–191 (cit. on pp. 52, 60).

Goring-Morris, A. (1987). *At the Edge: Terminal Pleistocene Hunter-Gatherers in the Negev and Sinai*. BAR International Series 361. Oxford: B.A.R, p. 509 (cit. on pp. 50, 52, 60).

Goring-Morris, A. and A. Belfer-Cohen (2003). *More than Meets the Eye: Studies on Upper Palaeolithic Diversity in the Near East*. Oxford, Oakville: Oxbow Books (cit. on p. 52).

Goring-Morris, A. and A. Davidzon (2006). "Straight to the point: upper paleolithic Ahmarian lithic technology in the Levant". In: *Anthropologie* XLIV.1, pp. 93–111 (cit. on p. 51).

Goring-Morris, N. (2017). "Loess, dunes, and human activities". In: *Quaternary of the Levant*. Ed. by Y. Enzel and O. Bar-Yosef. Cambridge University Press, pp. 493–504 (cit. on pp. 55, 56).

Goring-Morris, N. and A. Belfer-Cohen (2018). "The Ahmarian in the context of the earlier Upper Palaeolithic in the Near East". In: *The Middle and Upper Paleolithic Archeology of the Levant and beyond*. Ed. by Y. Nishiaki and T. Akazawa. Springer Singapore, pp. 87–104 (cit. on p. 51).

GRASS Development Team (2020). *Geographic Resources Analysis Support System (GRASS GIS) Software, Version 7.8.2*. Open Source Geospatial Foundation. USA. DOI: 10.5281/zenodo.5176030. URL: https://grass.osgeo.org (cit. on p. 200).

Greenbaum, N. and E. Zilberman (2017). "Palaeogeography and palaeohydrology of fluvial systems in the Levant, southeastern Mediterranean". In: *Quaternary of the Levant*. Ed. by Y. Enzel and O. Bar-Yosef. Cambridge University Press, pp. 401–416 (cit. on pp. 56, 75).

Gretener, B. and L. Strömquist (1987). "Overbank Sedimentation Rates of Fine Grained Sediments. A Study of the Recent Deposition in the Lower River Fyrisån". In: *Geografiska Annaler: Series A, Physical Geography* 69.1, pp. 139–146. DOI: 10.1080/04353676.1987.11880202 (cit. on p. 102).

Grimm, E. C. (2020). *TILIA, version 3.0.1.* Springfield Illinois (cit. on p. 90).

Grisel, O., A. Mueller, L. A. Gramfort, G. Louppe, P. Prettenhofer, M. Blondel, V. Niculae, J. Nothman, A. Joly, T. J. Fan, et al. (2021). *scikit-learn/scikit-learn: scikit-learn 1.0.1, version 1.0.0*. DOI: 10.5281/zenodo.5596244 (cit. on p. 142).

Guérin, G., N. Mercier, R. Nathan, G. Adamiec, and Y. Lefrais (2012). "On the use of the infinite matrix assumption and associated concepts: A critical review". In: *Radiation Measurements* 47.9. Proceedings of the 13th International Conference on Luminescence and Electron Spin Resonance Dating, 10–14 July, 2011, Toruń, Poland, pp. 778–785. DOI: 10.1016/j.radmeas.2012.04.004 (cit. on p. 90).

Gumnior, M. and A. Stobbe (2021). "First palynological results from lowland sites in the Romanian Banat and their implications for settlement and land use dynamics in the southeastern Carpathian Basin". In: *Quaternary International* 583, pp. 48–61 (cit. on p. 107).

Haaland, M. M., M. Czechowski, F. Carpentier, M. Lejay, and B. Vandermeulen (2018). "Documenting archaeological thin sections in high-resolution: A comparison of methods and discussion of applications". In: *Geoarchaeology* 34, pp. 100–114. DOI: 10.1002/gea.21706 (cit. on pp. 119, 123, 137).

Hammer, Ø., D. A. T. Harper, and P. D. Ryan (2001). "PAST: Paleontological statistics software package for education and data analysis". In: *Palaeontologia Electronica* 4.1, p. 9. URL: http://palaeo-electronica.org/2001_1/past/issue1_01.htm (cit. on p. 66).

Harel, M., R. Amit, N. Porat, and Y. Enzel (2017). "Evolution of the southeastern Mediterranean coastal plain". In: *Quaternary of the Levant*. Ed. by Y. Enzel and O. Bar-Yosef. Cambridge University Press, pp. 433–446 (cit. on p. 56).

Harrison, J. B. J. and A. Yair (1998). "Late Pleistocene aeolian and fluvial interactions in the development of the Nizzana dune field,

Negev Desert, Israel". In: *Sedimentology* 45.3, pp. 507–518. DOI: 10.1046/j.1365-3091.1998.00151.x (cit. on p. 102).

Hartmann, K., A. Boden, and B. Hannover, eds. (July 2024). *Bodenkundliche Kartieranleitung KA6 in 2 Bänden*. Stuttgart, Germany: Schweizerbart Science Publishers. URL: http://www.schweizerbart.de//publications/detail/isbn/9783510968695/Bodenkundliche%5C_Kartieranleitung%5C_KA6%5C_in%5C_2 (cit. on pp. 14, 89, 96).

Hayes, A., E. Rohling, S. d. Rijk, D. Kroon, and W. Zachariasse (1999). "Mediterranean planktonic foraminiferal faunas during the last glacial cycle". In: *Marine Geology* 153.1–4, pp. 239–252 (cit. on pp. 76, 184).

Hegi, G. (1987). *Illustrierte Flora von Mitteleuropa. Spermatophyta, Band VI, Angiospermae, Dicotyledones 4. Compositae II: Matricaria-Hieracium*. Berlin, Hamburg: Paul Parey, 903 pp (cit. on p. 107).

Hemmerich, W. A. (2018). *StatistikGuru. Normalverteilung online prüfen*. URL: https://statistikguru.de/rechner/normalverteilung-rechner.html (visited on 11/03/2020) (cit. on p. 66).

Henry, D., ed. (1995). *Prehistoric Cultural Ecology and Evolution: Insights from Southern Jordan*. Interdisciplinary Contributions to Archeology. New York, London: Plenum Press, p. 494 (cit. on pp. 52, 60, 73).

Hershkovitz, I. and B. Arensburg (2017). "Human fossils from the upper palaeolithic through the early Holocene". In: *Quaternary of the Levant*. Ed. by Y. Enzel and O. Bar-Yosef. Cambridge University Press, pp. 611–620 (cit. on p. 52).

Higham, T., T. Compton, C. Stringer, R. Jacobi, B. Shapiro, E. Trinkaus, B. Chandler, F. Groning, C. Collins, S. Hillson, et al. (2011). "The earliest evidence for anatomically modern humans in northwestern Europe". In: *Nature* 479.7374, p. 521 (cit. on p. 52).

Hill, C. L. (2017). "Geoarchaeology, History". In: *Encyclopedia of Geoarchaeology*. Ed. by A. S. Gilbert. Springer Netherlands, pp. 292–303. DOI: 10.1007/978-1-4020-4409-0_10 (cit. on p. 33).

Holcomb, J., C. Runnels, and K. Wegmann (2020). "Deposit-centered archaeological survey and the search for the Aegean Palaeolithic: a geoarchaeological perspective". In: *Quaternary International* 550, pp. 169–183 (cit. on p. 50).

Holliday, V. T. and W. G. Gartner (2007). "Methods of soil P analysis in archaeology". In: *Journal of Archaeological Science* 34.2, pp. 301–333. DOI: 10.1016/j.jas.2006.05.004 (cit. on p. 110).

Holting, B. and W. Coldewey (2009). *Hydrogeologie: Einführung in die allgemeine und angewandte Hydrogeologie*. 7. neu bearb. und erw. Aufl. Heidelberg: Spektrum Akad. Verl., p. 383 (cit. on pp. 75, 184).

Hošek, J., L. Lisá, U. Hambach, L. Petr, L. Vejrostová, A. Bajer, T. Matys Grygar, P. Moska, Z. Gottvald, and M. Horsák (2017). "Middle Pleniglacial pedogenesis on the northwestern edge of the Carpathian basin: A multidisciplinary investigation of the Bíňa pedo-sedimentary section, SW Slovakia". In: *Palaeogeography, Palaeoclimatology, Palaeoe-*

cology 487, pp. 321–339. DOI: 10.1016/j.palaeo.2017.09.017 (cit. on p. 109).

Hussain, S. (2015). "Betwixt seriality and sortiment: rethinking early Ahmarian blade technology in Al-Ansab 1". In: *Pleistocene Archaeology of the Petra Area in Jordan*. Ed. by D. Schyle and J. Richter. Rahden/Westfalen: Marie Leidorf GmbH, pp. 131–147 (cit. on p. 51).

International Committee for Phytolith Taxonomy (ICPT) (Sept. 2019). "International Code for Phytolith Nomenclature (ICPN) 2.0". In: *Annals of Botany* 124.2, pp. 189–199. DOI: 10.1093/aob/mcz064 (cit. on pp. 156, 176).

IUSS (WRB) WG (2015). *World Reference Base for Soil Resources 2014, International soil classification system for naming soils and creating legends for soil maps, update 2015*. Vol. 106. Rome, Italy: FAO. URL: http://www.fao.org/3/a-i3794en.pdf (cit. on pp. 14, 86, 89, 96, 107, 219).

IUSS (WRB) WG (2022). *World Reference Base for Soil Resources: International soil classification system for naming soils and creating legends for soil maps*. 4th ed. Vienna, Austria: International Union of Soil Sciences (IUSS). URL: https://www.isric.org/sites/default/files/WRB_fourth_edition_2022-12-18.pdf (cit. on pp. 38, 89, 107, 112, 121).

Jacomet, S. and A. Kreuz (1999). *Archäobotanik. Aufgaben, Methoden und Ergebnisse vegetations und agrargeschichtlicher Forschung*. Stuttgart, Germany: Ulmer (cit. on pp. 174, 176).

Jary, Z., M. Krawczyk, P. Moska, N. Piotrowska, G. Poręba, J. Raczyk, J. Skurzyński, M. Łopuch, and L. Zöller (2023). "Chronostratigraphy of the Periglacial Loess-Paleosol Sequence in Zaprężyn, SW Poland". In: *Geochronometria* 50.1, pp. 144–156 (cit. on p. 105).

Jenness, J. (2006a). *Topographic Position Index (TPI) v. 1.3a: Documentation paper*. http://www.jennessent.com/downloads/TPI_Documentation_online.pdf. Accessed 19 November 2016 (cit. on p. 199).

Jenness, J. (2006b). *Topographic Position Index (tpi_jen.avx) extension for ArcView 3.x* (cit. on p. 199).

Jiménez-Sanchez, M., I. González-Alvarez, O. Requejo-Pagés, and M. Domínguez-Cuesta (2011). "Enhancing rescue-archaeology using geomorphological approaches: archaeological sites in Paredes (Asturias, NW Spain)". In: *Geomorphology* 132.3–4, pp. 99–110 (cit. on p. 50).

Jurgiel, B. (2020). *Point sampling tool for QGIS*. Open Source Geospatial Foundation. URL: http://github.com/borysiasty/pointsamplingtool (visited on 09/01/2020) (cit. on p. 200).

Kadowaki, S., T. Omori, and Y. Nishiaki (2015). "Variability in Early Ahmarian lithic technology and its implications for the model of a Levantine origin of the Protoaurignacian". In: *Journal of Human Evolution* 82, pp. 67–87 (cit. on p. 52).

Karasiak, N. (2016). *Dzetsaka Qgis Classification plugin, version 3.7*. DOI: 10.5281/zenodo.2552284 (cit. on pp. 125, 126, 128, 231).

Karasiak, N. (2019). *lennepkade/dzetsaka: Fix bug in processing provider with vector files (Dzetsaka QGIS classification plugin), version 3.5.1*. DOI: 10.5281/zenodo.3463523 (cit. on p. 142).

Karkanas, P. (2007). "Identification of lime plaster in prehistory using petrographic methods: A review and reconsideration of the data on the basis of experimental and case studies". In: *Geoarchaeology* 22.7, pp. 775–796. DOI: https://doi.org/10.1002/gea.20186 (cit. on p. 176).

Karkanas, P. and N. Efstratiou (2009). "Floor sequences in Neolithic Makri, Greece: micromorphology reveals cycles of renovation". In: *Antiquity* 83.322, pp. 955–967. DOI: 10.1017/S0003598X00099270 (cit. on pp. 152, 176, 177).

Kars, R., F. Busschers, and J. Wallinga (2012). "Validating post IR-IRSL dating on K-feldspars through comparison with quartz OSL ages". In: *Quaternary Geochronology* 12, pp. 74–86. DOI: 10.1016/j.quageo.2012.05.001 (cit. on pp. 24, 90, 224).

Kehl, M., K. Seeger, S. Pötter, P. Schulte, N. Klasen, M. Zickel, A. Pastoors, and E. Claßen (2024). "Loess formation and chronology at the Palaeolithic key site Rheindahlen, Lower Rhine Embayment, Germany". In: *E&G Quaternary Science Journal* 73, pp. 41–67. DOI: 10.5194/egqsj-73-41-2024 (cit. on pp. 37, 43, 121, 122, 130, 132, 138, 139, 187).

Kempf, M. (2021). "Take a seed! Revealing Neolithic landscape and agricultural development in the Carpathian Basin through multivariate statistics and environmental modelling". In: *PLOS ONE* 16.10. DOI: 10.1371/journal.pone.0258206 (cit. on p. 108).

Kienlin, T. (Dec. 2020). "Bronze Age Tell Communities in Context: An Exploration into Culture, Society, and the Study of European Prehistory. Part 2". In: *Space, and Materiality. Archaeopress* 2. DOI: 10.2307/jj.15135935 (cit. on p. 153).

Kienlin, T. (2021). "Diversity rather than Uniformity: Bronze Age Tell Settlement in North-Western Romania". In: *Bronze Age Tell Settlements in North-Western Romania. Current Approaches and Recent Investigations*. Ed. by T. L. K. A. Găvan. Vol. Part II: Catalogue of Sites Covered by Magnetometry in Bihor and Satu Mare Counties. 364. Bonn: Universitätsforschungen zur prähistorischen Archäologie, pp. 79–216 (cit. on pp. 13, 17, 87, 92, 154, 220).

Kiss, A. (2019). "An Environmental Background: Floods, Modern Hydrology and Medieval Environment". In: *Floods and Long-Term Water-Level Changes in Medieval Hungary*. Cham: Springer International Publishing, pp. 51–137. DOI: 10.1007/978-3-319-38864-9_2 (cit. on pp. 84, 91, 112).

Kiss, T., P. Hernesz, B. Sümeghy, K. Györgyövics, and G. Sipos (2015). "The evolution of the Great Hungarian Plain fluvial system – Fluvial

processes in a subsiding area from the beginning of the Weichselian". In: *Quaternary International* 388, pp. 142–155. DOI: 10.1016/j.quaint.2014.05.050 (cit. on pp. 84, 102, 103, 105, 185).

Klinger, Y., J. Avouac, D. Bourles, and N. Tisnerat (2003). "Alluvial deposition and lake-level fluctuations forced by Late Quaternary climate change: the Dead Sea case example". In: *Sedimentary Geology* 162.1–2, pp. 119–139 (cit. on p. 53).

Kluiving, S., A. Verbers, and W. Thijs (2010). "Lithological analysis of 45 presumed pingo remnants in the northervlietn Netherlands (Friesland): substrate control and fill sequences". In: *Netherlands Journal of Geosciences - Geologie en Mijnbouw* 89.1, pp. 61–75. DOI: 10.1017/S0016774600000822 (cit. on pp. 109, 110, 185, 186).

Kokaly, R. F., R. N. Clark, G. A. Swayze, K. E. Livo, T. M. Hoefen, N. C. Pearson, R. A. Wise, W. Benzel, H. A. Lowers, R. L. Driscoll, et al. (2017). "USGS Spectral Library Version 7". In: *Data series 1035*. DOI: 10.3133/ds1035 (cit. on p. 136).

Kołodyńska-Gawrysiak, R. and J. Poesen (2017). "Closed depressions in the European loess belt – Natural or anthropogenic origin?" In: *Geomorphology* 288, pp. 111–128. DOI: 10.1016/j.geomorph.2017.02.004 (cit. on pp. 85, 110).

Kondo, Y., T. Omori, and P. Verhagen (2012). *Developing Predictive Models for Palaeoanthropological Research: a Preliminary Discussion*. Tech. rep. Tokyo: Tokyo Institute of Technology, Department of Computer Science, p. 11 (cit. on pp. 72, 184).

Konert, M. and J. Vandenberghe (1997). "Comparison of laser grain size analysis with pipette and sieve analysis: a solution for the underestimation of the clay fraction". In: *Sedimentology* 44.3, pp. 523–535. DOI: 10.1046/j.1365-3091.1997.d01-38.x (cit. on p. 89).

Kottek, M., J. Grieser, C. Beck, B. Rudolf, and F. Rubel (July 2006). "World Map of the Köppen?Geiger climate classification updated". In: *Meteorologische Zeitschrift* 15.3, pp. 259–263. DOI: 10.1127/0941?2948/2006/0130 (cit. on pp. 38, 86).

Kovács, G., A. Röpke, J. Anvari, K. P. Fischl, T. L. Kienlin, G. Kulcsár, M. Vicze, and Á. Pető (Aug. 2024). "Construction materials and building techniques – Comparing anthropogenic sediments of three Middle Bronze Age sites from Hungary". In: *Archaeological and Anthropological Sciences* 16.9. DOI: 10.1007/s12520-024-02027-z (cit. on pp. 152, 173, 175, 177).

Kretschmer, I. (2014). "Demographische Untersuchungen zu Bevölkerungsdichten, Mobilität und Landnutzungsmustern im späten Jungpaläolithikum". PhD thesis. A CRC 806 monograph Band 6 (cit. on pp. 42, 50).

Kreutzer, S., C. Schmidt, R. DeWitt, and M. Fuchs (2014). "The a-value of polymineral fine grain samples measured with the post-IR IRSL protocol". In: *Radiation Measurements* 69, pp. 18–29. DOI: 10.1016/j.radmeas.2014.04.027 (cit. on p. 90).

Kuhn, S. (2004). "Upper Paleolithic raw material economies at Üçagızlı cave, Turkey". In: *Journal of Anthropological Archaeology* 23.4, pp. 431–448 (cit. on pp. 51, 52, 60).

Kuhn, S., M. Stiner, E. Güleç, I. Ozer, H. Yilmaz, I. Baykara, A. Açikkol, P. Goldberg, K. Molina, E. Unay, et al. (2009). "The early upper paleolithic occupations at Uçagızlı cave (Hatay, Turkey)". In: *Journal of Human Evolution* 56.2, pp. 87–113 (cit. on p. 51).

Lászlóffy, W., I. Weiss, and B. Vályi (1938). *Magyarország vízborította és árvízjárta területei az ármentesítő és lecsapoló munkálatok megkezdése előtt (Waterlogged and inundation areas of Hungary before the systematic water regulation works), M=1:600 000*. Ed. by M. K. F. M. V. Intézet. URL: https://maps.hungaricana.hu/hu/HTITerkeptar/2206/ (cit. on pp. 13, 15, 38, 87, 91, 92, 103, 104, 112, 114).

Lehmkuhl, F., J. J. Nett, S. Pötter, P. Schulte, T. Sprafke, Z. Jary, P. Antoine, L. Wacha, D. Wolf, A. Zerboni, et al. (2020). *Geodata of continuous and discontinuous permafrost during the last glacial maximum in Europe*. DOI: 10.5880/SFB806.61 (cit. on p. 185).

Lehmkuhl, F., J. J. Nett, S. Pötter, P. Schulte, T. Sprafke, Z. Jary, P. Antoine, L. Wacha, D. Wolf, A. Zerboni, et al. (2021). "Loess landscapes of Europe – Mapping, geomorphology, and zonal differentiation". In: *Earth-Science Reviews*. DOI: 10.1016/j.earscirev.2020.103496 (cit. on pp. 85, 86, 105, 109, 185).

Lehner, B., K. Verdin, and A. Jarvis (2008). "New global hydrography derived from spaceborne elevation data". In: *Eos Trans. AGU* 89.10, p. 93 (cit. on pp. 58, 74, 196).

Lengyel, G. (2007). *Upper Palaeolithic and Epipalaeolithic Lithic Technologies at Raqefet Cave, Mount Carmel East, Israel*. BAR International Series 1681. Oxford: Archaeopress, p. 118 (cit. on pp. 52, 60).

Leser, H. (1977). *Feld- und Labormethoden der Geomorphologie*. J. Wiley, Hoboken (N.J.) (cit. on p. 199).

Li, Y., W. Zhang, A. Aydin, and X. Deng (2018). "Formation of calcareous nodules in loess–paleosol sequences: Reviews of existing models with a proposed new "per evapotranspiration model"". In: *Journal of Asian Earth Sciences* 154, pp. 8–16. DOI: https://doi.org/10.1016/j.jseaes.2017.12.002. URL: https://www.sciencedirect.com/science/article/pii/S1367912017306764 (cit. on p. 174).

Lie, M. A., A. Cordoș, C. Gavan, A. Fazecaș, T. L. Kienlin, and F. Gogâltan (2019). "An overview of the Bronze Age tell-settlement in Toboliu". In: *Gesta* 17.2, pp. 63–76 (cit. on pp. 38, 40, 153, 175).

Lie, M. (2024). "Structure layouts as a means of understanding household activities at the Bronze Age tell site of Toboliu (Western Romania)". In: *Household Practices and Houses – Current Approaches from Archaeology and the Sciences*. Ed. by T. Kienlin. Bonn: Verlag Dr. Rudolf Habelt GmbH, pp. 291–312 (cit. on pp. 152, 153).

Lie, M. A., A. Găvan, T. L. Kienlin, A. Röpke, M. Zickel, and T. Zerl (2024). "Exploring the chronostratigraphy of a Bronze Age settle-

ment through core drilling". In: *Praehistorische Zeitschrift*. DOI: doi:10.1515/pz-2023-2026. URL: 10.1515/pz-2023-2026 (cit. on pp. 84, 86, 108, 112, 173, 174, 220).

Ligouis, B. (2017). "Reflected Light". In: *Archaeological Soil and Sediment Micromorphology*. Ed. by C. Nicosia and G. Stoops. John Wiley & Sons, Ltd, pp. 461–470. DOI: 10.1002/9781118941065.ch44 (cit. on p. 118).

Lillesand, T., R. Kiefer, and J. Chipman (2015). *Remote Sensing and Image Interpretation*. New York, USA: John Wiley & Sons, Ltd. (cit. on pp. 74, 76, 102, 119, 124, 134).

Lindner, H., F. Lehmkuhl, and C. Zeeden (2017a). *Geodata set of 'Spatial loess distribution in the eastern Carpathian Basin: a novel approach based on geoscientific maps and data*. DOI: 10.1080/17445647.2017.1279083 (cit. on pp. 12, 17, 39, 84, 86, 87, 103, 154).

Lindner, H., F. Lehmkuhl, and C. Zeeden (2017b). "Spatial loess distribution in the eastern Carpathian Basin: a novel approach based on geoscientific maps and data". In: *Journal of Maps* 13, pp. 173–181. DOI: 10.1080/17445647.2017.1279083 (cit. on pp. 38, 85, 86, 103, 105).

Liritzis, I., K. Stamoulis, C. Papachristodoulou, and K. Ioannides (2013). "A re-evaluation of radiation dose-rate conversion factors". In: *Mediterranean Archaeology and Archaeometry* 13, pp. 1–15. DOI: 10.1016/0029-554x(82)90122-7 (cit. on p. 90).

Lisá, L., P. Kočár, A. Bajer, R. Kočárová, Z. Syrová, J. Syrový, M. Porubčanová, P. Lisý, M. Peška, and M. Ježková (May 2020). "The floor: a voice of human lifeways—a geo-ethnographical study of historical and recent floors at Dolní Němčí Mill, Czech Republic". In: *Archaeological and Anthropological Sciences* 12.6, p. 115. DOI: 10.1007/s12520-020-01060-y (cit. on p. 152).

Lloyd, C. (2010). *Spatial Data Analysis: an Introduction for GIS Users*. Oxford, New York: Oxford University Press, p. 206 (cit. on pp. 57, 58, 197).

Lo Russo, S., D. Brönnimann, S. Deschler-Erb, C. Ebnöther, and P. Rentzel (2022). "Mithraism under the microscope: new revelations about rituals through micromorphology, histotaphonomy and zooarchaeology". In: *Archaeological and Anthropological Sciences* 14, pp. 1–21. DOI: 10.1007/s12520-022-01505-6 (cit. on p. 118).

Lohrer, R., M. Bertrams, E. Eckmeier, J. Protze, and F. Lehmkuhl (2013). "Mapping the distribution of weathered Pleistocene wadi deposits in Southern Jordan using ASTER, SPOT-5 data and laboratory spectroscopic analysis". In: *Catena* 107, pp. 57–70 (cit. on p. 72).

Love, S. (2013a). "Architecture as material culture: Building form and materiality in the Pre-Pottery Neolithic of Anatolia and Levant". In: *Journal of Anthropological Archaeology* 32.4, pp. 746–758. DOI: https://doi.org/10.1016/j.jaa.2013.05.002 (cit. on p. 152).

Love, S. (2013b). "The Performance of Building and Technological Choice Made Visible in Mudbrick Architecture". In: *Cambridge Archaeological Journal* 23.2, pp. 263–282. DOI: 10.1017/S0959774313000292 (cit. on p. 152).

Lubos, C., S. Dreibrodt, V. Robin, O. Nelle, S. Khamnueva, I. Richling, U. Bultmann, and H.-R. Bork (2013). "Settlement and environmental history of a multilayered settlement mound in Niederröblingen (central Germany) – a multi-proxy approach". In: *Journal of Archaeological Science* 40.1, pp. 79–98. DOI: 10.1016/j.jas.2012.07.022 (cit. on pp. 89, 222).

Lukić, T., S. B. Marković, T. Stevens, D. A. Vasiljević, B. Machalett, N. Milojković, B. Basarin, and I. Obreht (2009). "The Loess "Cave" Near the Village of Surduk - an Unusual Pseudokarst Landform in the Loess of Vojvodina, Serbia". In: *Acta Carsologica* 38, pp. 227–235. DOI: 10.3986/ac.v38i2-3.124 (cit. on pp. 85, 108).

Lundstrom, V. and F. Riede (2019). "A spatially explicit model of Final Palaeolithic population densities for southern Scandinavia in the period between 14,000 and 12,700 cal BP". In: *Journal of Archaeological Science: Reports* 26, p. 101886 (cit. on p. 50).

Luo, L., X. Wang, C. Liu, H. Guo, and X. Du (2014). "Integrated RS, GIS and GPS approaches to archaeological prospecting in the Hexi Corridor, NW China: a case study of the royal road to ancient Dunhuang". In: *Journal of Archaeological Science* 50, pp. 178–190 (cit. on pp. 72, 184).

Mackay, J. (1998). "Pingo Growth and collapse, Tuktoyaktuk Peninsula Area, Western Arctic Coast, Canada: a long-term field study". In: *Géographie physique et Quaternaire* 52.3, pp. 271–323. DOI: 10.7202/004847ar (cit. on pp. 15, 109, 111).

Macphail, R. and P. Goldberg (2007). "Applied Soils and Micromorphology in Archaeology". In: *Archaeological Institute of the Hungarian Academy of Sciences*. Ed. by W. AWR, pp. 189–226. DOI: 10.1017/9780511895562 (cit. on p. 173).

Macphail, R. I. and P. Goldberg (2018). "Chapter 27 - Archaeological Materials". In: *Interpretation of Micromorphological Features of Soils and Regoliths (Second Edition)*. Ed. by G. Stoops, V. Marcelino, and F. Mees. Second Edition. Elsevier, pp. 779–819. DOI: https://doi.org/10.1016/B978-0-444-63522-8.00027-9 (cit. on pp. 152, 176).

Magyari, E., J. Chapman, D. Passmore, J. Allen, J. Huntley, and B. Huntley (2010). "Holocene persistence of wooded steppe in the Great Hungarian Plain". In: *Journal of Biogeography* 37.5, pp. 915–935. DOI: 10.1111/j.1365-2699.2009.02261.x (cit. on pp. 38, 85, 86, 107, 112, 186).

Magyari, E. K., P. Raczky, M. Merkl, I. Pálfi, G. Darabos, M. Hajnalova, and M. Moskal-Hoyo (2024). "Review on vegetation, landscape and climate changes in the Carpathian Basin during the Neolithic and

Chalcolithic period". In: *Vegetation History and Archaeobotany*, pp. 1–26 (cit. on pp. 86, 107, 112).

Malczewski, J. (2006). "GIS-based multicriteria decision analysis: a survey of the literature". In: *International Journal of Geographical Information Science* 20.7, pp. 703–726 (cit. on pp. 42, 57, 197).

Malczewski, J. and C. Rinner (2015). *Multicriteria Decision Analysis in Geographic Information Science*. Advances in Geographic Information Science. Berlin: Springer, p. 331 (cit. on pp. 57, 78, 197, 198).

Manner, H. (2004). "Ein Konzept zur Erfassung siedlungsarchäologischer Befunde im Hochgebirge und ihrer räumlichen Bezüge: Darstellung an einem Fallbeispiel in den Stubaier Alpen". PhD thesis. Kiel: Christian-Albrechts-Universität zu Kiel, p. 170 (cit. on p. 199).

Marder, O., B. Alex, A. Ayalon, M. Bar-Matthews, G. Bar-Oz, D. Bar-Yosef Mayer, F. Berna, E. Boaretto, V. Caracuta, A. Frumkin, et al. (2013). "The upper palaeolithic of Manot cave, western galilee, Israel: the 2011–12 excavations". In: *Antiquity* 87.337 (cit. on p. 51).

Marder, O., I. Milevski, R. Rabinovich, O. Ackermann, R. Shahack-Gross, and I. Fine (2008). "The lower paleolithic site of Revadim quarry, Israel". In: *Proceedings of the 5th International Congress on the Archaeology of the Ancient Near East*. Ed. by J. Cordoba. Madrid: Ediciones Universidad Autonoma de Madrid, pp. 481–490 (cit. on p. 62).

Marder, O., M. Shemer, T. Abulafia, D. Bar-Yosef Mayer, F. Berna, S. Caux, L. Edeltin, M. Goder-Goldberger, I. Hershkovitz, R. Lavi, et al. (2019). "Preliminary observations on the Levantine Aurignacian sequence of Manot Cave: cultural affiliations and regional perspectives". In: *Journal of Human Evolution* (cit. on p. 52).

Marković, S. B., M. P. Bokhorst, J. Vandenberghe, W. D. McCoy, E. A. Oches, U. Hambach, T. Gaudenyi, M. Jovanović, L. Zöller, T. Stevens, et al. (2007). "Late Pleistocene loess-palaeosol sequences in the Vojvodina region, north Serbia". In: *Journal of Quaternary Science* 23.1, pp. 73–84. DOI: 10.1002/jqs.1124 (cit. on pp. 85, 96, 105).

Marković, S. B., T. Stevens, G. J. Kukla, U. Hambach, K. E. Fitzsimmons, P. Gibbard, B. Buggle, M. Zech, Z. Guo, Q. Hao, et al. (2015). "Danube loess stratigraphy — Towards a pan-European loess stratigraphic model". In: *Earth-Science Reviews* 148, pp. 228–258. DOI: 10.1016/j.earscirev.2015.06.005 (cit. on p. 107).

Marks, A. (1976). *Prehistory and Paleoenvironments in the Central Negev, Israel: Volume I the Avdat/Aqev Area Part I*. Dallas: Southern Methodist University Press (cit. on pp. 50, 60, 73, 184).

Marks, A. (1977). *Prehistory and Paleoenvironments in the Central Negev, Israel: Volume II, the Avdat/Aqev Area, Part 2 and the Har Harif*. Dallas: Southern Methodist University Press (cit. on pp. 50, 52, 60, 73).

Marks, A. (1981). "The upper palaeolithic of the levant". In: *Préhistoire du Levant; Chronologie et organisation de l'espace depuis les origines*

jusqu'au VIe millénaire. Ed. by J. Cauvin and P. Sanlaville. Colloques internationaux du Centre national de la recherche scientifique, pp. 369–372 (cit. on p. 51).

Marks, A. (1983a). *Prehistory and Paleoenvironments in the Central Negev, Israel: Volume III the Avdat/Aqev Area, Part 3*. Dallas, USA: Southern Methodist University Press (cit. on pp. 50, 73).

Marks, A. (1983b). "The sites of Boker and Boker Tachtit: a brief introduction". In: *Prehistory and Paleoenvironments in the Central Negev, Israel: Volume III the Avdat/Aqev Area, Part 3*. Ed. by A. Marks. Dallas: Southern Methodist University Press, pp. 15–83 (cit. on p. 74).

Marks, A. and D. Freidel (1977). "Prehistoric settlement patterns in the Avdat/Aqev area". In: *Prehistory and Paleoenvironments in the Central Negev, Israel: Volume II, the Avdat/Aqev Area, Part 2 and the Har Harif*. Ed. by A. Marks. Dallas: Southern Methodist University Press, pp. 131–158 (cit. on p. 50).

Matmon, A. and E. Zilberman (2017). "Landscape evolution along the Dead Sea fault and its margins". In: *Quaternary of the Levant*. Ed. by Y. Enzel and O. Bar-Yosef. Cambridge University Press, pp. 17–30 (cit. on p. 53).

Matthews, W. (1995). "Micromorphological Characterisation of Occupation Deposits and Microstratigraphic Sequences at Abu Salabikh, Southern Iraq". In: *Archaeological Sediments and Soils: Analysis, Interpretation and Management*. Ed. by A. J. Barham and R. I. Macphail. London, UK: Institute of Archaeology, University College London, pp. 41–76 (cit. on p. 176).

Meer, J. J. M. van der and J. Menzies (2011). "The micromorphology of unconsolidated sediments". In: *Sedimentary Geology* 238, pp. 213–232 (cit. on p. 118).

Mentzer, S. M. (2017). "Micro XRF". In: *Archaeological Soil and Sediment Micromorphology*. John Wiley & Sons, Ltd. Chap. 41, pp. 431–440. DOI: https://doi.org/10.1002/9781118941065.ch41 (cit. on pp. 43, 140, 152, 177, 187).

Metzger, M. J., R. G. H. Bunce, R. H. G. Jongman, C. A. Mücher, and J. W. Watkins (2005). "A climatic stratification of the environment of Europe". In: *Global Ecology and Biogeography* 14.6, pp. 549–563. DOI: 10.1111/j.1466-822X.2005.00190.x (cit. on p. 86).

Michéli, E., Á. Csorba, T. Szegi, E. Dobos, and M. Fuchs (July 1, 2019). "The soil types of the modernized, diagnostic based Hungarian Soil Classification System and their correlation with the World reference base for soil resources". In: *Hungarian Geographical Bulletin* 68.2, pp. 109–117. DOI: 10.15201/hungeobull.68.2.1 (cit. on p. 108).

Miebach, A. (2016). "Climate- and Human-Induced Vegetation Changes in Northwestern Turkey and the Southern Levant since the Last Glacial". PhD thesis. Rheinische Friedrich-Wilhelms-Universität Bonn, p. 132 (cit. on pp. 76, 184).

Miebach, A., S. Stolzenberger, L. Wacker, A. Hense, and T. Litt (2019). "A new Dead Sea pollen record reveals the last glacial paleoenvironment of the southern Levant". In: *Quaternary Science Reviews* 214, pp. 98–116 (cit. on p. 79).

Mischke, S., H. Ginat, B. Al-Saqarat, G. Faershtein, N. Porat, P. Braun, and J. Rech (2017). "Fossil-based reconstructions of ancient water bodies in the levantine deserts". In: *Quaternary of the Levant*. Ed. by Y. Enzel and O. Bar-Yosef. Cambridge University Press, pp. 381–390 (cit. on p. 56).

Monigal, K. (2003). "Technology, economy, and mobility at the beginning of the levantine upper palaeolithic". In: *More than Meets the Eye: Studies on Upper Palaeolithic Diversity in the Near East*. Ed. by A. Goring-Morris and A. Belfer-Cohen. Oxford, Oakville: Oxbow Books, pp. 118–133 (cit. on p. 51).

Moore, P. D., J. A. Webb, and M. E. Collinson (1991). *Pollen analysis*. English. 2nd ed. Oxford: Blackwell Science (cit. on pp. 89, 90).

Murphy, C. P., P. Bullock, and R. H. Turner (1977). "The Measurement And Characterisation Of Voids In Soil Thin Sections By Image Analysis. Part I. Principles And Techniques". In: *Journal of Soil Science* 28, pp. 498–508. DOI: 10.1111/j.1365-2389.1977.tb02258.x (cit. on pp. 126, 138).

Murphy, C. (2014). "Mineralization of Macrobotanical Remains". In: *Encyclopedia of Global Archaeology*. Ed. by C. Smith. New York, NY: Springer New York, pp. 4948–4952. DOI: 10.1007/978-1-4419-0465-2_2256 (cit. on pp. 157, 174, 176).

Murray, A. and A. Wintle (2000). "Luminescence dating of quartz using an improved single-aliquot regenerative-dose protocol". In: *Radiation Measurements* 32.1, pp. 57–73. DOI: 10.1016/S1350-4487(99)00253-X (cit. on pp. 24, 224).

Murray, A. and A. Wintle (2003). "The single aliquot regenerative dose protocol: potential for improvements in reliability". In: *Radiation Measurements* 37.4. Proceedings of the 10th international Conference on Luminescence and Electron-Spin Resonance Dating (LED 2002), pp. 377–381. DOI: 10.1016/S1350-4487(03)00053-2 (cit. on pp. 24, 90, 224).

Nadel, D. (2017). "Ohalo II: a 23,000-year-old Fisher-Hunter-Gatherer's camp on the shore of fluctuating lake Kinneret (Sea of Galilee)". In: *Quaternary of the Levant*. Ed. by Y. Enzel and O. Bar-Yosef. Cambridge University Press, pp. 291–294 (cit. on p. 65).

Nádor, A., R. Sinha, Á. Magyari, S. K. Tandon, Z. Medzihradszky, E. Babinszki, E. Thamó-Bozsó, Z. Unger, and A. Singh (2011). "Late Quaternary (Weichselian) alluvial history and neotectonic control on fluvial landscape development in the southern Körös plain, Hungary". In: *Palaeogeography, Palaeoclimatology, Palaeoecology* 299.1, pp. 1–14. DOI: 10.1016/j.palaeo.2010.09.018 (cit. on pp. 107, 185).

Nádor, A., E. Thamó-Bozsó, Á. Magyari, and E. Babinszki (2007). "Fluvial responses to tectonics and climate change during the Late Weichselian in the eastern part of the Pannonian Basin (Hungary)". In: *Sedimentary Geology* 202.1, pp. 174–192. DOI: 10.1016/j.sedgeo.2007.03.001 (cit. on pp. 84, 102, 103, 112, 185).

Naseri, A. and A. Rezaei Nasab (2021). "Automatic identification of minerals in thin sections using image processing". In: *Journal of Ambient Intelligence and Humanized Computing* 14, pp. 3369–3381. DOI: 10.1007/s12652-021-03474-5 (cit. on pp. 119, 139).

National Agency for Cadastre and R. (ANCPI) (2014). *LiDAR sourced digital elevation model for the counties Arad and Bihor, 2009–2014*. URL: https://geoportal.ancpi.ro/portal/apps/webappviewer/index.html?id=3f34ee5af71c400396dda574f0d53274 (visited on 07/02/2024) (cit. on pp. 12, 13, 39, 87, 92).

Natural-Earth (2021). *Rivers + lake centerlines, version 5.0.0*. URL: https://www.naturalearthdata.com/downloads/10m-physical-vectors/10m-rivers-lake-centerlines (visited on 09/05/2023) (cit. on pp. 12, 17, 39, 87, 154).

Nesse, W. (2013). *Introduction to Optical Mineralogy*. Oxford University Press (cit. on p. 118).

Newcomer, M. (1974). "Outils en os du Paléolithique supérieur de Ksar Akil (Liban)". In: *1er Colloque International sur l'Industrie de l'Os dans la Prehistoire*. Ed. by H. Camps Fabrer. Aix-en-Provence: Editions de l'Université de Provence, pp. 60–65 (cit. on p. 52).

Nicosia, C. and G. Stoops (2017). *Archaeological Soil and Sediment Micromorphology*. Oxford, UK: Wiley Blackwell. DOI: 10.1002/9781118941065 (cit. on pp. 34, 43, 118).

Nir, D. (1978). "Geomorphology". In: *Survey of Israel* (cit. on pp. 58, 72, 74, 184, 195).

Nsanziyera, A., H. Rhinane, A. Oujaa, and K. Mubea (2018). "GIS and remote-sensing application in archaeological site mapping in the Awsard area (Morocco)". In: *Geosciences* 8.6, p. 207 (cit. on p. 57).

Olami, Y. (1984). "Prehistoric Carmel (Jerusalem and Haifa)". In: *Journal of the Israel Prehistoric Society* (cit. on p. 61).

Olami, Y. (1988). "A prehistoric survey of the Carmel area". In: *Journal of the Israel Prehistoric Society* 1987, pp. 173–175 (cit. on p. 61).

Olami, Y. and A. Ronen (1977). "Prehistoric sites in the Mount Carmel area, Israel". In: *Qartar* 27/28, pp. 147–151 (cit. on p. 61).

Ottaway, J. H. and M. R. Matthews (1988). "Trace element analysis of soil samples from a stratified archaeological site". In: *Environmental Geochemistry and Health* 10.3, pp. 105–112. DOI: 10.1007/BF01758678 (cit. on pp. 89, 222).

Out, W. A., J. J. García-Granero, M. H. Andreasen, C. N. Patús, W. Kirleis, G. H. Barfod, and N. H. Andersen (Dec. 2024). "Plant use at Funnel Beaker sites: combined macro- and microremains analysis at the Early Neolithic site of Frydenlund, Denmark (ca. 3600 bce)". In:

Vegetation History and Archaeobotany 34.2, pp. 177–203. DOI: 10.1007/s00334-024-01020-9 (cit. on p. 176).

Ovejanu, I., B. Candrea, and V. Crăciunescu (1968). *Harta Geologică a Republicii Socialiste România (Geological Map of the Socialist Republic of Romania)*. Map, scale 1:200,000. Bucharest (cit. on p. 103).

Parkinson, W. A., A. Gyucha, P. Karkanas, N. Papadopoulos, G. Tsartsidou, A. Sarris, P. R. Duffy, and R. W. Yerkes (June 2018). "A landscape of tells: Geophysics and microstratigraphy at two Neolithic tell sites on the Great Hungarian Plain". In: *Journal of Archaeological Science: Reports* 19, pp. 903–924. DOI: 10.1016/j.jasrep.2017.07.002 (cit. on pp. 173, 175).

Parow-Souchon, H. (2020). "The Wadi Sabra (Jordan): a contextual approach to the Palaeolithic landscape". In: *Pleistocene Archaeology of the Petra Area in Jordan*. Ed. by D. Schyle and J. Richter. Rahden/Westfalen: Marie Leidorf GmbH, p. 11 (cit. on pp. 51, 60, 67, 73).

Pató, Z., T. Standovár, M. Gałka, G. Jakab, M. Molnár, F. Szmorad, and E. Magyari (2020). "Exposure matters: Forest dynamics reveal an early Holocene conifer refugium on a north facing slope in Central Europe". In: *The Holocene* 30.12, pp. 1833–1848. DOI: 10.1177/0959683620950452 (cit. on p. 107).

Pedregosa, F., G. Varoquaux, A. Gramfort, V. Michel, B. Thirion, O. Grisel, M. Blondel, P. Prettenhofer, R. Weiss, V. Dubourg, et al. (2011). "Scikit-learn: Machine Learning in Python". In: *Journal of Machine Learning Research* 12, pp. 2825–2830. URL: http://jmlr.org/papers/v12/pedregosa11a.html (cit. on pp. 125, 126).

Perić, Z. M., T. Stevens, I. Obreht, U. Hambach, F. Lehmkuhl, and S. B. Marković (2022). "Detailed luminescence dating of dust mass accumulation rates over the last two glacial-interglacial cycles from the Irig loess-palaeosol sequence, Carpathian Basin". In: *Global and Planetary Change* 215, p. 103895. DOI: 10.1016/j.gloplacha.2022.103895 (cit. on p. 107).

Pires de Lima, R., D. Duarte, C. Nicholson, R. Slatt, and K. J. Marfurt (2020). "Petrographic microfacies classification with deep convolutional neural networks". In: *Computers and Geosciences* 142, p. 104481. DOI: 10.1016/j.cageo.2020.104481 (cit. on p. 118).

Polisca, F. (June 2025). "Exploring the impact of burial conditions and formation processes in intra-site contexts: a micromorphological comparison of waterlogged and well-drained Bronze Age deposits". In: *Archaeological and Anthropological Sciences* 17.7. DOI: 10.1007/s12520-025-02269-5 (cit. on p. 152).

Pötter, S., A. Schmitz, A. Lücke, P. Schulte, I. Obreht, M. Zech, H. Wissel, S. B. Marković, and F. Lehmkuhl (2021). "Middle to Late Pleistocene environments based on stable organic carbon and nitrogen isotopes of loess-palaeosol sequences from the Carpathian

Basin". In: *Boreas* 50.1, pp. 184–204. DOI: 10.1111/bor.12470 (cit. on pp. 85, 105, 107).

Punt, W., S. Blackmore, P. P. Hoen, and H. Kerp (1995). *The Northwest European Pollen Flora I- VII, 1976–1995*. Elsevier Science (cit. on p. 90).

QGIS Development Team (2022a). *Documentation for QGIS 3.22*. QGIS – Geographic Information System, last access: 18 January 2024. URL: https://docs.qgis.org/3.22/en/docs/ (cit. on pp. 126, 127, 140, 231).

QGIS Development Team (2022b). *QGIS Geographic Information System software, version 3.22*. Open Source Geospatial Foundation Project, last access: 18 January 2024. URL: http://qgis.org (cit. on pp. 119, 126).

QGIS Development Team (2022c). *QGIS Geographic Information System, version 3.14, 2020-06-19*. Open Source Geospatial Foundation. URL: https://www.qgis.org/en/site/index.html (visited on 09/01/2020) (cit. on pp. 24, 195, 200).

QGIS Development Team (2022d). *QGIS Geographic Information System, version 3.28, 2022-10-21*. Open Source Geospatial Foundation. URL: https://www.qgis.org/en/site/index.html (visited on 12/16/2023) (cit. on pp. 186, 220).

R Core Team (2023). *R: A Language and Environment for Statistical Computing*. R Foundation for Statistical Computing. Vienna, Austria. URL: https://www.R-project.org/ (cit. on pp. 157, 222).

Rabinovich, R., O. Ackermann, E. Aladjem, R. Barkai, R. Biton, I. Milevski, N. Solodenko, and O. Marder (2012). "Elephants at the Middle Pleistocene Acheulian open-air site of Revadim Quarry, Israel". In: *Quaternary International* 276–277, pp. 183–197 (cit. on p. 62).

Rees-Jones, J. (1995). "Optical Dating of Young Sediments using fine-grain quartz". In: *Ancient TL* 13.2 (cit. on p. 90).

Reille, M. (1998). "Pollen et spores d'Europe et d'Afrique du nord – supplement 2". In: *Laboratoire de Botanique hostorique et Palynologie*. Marseille, pp. 520–523 (cit. on p. 90).

Reimann, T., A. Román-Sánchez, T. Vanwalleghem, and J. Wallinga (2017). "Getting a grip on soil reworking – Single-grain feldspar luminescence as a novel tool to quantify soil reworking rates". In: *Quaternary Geochronology* 42, pp. 1–14. DOI: 10.1016/j.quageo.2017.07.002 (cit. on p. 107).

Reimer, P. J., W. E. N. Austin, E. Bard, A. Bayliss, P. G. Blackwell, C. Bronk Ramsey, M. Butzin, H. Cheng, R. L. Edwards, M. Friedrich, et al. (2020). "The IntCal20 Northern Hemisphere Radiocarbon Age Calibration Curve (0–55 cal kBP)". In: *Radiocarbon* 62.4, pp. 725–757. DOI: 10.1017/RDC.2020.41 (cit. on p. 90).

Renfrew, C. (1976). "Archaeology and the earth sciences". In: *Geoarchaeology: Earth Science and the Past*. Ed. by D. Davidson and M. Shackley. London, UK: Duckworth, pp. 1–5 (cit. on p. 33).

Richter, J. and D. Schyle (2015). "The final Levantine Aurignacian site of Sabra 4-Palm View 3". In: *Pleistocene Archaeology of the Petra Area in Jordan*. Ed. by D. Schyle and J. Richter. Rahden/Westfalen: Marie Leidorf GmbH, pp. 233–272 (cit. on pp. 60, 67).

Rohling, E. (2013). "Quantitative assessment of glacial fluctuations in the level of Lake Lisan, Dead Sea rift". In: *Quaternary Science Reviews* 70, pp. 63–72 (cit. on pp. 53, 76, 184).

Romanescu, G., L. Dénes, J. Dezső, and D. Carboni (2018). "Loess-Scape in the Dobrudja Plateau (Romania). Landforms and Updated Typology". In: *Present Environment and Sustainable Development* 12, pp. 114–95. URL: https://api.semanticscholar.org/CorpusID:133693857 (cit. on pp. 85, 108).

Ronen, A. (1968). "Excavations at the cave of Sefunim (Lraq el-Barud), Mt. Carmel preliminary report". In: *Qartar* 19, pp. 275–288 (cit. on pp. 52, 60).

Ronen, A. and A. Ben-Tor (1984). *Sefunim Prehistoric Sites, Mount Carmel, Israel*. BAR International Series 230. London: B.A.R, p. 533 (cit. on p. 52).

Ronen, A. and B. Vandermeersch (1972). "The upper Paleolithic sequence in the cave of Qafzeh (Israel)". In: *Quaternaria* 16, pp. 189–202 (cit. on p. 51).

Röpke, A. (2021). "Lowland Pollen Analyses of Căuaş-Sighetiu (Ier Valley, NW-Romania) with a Special Focus on Near-Site Bronze Age Human Influence". In: ed. by T. K. Găvan. Vol. 364. Bronze Age Settlements in North-Western Romania. Universitätsforschungen zur Prähistorischen Archäologie, pp. 281–394 (cit. on p. 107).

Röpke, A., Kovacs, G., Petö, A. (2024). "Household activities imprinted in floors". In: *Household Practices and Houses – Current Approaches from Archaeology and the Sciences*. Ed. by T. Kienlin. Bonn: Verlag Dr. Rudolf Habelt GmbH, pp. 271–290 (cit. on pp. 152, 176).

Roskin, J. and H. Tsoar (2017). "Late Quaternary chronologies of the northern Sinai/northwestern Negev dunefield and their palaeoclimatic and palaeoenvironmental implications". In: *Quaternary of the Levant*. Ed. by Y. Enzel and O. Bar-Yosef. Cambridge University Press, pp. 505–520 (cit. on p. 55).

Rothwell, R. G. and I. W. Croudace (2015). "Twenty Years of XRF Core Scanning Marine Sediments: What Do Geochemical Proxies Tell Us?" In: URL: https://api.semanticscholar.org/CorpusID:128600647 (cit. on p. 97).

Rouault, E., F. Warmerdam, K. Schwehr, A. Kiselev, H. Butler, M. Łoskot, T. Szekeres, E. Tourigny, M. Landa, I. Miara, et al. (2022). *GDAL, version 3.5.1*. DOI: 10.5281/zenodo.6801315 (cit. on p. 142).

Rubo, R. A., C. de Carvalho Carneiro, M. F. Michelon, and R. dos Santos Gioria (2019). "Digital petrography: Mineralogy and porosity identification using machine learning algorithms in petrographic thin section images". In: *Journal of Petroleum Science and Engineering*

183, p. 106382. DOI: 10.1016/j.petrol.2019.106382 (cit. on pp. 119, 125, 134, 136, 139, 140, 187).

Rust, A. (1950). *Die Höhlenfunde von Jabrud (Syrien)*. Neumünster (cit. on p. 52).

Ruszkiczay-Rüdiger, Z. and Z. Kern (2016). "Permafrost or seasonal frost? A review of paleoclimate proxies of the last glacial cycle in the East Central European lowlands". In: *Quaternary International* 415. Climate change in the Balkan-Carpathian region during Late Pleistocene and Holocene, pp. 241–252. DOI: 10.1016/j.quaint.2015.07.027 (cit. on pp. 38, 85, 86).

Ruttenberg, K. and M. Goñi (1997). "Phosphorus distribution, C:N:P ratios, and δ 13Coc in arctic, temperate, and tropical coastal sediments: tools for characterizing bulk sedimentary organic matter". In: *Marine Geology* 139.1. Phosphorus Cycling and Sedimentation in Marine and Freshwater Systems, pp. 123–145. DOI: 10.1016/S0025-3227(96)00107-7 (cit. on pp. 89, 222).

Salisbury, R. (2016). *Soilscapes in Archaeology. Settlement and Social Organization in the Neolithic of the Great Hungarian Plain*. Budapest: Archaeolingua Alapítvány (cit. on p. 110).

Sarig, R., C. Fornai, A. Pokhojaev, H. May, M. Hans, B. Latimer, O. Barzilai, R. Quam, and G. Weber (2019). "The dental remains from the early upper paleolithic of Manot cave, Israel". In: *Journal of Human Evolution* 102648 (cit. on p. 52).

Sauzet, O., C. Cammas, J. M. Gilliot, M. Bajard, and D. Montagne (2017). "Development of a novel image analysis procedure to quantify biological porosity and illuvial clay in large soil thin sections". In: *Geoderma* 292, pp. 135–148. DOI: 10.1016/j.geoderma.2017.01.004 (cit. on p. 119).

Schatz, A.-K., J.-P. Buylaert, A. Murray, T. Stevens, and T. Scholten (2012). "Establishing a luminescence chronology for a palaeosol-loess profile at Tokaj (Hungary): A comparison of quartz OSL and polymineral IRSL signals". In: *Quaternary Geochronology* 10. 13th International Conference on Luminescence and Electron Spin Resonance Dating - LED 2011 Dedicated to J. Prescott and G. Berger, pp. 68–74. DOI: 10.1016/j.quageo.2012.02.018 (cit. on pp. 85, 105, 107).

Scheidt, S., S. Berg, U. Hambach, N. Klasen, S. Pötter, A. Stolz, D. Veres, C. Zeeden, D. Brill, H. Brückner, et al. (2021). "Chronological Assessment of the Balta Alba Kurgan Loess-Paleosol Section (Romania) – A Comparative Study on Different Dating Methods for a Robust and Precise Age Model". In: *Frontiers in Earth Science* 8. DOI: 10.3389/feart.2020.598448 (cit. on pp. 101, 105).

Scherer, S., B. Höpfer, K. Deckers, M. Fuchs, E. Kandeler, E. Lehndorff, J. Lomax, S. Marhan, C. Poll, W. Kristen, et al. (2023). "Archaeopedological reconstruction of Middle Bronze Age subsistence farming in SW-Germany from sedimentary archives in the Western Allgäu". In:

Geoderma Regional 35, e00715. DOI: 10.1016/j.geodrs.2023.e00715 (cit. on p. 89).

Schiebel, V. (2013). "Vegetation and Climate History of the Southern Levant during the Last 30,000 Years Based on Palynological Investigation". PhD thesis. Rheinischen Friedrich-Wilhelms-Universität Bonn, p. 104 (cit. on pp. 11, 54).

Schmidt, I. and A. Zimmermann (2019). "Population dynamics and socio-spatial organization of the Aurignacian: scalable quantitative demographic data for western and central Europe". In: *PloS One* 14.2, e0211562 (cit. on pp. 42, 50).

Schöler, S., A. Bengsch, and W. Denk (1990). *Vorderer Orient - Hydrogeologie*. SFB 19 Tübinger Atlas des Vorderen Orients (TAVO). Tübingen (cit. on pp. 58, 74, 195).

Schulte, P., F. Lehmkuhl, F. Steininger, D. Loibl, G. Lockot, J. Protze, P. Fischer, and G. Stauch (2016). "Influence of HCl pretreatment and organo-mineral complexes on laser diffraction measurement of loess–paleosol-sequences". In: *CATENA* 137, pp. 392–405. DOI: 10.1016/j.catena.2015.10.015 (cit. on p. 89).

Schulte, P., T. Sprafke, L. Rodrigues, and K. E. Fitzsimmons (2018). "Are fixed grain size ratios useful proxies for loess sedimentation dynamics? Experiences from Remizovka, Kazakhstan". In: *Aeolian Research* 31. INQUA LoessFest 2016: Western Wisconsin, pp. 131–140. DOI: 10.1016/j.aeolia.2017.09.002 (cit. on pp. 20, 89, 95, 105, 229).

Schweingruber, F. H. (1978). *Mikroskopische Holzanatomie. Formenspektren mitteleuropaeischer Stamm- u. Zweighoelzer zur Bestimmung von rezentem u. subfossilem Material*. ger, eng, and fre. Text in dt., franz. u. engl. Sprache. Zug: Zuercher AG, 226 S. (Cit. on p. 177).

Schyle, D. (2015a). "Pleistocene deposits and archaeological sites". In: *Pleistocene Archaeology of the Petra Area in Jordan*. Ed. by D. Schyle and J. Richter. Rahden/Westfalen: Marie Leidorf GmbH, pp. 51–53 (cit. on p. 67).

Schyle, D. (2015b). "The Ahmarian site of Al-Ansab 1". In: *Pleistocene Archaeology of the Petra Area in Jordan*. Ed. by D. Schyle and J. Richter. Rahden/Westfalen: Marie Leidorf GmbH, pp. 91–130 (cit. on pp. 67, 73).

Schyle, D. (2015c). "The Levantine Aurignacian site of Sabra 2010/6". In: *Pleistocene Archaeology of the Petra Area in Jordan*. Ed. by D. Schyle and J. Richter. Rahden/Westfalen: Marie Leidorf GmbH, pp. 149–178 (cit. on pp. 52, 60, 67).

Schyle, D. (2015d). "The Levantine Aurignacian site of Sabra 4-Palmview 1". In: *Pleistocene Archaeology of the Petra Area in Jordan*. Ed. by D. Schyle and J. Richter. Rahden/Westfalen: Marie Leidorf GmbH, pp. 179–232 (cit. on p. 67).

Schyle, D. (2015e). "The upper palaeolithic sequence of the Petra area". In: *Pleistocene Archaeology of the Petra Area in Jordan*. Ed. by D. Schyle

and J. Richter. Rahden/Westfalen: Marie Leidorf GmbH, pp. 361–394 (cit. on p. 67).

Schyle, D. and H.-P. Uerpmann (1988). "Palaeolithic Sites in the Petra Area". In: *The Prehistory of Jordan. The State of Research in 1986*. Ed. by A. Garrard and H.-G. Gebel. BAR International Series 396(i). Oxford: B.A.R (cit. on p. 67).

Scikit-learn developers (2023). *User guide: 1.11.2. Forests of randomized trees, 2007-2023*. Scikit-learn community, last access: 18 January. URL: https://scikit-learn.org/stable/modules/ensemble.html%5C#random-forests (cit. on pp. 125, 126, 186).

Shahack-Gross, R. (2016). "Archaeological Micromorphology Self-Evaluation Exercise". In: *Geoarchaeology* 31.1, pp. 49–57. DOI: 10.1002/gea.21536 (cit. on p. 34).

Shahack-Gross, R. (2015). "Archaeological Micromorphology Self-Evaluation Exercise". In: *Geoarchaeology* 31, pp. 49–57. DOI: 10.1002/gea.21536 (cit. on p. 119).

Sheldon, N. D. and N. J. Tabor (2009). "Quantitative paleoenvironmental and paleoclimatic reconstruction using paleosols". In: *Earth-Science Reviews* 95.1, pp. 1–52. DOI: 10.1016/j.earscirev.2009.03.004 (cit. on pp. 89, 222).

Shillito, L.-M. (Aug. 2011). "Simultaneous thin section and phytolith observations of finely stratified deposits from Neolithic Çatalhöyük, Turkey: implications for paleoeconomy and Early Holocene paleoenvironment". In: *Journal of Quaternary Science* 26.6, pp. 576–588. DOI: 10.1002/jqs.1470 (cit. on p. 176).

Shimelmitz, R., D. Friesem, J. Clark, I. Groman-Yaroslavski, L. Weissbrod, N. Porat, and A. Kandel (2018). "The upper paleolithic and epipaleolithic of Sefunim cave, Israel". In: *Quaternary International* 464, pp. 106–125 (cit. on p. 52).

Siart, C., M. Forbriger, and O. Bubenzer (2018a). *Digital geoarchaeology: New techniques for interdisciplinary human-environmental research*. Natural Science in Archaeology. Cham, Switzerland: Springer (cit. on pp. 41, 58).

Siart, C., M. Forbriger, and O. Bubenzer (2018b). *Digital Geoarchaeology - New Techniques for Interdisciplinary Human-Environmental Research*. Natural Science in Archaeology. Cham, Switzerland: Springer. DOI: 10.1007/978-3-319-25316-9 (cit. on pp. 183, 186).

Siart, C., M. Forbriger, and O. Bubenzer (2018c). "Digital Geoarchaeology: Bridging the Gap Between Archaeology, Geosciences and Computer Sciences". In: *Digital Geoarchaeology - New Techniques for Interdisciplinary Human-Environmental Research*. Ed. by C. Siart, M. Forbriger, and O. Bubenzer. Natural Science in Archaeology. Cham, Switzerland: Springer, pp. 1–7. DOI: 10.1007/978-3-319-25316-9_1 (cit. on pp. 33, 34).

Sidoti, G., F. Antonelli, G. Galotta, M. C. Moscatelli, D. Kržišnik, V. Vinciguerra, S. Tamantini, R. Marabottini, N. Macro, and M. Romagnoli

(2023). "Inorganic component in oak waterlogged archaeological wood and volcanic lake compartments". In: *Biogeosciences* 20.15, pp. 3137–3149. DOI: 10.5194/bg-20-3137-2023 (cit. on p. 157).

Sivan, D. and N. Greenbaum (2017). "Middle–late quaternary wetlands along the coastal plain of Israel". In: *Quaternary of the Levant*. Ed. by Y. Enzel and O. Bar-Yosef. Cambridge University Press, pp. 447–456 (cit. on p. 56).

Skrdla, P. (2003). "Comparison of Boker Tachtit and Stranská Skála MP/UP transitional industries". In: *Journal of the Israel Prehistoric Society* 33, pp. 37–73 (cit. on p. 51).

Smeck, N. E. (1985). "Phosphorus dynamics in soils and landscapes". In: *Geoderma* 36.3, pp. 185–199. DOI: 10.1016/0016-7061(85)90001-1 (cit. on pp. 89, 222).

Sneh, A., Y. Bartov, and M. Rosensaft (1997). *Geological Map of Israel 1:200 000 Sheet 1*. Jerusalem (cit. on p. 55).

Sneh, A., A. Eylal, Y. Eidelman, and Y. Bartov (2014). *Geological Map of Israel: En Yahac, Sheet 22-II*. Jerusalem (cit. on p. 55).

Solecki, R. and R. Solecki (1986). "A reappraisal of Rust's cultural stratigraphy of Yabroud Shelter I". In: *Paléo* 12.1, pp. 53–59 (cit. on p. 52).

Sprafke, T., P. Schulte, S. Meyer-Heintze, M. Händel, T. Einwögerer, U. Simon, R. Peticzka, C. Schäfer, F. Lehmkuhl, and B. Terhorst (2020). "Paleoenvironments from robust loess stratigraphy using high-resolution color and grain-size data of the last glacial Krems-Wachtberg record (NE Austria)". In: *Quaternary Science Reviews* 248, p. 106602. DOI: 10.1016/j.quascirev.2020.106602 (cit. on p. 85).

Stănilă, A.-L. and M. Dumitru (2016). "Soils Zones in Romania and Pedogenetic Processes". In: *Agriculture and Agricultural Science Procedia* 10, pp. 135–139. DOI: 10.1016/j.aaspro.2016.09.042 (cit. on p. 108).

Stein, M. and S. Goldstein (2017). "Lake Lisan". In: *Quaternary of the Levant*. Ed. by Y. Enzel and O. Bar-Yosef. Cambridge University Press, pp. 107–114 (cit. on p. 53).

Steinberger, Y., A. Shmida, and W. Witford (1990). "Decomposition along a rainfall gradient in the Judean desert, Israel". In: *Oecologia* 82, pp. 322–324 (cit. on p. 55).

Stemmler, S. and J. Berthelin (Oct. 2003). "Microbial activity as a major factor in the mobilization of iron in the humid tropics". In: *European Journal of Soil Science* 54.4, pp. 725–733. DOI: 10.1046/j.1351-0754.2003.0571.x (cit. on p. 174).

Stevens, T., S. B. Marković, M. Zech, U. Hambach, and P. Sümegi (2011). "Dust deposition and climate in the Carpathian Basin over an independently dated last glacial–interglacial cycle". In: *Quaternary Science Reviews* 30.5, pp. 662–681. DOI: 10.1016/j.quascirev.2010.12.011 (cit. on pp. 85, 107).

Stockhecke, M., A. Timmermann, R. Kipfer, G. Haug, O. Kwiecien, T. Friedrich, L. Menviel, T. Litt, N. Pickarski, and F. Anselmetti (2016). "Millennial to orbital-scale variations of drought intensity in the Eastern Mediterranean". In: *Quaternary Science Reviews* 133, pp. 77–95 (cit. on p. 76).

Stockmaar, J. (1971). "Tablets with spores used in absolute pollen analysis". In: *Pollen et Spores* 13, pp. 615–621 (cit. on p. 89).

Stoops, G., V. Marcelino, and F. (Mees (2018). *Interpretation of Micromorphological Features of Soils and Regoliths*. 2nd. Elsevier. DOI: 10.1016/C2014-0-01728-5 (cit. on pp. 118, 119).

Stoops, G. (Nov. 2020). *Guidelines for Analysis and Description of Soil and Regolith Thin Sections*. DOI: 10.1002/9780891189763 (cit. on pp. 42, 118, 121, 122, 188).

Sümegi, P., K. Náfrádi, D. Molnár, and S. Sávai (2015). "Results of paleoecological studies in the loess region of Szeged-Öthalom (SE Hungary)". In: *Quaternary International* 372. Loess and Dust: Contributions in honour of Ian Smalley, pp. 66–78. DOI: 10.1016/j.quaint.2014.09.003 (cit. on p. 86).

Tallavaara, M., M. Luoto, N. Korhonen, H. Jarvinen, and H. Seppä (2015). "Human population dynamics in Europe over the last glacial maximum". In: *Proceedings of the National Academy of Sciences of the United States of America* 112.27, pp. 8232–8237 (cit. on p. 50).

Tang, C.-S., C. Zhu, Q. Cheng, H. Zeng, J.-J. Xu, B.-G. Tian, and B. Shi (2021). "Desiccation cracking of soils: A review of investigation approaches, underlying mechanisms, and influencing factors". In: *Earth-Science Reviews* 216, p. 103586. DOI: https://doi.org/10.1016/j.earscirev.2021.103586 (cit. on p. 176).

Tang, D. G., K. L. Milliken, and K. T. Spikes (2020). "Machine learning for point counting and segmentation of arenite in thin section". In: *Marine and Petroleum Geology* 120, p. 104518. DOI: 10.1016/j.marpetgeo.2020.104518 (cit. on pp. 118, 119, 137, 139).

Tarquini, S. and M. Favalli (2010). "A microscopic information system (MIS) for petrographic analysis". In: *Computers and Geosciences* 36, pp. 665–674. DOI: 10.1016/j.cageo.2009.09.017 (cit. on pp. 119, 140).

Team, O. D. (2018). *Orfeo ToolBox 6.6.0*. URL: https://www.orfeo-toolbox.org/orfeo-toolbox-6-6-is-out/ (cit. on p. 200).

Tejero, J.-M., R. Rabinovich, R. Yeshurun, T. Abulafia, O. Bar-Yosef, O. Barzilai, M. Goder-Goldberger, I. Hershkovitz, R. Lavi, M. Shemer, et al. (2020). "Personal ornaments from Hayonim and Manot caves (Israel) hint at symbolic ties between the Levantine and the European Aurignacian". In: *Journal of Human Evolution* 102870 (cit. on p. 52).

Tejero, J.-M., R. Yeshurun, O. Barzilai, M. Goder-Goldberger, I. Hershkovitz, R. Lavi, N. Schneller-Pels, and O. Marder (2016). "The osseous industry from Manot Cave (Western Galilee, Israel): technical and conceptual behaviours of bone and antler exploitation in the

Levantine Aurignacian". In: *Quaternary International* 403, pp. 90–106 (cit. on p. 52).

Thamó-Bozsó, E. and L. Ó. Kovács (2007). "Chapter 19 Evolution of Quaternary to Modern Fluvial Network in the Mid-Hungarian Plain, Indicated by Heavy Mineral Distributions and Statistical Analysis of Heavy Mineral Data". In: *Heavy Minerals in Use*. Ed. by M. A. Mange and D. T. Wright. Vol. 58. Developments in Sedimentology. Elsevier, pp. 491–514. DOI: 10.1016/S0070-4571(07)58019-2 (cit. on p. 102).

Thiemeyer, H. and D. Fritzsch (2011). "Mikromorphologie - Methode and Objekte, Beispiele". In: *Tagungen des Landesmuseums für Vorgeschichte Halle*. 6. Halle: Landesmuseums für Vorgeschichte Halle (cit. on p. 175).

Thierion, V. and M. Lang (2018). "Object-Based Classification for Mountainous Vegetation Physiognomy Mapping". In: *QGIS and Applications in Agriculture and Forest*. Ed. by N. Baghdadi, C. Mallet, and M. Zribi. John Wiley & Sons, Ltd, pp. 283–339. DOI: 10.1002/9781119457107.ch9 (cit. on pp. 135, 187).

Thomas, D. S. G. (2013). "Reconstructing paleoenvironments and palaeoclimates in drylands: what can landform analysis contribute?" In: *Earth Surface Processes and Landforms* 38.1, pp. 3–16. DOI: 10.1002/esp.3190 (cit. on p. 33).

Thomsen, K., A. Murray, M. Jain, and L. Bøtter-Jensen (2008). "Laboratory fading rates of various luminescence signals from feldspar-rich sediment extracts". In: *Radiation Measurements* 43.9, pp. 1474–1486. DOI: 10.1016/j.radmeas.2008.06.002 (cit. on pp. 24, 90, 224).

Thorne, R., R. Herrington, and S. Roberts (Mar. 2009). "Composition and origin of the Çaldağ oxide nickel laterite, W. Turkey". In: *Mineralium Deposita* 44.5, pp. 581–595. DOI: 10.1007/s00126-009-0234-6 (cit. on p. 152).

Timár, G., G. Molnár, B. Székely, S. Biszak, J. Varga, and A. Jankó (2006). *Digitized maps of the Habsburg Empire – The map sheets of the second military survey and their georeferenced version*. Tech. rep. Budapest. URL: https://maps.arcanum.com/de/map/secondsurvey-hungary/?layers=5&bbox=2414267.1191107966%2C5947651.172696448%2C2421471.3090266744%2C5950039.829830361 (cit. on pp. 15, 38, 87, 103, 104, 112).

Timmermann, A. (2020). "Quantifying the potential causes of Neanderthal extinction: abrupt climate change versus competition and interbreeding". In: *Quaternary Science Reviews* 238, p. 106331 (cit. on p. 52).

Torfstein, A. and Y. Enzel (2017). "Dead Sea Lake level changes and Levant palaeoclimate". In: *Quaternary of the Levant*. Ed. by Y. Enzel and O. Bar-Yosef. Cambridge University Press, pp. 115–126 (cit. on pp. 53, 76, 184).

Torfstein, A., S. Goldstein, Y. Kushnir, Y. Enzel, G. Haug, and M. Stein (2015). "Dead Sea drawdown and monsoonal impacts in the Levant

during the last interglacial". In: *Earth and Planetary Science Letters* 412, pp. 235–244 (cit. on p. 53).

Torfstein, A., S. Goldstein, M. Stein, and Y. Enzel (2013). "Impacts of abrupt climate changes in the Levant from last glacial Dead Sea levels". In: *Quaternary Science Reviews* 69, pp. 1–7 (cit. on pp. 53, 76, 184).

Usery, E. (1993). "Category theory and the structure of features in geographic information systems". In: *Cartography and Geographic Information Systems* 20.1, pp. 5–12 (cit. on p. 78).

USGS - United States Geological Survey (2009). *Shuttle Radar Topography Mission, 1 Arc Second scene tiles, Unfilled Unfinished 2.1, Global Land Cover Facility, University of Maryland, College Park, Maryland, February 2000, https://earthdata.nasa.gov/nasa-shuttle-radar-topography-mission-srtm-version-3-0-global-1-arc-second-data-released-over-asia-and-australia (last access: 20. April 2023)* (cit. on pp. 12, 17, 39, 58, 74, 87, 154, 195).

Uthmeier, T. (2004). "Micoquien, Aurignacien und Gravettien in Bayern: eine regionale Studie zum Übergang vom Mittel- zum Jungpalaolithikum". In: *Archäologische Berichte*. Vol. 18. Bonn: Rudolf Habelt (cit. on pp. 42, 50).

Uzdurum, M., J. Schönicke, M. Kinzel, and M. Z. Baranski (2023). "Studying the Use of Earth in Early Architecture of Southwest and Central Asia". English. In: *Open Archaeology* 9.1. DOI: 10.1515/opar-2022-0321 (cit. on p. 175).

van der Meer, F., H. van der Werff, and F. van Ruitenbeek (2014). "Potential of ESA's Sentinel-2 for geological applications". In: *Remote Sensing of Environment* 148, pp. 124–133 (cit. on p. 79).

van Vliet-Lanoë, B., A. Magyari, and F. Meilliez (2004). "Distinguishing between tectonic and periglacial deformations of quaternary continental deposits in Europe". In: *Global and Planetary Change* 43.1, pp. 103–127. DOI: 10.1016/j.gloplacha.2004.03.003 (cit. on pp. 85, 109, 110).

Vandermeersch, B. and O. Bar-Yosef (2017). "Qafzeh cave and terrace". In: *Quaternary of the Levant*. Ed. by Y. Enzel and O. Bar-Yosef. Cambridge University Press, pp. 251–254 (cit. on p. 51).

Vapnik, V. N. (2000). *The Nature of Statistical Learning Theory*. New York, USA: Springer New York. DOI: 10.1007/978-1-4757-3264-1 (cit. on pp. 135, 136).

Vepraskas, M. J., D. L. Lindbo, and M. H. Stolt (2018). "Redoximorphic Features". In: *Interpretation of Micromorphological Features of Soils and Regoliths (Second Edition)*. Ed. by G. Stoops, V. Marcelino, and F. Mees. Elsevier, pp. 425–445. DOI: 10.1016/b978-0-444-63522-8.00015-2 (cit. on pp. 122, 140).

Verhagen, J. (2008). "Testing archaeological predictive models: a rough guide". In: *Layers of Perception. Proceedings of the 35th International Conference on Computer Applications and Quantitative Methods in Ar-*

chaeology (CAA). Ed. by A. Posluschny, K. Lambers, and I. Herzog. Bonn: Rudolf Habelt, pp. 285–291 (cit. on pp. 57, 58).

Verhagen, P. (2006). "Quantifying the qualified: the use of multicriteria methods and Bayesian statistics for the development of archaeological predictive models". In: *GIS and Archaeological Site Location Modelling*. Ed. by M. Mehrer and K. Wescott. Boca Raton, Fla. and London: CRC, pp. 71–91 (cit. on p. 57).

Verhagen, P. and T. Whitley (2012). "Integrating archaeological theory and predictive modeling: a live report from the scene". In: *Journal of Archaeological Method and Theory* 19.1, pp. 49–100 (cit. on p. 57).

Verhagen, P. (2018). "Spatial Analysis in Archaeology: Moving into New Territories". In: *Digital Geoarchaeology - New Techniques for Interdisciplinary Human-Environmental Research*. Ed. by C. Siart, M. Forbriger, and O. Bubenzer. Natural Science in Archaeology. Cham, Switzerland: Springer, pp. 11–25. DOI: 10.1007/978-3-319-25316-9_2 (cit. on pp. 36, 41, 78).

Visalli, R., G. Ortolano, G. Godard, and R. Cirrincione (2021). "Micro-Fabric Analyzer (MFA): A New Semiautomated ArcGIS-Based Edge Detector for Quantitative Microstructural Analysis of Rock Thin-Sections". In: *ISPRS International Journal of Geo-Information* 10, p. 51. DOI: 10.3390/ijgi10020051 (cit. on pp. 119, 135, 140, 187).

Vita-Finzi, C., E. Higgs, D. Sturdy, J. Harriss, A. Legge, and H. Tippett (1970). "Prehistoric Economy in the Mount Carmel Area of Palestine: Site Catchment Analysis". In: *Proceedings of the Prehistoric Society* 36, pp. 1–37. DOI: 10.1017/s0079497x00013074 (cit. on p. 42).

Volkmann, A. (2018). "Methods and Perspectives of Geoarchaelogical Site Catchment Analysis: Identification of Palaeoclimate Indicators in the Oder Region from the Iron to Middle Ages". In: *Digital Geoarchaeology - New Techniques for Interdisciplinary Human-Environmental Research*. Ed. by C. Siart, M. Forbriger, and O. Bubenzer. Natural Science in Archaeology. Cham, Switzerland: Springer, pp. 27–44. DOI: 10.1007/978-3-319-25316-9_3 (cit. on pp. 36, 42).

Volkmann, P. (1983). "Boker Tachtit: core reductions". In: *Prehistory and Paleoenvironments in the Central Negev, Israel. Volume III the Avdat/Aqev Area, Part 3*. Ed. by A. Marks. Dallas: Southern Methodist University Press, pp. 127–190 (cit. on p. 51).

Volkmann, P. (1989). "Boker Tachtit: the Technological Shift from the Middle to the Upper Palaeolithic in the Central Negev, Israel". PhD thesis. Dallas: Southern Methodist University, p. 694 (cit. on p. 51).

von Suchodoletz, H., M. van Meer, P. Kühn, K. Wiedner, T. Schunke, and T. Reimann (Mar. 2023). "Deciphering timing and rates of Central German Chernozem/Phaeozem formation through high resolution single-grain luminescence dating". In: *Scientific Reports* 13.1. DOI: 10.1038/s41598-023-32005-9 (cit. on p. 107).

Vrydaghs, L., Y. Devos, and Á. Pető (2017). "Opal Phytoliths". In: *Archaeological Soil and Sediment Micromorphology*. John Wiley & Sons,

Ltd. Chap. 18, pp. 155–163. DOI: https://doi.org/10.1002/9781118941065.ch18. eprint: https://onlinelibrary.wiley.com/doi/pdf/10.1002/9781118941065.ch18. URL: https://onlinelibrary.wiley.com/doi/abs/10.1002/9781118941065.ch18 (cit. on p. 176).

Wachtel, I., R. Zidon, S. Garti, and G. Shelach-Lavi (2018). "Predictive modeling for archaeological site locations: comparing logistic regression and maximal entropy in north Israel and north-east China". In: *Journal of Archaeological Science* 92, pp. 28–36 (cit. on pp. 73, 184).

Weiss, A. (2001). *Topographic Position and Landform Analysis*. Poster presentation, ESRI user conference, San Diego, CA. URL: http://www.jennessent.com/arcview/TPI_Weiss_poster.htm (cit. on pp. 60, 199).

Whitcraft, A., E. F. Vermote, I. Becker-Reshef, and C. O. Justice (2015). "Cloud cover throughout the agricultural growing season: Impacts on passive optical earth observations". In: *Remote Sensing of Environment* 156, pp. 438–447. DOI: 10.1016/j.rse.2014.10.009 (cit. on p. 134).

Whitley, T., G. Moore, G. Goel, and D. Jackson (2010). "Beyond the marsh: settlement choice, perception and spatial decision-making on the Georgia coastal plain". In: *CAA 2009. Making History Interactive. Computer Applications and Quantitative Methods in Archaeology. Proceedings of the 37th Conference*. Ed. by B. Frischer, J. Crawford, and D. Kollers. Oxford, Williamsburg, VA, USA: Archaeopress, pp. 380–390 (cit. on p. 57).

Williams, J. (2003a). "An examination of upper palaeolithic flake technologies in the marginal zone of the Levant". In: *More than Meets the Eye. Studies on Upper Palaeolithic Diversity in the Near East*. Ed. by A. Goring-Morris and A. Belfer-Cohen. Oxford, Oakville: Oxbow Books, pp. 196–208 (cit. on p. 52).

Williams, J. (2003b). "Examining the Boundaries of the Levantine Aurignacian". PhD thesis. Dallas: Southern Methodist University, p. 409 (cit. on p. 52).

Williams, J. and C. Bergman (2010). "Upper palaeolithic levels XIII-VI (A and B) from the 1937-1938 and 1947-1948 Boston College excavations and the Levantine Aurignacian at Ksar Akil, Lebanon". In: *Paleorient* 36.2, pp. 117–161 (cit. on pp. 51, 52).

Yeshurun, R., J.-M. Tejero, O. Barzilai, I. Hershkovitz, and O. Marder (2018). "Upper palaeolithic bone retouchers from Manot cave (Israel): a preliminary analysis of an (as yet) rare phenomenon in the Levant". In: *The Origins of Bone Tool Technologies. Retouching the Palaeolithic: Becoming Human and the Origins of Bone Tool Technology Conference*. Ed. by J. Hutson, A. García-Moreno, E. Noack, E. Turner, A. Villaluenga, and S. Gaudzinski-Windheuser. Mainz, Heidelberg: Verlag des Romisch-Germanischen Zentralmuseums, Propylaeum, pp. 1–9 (cit. on p. 52).

Zech, M., R. Zech, W. Zech, B. Glaser, S. Brodowski, and W. Amelung (2008). "Characterisation and palaeoclimate of a loess-like permafrost palaeosol sequence in NE Siberia". In: *Geoderma* 143.3, pp. 281–295. DOI: 10.1016/j.geoderma.2007.11.012 (cit. on pp. 105, 109).

Zeeden, C., M. Hark, U. Hambach, B. Marković, and L. Zöller (2007). "Depressions on the Titel loess plateau : Form, pattern, genesis". In: *Geographica Pannonica* br. 11, pp. 4–8. DOI: 10.5937/GeoPan0711004Z (cit. on pp. 85, 108).

Zickel, M. (2020). "Spatial patterns of Moroccan transhumance: Geoarchaeological field work & spatial analysis of herder sites in the High Atlas Mountains of Morocco". In: *Kölner Ethnologische Beiträge* (cit. on p. 79).

Zickel, M., D. Becker, I. Verheul, Y. Yener, and C. Willmes (2016). *Paleocoastlines GIS dataset*. DOI: https://doi.org/10.5880/SFB806.20 (cit. on p. 53).

Zickel, M. and M. Gröbner (2023). *MiGIS toolbox for QGIS 3 [code], in: E&G Quaternary Science Journal (1.0)*. DOI: 10.5281/zenodo.10527165. URL: https://zenodo.org/records/10527165 (cit. on pp. 142, 186).

Zickel, M., M. Gröbner, A. Röpke, and M. Kehl (Jan. 2024). "MiGIS: micromorphological soil and sediment thin section analysis using an open-source GIS and machine learning approach". In: *E&G Quaternary Science Journal* 73.1, pp. 69–93. DOI: 10.5194/egqsj-73-69-2024 (cit. on pp. 21, 22, 156, 157, 237, 239, 241, 243, 245, 247).

Zickel, M., J. J. Nett, A. Röpke, S. Opitz, D. Handy, S. Rische, F. Steininger, N. Mantke, and T. Reimann (sub.). *Pleistocene-Holocene Landscape Evolution and Closed Depressions at the Eastern Carpathian Basin (Toboliu, Romania)*. (submitted) (cit. on pp. 17, 39, 153, 154, 173–175).

Zilberman, E. (2010). *Ze'elim: Sheet 14-III*. Jerusalem (cit. on pp. 61, 77).

Zohary, M. (1973). *Geobotanical Foundations of the Middle East*. Stuttgart (cit. on pp. 58, 74, 195).

Zupancich, A., M. Shemer, and R. Barkai (2021). "Biface use in the lower paleolithic Levant: first insights from late Acheulean Revadim and Jaljulia (Israel)". In: *Journal of Archaeological Science: Reports* 36, p. 102877 (cit. on p. 62).